

Martin Kroner

**Resonant photon-exciton
interaction in semiconductor
quantum dots**

München, März 2008

Resonant photon-exciton interaction in semiconductor quantum dots

Dissertation
an der Fakultät für Physik
der Ludwig-Maximilians-Universität München



vorgelegt von
Martin Kroner
aus Neuendettelsau

München, März 2008

Erstgutachter: Prof. Dr. K. Karrai

Zweitgutachter: Prof. Dr. J. Feldmann

Tag der mündlichen Prüfung: 27. Mai 2008

Zusammenfassung

Selbst-organisierte Halbleiter Quantenpunkte stellen eine dreidimensionale, räumliche Eingrenzung für Ladungsträger im Festkörpersystem dar. Diese Eingrenzung verändert die Zustandsdichte, was zu atomartigen optischen Eigenschaften von Quantenpunkten führt, die mit Hilfe von absorbierten oder emittierten Photonen untersucht werden können. Aufgrund der scharfen Resonanzlinien, die in optischen Spektren beobachtet werden, bezeichnet man Quantenpunkte auch oft als künstliche Atome. Selbst-organisierte Quantenpunkte sind jedoch Halbleiter Nanostrukturen, die in einem Festkörperkristall eingebettet sind. Dadurch werden ihre physikalischen Eigenschaften von ihrer Natur als Festkörper gegeben. Durch die geeignete Herstellung von Halbleiter Heterostrukturen in die die Quantenpunkte eingebettet sind, können ladungsdurchstimmbare Systeme erzeugt werden. Dies bedeutet, dass der Quantenpunkt kontrolliert mit einzelnen Elektronen geladen werden kann, indem eine Spannung an die Probe angelegt wird. Darüber hinaus kann die Probe so konstruiert werden, dass die Quantenpunktzustände an Kontinuumszustände gekoppelt sind, die sich in der Nähe des Quantenpunkts befinden. In dieser Arbeit werden sowohl die atomartigen Eigenschaften der einzelnen ladungsdurchstimmbaren Quantenpunkte als Zwei-Niveau System, als auch deren Festkörpereigenschaften untersucht. Dieses führt einerseits zur Beobachtung der Rabi-Aufspaltung der Quantenpunktzustände, einem typischen Merkmal eines Zwei-Niveau Systems. Andererseits führt die Tunnelkopplung der Quantenpunktzustände an ein Kontinuum in der Heterostruktur, zur Beobachtung des nichtlinearen Fano-Effekts. Dieser Effekt kann an Quantenpunkten in einem neuen, nichtlinearen Bereich untersucht werden, der in der Atomspektroskopie nicht so einfach zugänglich ist. Darüberhinaus wird die Dynamik von einzelnen Elektronen- oder Loch-Spins in einem Quantenpunkt untersucht. Hier spielt wieder der Festkörpercharakter der Quantenpunkte eine entscheidende Rolle, wie zum Beispiel in einem Einzel-Elektronen-Spin Resonanz Experiment gezeigt wird, welches an Quantenoptische Experimente aus der Atomoptik angelehnt ist. Hierbei zeigt sich, dass in einem Halbleiter Quantenpunkt, die Spin Dynamik von Elektronen oder Löchern von der Kopplung an ein Elektronen Reservoir und letztendlich von der Hyperfeinwechselwirkung dominiert ist.

Die Experimente in dieser Arbeit wurden mit beugungsbegrenzten Tieftemperaturmikroskopen durchgeführt. Diese Mikroskope wurden entwickelt um ein magnetisches Feld parallel oder senkrecht zur Lichtausbreitungsrichtung anlegen zu können. Die Probe wurde in flüssigem Helium auf eine Temperatur von 4.2 K gekühlt.

Um die natürliche Linienbreite ($1 - 2 \mu\text{eV}$) der exzitonischen Übergänge in einem Quantenpunkt auflösen zu können wurde resonante Rayleigh Streuung angewendet. Diese Methode wird zum ersten Mal auf neutrale, negativ sowie positiv geladene Zustände ein und desselben Quantenpunkts angewandt. Darüber hinaus wird in

diese Arbeit vorgestellt, wie Elektronen oder Löcher durch optisches Pumpen in einem Nichtgleichgewichtszustand gespeichert werden können. Dies erlaubt die nahezu perfekte Ausrichtung des Elektronen- oder Loch-Spins in einem Quantenpunkt, parallel oder antiparallel zu einem angelegten magnetischen Feld.

Abstract

Semiconductor self-assembled quantum dots form a three dimensional confinement for charge carriers in the solid state matrix. The confinement modifies the density of states, leading to atom like optical properties of quantum dots that can be studied by absorption or emission of photons. Due to the sharp resonance lines that are observed in optical spectra, quantum dots are often referred to as artificial atoms. However, self-assembled quantum dots are semiconductor nanostructures and they are incorporated into a solid state crystal yielding physical properties given by their solid state nature. By tailoring the semiconductor heterostructure around the quantum dot a charge tunable device can be fabricated. As a result, the quantum dot can be charged with single electrons in a controlled way via an applied bias. Furthermore, the device can be designed such that the quantum dot states are coupled to continuum states in the vicinity of the quantum dot. In this thesis, the two-level atom like optical properties of single charge tunable quantum dots are investigated as well as their solid state nature. This, on one hand, leads to the observation of Rabi splitting of the quantum dot states, a typical feature of a two-level system. On the other hand, the introduction of a tunnel coupled continuum of states into the device leads to the discovery of the nonlinear Fano effect. An effect that can be explored on quantum dots in a different, nonlinear regime that is not easily accessible by atom spectroscopy. Furthermore, the dynamics of a single electron or hole spin in a quantum dot are investigated. Here, again, the solid state nature of the quantum dot manifests itself in a single electron spin resonance experiment adopted from quantum optical experiments on atoms. We find that the spin dynamics of electrons and holes in a semiconductor quantum dot are dominated by coupling to the electron reservoir or finally by the hyperfine interaction.

The experiments presented in this thesis were performed with diffraction-limited cryogenic microscopes. The microscopes were designed such that they operate in a magnetic field that can be applied parallel or perpendicular to the light propagation direction. The sample was cooled to liquid helium temperature (4.2 K).

Resonant Rayleigh scattering spectroscopy is used to gain high spectral resolution, yielding the natural resonance linewidth of the excitonic transition in a quantum dot ($1 - 2 \mu\text{eV}$). This method is applied to neutral, negatively, and positively charged states on the very same quantum dot for the first time. Furthermore, resonant optical pumping of the electron or hole ground state into a shelving state is presented in this work. This optical pumping allows the alignment of electron or hole spins in the quantum dot with near-unity fidelity, parallel or antiparallel to an applied magnetic field.

Contents

Introduction	1
Scope of the thesis	3
References	5
1 Charge tunable self-assembled quantum dots	9
1.1 Self-assembled quantum dots	10
1.2 Charge-tunable quantum dots	13
1.3 Optical characterization of single quantum dots	16
1.3.1 The quantum confined Stark effect	18
1.3.2 Charging a quantum dot with holes or electrons	19
1.3.3 Magneto-luminescence of excitons in quantum dots	21
References	25
2 Confocal microscopy of single quantum dots	29
2.1 Confocal microscopy	30
2.2 Cryogenic microscopy	33
2.2.1 Spatial resolution	36
2.2.2 Fabry-Pérot cavity	37
2.2.3 Polarization properties	39
2.2.4 Confocal microscope for Voigt geometry	40
References	43
3 High resolution laser spectroscopy	45
3.1 Resonant laser spectroscopy in transmission	46
3.2 Stark-shift modulation spectroscopy	49
3.3 Interferometric Rayleigh scattering	50
3.4 Simultaneous measurement of the dispersive and absorptive scattering response of the neutral exciton	53
References	61
4 Saturation laser spectroscopy	63
4.1 Introduction	64
4.2 Power dependent laser spectroscopy	64

4.3	Saturation and power broadening of a single QD resonance	66
4.4	Conclusions	68
	References	69
5	Rabi splitting and ac-Stark shift of a charged exciton	71
5.1	Introduction	72
5.2	Two-laser pump and probe spectroscopy	72
5.3	The ac-Stark shift of a charged exciton	73
5.4	Rabi splitting of a charged exciton	75
5.5	Conclusion	76
	References	77
6	Voltage-Controlled Linewidth of Excitonic Transitions	79
6.1	Introduction	80
6.2	Electron tunnelling	82
6.3	Hole tunnelling	83
6.4	Conclusion	84
	References	87
7	The nonlinear Fano effect	89
7.1	Introduction	90
7.2	Coupling of a QD to a 2-dim continuum of states	90
7.3	Power dependent Fano effect	93
7.4	Voltage dependent tunnel coupling	93
7.5	Theory of a QD tunnel coupled to a continuum of states	94
7.6	Conclusions	96
	References	99
8	Two-color Spectroscopy on a Negatively Charged Exciton	101
8.1	Introduction	102
8.2	Methods	102
	8.2.1 The Sample	102
	8.2.2 Resonant Laser Spectroscopy	103
8.3	Spin Dependent Laser Spectroscopy	104
	8.3.1 Optical Spin Pumping	104
	8.3.2 Optical Pumping of the “Forbidden” Transition	108
	8.3.3 Polarization Dependence	109
8.4	Quantum Optics of the X^{1-} -state at a finite Magnetic field	110
	8.4.1 Quantum Optical Model	110
	8.4.2 Connection to the Experiment	112
8.5	Faraday Geometry	113
	8.5.1 Gate Voltage Dependence	114
	8.5.2 Magnetic Field Dependence	115

8.5.3	Power Dependence	117
8.5.4	Discussion	118
8.6	Voigt Geometry	119
8.6.1	High Resolution laser spectroscopy	120
8.6.2	Optical Spin Pumping in Voigt Geometry	121
8.6.3	Power Dependence of the Repump Signal	123
8.7	Summary and Conclusion	124
	References	127
9	Optical detection of single electron spin resonance	131
9.1	Introduction	132
9.2	ESR pumping scheme	132
9.3	Spin initialization	134
9.4	Determination of the electron g-factor	135
9.5	Optically detected electron spin resonance	136
9.6	Conclusion	139
	References	141
10	Optical pumping and probing of holes	143
10.1	Introduction	144
10.2	Optical pumping of holes	144
10.3	Power dependent hole lifetime	146
10.4	Conclusion	147
	References	149
11	Optically controlled hole spin lifetime in a optically charged quantum dot	151
11.1	Introduction	152
11.2	Spin shelving of an optically created hole in a QD	153
11.3	Laser power dependent hole spin lifetime	156
11.4	Conclusion	157
	References	159
	Summary and perspectives	161
	References	165
	List of publications	167
	Appendix A: Theory of a QD coupled to a two-dimensional continuum	171
A.1	General description	171
A.2	Nonlinear Fano effect	172
A.3	Fano factor for a tunnel coupling	174
	References	177

Appendix B: List of setup components	179
Acknowledgements	181
Danksagung	183
Lebenslauf	185

Introduction

Nano science and nano technology is probably the most dynamic and interdisciplinary field of research and development of these days [1, 2, 3, 4]. It is driven by the rapid progress towards the nano meter scale in the semiconductor industry [5] but also in the chemical [6] and pharmaceutical [7] industry as well as in engineering [8, 9]. Furthermore, the notion “nano” is present in every day life like no other development emerging of a science lab since nuclear power. Nano are called products from portable music players to cars [10, 11].

This high rating of nano science is not unfounded. The nano scale is a distinguished length scale, where the top down approach of semiconductor research and engineering, and the bottom up approach of chemistry, biology, and molecular physics merge. Furthermore, the nano scale represents the frontier of miniaturization limited by the atomic character of matter. Finally, on the nano scale the physical laws are not dominated by the classical macroscopic physics but rather by quantum mechanics. In consequence, nano science allows to tailor physical systems to study particular quantum mechanical phenomena or even to design nanoscopic systems to exploit their unique features for quantum mechanical devices.

Self-assembled quantum dots represent nanoscopic systems in a comprehensive way [12]. They are located at the very interface between solid state physics and atom optics [13, 14]. Being representatives of the bottom up approach, they are formed by self organization of atoms on a surface. However, they can be embedded in solid state devices like semiconductor heterostructures which are themselves achieved by top down fabrication. While self-assembly growth of quantum dots leads to a statistical distribution of sizes and material compositions, the molecular epitaxial growth of the heterostructure allows to design devices with atomic precision. The resulting nano scale objects are droplets of one semiconductor material incorporated in a crystal of another semiconductor. Within these islands electrons can be trapped. The spatial confinement of the electrons leads to a quantization of their energy. The result is an artificial device that is formed by about ≈ 10000 atoms of the solid state crystal while the electrons in this device behave very similar to an electron in the shell of a single atom. For this reason quantum dots are also often referred to as artificial atoms [15]. The devices into which a quantum dot can be incorporated are manifold. In a field effect structure, an electric field can be applied to the quantum dot [16, 17, 18]. Furthermore, a well designed structure allows a controlled charging

of the quantum dot with single electrons. In a different kind of heterostructures optical cavities can be fabricated around the quantum dot [19, 20, 21, 22]. This allows to modify the optical properties as the radiative decay time of quantum dot excited states [23, 24, 25, 26].

Like in many applications of nano scale systems, there are also applications for quantum dots that utilize their obvious features. In quantum dot lasers, for example, the artificial atom properties are exploited making use of quantum dots as gain medium [27]. In electronic devices, quantum dots can be used for charge storage, even at room temperature [28]. Such systems are very promising for solid state nonvolatile memory cells in computers [29]. On the other hand, there is the idea of utilizing quantum mechanical properties of a coherent system, a quantum bit or qubit, for novel computation schemes [30]. A single atom represents a perfect qubit that seems to be ideal for quantum computation. However, an atom has to be kept in a complex electrostatic trap, and the coupling of many atoms to form a quantum register turns out to be nontrivial and impractical for industrial application [31]. In solid state nano systems, like quantum dots or superconducting circuits, it might be possible to fabricate coupled qubits in a scalable way [32, 33, 34, 35]. This is expected to be possible by using standard technology for the fabrication of integrated circuits. Another application for quantum dots is given by their unique feature as a two level system [36, 37]. A quantum dot that contains only a single electron hole pair - an exciton - emits only one single photon under recombination of this exciton [37]. Since single excitons can be injected in a quantum dot with high degree of control, it represents an ideal single photon source [38, 39]. By injecting two excitons in a quantum dot - a so called biexciton [40, 41] - the quantum dot can act as a triggered source for single, polarization entangled photon pairs [42, 43], as they are important for secure communication based on quantum key distribution [44].

Beyond the applications of nano systems for novel devices in quantum computation or optoelectronics, quantum dots are promising model systems to study fundamental physics. Quantum mechanics, electronics and optics merge in nano science in a natural way and the controlled fabrication allows for a specific design of a quantum system for a specific experiment. For example, a self-assembled quantum dot device can be designed for performing quantum optical experiments similar to those on atoms. A single quantum dot in a high finesse cavity exhibits a strong coupling of the excitonic transition to the vacuum cavity mode [45, 46], while on a single isolated quantum dot Rabi splitting can be observed [47]. In another device a continuum is deliberately introduced leading to the observation of Fano resonances [48, 49]. Furthermore a quantum dot can act as a local probe for particular solid state properties of its host material. A single electron that is trapped in a quantum dot can be used to study the coupling of the spin degree of freedom of the electron to the nuclei of the semiconductor [50, 51]. This coupling is strongly dependent on the quantum mechanical state of the electron in the quantum dot and the composition of the different semiconductor materials. In addition, the electron spin can also couple to a reservoir of electron spins nearby the quantum dot [52, 53]. Such a coherent

coupling will lead to the observation of the Kondo effect [54, 55, 56].

Scope of the thesis

In the presented work, the optical properties of single self-assembled quantum dots were studied by coherent laser spectroscopy [57]. The quantum dots were embedded in semiconductor field effect heterostructures allowing for controlled charging of the quantum dots with single electrons [16]. The devices were tailored to study either the two level atomic properties of the quantum dot or to investigate the solid state nature of the quantum dot states [P15, P13, P16].

The fabrication of self-assembled quantum dot samples is described in chapter 1. There, the different field effect heterostructures in which the quantum dots are embedded are explained as well. The devices were designed to couple the quantum dot in a controlled way to various reservoirs present in the structure. The method of charging the quantum dot with single electrons or holes, by applying a voltage to the field effect device or by optical pumping, is introduced. Furthermore, the characterization of samples by optical means is discussed.

For the optical investigation of single self-assembled quantum dots a high resolution optical setup is required to work at cryogenic temperatures of liquid helium. In chapter 2, the microscopes that fulfill these requirements, and that were used in the presented work, are introduced. A microscope is described that was developed to perform experiments in a magnetic field applied in Voigt geometry.

The concept of high resolution resonant laser spectroscopy is introduced in chapter 3. The experimental setup for the detection of resonant transmission of a single quantum dot under excitation with one or two lasers is explained. The basic principles of resonant Rayleigh scattering are derived and the influence of laser power and polarization on the transmission signal are discussed. Finally, the concurrent measurement of the real and imaginary scattering response of a single quantum dot is presented.

Power dependent resonant laser spectroscopy on a single quantum dot reveals the two level nature of the ground state excitonic transitions. The unmistakable signatures are the saturation of the transmission contrast and power induced broadening of the resonance. In chapter 4, experimental results of power dependent laser spectroscopy are presented. The contribution of dephasing and radiative decay to the linewidth as well as spectral fluctuations are discussed. An analysis of the signal to noise of the experiment is given.

A further optical signature of a two-level system is explored in chapter 5. The Rabi splitting and ac-Stark effect of a single exciton in a quantum dot is studied by a resonant two color pump and probe experiment.

The possibility to tailor the quantum dot heterostructure allows to introduce a continuum of states that is coupled via tunnelling to the excited state of the quantum dot. In chapter 6, the voltage controlled tunnel coupling is introduced.

The coherent optical coupling of the ground state of the quantum dot and the two tunnel coupled excited states, one being a discrete state, one a two-dimensional continuum state, lead to quantum mechanical interference and hence to a characteristic absorption line shape - the Fano resonance. The non-linear power dependent Fano effect is presented in chapter 7 that was discovered in the framework of this thesis. Reducing the tunnel coupling of the electronic states in the quantum dot to the back contact continuum of states allows for an optical pumping of the spin of a resident electron in the quantum dot within weak magnetic fields. Spin shelving of the electron ground state is presented in chapter 8. Two-color laser spectroscopy is used to uncover ideally forbidden but in reality weakly allowed optical transitions in the quantum dot that are exploited in the optical spin pumping scheme. This allows to measure the electron g-factor in an optical experiment, a method that was pioneered in this work.

Optical spin pumping and the precise determination of the electron Zeeman splitting is the prerequisite to perform the first optically detected spin resonance experiment on a single electron in a quantum dot. This is presented in chapter 9 exhibiting electron spin dynamics that are dominated by the interaction of electrons with the nuclei.

Charging a single quantum dot with electrons or holes is introduced in chapter 10. The hole is created by non-resonant optical pumping and the lifetime of the hole is determined by power dependent spectroscopy. In chapter 11, optical pumping of the spin of the resident hole in a quantum dot with an external magnetic field is investigated. The hole spin lifetime is studied as a function of the non-resonant excitation power.

References

- [1] http://www.nsf.gov/news/index.jsp?prio_area=10.
- [2] <http://www.bmbf.de/de/nanotechnologie.php>.
- [3] http://www.uni-muenchen.de/lmu_excellent/nim/index.html.
- [4] <http://www.cens.de/>.
- [5] http://www.intel.com/pressroom/archive/releases/20070918corp_a.htm.
- [6] Sun cream with nano particles, www.loreal.com/.
- [7] Antimicrobial bandages/ wound dressings, <http://global.smith-nephew.com>.
- [8] Self cleaning glass, <http://www.pilkington.com/>.
- [9] Scratch resistant coatings, <http://www.nanophase.com/>.
- [10] <http://www.apple.com/de/ipodnano/>.
- [11] http://de.wikipedia.org/wiki/Tata_Nano.
- [12] P. Michler (Ed.): Single Quantum Dots, Topics Appl. Phys. 90 (Springer, Berlin, Heidelberg, 2003).
- [13] P.M. Petroff, A. Lorke, and A. Imamoglu, Phys. Today **54**, 46 (2001).
- [14] K. Karrai, R.J. Warburton, C. Schulhauser, A. Högele, B. Urbaszek, E.J. McGhee, A.O. Govorov, J.M. Garcia, B.D. Gerardot, and P.M. Petroff, Nature **427**, 135 (2004).
- [15] D.D. Awschalom, and J.M. Kikkawa, Phys. Today **52**, 33 (1999).
- [16] H. Drexler, D. Leonard, W. Hansen, J.P. Kotthaus, and P.M. Petroff, Phys. Rev. Lett. **73**, 2252 (1994).
- [17] R.J. Warburton, C. Schäfflein, D. Haft, F. Bickel, A. Lorke, K. Karrai, J.M. García, W. Schoenfeld, and P. M. Petroff, Nature **405**, 926 (2000).
- [18] J.J. Finley, A.D. Ashmore, A. Lemaître, D.J. Mowbray, M.S. Skolnick, I.E. Itskevich, P.A. Maksym, M. Hopkinson, and T.F. Krauss, Phys. Rev. B **63**, 073307 (2001).

- [19] P. Michler, A. Kiraz, C. Becher, W.V. Schoenfeld, P.M. Petroff, Lidong Zhang, E. Hu, A. Imamoglu, *Science* **290**, 2282 (2000).
- [20] E. Moreau, I. Robert, J.M. Gerard, I. Abram, L. Manin, and V. Thierry-Mieg, *Appl. Phys. Lett.* **79**, 2865 (2001).
- [21] M. Pelton, C. Santori, J. Vuckovic, B. Zhang, G.S. Solomon, J. Plant, and Y. Yamamoto, *Phys. Rev. Lett.* **89**, 233602 (2002).
- [22] A. Badolato, K. Hennessy, M. Atatüre, J. Dreiser, E. Hu, P.M. Petroff, and A. Imamoglu, *Science* **308**, 1158 (2005).
- [23] E.M. Purcell, H.C. Torrey, and R.V. Pound, *Phys. Rev.* **69**, 37 (1946).
- [24] K. Hennessy, A. Badolato, M. Winger, D. Gerace, M. Atatüre, S. Gulde, S. Fält, E. L. Hu, and A. Imamolu, *Nature* **445**, 896 (2007).
- [25] P. Lodahl, A. Floris van Driel, I.S. Nikolaev, A. Irman, K. Overgaag, D. Vanmaekelbergh, W.L. Vos, *Nature* **430**, 654 (2004).
- [26] A. Kress, F. Hofbauer, N. Reinelt, M. Kaniber, H.J. Krenner, R. Meyer, G. Böhm, and J.J. Finley, *Phys. Rev. B* **71**, 241304 (2005).
- [27] H. Ishikawa, H. Shoji, Y. Nakata, K. Mukai, M. Sugawara, M. Egawa, N. Otsuka, Y. Sugiyama, T. Futatsugi, and N. Yokoyama, *J. Vac. Sci. Technol. A* **162**, 794 (1998).
- [28] A. Marent, M. Geller, D. Bimberg, A.P. Vasiev, E.S. Semenova, A.E. Zhukov, and V.M. Ustinov, *Appl. Phys. Lett.* **89**, 072103 (2006).
- [29] C.R. Müller, L. Worschech, A. Schliemann, and A. Forchel, *IEEE El. Dev. Lett.* **27**, 955 (2006).
- [30] D. Loss and D.P. DiVincenzo, *Phys. Rev. A* **57**, 120 (1998).
- [31] C.F. Roos, M. Riebe, H. Haffner, W. Hansel, J. Benhelm, C. Becher, F. Schmidt-Kaler, R. Blatt, *Science* **304**, 1478 (2004).
- [32] J.R. Petta, A.C. Johnson, J.M. Taylor, E.A. Laird, A. Yacoby, M.D. Lukin, C.M. Marcus, M.P. Hanson and A.C. Gossard, *Science* **309**, 2180 (2005).
- [33] E.A. Stinaff, M. Scheibner, A.S. Bracker, I.V. Ponomarev, V.L. Korenev, M.E. Ware, M.F. Doty, T.L. Reinecke, and D. Gammon, *Science* **311**, 636 (2006).
- [34] F. H. L. Koppens, C. Buizert, K. J. Tielrooij, I. T. Vink, K. C. Nowack, T. Meunier, L. P. Kouwenhoven, and L. M. K. Vandersypen, *Nature* **442**, 766 (2006).
- [35] J.H. Plantenberg , P.C. de Groot , C.J.P.M. Harmans, and J. E. Mooij, *Nature* **447**, 836 (2007).

- [36] A. Zrenner, E. Beham, S. Stuffer, F. Findeis, M. Bichler, and G. Abstreiter, *Nature* **418**, 612 (2002).
- [37] P. Michler, A. Imamoglu, M.D. Mason, P.J. Carson, G.F. Strouse, and S.K. Buratto, *Nature* **406**, 968 (2000).
- [38] O. Benson, C. Santori, M. Pelton, and Y. Yamamoto, *Phys. Rev. Lett.* **84**, 2513 (2000).
- [39] C. Santori, M. Pelton, G. Solomon, Y. Dale, and Y. Yamamoto, *Phys. Rev. Lett.* **86**, 1502 (2001).
- [40] M. Bayer, T. Gutbrod, A. Forchel, V.D. Kulakovskii, A. Gorbunov, M. Michel, R. Steffen, and K.H. Wang, *Phys. Rev. B* **58**, 4740 (1998).
- [41] A. Kiraz, S. Falth, C. Becher, B. Gayral, W.V. Schoenfeld, P.M. Petroff, L. Zhang, E. Hu, and A. Imamoglu, *Phys. Rev. B* **65**, 161303 (2002).
- [42] N. Akopian, N. H. Lindner, E. Poem, Y. Berlatzky, J. Avron, D. Gershoni, B. D. Gerardot and P. M. Petroff, *Phys. Rev. Lett.* **96**, 130501 (2006).
- [43] R.J. Young, R.M. Stevenson, P. Atkinson, K Cooper, D.A. Ritchie, A.J. Shields, *New Journal of Physics* **8**, 29 (2006).
- [44] E. Waks, K. Inoue, C. Santori, D. Fattal, J. Vuckovic, G.S. Solomon, Y. Yamamoto, *Nature* **420**, 762 (2002).
- [45] J.P. Reithmaier, G. Sek, A. Löffler, C. Hofmann, S. Kuhn, S. Reitzenstein, L.V. Keldysh, V.D. Kulakovskii, T.L. Reinecke, A. Forchel, *Nature* **432**, 197 (2004).
- [46] T. Yoshie, A. Scherer, J. Hendrickson, G. Khitrova, H.M. Gibbs, G. Rupper, C. Ell, O.B. Shchekin, D.G. Deppe, *Nature* **432**, 200 (2004).
- [47] X. Xu, B. Sun, P.R. Berman, D.G. Steel, A.S. Bracker, D. Gammon, L.J. Sham, *Science*, **371**, 929 (2007).
- [48] U. Fano, *Phys. Rev.*, **124**, 1866 (1961).
- [49] M. Kroner, A.O. Govorov, S. Remi, B. Biedermann, S. Seidl, A. Badolato, P.M. Petroff, W. Zhang, R. Barbour, B.D. Gerardot, R.J. Warburton, and K. Karrai, *Nature* **451**, 311 (2008).
- [50] D. Gammon, S.W. Brown, E.S. Snow, T.A. Kennedy, D. S. Katzer, and D. Park, *Science* **277**, 85 (1997).
- [51] P. Maletinsky, A. Badolato and A. Imamoglu, *Phys. Rev. Lett.* **99**, 056804 (2007).
- [52] J.M. Smith, P.A. Dalgarno, R.J. Warburton, A.O. Govorov, K. Karrai, B.D. Gerardot and P.M. Petroff, *Phys. Rev. Lett.* **94**, 197402 (2005).

- [53] M. Atatüre, J. Dreiser, A. Badolato, A. Högele, K. Karrai, and A. Imamoglu, *Science* **312** 551 (2006).
- [54] L. Kouwenhoven and L. Glazman, *Revival of the Kondo effect*, *Physics World*, January 2001, 33-38 (2001).
- [55] A.O. Govorov, K. Karrai, and R.J. Warburton, *Phys. Rev. B* **67**, 241307 (2003).
- [56] R.W. Helmes, M. Sindel, L. Borda, and J. von Delft, *Phys. Rev. B* **72**, 125301 (2005).
- [57] A. Högele, S. Seidl, M. Kroner, K. Karrai, R.J. Warburton, B.D. Gerardot, P.M. Petroff, *Phys. Rev. Lett.* **93**, 217401 (2004).

Chapter 1

Charge tunable self-assembled quantum dots

The experiments presented in this thesis are performed on self-assembled InGaAs quantum dots. In this chapter, a brief introduction to the fabrication of self-assembled quantum dots by the Stransky-Krastanov technique is given. In order to achieve a controlled charging, the quantum dots were embedded in a field effect structure. Different heterostructures and their influence on the coupling of the quantum dot states to continuum states of the solid state system are discussed. Photoluminescence spectroscopy is introduced as a tool to characterize the optical properties of single quantum dots. Finally, the effect of electric and magnetic fields on the optical spectra of a single quantum dot is described.

1.1 Self-assembled quantum dots

Quantum dots in general are artificial semiconductor nanostructures that confine charge carriers in all three spatial dimensions. Depending on the design of the quantum dot, it can confine electrons, holes, or excitons. Excitons are quasi particles formed by an electron in the conduction band bound to a hole in the valence band. To generate a confinement for electronic quantum dots, the electron distribution in a two-dimensional electron gas in a semiconductor heterostructure can be modified by gates on the surface of the crystal or by oxidation [1, 2, 3]. Such puddles of electrons are tunnel coupled to the leads and hence the physical properties of these systems are usually studied in electron transport measurements. The potential behind these kinds of quantum dots is that they can be coupled potentially to arrays [4, 5]. For the vision of a solid state based quantum computer, these systems seem to be the most promising candidates [6].

Semiconductor nanocrystals form a confinement potential for excitons [7, 8]. In these colloidal quantum dots, excitons can be created optically, and their transition energy strongly depends on the size of the nanocrystal. The size can be controlled in the growth process, which takes place by crystallization in a colloidal solution [7]. The larger the nanocrystal, the smaller the transition energy [9]. The chemical stability and high optical quality of these so-called colloidal quantum dots makes them ideal fluorescence markers for applications in biology and medicine [9].

Self-assembled semiconductor quantum dots combine the most prominent features of the above introduced quantum dot types [10] as they confine excitons in a semiconductor heterostructure. They are grown by molecular beam epitaxy by the Stransky Krastanov method (see Fig. 1.1). Depositing InAs on a GaAs [001] surface leads to growth of a strained InAs monolayer layer, the so-called wetting layer. The strain is due to the different lattice constants of InAs and GaAs: The lattice constant of InAs is with 6.06 \AA by 6.8% larger than the lattice constant of GaAs (5.65 \AA). If more InAs is deposited on the GaAs substrate, the strain in the InAs layer relaxes by the formation of InAs islands on the wetting layer. These islands are defect free and their dimensions are $\approx 20 - 30 \text{ nm}$ in diameter and up to 10 nm in height [11].

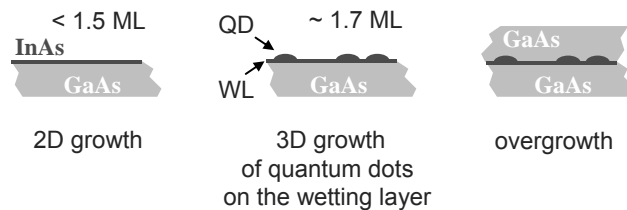


Figure 1.1: Growth of self-assembled quantum dots by the Stransky-Krastanov method. InAs grows as a strained layer on a GaAs surface until material corresponding to a layer thickness of ≈ 1.7 monolayer is deposited (left). Further deposition of InAs leads to three dimensional growth of InAs islands (middle). The growth of InAs is stopped after the deposition of 2.5 monolayer and the InAs islands are overgrown with GaAs (right).

The growth process is stopped after the deposition of an amount corresponding to 2.7 monolayers of InAs. Otherwise, the strain in the islands would relax by the formation of crystal defects. The quantum dots are then capped by GaAs to increase their distance from the crystal surface. Capping is important in order to isolate the electronic states in the quantum dot from fluctuating surface states. The result of the growth scheme is a layer of individual islands of strained InAs in a GaAs matrix. The reduced bandgap of InAs in the quantum dots with respect to the surrounding GaAs leads to a confinement of electrons and holes on the nanometer scale. The confinement leads to a quantization of the energy of the electron and hole states in the quantum dot. An electron and a hole form an exciton in the quantum dot, which recombines through the emission of a photon. The energy of the emitted photon can reveal information on the quantum mechanical electronic states in the quantum dot. In particular, the geometry of the quantum dot determines the confinement and hence the energy range of the emitted photons. Transition energies of quantum dots grown in the described way lie in the range of 0.95 eV [10], which corresponds to a wavelength of 1300 nm. An inconvenient wavelength range to work with standard silicon based photodetectors, which lose sensitivity above 1000 nm wavelength. However, silicon based photodetectors provide a high quantum efficiency and a superior signal to noise ratio at moderate pricing and hence their applicability is highly desirable. In order to shift the emission energy of the quantum dots into the range of Si-photodetectors, the size of the quantum dot has to be reduced. This can be achieved by introducing an annealing step in the growth process after overgrowth of the InAs islands with a capping layer of GaAs [11]. The heating of the sample leads to a diffusion of the Indium out of the island into the neighboring GaAs [11]. the height of the quantum dot is reduced leading to a volcano like shape as it is revealed by cross section STM measurements [12]. Quantum dots grown by the introduced “partly covered island” (PCI) technique emit photons at a wavelength of ≈ 950 nm. Due to the admixture of Gallium to the InAs, PCI quantum dots are also often referred to as InGaAs quantum dots. The quantum dot samples that were studied in the framework of this thesis have been grown by W. Schoenfeld, J. M. García and A. Badolato in the group of P. M. Petroff at UCSB in Santa Barbara (California, USA).

Generally, self-assembled quantum dots are distributed in size, shape and furthermore their Indium and Gallium content. This leads to a distribution of their characteristic properties; in particular their transition energies within the same sample. An optical spectrum measured on an ensemble of such dots exhibits an inhomogeneous broadening [13]. The broadening depends on the growth process and it is of the order of 10 meV, which is approximately 4 orders of magnitude broader than the natural linewidth ($\approx 1 \mu\text{eV}$) of the individual quantum dot resonances [14]. In order to resolve the linewidth and the shape of the resonance of an excitonic transition in a quantum dot, the signal of a single quantum dot needs to be isolated from the ensemble. Furthermore, single quantum dots have to be studied in order to perform coherent experiments on single electrons, excitons or holes. The optical setup that

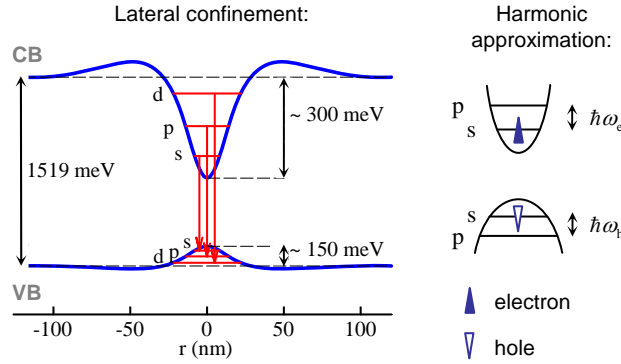


Figure 1.2: Potential landscape of a self-assembled InGaAs quantum dot in the growth plane. The reduced bandgap, given by the material distribution in the quantum dot (InGaAs), with respect to the surrounding GaAs leads to a confinement for electrons in the conduction band and holes in the valence band. The discrete states in the quantum dot are labelled s,p,d,... similar to the nomenclature of atomic states. The potential can be described in first order by a two-dimensional harmonic oscillator with an energy separation of $\hbar\omega_e$ for electrons in the conduction band and $\hbar\omega_h$ in the valence band, respectively.

is used for single quantum dot spectroscopy will be discussed in detail in the next chapter.

The confinement potential of a self-assembled quantum dot is given by the InAs distribution. The InAs distribution is rather narrow and it changes abruptly in the growth direction. Hence, the conduction and valence band edge can be described by a square-well potential [15]. Due to the small height (≈ 3 nm) of the InGaAs quantum dots, only the lowest energy level forms a bound state (Fig. 1.3). In lateral directions the InAs distribution changes smoothly, and the diameter of the quantum dot is large (≈ 20 nm). The potential landscape of the quantum dot can be approximated by a two-dimensional harmonic oscillator as shown in Fig. 1.2 [16]. A ladder of discrete states that can be occupied by electrons (in the conduction band) or holes (in the valence band) is created. The strain in the material of the quantum dot leads to a splitting of the hole band into the heavy hole band and the light hole band [17]. The light hole band is shifted in energy down by several tens of meV with respect to the heavy hole states. As a result, only heavy holes contribute to quantum dot excitons. In analogy to the shell structure of atoms the harmonic oscillator quantum dot states are called s, p, and d [18]. This however does not say anything about the symmetry of the Bloch-wavefunction of the electrons. In the conduction band the wavefunction of the electrons is s-type, while in the valence band it is p-type. Later on this will be discussed in more detail.

In contrast to colloidal nano crystals, in self-assembled quantum dots the electrons and holes are far away from the crystal surface. The wave function of the confined particles is isolated from the fluctuating surface states, and the optical spectrum of a single self-assembled quantum dot resembles the optical spectrum of an atom with narrow resonances. The optical resonance linewidths are mainly limited by the

radiative recombination rate and they exhibit only very reduced spectral jitter of the order of the linewidth [14]. Blinking and spectral jumps are not observed on the present self-assembled quantum dots, as known from optical studies of colloidal nano crystals [19]. Since self-assembled quantum dots are embedded in a solid state material, they can be easily incorporated into electronic devices. The most prominent example of such a device is a field effect structure, in which the quantum dots can be submitted to an electric field allowing single electron or hole charging in a controlled way [15].

1.2 Charge-tunable quantum dots

Self-assembled quantum dots (QDs) are grown by molecular beam epitaxy (MBE) on a GaAs substrate [10], It is the same technique also used to grow semiconductor heterostructures layer by layer with atomic precision. These structures can contain conducting layers of doped material and insulating layers with a larger bandgap than GaAs like AlAs. The samples, studied in the presented work, contain a QD-layer embedded in a field-effect device as shown in Fig. 1.3 [15, 20, 21]. The details of the structures differ from sample to sample in order to meet the specific needs of different experiments. However, the general concept of all samples is always the same and shall be discussed in this chapter.

In order to apply an electric field, the QD is positioned in between two plates of a capacitor. One of the plates is formed by a highly doped layer of GaAs which serves as a back contact. This layer is deposited on the wafer before the QD-layer is grown. The QD-layer is separated from the back contact by a layer of intrinsic GaAs, which acts as a tunnel barrier. The other plate of the capacitor is provided by a metallic

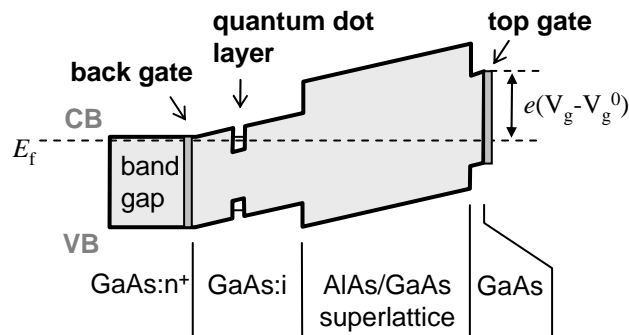


Figure 1.3: Conduction and valence band edge of the charge tunable device along the growth direction. The back gate is n-doped and pins the Fermi energy to the conduction band edge. A voltage applied to the sample falls off between the top gate and the back contact leading to a tilt of the band edges. The QD-layer is separated from the back contact by a layer of intrinsic GaAs, the tunnelling barrier. Between the top gate and the QD-layer, an AlAs/GaAs superlattice prevents current flow in the sample. Intrinsic GaAs separates the superlattice from the QD-layer and from the sample surface, where a semitransparent 5 nm thick NiCr electrode is deposited - the top gate.

top gate that is evaporated on the sample surface forming a Schottky contact to the GaAs. The geometry of the optical setup that is used for single QD spectroscopy as it will be introduced in the next chapter allows only top illumination of the sample. Hence, the metal top gate has to be semitransparent, which is achieved by a 5 nm thick layer of NiCr. In order to prevent current flow in the sample, an AlAs/GaAs superlattice is grown between the QD-layer and the sample surface. The superlattice is formed by a sequence of 2 nm thick AlAs layers separated by 2 nm thick layers of GaAs. An intrinsic GaAs capping layer above the QDs isolates them from the disorder potential, which is inherent to the growth of AlAs on GaAs. On the top of the wafer, a 5 nm thick layer of GaAs prevents oxidation of the Al in the superlattice. A sketch of the band edges of the sample in growth direction is shown in Fig. 1.3. We assume that the applied field between the top gate and the back contact drops off linearly over the whole intrinsic region between the top gate and the back contact. The conduction and valence band edge of the sample in the growth direction can be assumed to be linear, with a slope given by the applied bias [15, 20, 22]. The potential at the QD layer can be calculated with a simple lever arm argument. The electrostatic energy of an electron that is confined in the QD is [23]:

$$E_{\text{el}} = \frac{e(V_g + V_g^0)}{\eta}. \quad (1.1)$$

Here, the voltage applied to the gate V_g has to be complemented by the built-in voltage V_g^0 that is generated by the metal-semiconductor Schottky contact. The lever arm $\eta = d/b$ is the ratio between the distance d of the top gate from the back contact and b , the thickness of the tunnel barrier between the QD-layer and the back contact [20]. By applying a voltage to the sample the excitonic transition energy of the QD can be changed, but also the electrostatic energy of the electronic states in the QD is modified relative to the Fermi energy of the back contact which is pinned to the conduction band edge. The gate voltage can be chosen such that the electronic state of the QD can be shifted below the Fermi energy. As a result, an electron tunnels into the QD from the back contact [15, 20]. Here, the back contact is electrically grounded and it acts as an electron reservoir. The Coulomb repulsion between electrons prohibits a second electron to tunnel into the dot. For more positive gate voltages the Coulomb energy can be overcome and a second electron tunnels into the dot. The two electrons form a singlet in the QD ground state. By applying even more positive gate voltages, the excited states, the p states, of the QD are filled. The charging behavior of QDs has been studied extensively by capacitance spectroscopy [15, 24].

In this work, quantum dots in three different sample structures have been studied (see Fig. 1.4). All samples follow the general concept described above, but they differ in details. The first sample, A, contains a back contact that was obtained by Si-doping of the GaAs. The QD-layer is separated from the three dimensional back contact by a 25 nm tunnel barrier. Above the QD-layer, a 35 nm capping layer was deposited, before the AlAs/GaAs superlattice was grown. The distance of the back

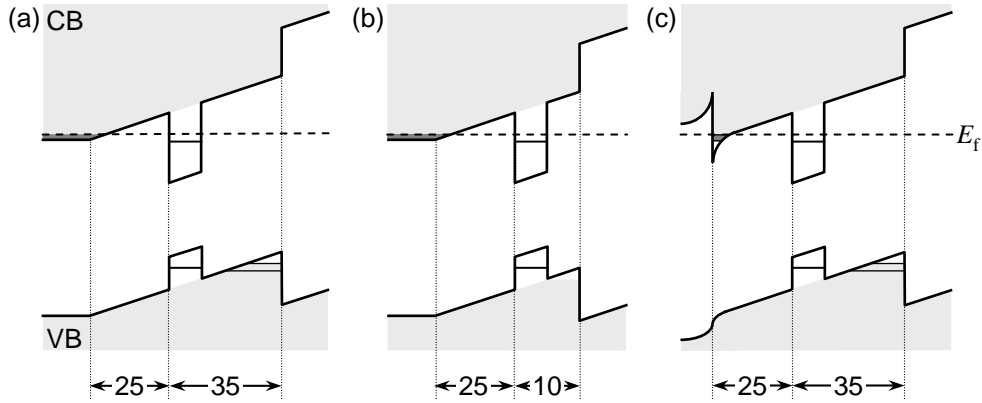


Figure 1.4: Schematic band edge characteristics in growth direction of the three different sample geometries studied in this work. The valence band (VB) and conduction band (CB) continuum is depicted by the light gray regions, the dark gray regions indicate the filled states in the conduction band. In (a) the potential of sample (A) is shown. The back contact is formed by n-doped GaAs. The QD-layer lies 25 nm above the back contact. At the interface to the AlAs/GaAs superlattice that is 35 nm above the QD-layer, a two-dimensional continuum of states develops in the valence band. The subbands of this continuum are indicated by the black lines. In sample B, shown in (b) the reduced distance of 10 nm between the QD-layer and the superlattice (with respect to sample A) shifts the two-dimensional continuum out of resonance with the QD hole states. In (c) the potential landscape of sample C is shown. The three dimensional back contact is replaced by a two-dimensional electron gas. The Fermi energy (E_f) is marked by the dashed line. All dimensions are given in nm.

contact to the sample surface with the NiCr top gate is $d = 175$ nm, leading to a lever arm of $\eta = 7$. By applying a gate voltage to the sample, the interface between the intrinsic GaAs capping layer and the AlAs/GaAs superlattice resembles a triangular potential well [25, 26]. Two-dimensional subbands are formed in this potential well [22, 27, 28]. These subbands can be occupied by photogenerated holes. Due to the large distance of 35 nm between the QD-layer and the GaAs-AlAs interface, the lowest two-dimensional subbands can be resonant with the zero dimensional hole state in the QD [22, 27]. As a result, a hole in the QD can be tunnel coupled to the two-dimensional continuum of states. This leads to the observation of the non-linear Fano effect as it is described in chapter 7. The potential along the growth direction for the region between the back contact and the superlattice is shown in Fig. 1.4 (a).

In sample B, the distance between the QD-layer and the AlAs/GaAs superlattice was reduced to 10 nm, in order to isolate the QD states from the hole continuum states in the surrounding heterostructure (Fig. 1.4 (b)). The tunnel barrier between the three dimensional n-doped back contact and the QD-layer is 25 nm, as in sample A. The distance to the sample surface, however is increased to 301 nm to the back contact and 276 nm to the QD-layer, respectively. This leads to a lever arm $\eta = 12$. Optical interference between light scattered by the QD and light reflected the surface could be reduced this way [29, 30].

The third structure was designed to reduce the tunnel coupling between the electronic conduction band states of the QD and the continuum of states in the back contact. Therefore, the dimensionality of the back contact was reduced, rather than the distance to the QD-layer. In sample C, the back contact is formed by a 300 nm thick layer of $\text{Al}_{0.35}\text{Ga}_{0.65}\text{As}$, with a Si-delta doping at the interface to the 25 nm thick intrinsic GaAs tunnel barrier (Fig. 1.4 (c)). The capping layer of this sample has a thickness of 35 nm corresponding is the leverarm $\eta = 12$.

The QD-layer of the wafers of sample B and C was grown with a QD density gradient. This is achieved by not rotating the wafer during the growth of the QDs. As a result, samples could be prepared from these wafers with a QD density low enough ($\approx 1 \times 10^8$ per cm^2) to resolve single quantum dots spatially separated within the diffraction-limited microscope resolution of $\approx 1 \mu\text{m}$. The sample A contains a large density of QDs which have to be spectrally resolved to perform single QD spectroscopy. The preparation of the samples is done in the clean room. Pieces with a dimension of $4 \times 5 \text{mm}^2$ are cleaved from the wafer region with the desired QD density. Indium is diffused into the sample to electrically contact the back contact. As a top gate 5 nm NiCr with an area of 1.8mm^2 is evaporated onto the sample surface.

1.3 Optical characterization of single quantum dots

In order to perform optical spectroscopy on single QDs, the sample is mounted in a fiber-based confocal microscope operating at cryogenic temperatures [31]. The details of the microscopes used in this work are explained in detail in chapter 2. Photoluminescence spectroscopy (PL) [20, 21, 32, 33, 34] is used to characterize a sample and to locate a suitable QD to be studied with high resolution laser spectroscopy [14]. The details of the setup can be found in chapter 3. In short, the sample is

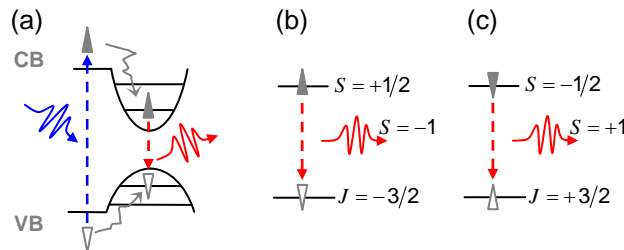


Figure 1.5: Photoluminescence spectroscopy on a single QD. In (a) it is shown how a laser photon creates an electron (filled triangle) hole (open triangle) pair in the wetting layer. The electron and hole relax into the QD by phonon scattering. The exciton in the QD decays under emission of a photon with a lower energy than that of the photon which created the electron and the hole in the wetting layer. The optical selection rules are depicted in (b) and (c). In (b) the spin of the electron is $+1/2$ and the angular momentum of the hole is $-3/2$. The total angular momentum of the exciton is hence -1 . The photon that is emitted in the decay process carries the angular momentum of the exciton. In (c) the case for an exciton spin $+1$ is shown.

illuminated with laser light with an energy that lies above the QD emission energy, therefore a laser diode emitting at 822 nm is used. This is the wavelength to create excitons in the wetting layer of the QD sample. The photo generated electrons and holes can relax into the QD by phonon scattering on the ps timescale [35, 36]. In the QD, the electrons and holes form an exciton that decays under emission of a photon after a characteristic lifetime of ≈ 1 ns [37]. Emitted photons are collected by the microscope objective and guided out of the cryogenic setup in the same fiber that is used for illumination. A fiber beam splitter passes 99% of the collected light into a grating spectrometer. In the spectrometer, the light is dispersed and the energy spectrum is measured with a CCD-camera.

The optical selection rules for interband transitions in a QD are as follows. The spin of the electron in the QD is either $S = +1/2$ (up) or $S = -1/2$ (down). The heavy holes involved in the optical scheme have an angular momentum of $\pm 3/2$. Hence, four different combinations of angular momentum of the exciton are possible: $\pm 1, \pm 2$. The recombination of the exciton happens under photon emission. Due to the conservation of angular momentum, the photon carries the spin of the exciton. As a result, only the exciton with spin ± 1 can decay radiatively. Such an exciton is composed out of an electron with $S = -1/2$ and a heavy hole with $J = +3/2$ or $S = +1/2$ and $J = -3/2$, respectively (as shown in Fig. 1.5 (b) and (c)). These excitons are called bright. The other combinations lead to an exciton with a spin of ± 2 . They can not decay under photon emission and are therefore called dark [38, 39, 40, 41].

The QD can be charged with extra which enter the QD via tunnelling from the back contact (see also section 1.2). One resident electron in the QD forms a singlet

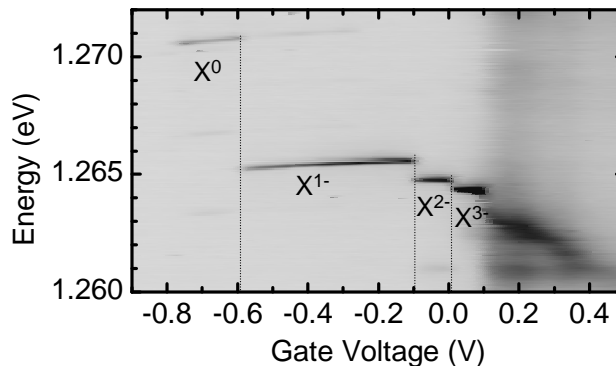


Figure 1.6: Charging diagram of a single QD measured in PL on sample A. The PL intensity is plotted as a function of the applied gate voltage and the energy. Dark areas represent large count rates. The jumps in energy that occur at the charging voltages can be clearly resolved. The charge states are labelled according to the exciton charge as X^0 for the neutral exciton, X^{1-} for the singly negatively charged exciton and X^{2-} for the doubly negatively charged exciton and so on. For large negative gate voltages, the exciton is ionized by the strong vertical electric field. Then electrons and holes tunnel out of the QD and no PL can be observed. The temperature was 4.2 K.

together with the photogenerated electron under compliance of the Pauli exclusion principle. The total angular momentum of the electrons in the QD is then 0, and the angular momentum of the negatively charged exciton is given by the angular momentum of the hole. Highly charged excitons can also be observed in the QD. The third electron occupies a p-state. After emission of a photon, the remaining two electrons can either form a singlet or a triplet state. These states possess different energies, hence, they can be distinguished in the PL spectra [40, 42]. The charging of an exciton with extra electrons alters the binding energy of the exciton. The energy of the emitted photons from a neutral exciton differ by 6 meV from a singly negatively charged exciton. This allows a determination of the charge state of a quantum dot by performing PL spectroscopy.

In Fig. 1.6 the PL signal of a QD from sample A is plotted as a function of gate voltage and energy. The charging of the QD leads to jumps of the resonance energy. It is obvious that for large negative gate voltages no PL can be observed. In this voltage regime, the large electric field ionizes the exciton. The electron then tunnels out of the QD into the back contact. The hole also leaves the QD and tunnels into the two-dimensional continuum of states at the interface to the superlattice as shown in Fig. 1.4 (a) [22]. Due to the weak confinement of this QD, the X^{3-} was the highest charge state to be observed. For more positive voltages, the onset of the filling of the wetting layer with electrons from the back contact makes the interpretation of the spectra difficult.

1.3.1 The quantum confined Stark effect

Apart from the charging that leads to jumps of the resonance the quantum confined Stark effect is observed in the charging diagram in Fig. 1.6. In Fig. 1.7 the resonance energy of a quantum dot is plotted versus the gate voltage. The resonance energy is

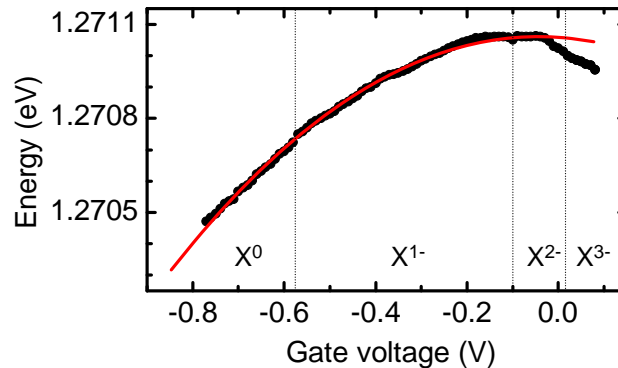


Figure 1.7: Quantum confined Stark effect of excitons in a QD. The energy jumps due to charging are subtracted and the data is fit by eqn. (1.2). The fit yields the values $E_0 = 1.271060 \pm (3 \times 10^{-6})$ eV and $p = 102 \pm 18$ meV/V, corresponding to a dipole length of 0.2 ± 0.03 nm and the polarizability $\beta = 1.15 \pm 2.3 \times 10^{-3}$ meV/V²

stitched by subtracting the charging energy. It is shifted by the gate voltage following a quadratic behavior. The exciton in the QD possesses a permanent dipole moment p . In an external electric field, the exciton furthermore exhibits a polarizability β . Hence, the energy of an exciton E in an external electric field F is given by [23]:

$$E = E_0 - pF + \beta F^2. \quad (1.2)$$

With E_0 the energy of the unperturbed exciton. For voltages $V_g \gtrsim 0$ V, a deviation from the quadratic behavior is observed (Fig. 1.7). This is caused by a filling of the wetting layer with electrons from the back contact at these voltages.

1.3.2 Charging a quantum dot with holes or electrons

A two-dimensional continuum of hole states is formed at the interface of the superlattice. The subbands of this hole continuum can be resonant with the hole state of the QD (Fig. 1.4 (a) and (c)). If the distance from the QD-layer to the superlattice

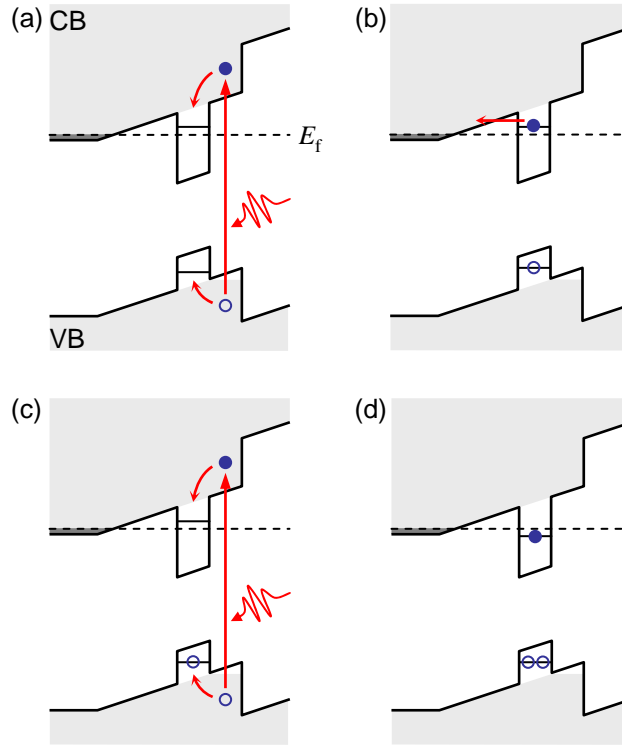


Figure 1.8: Optical charging of a QD with a hole. Electron and hole relax into the QD after their optical excitation into the wetting layer (a). The photogenerated electron tunnels out of the QD for voltages, at which the electronic state of the QD lies above the Fermi energy E_f (b). The hole remains trapped in the QD because the two-dimensional continuum of states is shifted below the QD hole state (c). Together with a second photogenerated electron hole pair an X^{1+} state is formed in the QD. This state is stable, because the additional Coulomb energy of the second hole pulls the electronic level below the Fermi energy (d).

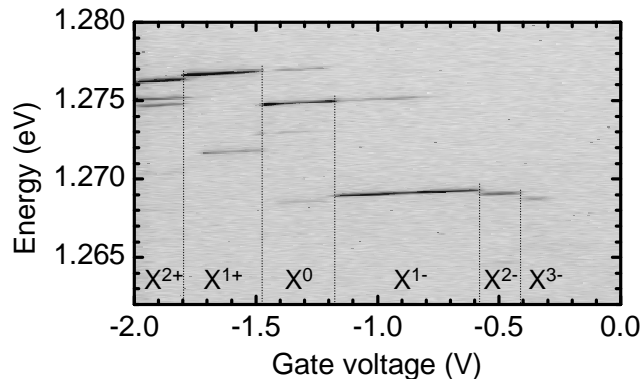


Figure 1.9: PL charging diagram of a QD from sample B. Charge states from X^{2+} to X^{3-} can be distinguished. The neutral and singly charged exciton can be identified by the characteristic energy offset of ≈ 6 meV. The charging voltages differ from those observed on sample A (see Fig. 1.6) due to the extended lever arm.

is reduced, the lowest subband energy of the hole continuum is shifted below the QD hole state. As a result, hole tunnelling out of the QD is prohibited. In sample B, the distance between the QD-layer and the superlattice was reduced to 10 nm (Fig. 1.4 (b) and Fig. 1.8). PL spectroscopy reveals positively charged excitons for gate voltages beyond the ionization voltage for the X^0 state. For gate voltages below the ionization voltage, the electron and hole tunnel out of the QD as described above (Fig. 1.8 (a)). In sample B, there is no empty state which is tunnel coupled to the QD hole state. At the same time the electron can still tunnel into the back contact as depicted in Fig. 1.8 (b). As a consequence, the hole remains trapped in the quantum dot. Together with another photogenerated electron hole pair (Fig. 1.8 (c)), the resident hole can form a positively charged exciton X^{1+} (Fig. 1.8 (d)) [43]. Due to the additional binding energy of the second hole, the electronic state in the QD is pulled below the Fermi energy and the X^{1+} state is stable for a certain gate voltage range. For more negative gate voltages, the additional attractive Coulomb energy is overcome, and the electron tunnels out of the quantum dot leaving behind two holes. This leads to the initial state for the formation of a doubly positively charged exciton, X^{2+} . Charge states from X^{6+} to X^{7-} can be observed on the very same InAs QD [44]. The InGaAs QDs, as they are studied in this work, exhibit a rather shallow confinement potential. Hence, only the states from the X^{2+} to the X^{3-} can be clearly resolved. This is shown in Fig. 1.9.

As already described above, the jumps in energy that occur on charging an exciton with additional electrons are well understood and vary only slightly from QD to QD. Even QDs from different samples and different sample geometries exhibit the same charging energies for additional electrons. A detailed analysis of the charging of QDs and the involved Coulomb interactions is given in [22]. The charging energies for holes do not follow a simple general law that can be applied to all QDs. On the same sample, we observe the X^{1+} to be red shifted or blue shifted with respect to the X^0

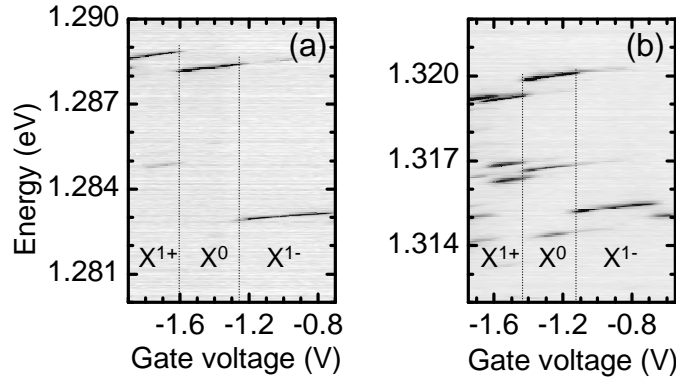


Figure 1.10: PL charging diagram of two different QDs from sample B. Shown is only the gate voltage region of the X^{1+} , X^0 and X^{1-} . The energy difference between the X^0 and X^{1-} is always ≈ 6 meV, while the X^{1+} can be red (a) or blue (b) shifted relative to the X^0 state. The charging diagram shown in (b) was obtained by much larger pumping power, which brings out the bi-exciton (two electron hole pairs in the QD) and the excited states of the positive exciton. Those features can easily be distinguished from the single exciton ground states due to their red shift.

resonance energy (see Fig. 1.10 (a) for a red shifted X^{1+} and (b) for a blue shifted X^{1+} respectively). This observation indicates a rich physical structure of the hole states in QDs. A detailed investigation of the underlying effects is necessary to fully understand the charging mechanisms of InGaAs QDs. The confinement potential for holes in the valence band seems to deviate significantly from the harmonic oscillator picture.

1.3.3 Magneto-luminescence of excitons in quantum dots

In order to gain more information about the electronic and excitonic states in a QD, a magnetic field can be applied. Magnetic field aligned along the growth direction

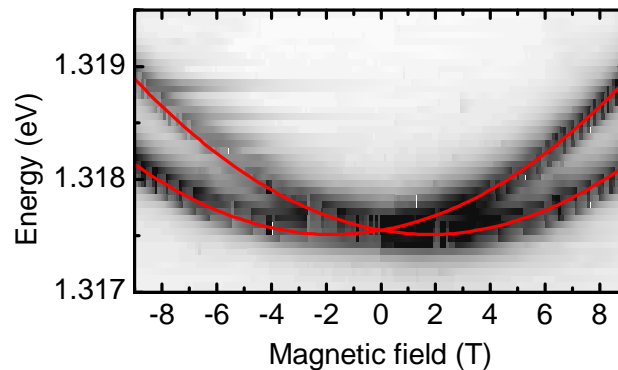


Figure 1.11: Photoluminescence of a charged exciton as a function of the external magnetic field. The field is swept from -9 to 9 T inducing a splitting and a shift of the resonance line. The behavior can be described by two parabolas according to eq. (1.3). The line in the figure is produced with the parameters $E_0 = 1.31755$ eV, $g_X = 1.3$ and $\alpha = 11.9 \mu\text{eV}/\text{T}^2$.

in Faraday geometry, imposes a quantization axis for the angular momentum of the electrons and holes in the sample. The angular momentum or spin can be aligned either parallel or antiparallel to the magnetic field axis. As a result the resonance in the PL spectra splits into two branches [38, 45, 46, 47, 48, 49]. In Fig. 1.11 the observed photoluminescence of a negatively charged exciton is plotted against the magnetic field. The field is swept from -9 to 9 T at a temperature of 4.2 K. The single resonance line of the X^{1-} state that is observed at zero field, splits in two lines with increasing magnetic field. The splitting is linear in the magnetic fields and can be described by the Zeeman splitting formula $E_Z = g_X \mu_B B$ (see Fig. 1.12 (c)). The Landé g-factor g_X is given by the sum of the g-factors of the electron and the hole $g_X = g_e + g_h$ [38]. The electronic and excitonic levels involved are illustrated in Fig. 1.12. Also the Zeeman splitting of the states in an external magnetic field is shown. The optical selection rules, as they are described in section 1.3, determine which transitions are optically allowed and can take place under emission of a photon. The energetically higher excitonic state with a spin of $+3/2$ can decay into the energetically lower ground state with an electron spin $+1/2$. This transition is mediated by a photon with a spin $+1$ which corresponds to a σ^+ polarization. The excitonic state with a spin $-3/2$, which has a lower energy in a magnetic field, decays under emission of a photon with spin -1 into the electronic state with a spin of $-1/2$ (Fig. 1.12 (a))[50].

Additional to the Zeeman splitting, the resonance lines are shifted in the magnetic

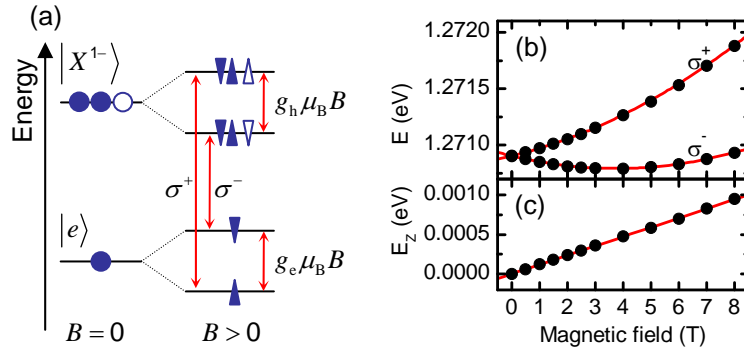


Figure 1.12: (a) Level scheme of the X^{1-} in zero magnetic field (left) and finite magnetic field (right). The ground state of the system is given by a QD containing a single electron (full circle), the excited state by two electrons and a hole (open circle) in the QD. At zero field, the spin states are degenerate and no spin quantization axis is defined. In a finite magnetic field, the ground and excited states are split by the Zeeman energy and the spins of the electron or excitons are aligned along the direction of the external magnetic field. The observed splitting between the energetically higher excited state and energetically lower ground state and vice versa is given by the sum of the Zeeman splitting and hence the sum of the electron and hole g-factors. In (b) the quadratic dispersion of the exciton resonance is plotted as a function of the magnetic field (the lines are fits of two parabolas to the data points). The splitting between the two branches are plotted in (c), it follows a linear behavior yielding the excitonic g-factor g_X .

field. The shift follows a quadratic behavior, so that the energy dependence of the resonance line can be described by [47]:

$$E = E_0 \pm \frac{1}{2}g_X\mu_B B + \alpha B^2. \quad (1.3)$$

The excitonic g-factor that is obtained for different QDs differs from $g_X = 1.3$ (shown in Fig. 1.11) up to $g_X = 2.2$. The different charge states of the same QD show no difference in the measured values for g_X . Even smaller variations are observed for the diamagnetic shift α . The values for α always lie around $10 \mu\text{eV}/T^2$. The variations for the different charge states are negligible. However, the X^{3-} state exhibits a rich behavior that differs dramatically from the observations of the other charge states. This comes from a hybridization of the final state after photoemission with the Landau levels that are formed in the back contact [49]. An important conclusion can be drawn from the value of the diamagnetic shift α . The origin of the diamagnetic shift arises from the wave function overlap between the excited state of the QD (in this case the X^{1-} state) and the ground state (here the QD occupied by an electron). The wave functions of the two states are modified by the magnetic field. The value of the diamagnetic shift corresponds to the size of the wave function of the electron l_e in the QD, as described in detail in [51]: $\alpha = e^2 l_e^2 / 8m_e$. Here, $m_e = 0.07m_0$ is the effective mass of the electron. For a value $\alpha = 11.9 \mu\text{eV}/T^2$, the corresponding value for $l_e = 6$ nm. The sign of α defines, whether the behavior of the exciton is diamagnetic ($\alpha > 0$) or paramagnetic ($\alpha < 0$). The difference between these two cases arises from the different sizes of the wave functions. In the diamagnetic case, the wave function of the excited state is larger than the wave function of the ground state. In case of a paramagnetic behavior it is the other way around.

In order to perform single QD spectroscopy at cryogenic temperatures and in large magnetic fields as it is shown in Fig. 1.3.3 requires an extraordinarily stable optical setup. In the next chapter, the microscopes that were used for high resolution spectroscopy on single QDs are introduced.

References

- [1] P.L. McEuen, E.B. Foxman, U. Meirav, M.A. Kastner, Y. Meir, N.S. Wingreen, and S.J. Wind, *Phys. Rev. Lett.* **66**, 1926 (1991).
- [2] L.M.K. Vandersypen, R. Hanson, L.H. Willems van Beveren, J.M. Elzerman, J.S. Greidanus, S. De Franceschi, and L.P. Kouwenhoven, Kluwer Academic, Plenum Publishers (New York, 2003).
- [3] R.S. Becker, J.A. Golovchenko, and B.S. Swartzentruber, *Nature* **325**, 419 (1987).
- [4] L. Gaudreau, S.A. Studenikin, A.S. Sachrajda, P. Zawadzki, A. Kam, J. Lapointe, M. Korkusinski, and P. Hawrylak, *Phys. Rev. Lett.* **97**, 036807 (2006).
- [5] D. Schröder, A.D. Greentree, L. Gaudreau, K. Eberl, L.C.L. Hollenberg, J.P. Kotthaus, and S. Ludwig, *Phys. Rev. B* **76**, 075306 (2007).
- [6] D. Loss and D.P. DiVincenzo, *Phys. Rev. A* **57**, 120 (1998).
- [7] A.P. Alivisatos, *Science* **271**, 933 (1996).
- [8] O. Millo, D. Katz, Y.W. Cao und U. Banin, *Phys. Rev. Lett.* **86**, 5751 (2001).
- [9] M. Bruchez, M. Moronne, P. Gin, S. Weiss, and A.P. Alivisatos, *Science* **25**, 2013 (1998).
- [10] D. Leonard, M. Krishnamurthy, C.M. Reaves, S.P. Denbaars, and P.M. Petroff, *Appl. Phys. Lett.* **63**, 3203 (1993).
- [11] J.M. García, G. Medeiros-Ribeiro, K. Schmidt, T. Ngo, J.L. Feng, A. Lorke, J. Kotthaus, and P.M. Petroff, *Appl. Phys. Lett.* **71**, 2014 (1997).
- [12] P. Offermans, P.M. Koenraad, J.H. Wolter, D. Granados, J.M. García, V.M. Fomin, V.N. Gladilin und J.T. Devreese, *Appl. Phys. Lett.* **87**, 131902 (2005).
- [13] J.Y. Marzin, J.M. Gerard, A. Izrael, D. Barrier, G. Bastard, *Phys. Rev. Lett.* **73**, 716 (1994).

- [14] A. Högele, S. Seidl, M. Kroner, R.J. Warburton, B.D. Gerardot, P.M. Petroff, and K. Karrai, *Phys. Rev.Lett.* **93**, 217401 (2004).
- [15] H. Drexler, D. Leonard, W. Hansen, J.P. Kotthaus, and P.M. Petroff, *Phys. Rev. Lett.* **73**, 2252 (1994).
- [16] R.J. Warburton, B.T. Miller, C.S. Dürr, C. Bödefeld, K. Karrai, J.P. Kotthaus, G. Medeiros-Ribeiro, P.M. Petroff, and S. Huant, *Phys. Rev. B* **58**, 16221 (1998).
- [17] D.V. Bulaev and D. Loss, *Phys. Rev.Lett.* **98**, 097202 (2007).
- [18] D.D. Awschalom, and J.M. Kikkawa, *Phys. Today* **52**, 33 (1999).
- [19] X. Michalet, F. Pinaud , T.D. Lacoste, M. Dahan, M.P. Bruchez, A.P. Alivisatos, and S. Weiss, *Single Mol.* **2** (2001).
- [20] R.J. Warburton, C. Schäfflein, D. Haft, F. Bickel, A. Lorke, K. Karrai, J.M. García, W. Schoenfeld, and P. M. Petroff, *Nature* **405**, 926 (2000).
- [21] J.J. Finley, A.D. Ashmore, A. Lemaître, D.J. Mowbray, M.S. Skolnick, I.E. Itskevich, P.A. Maksym, M. Hopkinson, and T.F. Krauss, *Phys. Rev. B* **63**, 073307 (2001).
- [22] S. Seidl, M. Kroner, P.A. Dalgarno, A. Högele, J.M. Smith, M. Ediger, B.D. Gerardot, J. M. García, P.M. Petroff, K. Karrai, and R.J. Warburton, *Phys. Rev. B* **72**, 195339 (2005).
- [23] R.J. Warburton, C. Schulhauser, D. Haft, C. Schäfflein, K. Karrai, J.M. García, W. Schoenfeld, and P.M. Petroff, *Phys. Rev. B* **65**, 113303 (2002).
- [24] R.J. Luyken, A. Lorke, A.O. Govorov, J.P. Kotthaus, G. Medeiros-Ribeiro, and P.M. Petroff, *Appl. Phys. Lett.* **74**, 2486, (1999).
- [25] J.M. Smith, P.A. Dalgarno, B. Urbaszek, E.J. McGhee, G.S. Buller, G.J. Nott, R.J. Warburton, J.M. García, W. Schoenfeld and P.M. Petroff, *Appl. Phys. Lett.* **82**, 3761, (2003).
- [26] S. Lüttjohann, C. Meier, A. Lorke, D. Reuter, and A.D. Wieck, *Appl. Phys. Lett.* **87**, 163117 (2005).
- [27] M. Kroner, A. Högele, S. Seidl, R.J. Warburton, B.D. Gerardot, A. Badolato, P.M. Petroff, and K. Karrai, *Physica E* **32**, 61 (2006).
- [28] M. Kroner, A.O. Govorov, S. Remi, B. Biedermann, S. Seidl, A. Badolato, P.M. Petroff, W. Zhang, R. Barbour, B.D. Gerardot, R.J. Warburton, and K. Karrai, *Nature* **451**, 311 (2008).
- [29] B. Alen, A. Högele, M. Kroner, S. Seidl, K. Karrai, R. J. Warburton, A. Badolato, G. Medeiros-Ribeiro, and P. M. Petroff, *Appl. Phys. Lett.* **89**, 123124 (2006).

- [30] K. Karrai, R.J. Warburton, Superlattices and Microstructures **33**, 311 (2003).
- [31] A. Högele, S. Seidl, M. Kroner, K. Karrai, C. Schulhauser, O. Sqalli, J. Scrimgeour, and R. J. Warburton, Rev. Sci. Instrum. **79**, 023709 (2008).
- [32] D. Gammon and D. Steel, Phys. Today **55**, 36 (2002).
- [33] J.Y. Marzin, J.M. Gerard, A. Izrael, D. Barrier, G. Bastard, Phys. Rev. Lett. **73**, 716 (1994).
- [34] K. Brunner, G. Abstreiter, G. Bohm, G. Trankle, G. Weimann, Appl. Phys. Lett. **64**, 3320 (1994).
- [35] S. Trumm, M. Wesseli, H.J. Krenner, D. Schuh, M. Bichler, J.J. Finley, and M. Betz, Appl. Phys. Lett. **87**, 153113 (2005).
- [36] M. Wesseli, C. Ruppert, S. Trumm, H.J. Krenner, J.J. Finley, and M. Betz Appl. Phys. Lett. **88**, 203110 (2006).
- [37] R. Heitz, A. Kalburge, Q. Xie, M. Grundmann, P. Chen, A. Hoffmann, A. Madhukar, and D. Bimberg, Phys. Rev. B **57**, 9050 (1998).
- [38] M. Bayer, G. Orter, O. Stern, A. Kuther, A.A. Gorbunov, A. Forchel, P. Hawrylak, S. Fafard, K. Hinzer, T.L. Reinecke, S.N. Walck, J.P. Reithmaier, F. Klopff, and F. Schäfer, Phys. Rev. B **65**, 195315 (2002).
- [39] M. Bayer, O. Stern, A. Kuther, and A. Forchel, Phys. Rev. B **61**, 7273 (2000).
- [40] B. Urbaszek, R.J. Warburton, K. Karrai, B. Gerardot, P.M. Petroff and J.M. García, Phys. Rev. Lett. **90**, 247403-1 (2003).
- [41] J.M. Smith, P.A. Dalgarno, R.J. Warburton, A.O. Govorov, K. Karrai, B.D. Gerardot und P.M. Petroff, PRL **94**, 197402 (2005).
- [42] M. Ediger, G. Bester, B.D. Gerardot, A. Badolato, P.M. Petroff, K. Karrai, A. Zunger, and R.J. Warburton, Phys. Rev. Lett. **98**, 036808 (2007).
- [43] M. Ediger, P.A. Dalgarno, J.M. Smith, B.D. Gerardot, R.J. Warburton, K. Karrai, and P.M. Petroff, Appl. Phys. Lett. **86**, 211909 (2005).
- [44] M. Ediger, G. Bester, A. Badolato, P. M. Petroff, K. Karrai, A. Zunger, and R. J. Warburton, Nature Physics **3**, 774 - 779 (2007).
- [45] M. Bayer, A. Kuther, A. Forchel, A. Gorbunov, V.B. Timofeev, F. Schäfer, J.P. Reithmaier, T.L. Reinecke and S.N. Walck, Phys. Rev. Lett. **82**, 1748, (1999).
- [46] J.G. Tischler, A.S. Bracker, D. Gammon, and D. Park, Phys. Rev. B **66**, 081310 (2002).

- [47] C. Schulhauser, D. Haft, R.J. Warburton, K. Karrai, A.O. Govorov, A.V. Kalameitsev, A. Chaplik, W. Schoenfeld, J.M. García and P.M. Petroff, Phys. Rev. B **66**, 193303 (2002).
- [48] J.J. Finley, D.J. Mowbray, M.S. Skolnick, A.D. Ashmore, C. Baker, and A.F.G. Monte, and M. Hopkinson, Phys. Rev. B **66**, 153316 (2002).
- [49] K. Karrai, R.J. Warburton, C. Schulhauser, A. Högele, B. Urbaszek, E.J. McGhee, A.O. Govorov, J.M. García, B.D. Gerardot, and P.M. Petroff, Nature **427**, 135 (2004).
- [50] A. Högele, S. Seidl, M. Kroner, K. Karrai, M. Atatüre, J. Dreiser, A. Imamoglu, R.J. Warburton, B.D. Warburton, B.D. Gerardot, and P.M. Petroff, Appl. Phys. Lett. **86**, 221905 (2005).
- [51] C. Schulhauser, *Elektronische Quantenzustände induziert durch Photonemission*, Dissertation, Ludwig-Maximilians-Universität München, ISBN 3-8325-0563-6, Logos, Berlin (2004).

Chapter 2

Confocal microscopy of single quantum dots

Quantum dots that were introduced in the previous chapter were studied by means of optical spectroscopy. A QD sample is mounted in a fiber-based confocal microscope developed to operate at liquid helium temperature. The microscope is designed to be very compact to guarantee mechanical stability of single dot measurements over periods of months. In this chapter we introduce different microscope geometries that were used to study a single QD in a magnetic field of up to 9 T applied along the growth direction in Faraday geometry, or in the plane of the QD-layer in Voigt geometry.

2.1 Confocal microscopy

Confocal microscopy is a very convenient instrument to study microscopic systems at the frontier of the diffraction limit [1]. Especially in biological or medical research scanning confocal microscopes are used because of their unique feature of acquiring three dimensional information of a sample without cutting it in slices. The ability to collect light from a small area or to illuminate only a diffraction-limited focal area is crucial for single QD spectroscopy. The high spatial resolution of a confocal microscope allows to perform single QD spectroscopy on samples that require no special processing like shadow masks or mesa etching in order to reduce the number of QDs in the focal area. Furthermore, an important feature of the here used confocal microscopes is that a large amount of light can be collected from the sample due to the large numerical aperture (NA) of the objective. Finally, the electric field distribution of a focused Gaussian beam is known, and the interaction of the laser light with a scattering QD can be modelled easily. This becomes particularly important in the analysis of the resonant laser spectroscopy data. In particular, the knowledge of the amplitude and polarization of the illuminating laser light is very important to study the optical properties of a QD under resonant excitation. This is much more difficult to achieve in a nearfield microscope, which provides a spatial resolution more than one order of magnitude better than that of a confocal microscope. Nearfield microscopy also requires a very precise control over the tip-sample

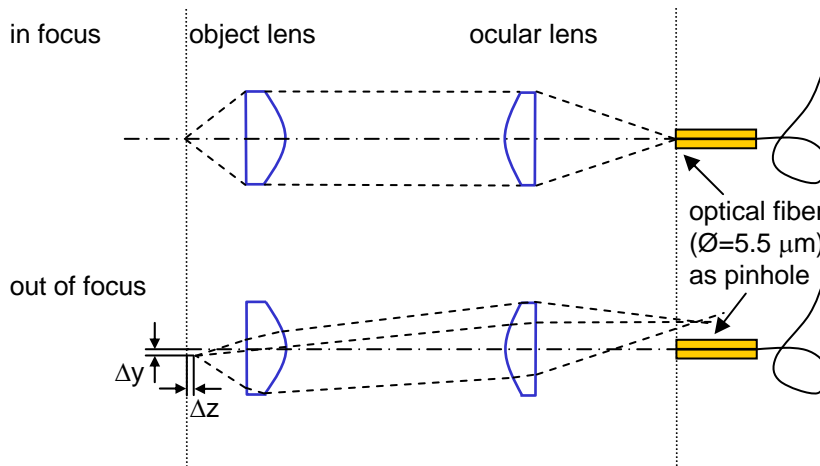


Figure 2.1: Schematic drawing of a fiber-based confocal objective. The illuminating light is coupled into the objective by an optical fiber. The diverging light leaving the fiber is collimated with an ocular lens. The parallel light beam is then focused with an objective lens to a diffraction-limited spot in the focal plane of the lens (upper drawing). All the light, emitted or reflected from the focal area into the solid angle of the objective lens, follows the way of the illuminating light back into the fiber core, and ported back to the analyzing setup. Any light coming from out of focus will not be imaged onto the fiber core, hence, the light will not be coupled into the fiber and it is not seen by the analyzing setup (lower part). The fiber core acts as a pin hole.

distance that would not remain stable over periods of days or even months. The principle of a confocal microscope was described and patented by M. Minsky [2] in 1957. The underlying principle is shown in Fig. 2.1 for the case of an optical fiber-based confocal microscope. The idea is to place a pinhole in the image plane of an objective. The objective in our case consists of two lenses, that are aligned such that the focal area of one lens, the object lens, is imaged by the second lens, the ocular lens, onto a pinhole. In the system that is shown in Fig. 2.1 the core of a single mode optical fiber with a diameter of $5.5 \mu\text{m}$ acts as the pinhole. Only the light that hits the fiber core in the solid angle given by the NA of the fiber is coupled into the fiber and can be directed out of the microscope to the analyzing setup. The light that is emitted by the sample out of the focal region of the confocal setup is imaged besides the fiber core (lower sketch of Fig. 2.1). Therefore, it is not be coupled efficiently into the fiber. As a consequence, the spatial resolution of a confocal microscope is better than that of a conventional optical far-field microscope [3]. However, the drawback of the diffraction-limited resolution of the confocal microscope is that the sample can not be imaged at once. Only the light from a single spot is detected at a time. A three dimensional image of the sample can be obtained by scanning. In our work, this feature plays a minor role. Scanning is only used in the process of finding a QD. As soon as a suitable QD is found, it remains in the focus of the microscope until all necessary measurements have been performed.

The resolution of the confocal microscope depends on the objective lens, the operating wavelength and the geometry of the setup. The diffraction limit of an optical far-field microscope is given by Gaussian beam optics [4]. In Fig. 2.2 the radius r of a focused Gaussian beam is plotted as a function of the distance z from the focal plane. Along the x and y directions, the electric field amplitude of a Gaussian beam

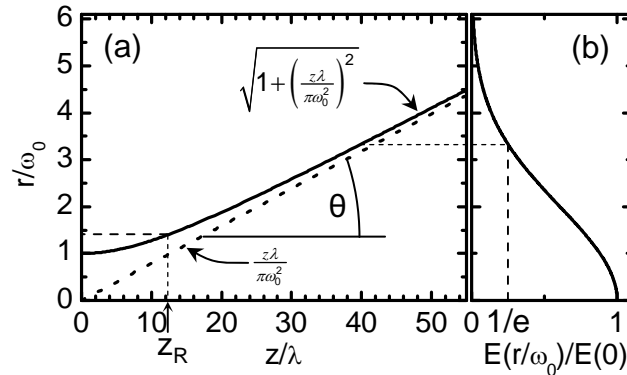


Figure 2.2: (a) Divergence of a Gaussian beam. The beam radius is plotted as a function of the distance from the focus z/λ along the propagation of the beam (solid line). The waist in the focus is given by ω_0 . For large z , the beam radius converges towards the linear law given by the dashed line. The distance at where the beam radius is $\sqrt{2}\omega_0$ is called Rayleigh range z_R . The divergence angle of the gaussian beam in the far-field ($z \gg z_R$) is $\theta = \lambda/\pi\omega_0$. (b) Electric field distribution of a Gaussian beam perpendicular to the propagation direction. The r at which the electric field component is $1/e$ of the maximum value is defined as the radius of the Gaussian beam.

drops off from its maximum value in the center following a Gaussian distribution. The radius of a Gaussian beam is defined as the radius where the electric field has dropped to $1/e$ of its maximum value in the center of the beam. The beam waist – the radius of the beam in the focus – is ω_0 and the divergence angle is θ . The radius of the Gaussian beam as a function of z is then given by [4]

$$r = \omega_0 \sqrt{1 + \left(\frac{z\lambda}{\pi\omega_0^2} \right)^2}. \quad (2.1)$$

The distance from the focal plane at which the radius of the Gaussian beam is $\sqrt{2}\omega_0$ is the Rayleigh range z_R . The Rayleigh range gives an approximative dividing line between the near-field and the far-field for a focussed Gaussian beam. For $z \gg z_R$, the beam radius follows the linear divergence

$$r \approx \frac{z\lambda}{\pi\omega_0} = z\theta \quad (2.2)$$

with the divergence angle θ :

$$\theta = \frac{\lambda}{\pi\omega_0}. \quad (2.3)$$

For an ideal lens that focusses a Gaussian beam to its diffraction-limited spot the radius of the spot is connected to the NA of the lens according to eq. (2.2). This is because for $n = 1$, $\theta \approx \sin \theta = n \sin \theta = NA$ is the half angle of the light cone exiting a lens that is illuminated with a plane wave. In reality, a lens not only focusses light. The finite diameter of the lens acts as an aperture at which diffraction takes place. Hence, the intensity distribution in the focus of a lens strongly depends on the intensity distribution illuminating the lens. So, a uniformly illuminated lens creates an Airy disc intensity profile in the focus. By illuminating the lens such that the radius of the lens equals the $1/e^2$ beam waist of the impinging Gaussian beam, the intensity distribution in the focal plane is Gaussian. The truncation ratio is introduced, to account for a finite illumination of the focussing lens:

$$T = \frac{r_{\text{beam}}}{r_{\text{lens}}}. \quad (2.4)$$

The diffraction-limited spot size d_{FWHM} of a lens can be calculated as follows [4]:

$$d_{\text{FWHM}} = K_{\text{FWHM}} \frac{\lambda}{2 \tan \theta} \approx K_{\text{FWHM}} \frac{\lambda}{2NA}. \quad (2.5)$$

The geometry factor K_{FWHM} is given as a function of the truncation ratio by:

$$K_{\text{FWHM}} = 1.029 + \frac{0.7125}{(T - 0.2161)^{2.179}} - \frac{0.6445}{(T - 0.2161)^{2.221}}. \quad (2.6)$$

The size of the focus spot and the light flux through the focus spot depends on the illumination profile, which is given by the ocular lens as shown in Fig. 2.1. In

the presented setup, the ocular lens was optimized for collimating the light from the single mode fiber. The diameter of the ocular lens which gives the diameter of the collimated Gaussian beam, matches the objective lens for optimal focussing ($T \approx 0.72 \rightarrow K_{\text{FWHM}} \approx 1.25$). For a wavelength $\lambda = 970$ nm which is of the order of the resonance wavelength of QDs, and an $NA = 0.68$ of the objective lens, the diffraction-limited spot size is $d_{\text{FWHM}} = 0.89 \mu\text{m}$.

With the concept of the confocal microscope objective in mind, the cryogenic microscopes that were used in the experiments presented in this thesis are introduced and characterized in the following sections.

2.2 Cryogenic microscopy

The above presented concept of confocal microscopy is a standard microscopy technique with a lot of different solutions that are available commercially. However, in order to study the optical properties of nano-objects, such as QDs in a solid state environment, cryogenic temperatures are necessary. Hereby, the phonon interaction

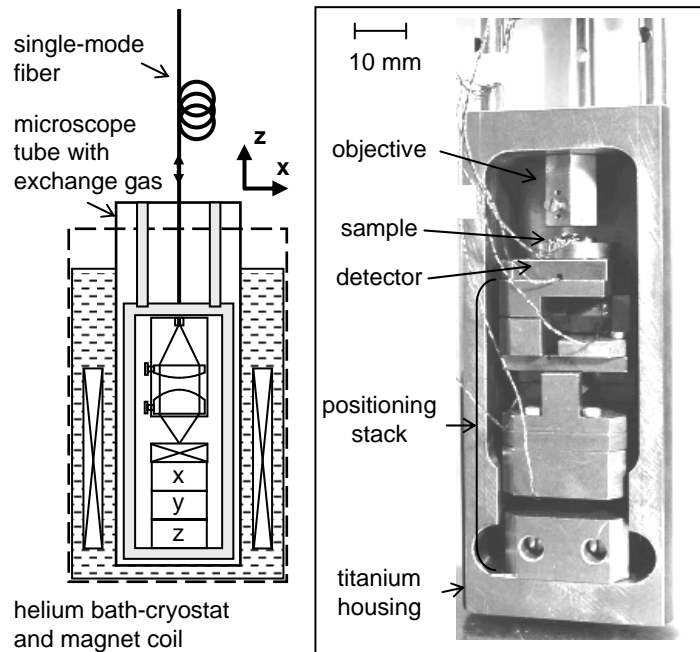


Figure 2.3: Confocal microscope for cryogenic environments. The light is directed into the confocal objective with a single mode fiber. Two lenses create a diffraction-limited spot on the sample, as described in the text. Behind the sample, a Si-photodiode measures the transmitted light. Sample and detector are mounted on a cryogenic xyz -positioning unit. All metal parts of the setup, as well as the compact housing in which the setup is mounted in, are made out of titanium. The microscope is mounted in a thin wall stainless steel tube that is evacuated and filled with helium exchange gas. The tube can be immersed in a liquid helium bath cryostat that is equipped with a super-conducting coil magnet, which allows a magnetic field up to 11 T.

in the solid state system and the thermal excitation of the excitonic states of the QD can be reduced and the coherent properties of single electrons can be studied. Furthermore, for many experiments, a magnetic field as strong as 11 T has to be applied. These experimental conditions require special solutions. The microscope has to be build out of non-magnetic material that can withstand temperatures as low as 1.5 K. In order to minimize movement of the microscope objective relative to the sample due to differential thermal contraction or due to the residual magnetization of the material, the system needs to be constructed as compact as possible. Solutions for the application of high spatial resolution optical microscopy at cryogenic temperatures and high magnetic fields are commercially available from *attocube systems* which supplied most of the microscopes that were used here.

The standard fiber-based confocal microscope for cryogenic environment is shown in Fig. 2.3 [B1]. It is a compact miniature microscope that is described in detail in [5]. The light is directed into the microscope via a single mode fiber. The confocal objective consists of two aspheric lenses as described above. The first one [B2] has a numerical aperture $NA = 0.16$ that matches the NA of the fiber. The diameter of the lens is 5 mm which defines the diameter of the collimated Gaussian beam. The objective lens [B3] has an $NA = 0.68$ and a diameter of 3.6 mm which leads to the diffraction-limited spot size of $d_{\text{FWHM}} = 0.89 \mu\text{m}$. The working distance of the objective is 1.56 mm. The light that is transmitted through the sample, is collected by a Si-photodetector [B4]. The detector has an active area of $\approx 7 \text{ mm}^2$ with a diameter of 2.7 mm. This means that for optimum collection efficiency the distance between the sample and the detector is $\leq 4 \text{ mm}$. Hence, also the detector is at liquid helium temperature. A detailed sketch of the microscope objective and the transmission detector is shown in Fig. 2.4. The sample and detector unit

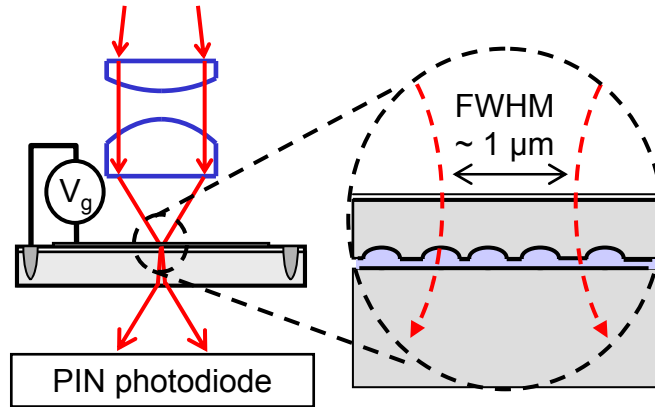


Figure 2.4: Detailed sketch of the confocal objective. The light is focused on the sample with a diffraction-limited spot size of $\approx 1 \mu\text{m}$. The transmitted light is collected with an Si-photodetector. The whole setup as shown here is at 4.2 K. The gate voltage that is applied to the sample can be controlled from outside the cryogenic setup via twisted pair cables in the microscope.

are mounted on a positioning stack [B5], which is a three axis slip-stick stepper positioning unit that was designed to work at cryogenic temperatures. It allows a positioning of the sample with respect to the objective with a precision of ≈ 10 nm. In order to guarantee optimal stability in the magnetic field, the setup is mounted in a compact titanium housing as shown in Fig. 2.3. The whole microscope is mounted in a 5 cm diameter, thin wall, stainless steel tube. To avoid icing during the cool down process, the tube is evacuated to a pressure of $\approx 2 \times 10^{-5}$ mbar, measured at the turbo pump, used for evacuation. The tube is then filled with a small amount of helium exchange gas to allow for heat exchange of the microscope that has no direct contact to the tube. The exchange gas is cleaned in a liquid nitrogen cold trap and about a pressure of ≈ 30 mbar is measured in the whole volume of the microscope and the cool trap. The microscope in the tube is then immersed in a liquid helium bath cryostat [B6]. The cryostat is equipped with a superconducting solenoid coil magnet [B7]. At a temperature of 4.2 K, the magnet can generate a field of up to 9 T. Larger fields can be reached by cooling down further by evaporative cooling [6]. However, this was not necessary for any experiment presented in this thesis.

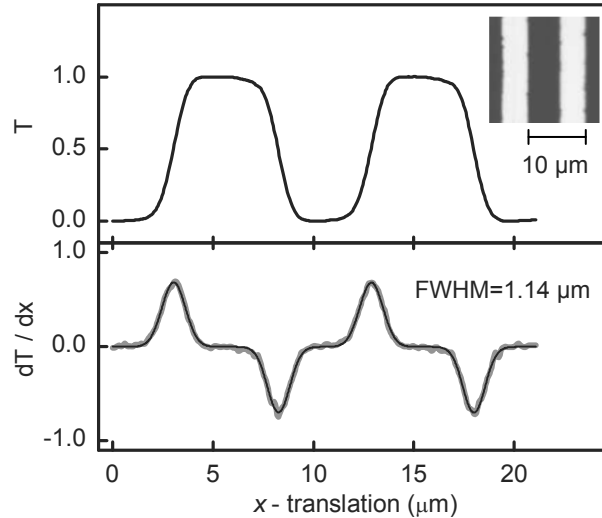


Figure 2.5: Measurement of the spatial resolution of the confocal microscope objective. The upper figure shows the normalized transmission measured with the transmission detector as the sample is scanned through the focus with a wavelength of 950 nm. The inset shows a photograph of the sample, that was done with a commercial imaging microscope in reflection (white stripes represent the high reflectivity of the Aluminium). In the lower figure the numerically differentiated signal along the scan direction is shown (gray line). For a rising edge of the signal the Gaussian peak goes up, for a declining edge the Gaussian peak goes down. The peaks are fit by Gaussian functions (black line) yielding a value for the focus diameter $d_{\text{FWHM}} = 1.14 \mu\text{m}$.

2.2.1 Spatial resolution

The spatial resolution of the confocal microscope objective is measured by scanning over an edge, while measuring the transmitted light. The measured transmission signal is the convolution of the step transition function of the sample and the Gaussian beam profile in the focus. A grating of aluminium stripes on quartz is used (period $10\ \mu\text{m}$) as a sample which is supposed to provide a perfect Heaviside transmission function. Hence, the measured transmission signal as a function of the scan direction is given by the integral over a Gaussian curve. The derivative of the measured trace is directly proportional to the intensity profile in the focus. The measurement is shown in Fig. 2.5. The fit of a Gaussian function to the derivative of the transmission signal yields a diffraction-limited spot size of $d_{\text{FWHM}} = 1.14\ \mu\text{m}$ [5]. The discrepancy between the measured spot size and the calculated one is most probably due to a misalignment of the fiber. This leads to an over-illumination of the ocular lens and hence to an under-illumination of the objective lens. As a result, the geometry factor T is smaller than expected and hence the spot size is larger.

In Fig. 2.6, the image of the focus of a confocal microscope is shown. The image was taken with a transmission microscope [B8]. It consists of two identical confocal objectives that are mounted each on a xyz -positioning unit. The objectives face each

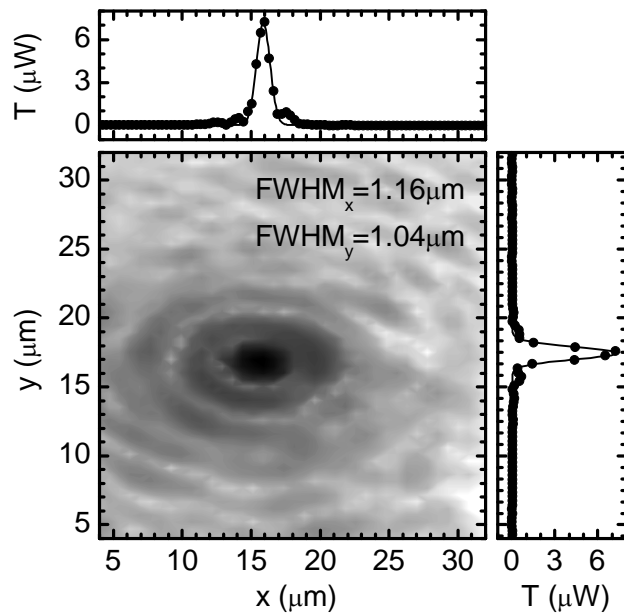


Figure 2.6: Image of the focus of the confocal objective on a quartz substrate. The image is measured in transmission with a second identical objective mounted below the sample. The color scale follows a logarithmic function of the transmitted intensity. In the setup, the objectives are mounted on xyz -positioning units, while the sample remains fixed in the center of the two objectives. The image was measured with a laser power of $163\ \mu\text{W}$. The transmission efficiency is 4.3%. The laser wavelength is $\lambda = 950\ \text{nm}$. The spatial resolution is measured by fitting a Gaussian function to two cuts through the focus. The Airy pattern is clearly visible.

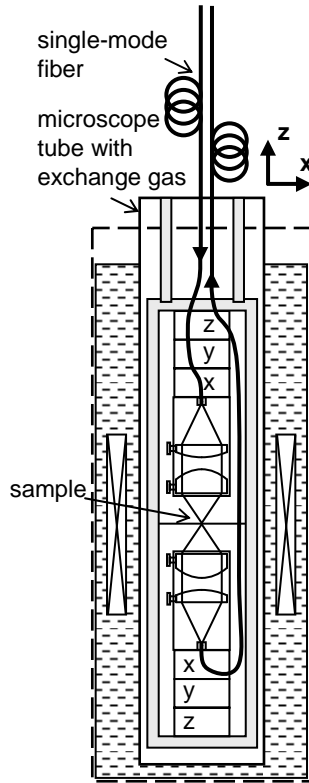


Figure 2.7: Schematic drawing of the transmission microscope that is the basis for most of the advanced microscopes that were developed in this thesis. In the shown configuration the focus of the objectives was imaged in transmission (shown in Fig. 2.6). The two identical objectives are mounted on xyz -positioners each. The sample is mounted in-between the two objectives. The light that is directed into the system by one fiber is focused onto the sample by the upper objective. The second objective collects the transmitted light and couples it into a fiber, which guides the light out of the microscope to be analyzed at room temperature.

other so that the two foci can be aligned, and transmission through both objectives can be measured. The sample remains fixed in-between the two objectives. A scan of one objective with respect to the sample and the other objective is shown in Fig. 2.6. The setup is schematically sketched in Fig. 2.7

2.2.2 Fabry-Pérot cavity

The confocal properties of the objective are exploited to position the sample in the focal plane of the microscope. An adjustment laser is coupled into the microscope. The laser wavelength corresponds to the resonance wavelength of the QDs avoiding chromatic aberrations. This is done via a fiber-based beam splitter [B 9] so that the light that is reflected from the sample surface can be detected. Due to the confocal setup of the objective, the reflected light is coupled efficiently into the fiber only when the sample surface is located in the focal plane. The position at which the maximum

reflected intensity is measured, corresponds to the sample surface in the focal plane. While scanning the sample through the focus we find a peak in the reflected light intensity [5]. However, the reflected light intensity is strongly modulated, as shown by the gray line in Fig. 2.8. The confocal system of the two lenses imaging the focal area from the sample onto the fiber ending and vice versa leads to a Fabry-Pérot cavity in the optical setup. The sample surface and the fiber ending make the cavity mirrors. In case of illumination with a coherent light source, such as a laser with a coherence length larger than the cavity length ≈ 1 cm, the reflected light is modulated by the Fabry-Pérot cavity periodic reflectivity characteristics. The same oscillatory behavior is observed when the laser wavelength is scanned and the sample surface remains fixed in the focal plane of the objective. This makes resonant laser spectroscopy difficult to perform. The QD is no longer decoupled from its environment, but it is coupled to a low finesse cavity. This leads to phase shifts and hence to asymmetric line shapes in the interference signal of the transmitted laser light and the coherently scattered QD light on the detector. The effect of this is described in great detail in an earlier work by A. Högele [7] and B. Alén *et al.* [8]. The ability to tune the phase of the laser light at the QD position in situ allowed to measure the dispersive and absorptive part of the optical QD response [8]. In the presented experiments it is desired to keep the QD response free from cavity effects in order to study not optical but quantum mechanical interferences [9]. The fiber ending that was originally polished perpendicular to the light propagating path and acting as a mirror is polished under an angle of 8° . This angle is the standard angle of angle polished fiber connectors (FC/APC). The tilted fiber ending reduces back reflections of the impinging light into the light path and, hence, effectively suppresses the cavity transmission and reflection characteristic of the fiber ending - sample surface system. This is shown in Fig. 2.8 by the black line. With a fiber

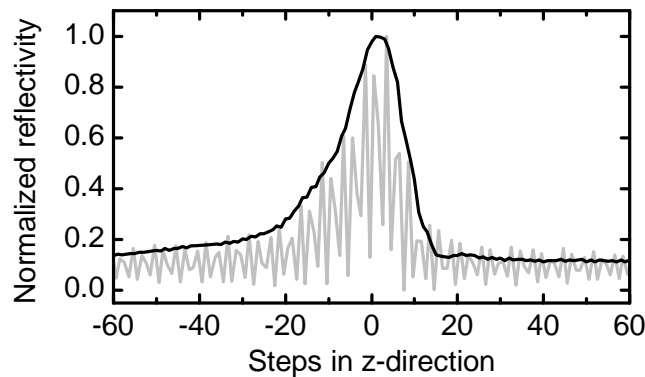


Figure 2.8: Measured reflectivity of the confocal microscope as the sample is moved through the focus in z -direction. The black line was measured with the fiber ending polished under 8° . The increased reflectivity in the focus (0 steps in z) is due to the confocal setup of the objective. The gray line corresponds to the measurement performed with a fiber ending polished perpendicular to the light propagation direction. The oscillation resemble the Fabry-Pérot cavity characteristic of the objective.

ending polished under 8° , the light that exits the fiber has an angle of 4° with respect to the optical axis. This leads to aberration in the optical path which can in principle be compensated using a tilted mount for the fiber. However, here the measured spatial resolution ($d_{\text{FWHM}} = 1.3 \text{ nm}$) is tolerable, while the more complex mounting and adjustment of a tilted fiber after cool down can easily lead to a comparable loss of spatial resolution.

2.2.3 Polarization properties

The disadvantage of the fiber-based miniature confocal microscope is that the polarization of the laser light is lost on the way into the microscope. The single mode fiber acts as a combination of $\lambda/2$ and $\lambda/4$ -plates with unknown alignment of the fast axes. At the position of the sample, the light has an arbitrary elliptical polarization. The polarization of the transmitted light can be analyzed in a polarization analyzing unit that can be mounted in the microscope behind the sample. The analyzing unit is described in detail and characterized in [5] and [7]. It was already used in earlier work to determine the polarization properties of a single negatively

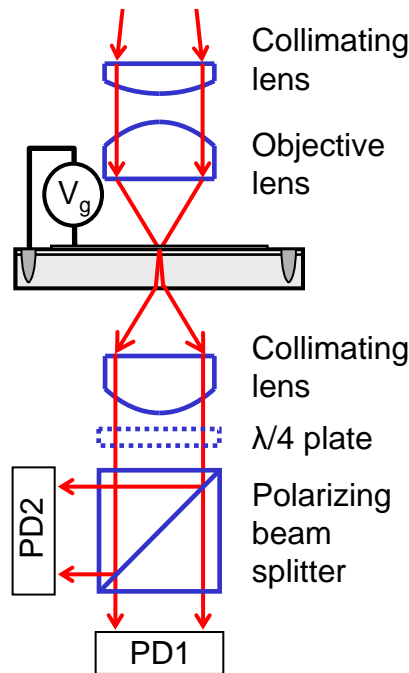


Figure 2.9: The polarization unit is shown schematically. The light from the fiber is focused onto the sample by the confocal objective as described above. After passing the sample, the laser light is collimated by a lens that is identical to the focussing lens. A polarizing beam splitter divides the light according to its linear polarization components onto two photodetectors (PD1 and PD2). The polarization basis can be switched from linear to circular polarization by positioning a $\lambda/4$ -plate in the collimated light path between the lens and the beam splitter (indicated by the dashed rectangle).

charged exciton in a magnetic field [6] or to measure the Faraday rotation of a single spin in a QD [10].

The schematics of the polarization unit is shown in Fig. 2.9. The light that passes through the sample is collimated by a lens that is identical to the focussing lens of the objective [B 3]. The position of the lens can not be adjusted in situ. Hence, the setup is built such that the sample is in the focal plane of the collimating lens when it is mounted on the polarization analyzing unit. The small changes of the distance due to thermal contraction at 4.2 K do not influence the operability of the setup. The collimated laser beam is split by a polarizing beam splitter [B 10] into two orthogonal linear parts. Two photodetectors [B 4] measure the intensity of the two beams that were filtered according to their linear polarization. The signal from the two photodetectors can be used to alter the polarization of the laser beam that is coupled into the microscope such that the light in the focus is polarized along one of the two orthogonal directions defined by the beam splitter. A $\lambda/4$ -plate [B 11] can be introduced into the collimated beam between the lens and the beam splitter. The fast axis of the $\lambda/4$ -plate is aligned along 45° with respect to the polarization axis of the beam splitter. A circularly polarized light beam that impinges onto the $\lambda/4$ -plate is transformed into a linearly polarized beam that is then directed entirely onto one of the two photodetectors.

The effect of the described polarization optics will be discussed in chapter 3.4 in detail. There the propagation of a polarized beam through the setup is described by Jones calculus.

2.2.4 Confocal microscope for Voigt geometry

Within the framework of this thesis, a microscope was developed to study the optical properties of single QDs with a magnetic field applied in the plane of the QD-layer. The cryostat and the magnet presently available for measurements, constrain the magnetic field along the z -direction, as shown in Figs. 2.3, 2.7 and 2.10. The sample has to be rotated, in order to apply the magnetic field along other directions. For experiments in Voigt-geometry the sample has to be tilted by 90° which means that the magnetic field is applied perpendicular to the light propagation direction. The restricted space available in the microscope setup requires to modify the objective in order to illuminate the sample perpendicular to the in-plane magnetic field. The modified microscope setup for Voigt-geometry is shown in Fig. 2.10. The sample and detector unit are mounted on an L-shape angle piece, which is itself fixed to the xyz -positioning unit. The positioning unit is mounted on the top of the microscope housing, similar to the configuration in the transmission microscope. The objective is mounted on the bottom of the microscope housing. A mirrored prism [B 12] redirects the light onto the sample. The same type of lenses as used before form a confocal microscope setup. The mirror is introduced in-between the two lenses, as shown in Fig. 2.10. The light is directed into the microscope by a single mode fiber. Again, the spatial resolution was determined by scanning over a checker-board pat-

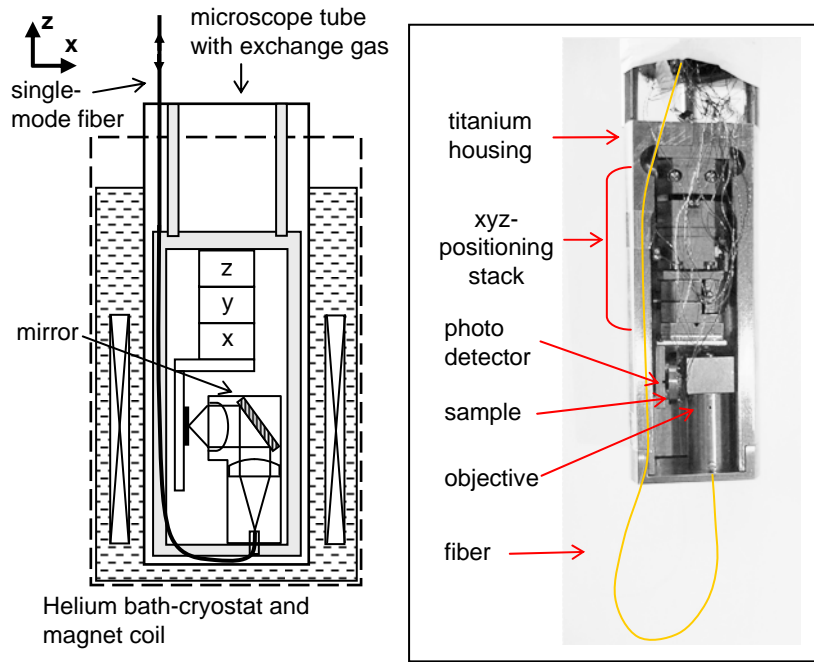


Figure 2.10: Illustration of the confocal microscope setup for Voigt geometry measurements. The setup is based on the transmission microscope as shown in Fig. 2.7. The sample and detector unit are mounted on an L-shaped angle piece, such that the sample is tilted by 90° with respect to the magnetic field which is aligned along the z -direction. The confocal objective is mounted on the bottom of the microscope housing. The light beam is reflected by 90° by a mirror that is introduced in the collimated beam path between the two lenses.

tern as described above. The measured spot size was $d_{\text{FWHM}} = 1.5 \mu\text{m}$. This is significantly larger than the spot size of the linear objective described above. However, the alignment of the two lenses and the mirror is limited by the fabrication tolerance of the titanium parts in the workshop.

References

- [1] J.G. White, W.B. Amos, *Nature* **328**, 183 (1987).
- [2] M. Minsky, *Scanning* **10**, 128 (1988). and M. Minsky, U.S. Patent 3013467.
- [3] S. Wilhelm, B. Gröbler, M. Gluch, H. Heinz, *Principles - Confocal Laser Scanning Microscopy*, Carl Zeiss Advanced Imaging Microscopy, Jena (2003).
- [4] L.D. Dickson, *Appl. Opt.* **9**, 1854 (1970), S.A. Self, *Appl. Opt.* **22**, 658 (1983), A.E. Siegman *Lasers*, University Science Books, Sausalito, California (1986), *Introduction to Gaussian Beam Optics* Melles Griot, www.mellesgriot.com.
- [5] A. Högele, K. Karrai, C. Schulhauser, O. Squalli, J. Scrimgeour, R.J. Warburton, M. Atatüre, J. Dreiser, and A. Imamoglu, to appear in 2008.
- [6] A. Högele, S. Seidl, M. Kroner, K. Karrai, M. Atatüre, J. Dreiser, A. Imamoglu, R.J. Warburton, B.D. Warburton, B.D. Gerardot, and P.M. Petroff, *Appl. Phys. Lett.* **86**, 221905 (2005).
- [7] A. Högele, *Laser spectroscopy of single charge-tunable quantum dots*, Dissertation, Ludwig-Maximilians-Universität München, ISBN 3899633253, Dr. Hut, München (2006).
- [8] B. Alén, A. Högele, M. Kroner, S. Seidl, K. Karrai, R.J. Warburton, A. Badolato, G. Medeiros-Ribeiro, and P.M. Petroff, *Appl. Phys. Lett.* **89**, 123124 (2006).
- [9] M. Kroner, A.O. Govorov, S. Remi, B. Biedermann, S. Seidl, A. Badolato, P.M. Petroff, W. Zhang, R. Barbour, B.D. Gerardot, R.J. Warburton, and K. Karrai, *Nature* **451**, 311-314 (2008).
- [10] M. Atatüre, J. Dreiser, A. Badolato, and A. Imamoglu, *Nature Physics* **3**, 101 (2007).

Chapter 3

High resolution laser spectroscopy

The experimental principles of high resolution resonant laser spectroscopy are introduced in this chapter. The optical and electronic setup to perform Stark shift modulation spectroscopy in transmission are presented. The setup was used to measure the resonant Rayleigh scattering of a narrow band laser by an exciton transition in a QD. Finally, a novel phase sensitive detection method allowing the simultaneous measurement of the real and imaginary parts of the QD first order optical susceptibility is presented.

3.1 Resonant laser spectroscopy in transmission

The non-resonant spectroscopy technique of PL that was introduced in the previous chapter, is a powerful and versatile way to study single QDs [1, 2, 3, 4, 5, 6]. It is widely used in the scientific community of groups performing optical studies on self-assembled QDs. However, the disadvantages of PL are manyfold.

First, spectral resolution is limited. The natural linewidth of an excitonic transition in a QD is $\hbar\Gamma \approx 1 \mu\text{eV}$, a value which is given by the exciton lifetime $\tau \approx 1 \text{ ns}$ via the relation $\Gamma = 1/\tau$. Such an energy can hardly be resolved by a standard grating monochromator. Sufficiently high spectral resolution can be achieved with monochromators based on multiple gratings or Fabry-Pérot cavity filters [7]. However, these solutions usually have a low photon throughput, a major drawback considering the emission rate of a single QD. The maximum photon emission rate $\approx 1 \text{ GHz}$, given by the lifetime of an exciton in a QD, corresponds to an optical power of 0.2 nW . This power is emitted isotropically into space. Second, coherence of the optical excitation is lost during the relaxation process of the non-resonantly created electrons and holes in a PL experiment.

Photocurrent experiments on a single QD performed under resonant laser excitation represents a high resolution absorption spectroscopy. It provides high spectral resolution and allows e.g. the observation of coherent Rabi oscillations of the population of the excitonic state [8]. However, photocurrent experiments can only be performed in the ionization regime (see Fig. 1.6). Hence, electrons or holes that are stored in the QD can not be manipulated with this method. A direct resonant laser spectroscopy technique is highly desirable to achieve a coherent control of electronic and excitonic states in a QD.

All experiments described in this thesis have been performed with resonant Rayleigh scattering spectroscopy measured in transmission [9]. A narrow band laser is brought into resonance with the excitonic transition of a single QD, while the transmitted light intensity is measured. In order to detune the excitonic resonance of the QD relative to the laser photon energy, either the laser wavelength or the exciton resonance energy is scanned. The resonance of the exciton can be controlled via the applied gate voltage, exploiting the quantum confined Stark effect (see chapter 1.3.1). Lock-In detection is used in order to reduce noise by modulating the gate voltage with a square wave. A typical transmission spectrum of a neutral or charged QD is shown in Fig. 3.1. The fine structure splitting of the neutral exciton can be clearly resolved [3, 9, 10]. The measured linewidth of the resonances is of the order of $\approx 2 \mu\text{eV}$ emphasizing the high spectral resolution of laser spectroscopy which is only limited by the linewidth of the laser ($< 5 \text{ MHz}$ ($= 0.02 \mu\text{eV}$) over 20 s).

The setup that is used to prepare the laser light and to measure the transmission signal, is shown in Fig. 3.2. Two identical external cavity diode lasers [B 13] can be used to perform two color experiments. The wavelength of each laser is tunable in the range of $930 \text{ nm} - 990 \text{ nm}$ with a mode-hop free tuning range of $> 10 \text{ GHz}$. Faraday isolators [B 14] are used to protect the laser from back reflections, which

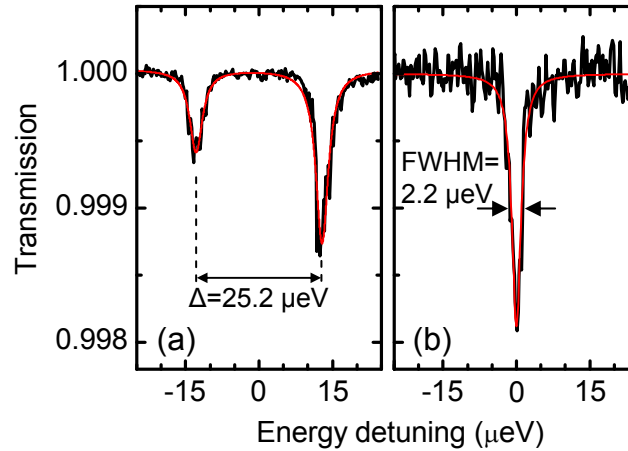


Figure 3.1: Transmission spectrum of a neutral QD (a) and a QD charged with a single electron (b). The resonances appear as a dip in the spectrum and can be fitted by Lorentzian functions (gray lines). The laser was arbitrarily polarized, so that the two fine structure lines of the neutral exciton are of different strength. The lines are separated by $25.2 \mu\text{eV}$ as shown in (a). The full linewidth at half maximum of the negatively charged exciton is measured to be $2.2 \mu\text{eV}$ in (b), revealing the high spectral resolution potential of laser spectroscopy. The laser power at the sample was $\approx 1 \text{ nW}$

can lead to mode hops and instabilities of the laser frequency and intensity. Two polarization units allow the preparation of any desired polarization of the two laser beams independently. The polarization units contain a Glan-Thompson linear polarizer [B 15], a quarter-wave plate [B 16] and a half-wave plate [B 17]. The degree of polarization can be measured by placing a polarimeter [B 18] into the beam. The two laser beams are mixed and split in a non-polarizing beam splitter cube [B 19]. Both beams are divided with a ratio of 50/50, leading to two beams behind the beam splitter. One of the two beams is used for monitoring the wavelength and mode stability. Therefore, the light is coupled into a fiber beam splitter [B 20] with a dividing ratio of 60/40 directing one part of the light into a wavemeter [B 21], the other into the scanning Fabry-Pérot [B 22]. The other laser beam is coupled into a single mode fiber after being attenuated by neutral density filters ^a. The single mode fiber leads the laser light into the fiber-based miniature microscope (see chapter 2), cooled in a liquid helium bath cryostat to 4.2 K through a low pressure helium exchange gas. The laser light is focused on the sample, where it interacts with the QD. The transmitted light is collected by the transmission detector [B 4]. A preamplifier is used [B 23] for amplification of the photo-current generated by the photodetector. The signal from the preamplifier is then analyzed with a Lock-In amplifier [B 24]. When the polarization analyzing unit that is described in chapter 3.4 was used, two preamplifiers and two Lock-In amplifiers are required, one for each photodetector. For performing Stark-shift modulation spectroscopy [11], the volt-

^a The optical density $OD = -\log_{10}(I/I_0)$, where I is the transmitted light intensity and I_0 the impinging light intensity.

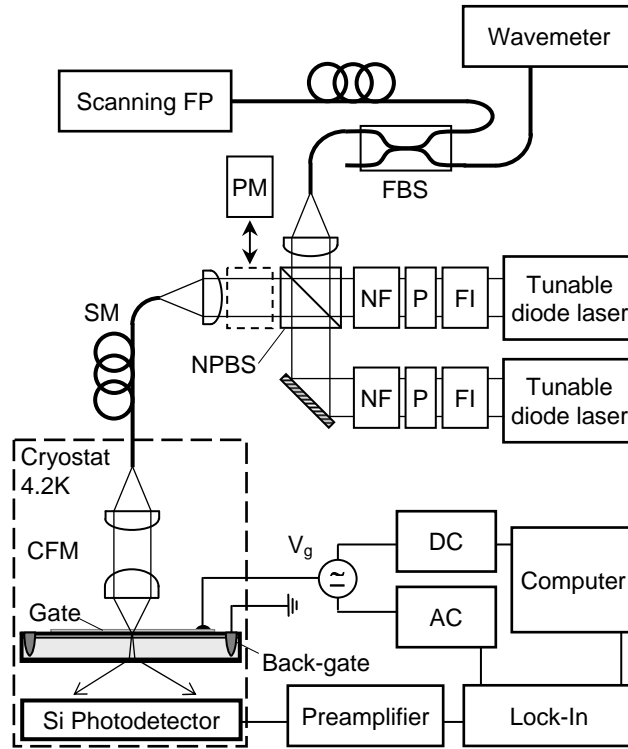


Figure 3.2: Setup for high resolution laser spectroscopy of single QDs in transmission. The light from each laser is passing through a Faraday isolator (FI) [B 14], polarization optics (P) [B 15, B 16, B 17] and neutral density filter (NF) ($OD = 0.05 - 6$). The light of the two lasers is mixed in a non-polarizing beam splitter (NPBS) [B 19]. One part of the mixed light is coupled into a fiber-based beam splitter (FBS) [B 20] to analyze it in a wavemeter [B 21] and a scanning Fabry-Pérot cavity [B 22]. The other part of the light is coupled into a single mode fiber (SM) leading into the confocal miniature microscope (CFM) [B 1] in the cryostat at 4.2 K. The transmitted light is collected by a Si photodetector [B 4]. The measured photocurrent is amplified by a preamplifier [B 23] and a Lock-In amplifier [B 24] to be finally recorded with a computer. The DC voltage of the applied gate voltage is generated with a computer controlled DC-voltage source (DC) [B 25, B 26], while the AC voltage comes from a function generator (AC) [B 27]. To control the polarization of the laser, a polarimeter (PM) [B 18] can be placed into the beam.

age applied to the gate contains a DC and an AC component. The DC component is used to tune the excitonic transition into resonance with the laser field and to choose the charge state of the QD. A DC calibrator [B 25] or a computer controlled voltage source [B 26] are used to generate the DC voltage. The AC voltage is generated by a waveform generator [B 27] and it is mixed with the DC voltage in a home built Bias-T. The AC voltage is usually a square wave with a frequency of 77 Hz or 777 Hz and with a peak to peak amplitude $V_{pp} = 10$ V. The voltage output of the frequency generator is connected to an attenuator reducing both the AC-amplitude to $V_{pp} = 100$ mV and the noise generated by the frequency generator by a factor of 100. The computer, used for signal recording also controls the gate voltage and the laser wavelength via a piezo actuator that rotates the external cavity grating in

the laser head. The wavelength measured by the wavemeter and the mode stability monitored by the scanning Fabry-Pérot are recorded during the measurement. A Labview based computer program was written and used to control the measurement.

3.2 Stark-shift modulation spectroscopy

Considering the amplitude of the transmission spectra shown in Fig. 3.1, it is obvious that the challenge of detecting the transmission signal of a single QD lies in the ability to resolve a change in transmission of $\approx 0.1\%$. Without enhancing the signal to noise ratio by solid immersion optics [12, 13], this is only possible by using Lock-In technique. The quantum confined Stark effect allows to control the transition energy of an exciton via a voltage applied to the gate of the sample. This can be used to tune the quantum dot into resonance with the laser and furthermore to modulate the resonance energy of the exciton. The spectral features of an excitonic transition are of the order of $2 - 5 \mu\text{eV}$ corresponding to a voltage of $\approx 2 - 5 \text{ mV}$ depending on the conversion factor of typically $1 \text{ mV}/\mu\text{eV}$. The conversion factor is obtained by a linear approximation of the Stark shift and it depends on both the charge state of the QD, and the lever arm of the sample. Usually, a signal obtained in a Lock-In measurement yields the derivative of the quantity to be measured with respect to the modulated parameter. In order to resolve the true lineshape of the resonance with this Stark-shift modulation spectroscopy technique, a square wave modulation is used with a peak to peak amplitude $V_{\text{pp}} = 100 \text{ mV}$. The amplitude is at least one order of magnitude larger than the resonance linewidth.

In Fig. 3.3, the concept of the Stark-shift modulation spectroscopy is shown. The

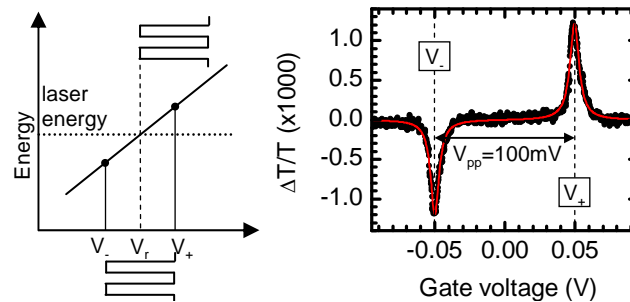


Figure 3.3: Left: exciton transition energy as a function of the gate voltage. The linearly approximated quantum confined Stark effect of the exciton transition is shown by the black line, the constant laser energy by the dotted line. The gate voltage is modulated by a square wave (indicated below the voltage axis) leading to the appearance of two resonances during a gate voltage sweep. The exciton transition is resonant to the laser photon energy for the DC-voltages V_- and V_+ , but not for the real resonance voltage V_r , for which the exciton transition energy equals the laser energy. Right: the corresponding differential transmission spectrum of a X^- measured with a Lock-In. Two replica of the resonances appear at the voltages V_- and V_+ , separated by $V_{\text{pp}} = 100 \text{ mV}$. The sign results from the phase sensitivity of the Lock-In detection. The peaks reveal the real lineshape of the resonance and can be described by Lorentzians.

measured spectrum exhibits two replica of the resonance at gate voltages $V_- = V_r - 1/2V_{pp}$ and $V_+ = V_r + 1/2V_{pp}$. The amplitude of the signal is given by the x -channel of the Lock-In, while the sign of the signal arises from the phase information. The real amplitude of the signal is a factor of 2.2 larger than the measured amplitude, since the Lock-In detection only integrates the first Fourier component of the modulation frequency. The higher Fourier components of the square wave modulation are filtered out and $\approx 55\%$ of the signal amplitude are not detected.

For the calculation of the transmission contrast $\Delta T/T$, the differential transmission signal from the Lock-In detection ΔT is normalized by the transmission T . The transmission T corresponds to the laser intensity at the position of the QD. In order to calculate this intensity, the transmitted laser power measured on the detector, has to be corrected for the non-Lorentzian spectral emission characteristics of the laser [14]. The transmission contrast is therefore:

$$\frac{\Delta T}{T} = \frac{2.2}{0.6} \left(\frac{\Delta T}{T} \right)_{\text{measured}}. \quad (3.1)$$

3.3 Interferometric Rayleigh scattering

The measured quantity in the differential transmission experiment is the transmission contrast $\Delta T/T$ of the laser resonant with the QD transition. The QD can be treated as a scatterer, while the forward scattered light of the QD interferes with the transmitted laser light on a photodetector that is placed behind the QD sample. In this sense, the resonant laser spectroscopy is an interferometric Rayleigh scattering experiment (Fig. 3.4). The differential transmission is given by the difference between the transmitted intensity on-resonance $|\mathbf{E}_L + \mathbf{e}_s|^2$ and off-resonance $|\mathbf{E}_L|^2$:

$$\frac{\Delta T}{T} = \left\langle \frac{|\mathbf{E}_L + \mathbf{e}_s|^2 - |\mathbf{E}_L|^2}{|\mathbf{E}_L|^2} \right\rangle \approx \left\langle \frac{2\mathbf{E}_L \mathbf{e}_s}{|\mathbf{E}_L|^2} \right\rangle. \quad (3.2)$$

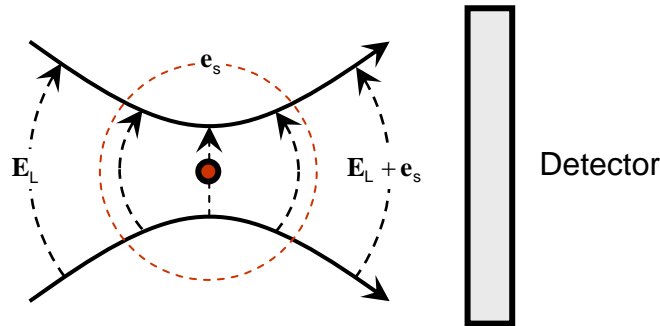


Figure 3.4: A quantum dot in the focus of a resonant Gaussian laser beam. The electric field component of the laser light \mathbf{E}_L and the electric field of the scattered light from the QD \mathbf{e}_s are detected on the photodiode.

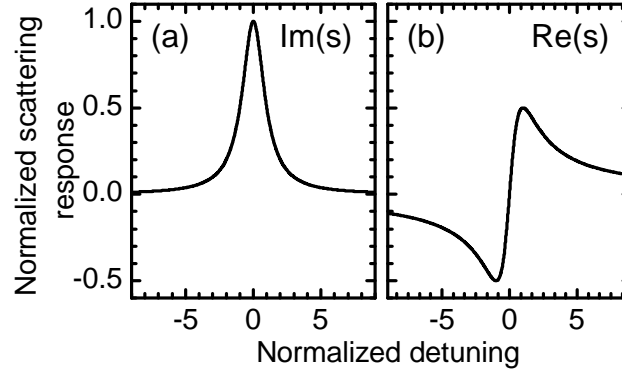


Figure 3.5: Real (b) and imaginary part (a) of the normalized scattering response ($E_L \sigma_0 = 1$) plotted as a function of the detuning δ normalized to the damping term γ .

Here, $\mathbf{E}_L = E_L \exp(i\omega_L t) \hat{\mathbf{E}}_L$ and $\mathbf{e}_s = e_s \exp(i\omega_s t) \hat{\mathbf{e}}_s$ are the electric field components of the laser field and the scattered light, respectively. The time averaging of the experiment is represented by the brackets. The intensity of the scattered signal is assumed to be small compared to the intensity of the laser ($|\mathbf{e}_s|^2 \ll |\mathbf{E}_L|^2$). The scattering response of a driven QD is given by [14, 15]

$$s(\delta) = E_L \sigma_0 \frac{\delta\gamma + i\gamma^2}{\delta^2 + \gamma^2}, \quad (3.3)$$

with the scattering cross-section σ_0 , the radiative damping rate $\gamma = 1/2\Gamma$ and the detuning $\delta = \omega_0 - \omega_L$ between the laser energy ($\hbar\omega_L$) and the excitonic transition energy ($\hbar\omega_0$). A detailed derivation of this equation based on the optical theorem is given in [14] and [15] and is not reproduced here. Equation (3.3) is valid for the geometry indicated in Fig. 3.4, where the collection NA of the detector is large, meaning that all the laser light is collected by the detector. In case of resonant Rayleigh scattering the scattering cross-section depends only on the wavelength of photons resonant with the transition: $\sigma_0 = \frac{3}{2\pi} \left(\frac{\lambda}{n}\right)^2$ with n being the refractive index of the surrounding material.

Eq. (3.3) includes the absorptive $\gamma^2/(\delta^2 + \gamma^2)$ and dispersive $\delta\gamma/(\delta^2 + \gamma^2)$ responses of the QD to laser illumination (see Fig. 3.5). The two parts are phase shifted by $\pi/2$. While propagating through the focus the focused laser field undergoes a phase shift of π , the so called Gouy's phase [16]. Hence, the laser field is in phase with the absorptive part of the QD response in the far-field and the interference can be detected on the photodetector. For low excitation power the scattered light is almost completely coherent [17]. The measured signal of the differential transmission as a function of the detuning is given by:

$$\frac{\Delta T}{T} = \frac{\sigma_0}{A} \frac{\gamma^2}{\delta^2 + \gamma^2}. \quad (3.4)$$

The ratio of the scattering cross-section σ_0 and the illuminated area $A = \pi(d_{\text{FWHM}}/2)^2$

represents the maximum transmission contrast α_0 .

The scattered field consists of a coherently and an incoherently scattered part $\mathbf{e}_s = \mathbf{e}_{\text{coh}} + \mathbf{e}_{\text{incoh}}$, depending on the laser excitation power [17]. The incoherently scattered light exhibits no constant phase relative to the laser field. Interference of this field with the laser light can not be detected in a time integrating detection scheme. With increasing laser power the fraction of the incoherently scattered light increases. The scattering response of a driven two-level system was derived by B.R. Mollow in 1969 [17] and there, the fraction of coherently scattered light to the total intensity of the scattered light by a two level system is given by:

$$\frac{I_{\text{coh}}}{I_{\text{tot}}} = \frac{\delta^2 + \gamma^2}{\delta^2 + \gamma^2 + \frac{1}{2}\Omega^2}. \quad (3.5)$$

The Rabi energy Ω connects the dipole matrix element of the two-level system μ_{12} to the driving electric field component E_L

$$\Omega = |\mu_{12}|E_L \sim \sqrt{P_L} \quad (3.6)$$

with P_L the driving laser power. Following the derivation in [17] and [14], the transmission spectrum for a finite laser power is given by:

$$\frac{\Delta T}{T} = \alpha_0 \frac{\gamma^2}{\delta^2 + \gamma^2 + \frac{1}{2}\Omega^2}. \quad (3.7)$$

According to this equation, the maximum transmission contrast in resonance follows a saturation curve as the laser power is increased (see Fig. 3.6 and in chapter 4).

Up to now, the conducted analysis only applies to a two-level system with a damping given by purely radiative recombination. This is not necessarily true for an artificial two-level system such as a QD, which is formed by ≈ 10000 atoms in a semiconductor crystal. It is reasonable to assume that fluctuations of the environment (e.g. charge

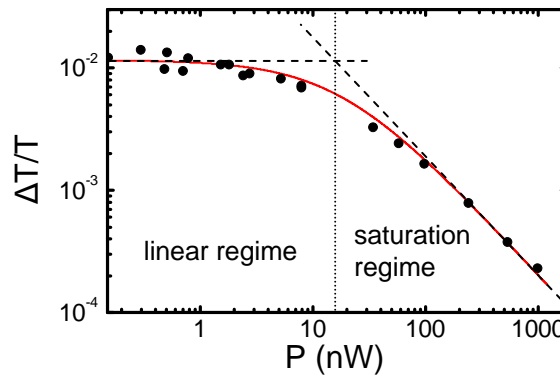


Figure 3.6: Transmission contrast in resonance with an X^{1-} transition as a function of the laser power. Two regimes can be distinguished. For small power in the linear response regime, the transmission contrast is constant, while the transmission contrast decreases for elevated laser power, when the transition is saturated. The line is a fit to the data points based on eq. (3.7).

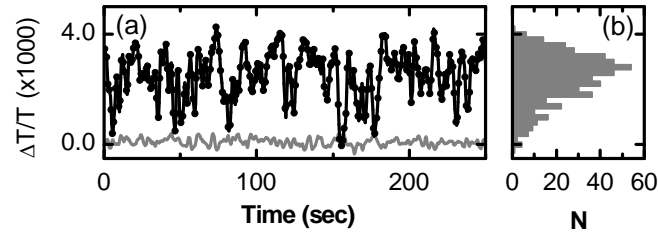


Figure 3.7: Spectral fluctuations observed in the transmission spectrum of a neutral QD. (a) The transmission contrast for constant gate voltage is plotted versus time. On resonance (black curve) and off resonance (gray line). (b) Histogram of the transmission contrast in resonance over time.

fluctuations in the back contact) lead to dephasing of the excited QD state. Indeed, we observe spectral fluctuations leading to an inhomogeneous broadening of the resonance line [9]. In Fig. 3.7, the transmission contrast of a neutral exciton is plotted as a function of time. Strong fluctuations are observed and the differential transmission signal even goes to zero. This jitter is interpreted as a frequency fluctuation of the exciton transition, since the gate voltage and laser frequency noise lies much below the observed resonance linewidth. Also noise in the detection system can be excluded by comparing the on-resonance transmission signal to a measurement of the transmission off-resonance with the excitonic transition (gray line in Fig. 3.7). The origin of the spectral fluctuations is not exactly identified yet. More systematic studies are necessary to gain insight into the microscopic dynamics existing in such an artificial solid-state nanostructure.

In chapter 4, the power dependency of the transmission signal is discussed in detail. Also the contribution of the spectral fluctuations to the linewidth as well as radiative and non-radiative decay processes will be analyzed.

3.4 Simultaneous measurement of the dispersive and absorptive scattering response of the neutral exciton

Until now, the polarization properties of the QD transitions and the excitation laser field have not been discussed. The scattering response of a QD, as it is given by eq. (3.3), strongly depends on the polarization of the photons in the laser beam and the polarization of the scattered photon. The polarization of the photon scattered by a particular QD transition will hereafter be associated to the excitonic transition. In this sense, the two fine structure transitions of a neutral exciton are linearly polarized and their linear polarizations are orthogonally oriented to each other. A linearly polarized laser field only interacts with one particular fine structure line, if it is polarized parallel to this line. The other fine structure transition is completely transparent for this laser field. This is shown in Fig. 3.8. By switching the laser polarization between the two orthogonal linear polarizations π_x and π_y of the neutral

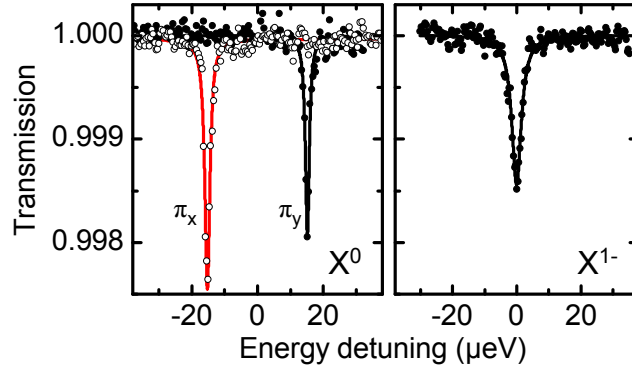


Figure 3.8: Transmission spectra of the neutral (X^0) and negatively charged (X^{1-}) exciton. For the X^0 , the laser was linearly polarized to match the two orthogonal polarizations π_x (open circles) and π_y (black dots) of the two fine structure lines. For the X^{1-} , the laser was arbitrarily polarized. The laser power was the same for both experiments ≈ 10 nW. The data points are fit by Lorentzian functions.

exciton, only one of the fine structure lines is visible in the spectrum. In contrast, the negatively charged exciton transition is unpolarized, hence, the line strength is independent of the photon polarization. For small laser power, it exhibits half the transmission contrast as each of the fine structure lines of the X^0 state with their corresponding linearly polarized excitation [12]. The spectra in Fig. 3.8 were measured for equal laser powers of ≈ 10 nW at the transition from the linear regime to the saturation regime (see also Fig. 3.6). The X^0 resonances are already saturated and the transmission contrast is reduced as compared to low power excitation. For the measurement of the X^{1-} resonance, the laser power is the same but since the transition is unpolarized, it is only sensitive to half of the intensity in the laser beam. As a result, the transition only interacts with half of the laser power and it exhibits a transition into the saturation regime at twice as high laser powers [18]. For this reason, the X^{1-} resonance shown in Fig. 3.8 shows a contrast stronger than half the contrast of the X^0 resonances.

The polarization properties of the optical transitions discussed above, which are conveyed to the scattered photons, can be used to measure the full complex scattering response of a QD transition, first performed by B. Alén *et al.* [19] by phase sensitive absorption. In [20] M. Atatüre *et al.* showed the simultaneous measurement of the dispersive and absorptive response of a negatively charged QD transition by Faraday rotation. In the following, a similar experiment is performed on a neutral QD transition. The possibility to carry out such an experiment on a neutral exciton demonstrates that neither a circularly polarized transition is required nor an external magnetic field.

The experimental setup for the experiment was introduced in chapter 2.2.3 and it is shown in Fig. 3.9. After interacting with the QD, the laser light is passing through a $\lambda/4$ -plate. The coordinate system is defined by the fast axis of the $\lambda/4$ -plate which is chosen to be parallel to the x -axis, the z -axis is given by the propagation direction

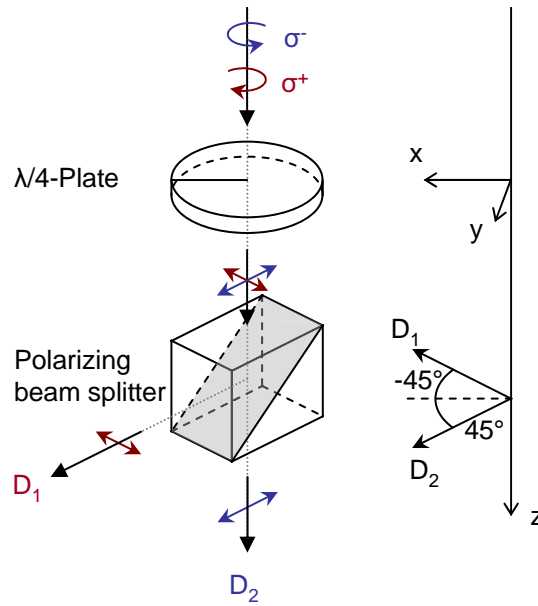


Figure 3.9: Polarization analyzing unit as introduced in chapter 2.2.3. Circularly polarized light is converted to linearly polarized light, which is then detected by the two photodetectors ($\sigma^+ \rightarrow D_1$, $\sigma^- \rightarrow D_2$). The coordinate system, that is defined by the $\lambda/4$ -plate is shown on the right. The fast axis of the $\lambda/4$ -plate is parallel to the x -axis. The light propagates along the z -axis. The beam splitter and detectors act as two linearly polarized detectors, which are sensitive to the electric field component along D_1 and D_2 .

of the laser light (see also Fig. 3.9). Behind the $\lambda/4$ -plate, a polarizing beam splitter (PBS) cube is rotated by 45° with respect to the fast axis of the $\lambda/4$ -plate. The transmitted or reflected light is then detected by two photodetectors D_1 and D_2 . The PBS-cube together with the two detectors acts as a detector for both components of the linear polarization. The corresponding coordinate system is depicted on the right of Fig. 3.9. The x -axis of the coordinate system was chosen to be along the fast axis of the $\lambda/4$ -plate. Hence, the PBS acts as a linear polarization filter with axes of transmission at 45° (-45°), respectively. In the Jones matrix formalism, the setup can be written as follows [21]:

- The $\lambda/4$ -plate with the fast axis along the x -direction

$$\text{QWP} = \frac{1}{2} \begin{pmatrix} 1 - i & 0 \\ 0 & 1 + i \end{pmatrix}. \quad (3.8)$$

- The polarized detector along 45° :

$$D_2 = \frac{1}{2} \begin{pmatrix} 1 & 1 \\ 1 & 1 \end{pmatrix}, \quad (3.9)$$

- and along -45° :

$$D_1 = \frac{1}{2} \begin{pmatrix} 1 & -1 \\ -1 & 1 \end{pmatrix}. \quad (3.10)$$

The unit vector of an arbitrarily polarized laser field is given by

$$\hat{\mathbf{E}}_L = \frac{1}{\sqrt{2}} \begin{pmatrix} \cos(\alpha) - \sin(\alpha) (\cos(\phi) + i \sin(\phi)) \\ \sin(\alpha) + \cos(\alpha) (\cos(\phi) + i \sin(\phi)) \end{pmatrix}. \quad (3.11)$$

Here, α is the angle of the linear polarization to the x -axis and ϕ is the phase between the two electric field components. In the given coordinate system, for $\alpha = 0$ and $\phi = 0$, the electric field vector of the laser field is tilted by 45° with respect to the x -direction:

$$\hat{\mathbf{E}}_L(\alpha = 0, \phi = 0) = \frac{1}{\sqrt{2}} \begin{pmatrix} 1 \\ 1 \end{pmatrix}. \quad (3.12)$$

The phase ϕ gives the relative phase between the x and the y -component of the electric field vector. So, for $\phi = \pi/2$ and $\alpha = 0$ the laser field is left-handed circularly polarized:

$$\hat{\mathbf{E}}_L(\alpha = 0, \phi = \pi/2) = \frac{1}{\sqrt{2}} \begin{pmatrix} 1 \\ i \end{pmatrix}. \quad (3.13)$$

The same way, for $\phi = -\pi/2$, the laser field is right-handed circularly polarized.

The scattering of the laser by the QD takes place in the focus of a Gaussian beam, however, the phase of the laser field behind the focus shifts by a global phase i with respect to the scattered light [16], the Gouy-Phase.

The laser field which is coherently scattered by the neutral QD, is linearly polarized along one of the main axes of the dot. The direction of this axis is unknown. The scattering cross-section of the interaction is dependent on the relative polarization between the laser and the excitonic transition in the QD. First, we define the polarization direction of the QD:

$$\hat{\mathbf{e}}_s = \frac{1}{\sqrt{2}} \begin{pmatrix} \sin(\beta) \\ \cos(\beta) \end{pmatrix}. \quad (3.14)$$

Based on equation (3.3) and the polarization dependence of the interaction between the QD transition and the laser field, the scattering response of an X^0 transition is proportional to the projection of the laser field onto the X^0 polarization direction:

$$\mathbf{e}_s = s \frac{\gamma\delta + i\gamma^2}{\delta^2 + \gamma^2} \hat{\mathbf{e}}_s \quad (3.15)$$

and the scattering response according to eq. (3.3) is given by:

$$s = \frac{\sigma E_L}{2} |\hat{\mathbf{E}}_L \cdot \hat{\mathbf{e}}_s|. \quad (3.16)$$

The scattered light is polarized along the unit vectors of the coordinate system that is given by the fine-structure of the QD. Here, this is represented by the vector $\hat{\mathbf{e}}_s$, which was defined in (3.14). The laser is not necessarily polarized in the same way.

However, the scattering cross-section depends on the relative angle between the QD axis and the laser polarization. In a usual transmission experiment, the laser and the scattered light interfere on a detector that is mounted beneath the sample. In that case, the polarization of the two light fields is unchanged and only the projection of the scattered light onto the polarization direction of the laser light is contributing to the signal.

In the presented experiment, the light passes through a $\lambda/4$ -plate and is then detected polarization sensitively by two photo-diodes simultaneously. Since the polarization of the laser light and the scattered light can be different, the polarization of the two fields are modified differently by the $\lambda/4$ -plate. Hence, the relative phase between the two light fields is changed. This leads to different interference conditions on the two detectors, and for the matching polarization of the laser light, absorptive and dispersive signals can be detected on the two detectors. This corresponds to a measurement of the real and imaginary part of the scattering signal. In order to calculate the spectra on the two detectors, the propagation of the two light fields through the polarization optics is calculated and brought to interference. So, for the laser on the two detectors one gets:

$$\mathbf{E}_L^{D_1} = D_1 \cdot \text{QWP} \cdot i \cdot \mathbf{E}_L, \quad (3.17)$$

and

$$\mathbf{E}_L^{D_2} = D_2 \cdot \text{QWP} \cdot i \cdot \mathbf{E}_L. \quad (3.18)$$

Where the i accounts for the Gouy-Phase as described above. In the same way, the scattered field is treated:

$$\mathbf{e}_s^{D_1} = D_1 \cdot \text{QWP} \cdot \mathbf{e}_s, \quad (3.19)$$

and

$$\mathbf{e}_s^{D_2} = D_2 \cdot \text{QWP} \cdot \mathbf{e}_s. \quad (3.20)$$

Although the terms for the scattered light and the laser light that impinge on the detectors look almost identical, it is important that the interference only takes place after the passage of the light through the polarization optics and at the detector.

We write the interference on the detectors in the following way:

$$I_{D_1} = \left| \mathbf{E}_L^{D_1} + \mathbf{e}_s^{D_1} \right|^2 \quad (3.21)$$

for detector D_1 and

$$I_{D_2} = \left| \mathbf{E}_L^{D_2} + \mathbf{e}_s^{D_2} \right|^2 \quad (3.22)$$

for detector D_2 . Using all the definitions, introduced above, we get:

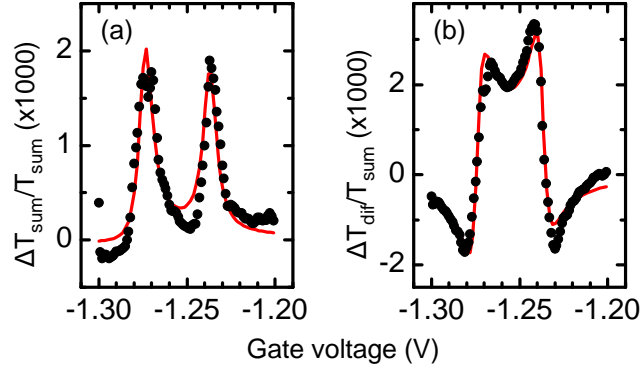


Figure 3.10: Sum (a) and difference (b) of the transmission signals measured at detector 1 and 2. $\Delta T_{\text{sum}} \equiv \Delta T_{D1} + \Delta T_{D2}$ while $\Delta T_{\text{dif}} \equiv \Delta T_{D1} - \Delta T_{D2}$ and $T_{\text{sum}} \equiv T_{D1} + T_{D2}$. The lines are fits of eq. (3.25) (a) and (3.26) (b) to the data points as described in the text

$$I_{D1} = s(\theta, \phi) \frac{\gamma(-\delta \cos(\theta) + \gamma(\cos(\theta - \phi) + \sin(\theta)) + \delta \sin(\theta - \phi))}{2(\gamma^2 + \delta^2)}, \quad (3.23)$$

and

$$I_{D2} = s(\theta, \phi) \frac{\gamma(\delta \cos(\theta) + \gamma(\cos(\theta + \phi) + \sin(\theta)) - \delta \sin(\theta + \phi))}{2(\gamma^2 + \delta^2)}. \quad (3.24)$$

For simplification, we introduce $\theta = \alpha + \beta$, which is the sum of the angles of the laser polarization and the QD polarization axis. Furthermore, we use the polarization dependent scattering cross-section: $s(\theta, \phi) = \frac{\sigma_{E_L}}{2} \sqrt{1 + \sin(2\theta) \cos(\phi)}$. The requirements for observing the dispersive contribution of the QD scattering and the absorptive contribution of the QD response on the two detectors are only accessible for the matching values of θ and ϕ . However, the sum and difference signal allows a far more simple control of the simultaneous measurement of the absorptive and dispersive scattering response of a single QD.

$$I_{\text{sum}} = I_{D1} + I_{D2} = s(\theta, \phi) \frac{\gamma(\gamma \sin(\theta) + \cos(\theta)(\gamma \cos(\phi) - \delta \sin(\phi)))}{\gamma^2 + \delta^2}, \quad (3.25)$$

and

$$I_{\text{dif}} = I_{D1} - I_{D2} = s(\theta, \phi) \frac{\gamma(-\delta \cos(\theta) + \sin(\theta)(\delta \cos(\phi) + \gamma \sin(\phi)))}{\gamma^2 + \delta^2}. \quad (3.26)$$

In order to receive the absorptive and dispersive response simultaneously, one would have to choose for example $\phi = 0$, then θ only influences the amplitude of the signal. In order to account for the fine-structure splitting of the X^0 resonance, a superposition of two resonances is applied (3.25) and (3.2). Of course, the resonance condition has to be chosen differently for the two curves. In addition, the polarization angle of the QD resonance of the two curves has to differ by $\pi/2$. In Fig. 3.10, the sum

and the difference signal of the two detectors is plotted. The curve show calculated spectra that were obtained with the derived formulas. All parameters were the same for both spectra. Only the scattering cross-section σ was different to account for differences in the collection efficiency of the two detectors. The relevant angles were: $\theta = 2.5^\circ$ and $\phi = -14.4^\circ$.

The presented results demonstrate the ability to measure the complex optical susceptibility of a neutral single QD in a resonant Rayleigh scattering experiment. For this demonstrated ellipsometry on a single QD, no magnetic field or circularly polarized transition is needed as for a Faraday rotation experiment [20]. To perform non destructive optical measurements on a QD, the dispersive scattering component is very interesting, since it decays with $1/\delta$ for large detuning, while the absorption decays with $1/\delta^2$. For large detuning the laser photon interact with the QD while it hardly gets absorbed.

References

- [1] J.Y. Marzin, J.M. Gerard, A. Izrael, D. Barrier, G. Bastard, Phys. Rev. Lett. **73**, 716 (1994).
- [2] K. Brunner, U. Bockelmann, G. Abstreiter, M. Walther, G. Böhm, G. Tränkle, and G. Weimann, Phys. Rev. Lett. **69**, 3216 (1992).
- [3] D. Gammon, E.S. Snow, B.V. Shanabrook, D.S. Katzer, and D. Park, Phys. Rev. Lett. **76**, 3005 (1996).
- [4] N.H. Bonadeo, Gang Chen, D. Gammon, D.S. Katzer, D. Park, and D.G. Steel, Phys. Rev. Lett. **81**, 2759 (1998).
- [5] R.J. Warburton, C. Schäfflein, D. Haft, F. Bickel, A. Lorke, K. Karrai, J.M. Garcia, W. Schoenfeld, and P.M. Petroff, Nature **405**, 926 (2000).
- [6] M. Bayer, A. Kuther, A. Forchel, A. Gorbunov, V.B. Timofeev, F. Schäfer, J.P. Reithmaier, T.L. Reinecke and S.N. Walck, Phys. Rev. Lett. **82**, 1748, (1999).
- [7] C.W. Lai, P. Maletinsky, A. Badolato, and A. Imamoglu, Phys. Rev. Lett. **96**, 167403 (2006).
- [8] A. Zrenner, E. Beham, S. Stuffer, F. Findeis, M. Bichler, and G. Abstreiter, Nature **418**, 612 (2002).
- [9] A. Högele, S. Seidl, M. Kroner, R.J. Warburton, B.D. Gerardot, P.M. Petroff, and K. Karrai, Phys. Rev. Lett. **93**, 217401 (2004).
- [10] M. Bayer, G. Ortner, O. Stern, A. Kuther, A.A. Gorbunov, A. Forchel, P. Hawrylak, S. Fafard, K. Hinzer, T.L. Reinecke, S.N. Walck, J.P. Reithmaier, F. Kloppe, and F. Schäfer, Phys. Rev. B **65**, 195315 (2002).
- [11] B. Alen, F. Bickel, K. Karrai, R.J. Warburton and P.M. Petroff, Appl. Phys. Lett. **83**, 2235 (2003).
- [12] B.D. Gerardot, S. Seidl, P.A. Dalgarno, M. Kroner, K. Karrai, A. Badolato, P.M. Petroff, R.J. Warburton, Appl. Phys. Lett. **90**, 221106 (2007).
- [13] A.N. Vamivakas, M. Atatüre, J. Dreiser, S.T. Yilmaz, A. Badolato, A.K. Swan, B.B. Goldberg, A. Imamoglu, and M.S. Unlu, Nano Lett. **7**, 2892 (2007).

- [14] A. Högele, *Laser spectroscopy of single charge-tunable quantum dots*, Dissertation, Ludwig–Maximilians–Universität München, ISBN 3899633253, Dr. Hut, München (2006).
- [15] K. Karrai, R.J. Warburton, *Superlattice Microst.* **311**, 33, (2003).
- [16] M. Born and E. Wolf, *Optical Coherence and Quantum Optics*, Cambridge University Press, 2005, 7th ed.
- [17] B.R. Mollow, *Phys. Rev.* **188**, 1969 (1969).
- [18] S. Seidl, *Resonant interband transmission spectroscopy on single charge-tunable quantum dots*, Dissertation, Ludwig–Maximilians–Universität München, ISBN 378-3-89963-586-7, Dr. Hut, München (2007).
- [19] B. Alén, A. Högele, M. Kroner, S. Seidl, R.J. Warburton, A. Badolato, G. Medeiros-Ribeiro, P.M. Petroff and K. Karrai, *Appl. Phys. Lett.* **89**, 123124 (2006).
- [20] M. Atatüre, J. Dreiser, A. Badolato, and A. Imamoglu, *Nature Physics* **3**, 101 (2007).
- [21] R.C. Jones, *J.O.S.A.* **31**, 488 (1941).

Chapter 4

Saturation laser spectroscopy

We performed high resolution resonant laser spectroscopy on a single self-assembled quantum dot at liquid He temperatures. We explore the two-level nature of the quantum dot (QD) excitonic transition through the investigation of its behavior as a function of the laser power. The quantum ground state exciton absorption peak size diminishes with increasing power while its width increases. Fitting these dependencies to the predictions of a two-level atom model we extract unambiguously a radiative lifetime of 660 ps, a residual collisional broadening about $0.18 \mu eV$ as well as the spectral fluctuation $1.3 \mu eV$. We find that at high power the line width of the exciton absorption is essentially given by the Rabi frequency.

4.1 Introduction

The atom like optical behavior of self-assembled quantum dots (QD) makes them interesting candidates for quantum optics and quantum information processing. In particular the two-level nature of their ground state exciton provides a crucial prerequisite to use them as quantum bits [1] and non classical light sources for quantum cryptography [2] or quantum dot lasers [3]. High resolution, resonant laser spectroscopy [7] gives direct access to the two-level properties of the excitonic transitions in a single QD.

Here we present a detailed analysis of the power dependency of the linewidth and peak intensity, which are obtained by resonant laser-spectroscopy in transmission at liquid He temperatures. We study a single self-assembled InGaAs QD grown by molecular beam epitaxy in the Stransky-Krastanow mode. The QD is embedded in a field effect structure [4] allowing discrete charging of the dot with single electrons through the control of a gate voltage[5].

We investigated the QD charged with a single resident electron, so that the excitonic transition was that of a trion or X^{1-} . Unlike the neutral exciton transition (X^0) which has a fine structure splitting, the X^{1-} transition manifests itself through a single Lorentzian peak at zero magnetic field [6]. Resonant laser transmission spectroscopy has a typical resolution limited by the linewidth of our tunable external cavity laser diode which was typically $0.01 \mu\text{eV}$. Details of this technique can be found in [6].

4.2 Power dependent laser spectroscopy

In Fig. 4.1 we show two typical transmission spectra for two different laser powers. We choose to plot the contrast in the differential transmission (α), since it will appear later in the text as the variable used in our analysis. Increasing the laser power from 0.5 nW to $3 \mu\text{W}$ we find that the linewidth increases from $3.5 \mu\text{eV}$ to $40 \mu\text{eV}$ while at the same time the contrast drastically diminishes by a factor of 100. To describe this behavior, we calculated the optical resonant transmission properties of the exciton using a two-level model, as known from atom optics [8, 9]. In all measured dots we observed that even at lowest laser power ($\sim 0.1 \text{ nW}$) the measured linewidths were about a factor two broader than expected from lifetime measurements obtained on similar QD samples [10]. This excess broadening is believed to originate from dot-level fluctuations through electron and host-material interactions. We treat these fluctuations in two different limits, dependent on their timescale. Fluctuations that occur on a timescale shorter than the exciton lifetime contribute to a homogeneous collisional-like broadening accounted for in typical two-level atom models [8]. Fluctuations with larger time scales but still small compared to the measurement time (here $\sim 1\text{s}$) leads to inhomogeneous broadening. Such broadening is generally not expected to be Lorentzian however most of our data

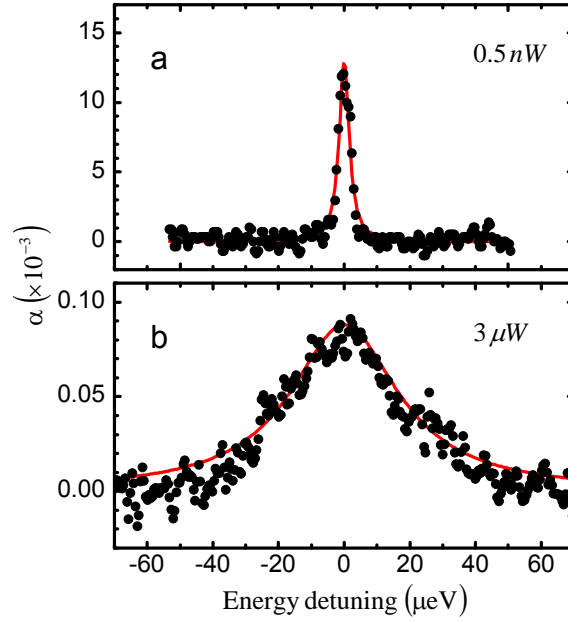


Figure 4.1: Two typical transmission spectra of the X^{1-} -transition at two different laser powers. The upper spectrum (a) was obtained by illuminating the QD with 0.5 nW , the lower one (b) with $3 \mu\text{W}$. The lines correspond to Lorentzian line fits with a FWHM of $3.5 \mu\text{eV}$ (a) and $40 \mu\text{eV}$ (b).

show invariably Lorentzian lines. In all cases broadened lines have a weaker peak than expected from an ideal two-level system. The differential transmission line shape for a homogeneous broadened excitonic transition is given by [8]:

$$\frac{\Delta T}{T} = \alpha_0 \frac{\gamma_0^2}{\delta^2 + \gamma_0^2 + \frac{\gamma_0}{2\gamma_{\text{sp}}}\Omega^2}. \quad (4.1)$$

Here α_0 is the contrast in the limit of vanishing laser power P . $2\gamma_0$ is the effective full width at half maximum of the resonance likewise at vanishing P . In a collisional broadened two-level system $\gamma_0 = \gamma_{\text{sp}} + \gamma_{\text{coll}}$ where $1/\gamma_{\text{sp}}$ is the exciton radiative life time through spontaneous emission and γ_{coll} is the contribution of the collision broadening. $\delta = \hbar\omega_L - \hbar\omega_X$ is the detuning between the photon energy $\hbar\omega_L$ and the exciton energy $\hbar\omega_X$. The Rabi frequency $\Omega^2 = 2\alpha_0\gamma_0 P/\hbar\omega_L$. The oscillator strength of the resonance is proportional to $\alpha_0\gamma_0$ implying that $\alpha_0\gamma_0 = \alpha_{\text{sp}}\gamma_{\text{sp}}$ where α_{sp} would be the resonance contrast in an ideal two-level system. This contrast is $\alpha_{\text{sp}} = 3(\lambda/n)^2/2\pi A$ which only depends on the laser wavelength at resonance λ and the area A of the focused laser spot in the plane of the dot. n is the refractive index of the QD host material.

The resonance contrast α is obtained at zero detuning ($\delta = 0$):

$$\alpha = \frac{\alpha_0}{1 + \frac{pP}{\hbar\omega\gamma_{\text{sp}}}\alpha_0} \quad (4.2)$$

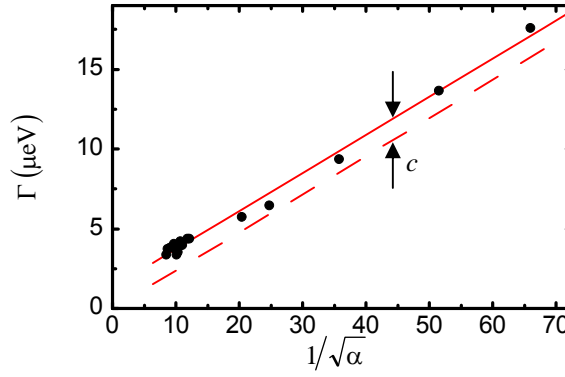


Figure 4.2: Plot of the measured linewidth as a function of the square root of the differential transmission contrast. The line is a linear fit to the data with an offset by a constant c from the theoretically expected dashed line.

Likewise the power dependency of the full width at half maximum (Γ) is given by

$$\Gamma = 2\gamma_0 \left(1 + \frac{pP}{\hbar\omega\gamma_{sp}}\alpha_0\right)^{1/2}, \quad (4.3)$$

The QD is illuminated through an Al shadow mask with a circular aperture of diameter $d = 300 \text{ nm}$. The transmitted light is collected using a 4 mm^2 PIN photodetector placed 1.5 mm behind the sample. In such a geometry and because of diffraction the transmitted photons are collected only in part and we calculated that the power P_{det} at the detector is related to P , the power experienced by the dot, through $P = pP_{\text{det}}$ ^a with here $p=17$.

4.3 Saturation and power broadening of a single QD resonance

We obtain both the linewidth and the amplitude of the resonance independently and using (4.2) and (4.3) we can eliminate their explicit power dependency in order to get $\Gamma = \Gamma_0\sqrt{\alpha_0/\alpha}$ which we plot in Fig. 4.3 along with the data. In order to fit the data, we found it necessary to add a constant $c = 1.34 \text{ } \mu\text{eV}$ to the linewidth. Such an additional constant is not expected in a collisional broadened two-level model but would be the slow contribution to dot level fluctuations. At the lowest power we measure an effective line width of $3.5 \text{ } \mu\text{eV}$ so we deduce that $\Gamma_0 = 2.36 \text{ } \mu\text{eV}$. The linear dependency gives a slope $\Gamma_0\sqrt{\alpha_0} = 0.24 \text{ } \mu\text{eV}$ from which we deduce $\alpha_0 = 0.012$ which also turnout to be the contrast directly measured at very low power.

^a $p = \left(1 - J_0\left(\frac{2\pi nr \sin(\theta)}{\lambda}\right) + J_0\left(\frac{2\pi nr \sin(\theta)}{\lambda}\right)\right)^{-1}$ [11]. J_n is the n -th Bessel function and $\theta = 0.15$ is the illumination angle of the detector, seen from the aperture with radius r . The diffraction index of GaAs is n and the laser wavelength is λ

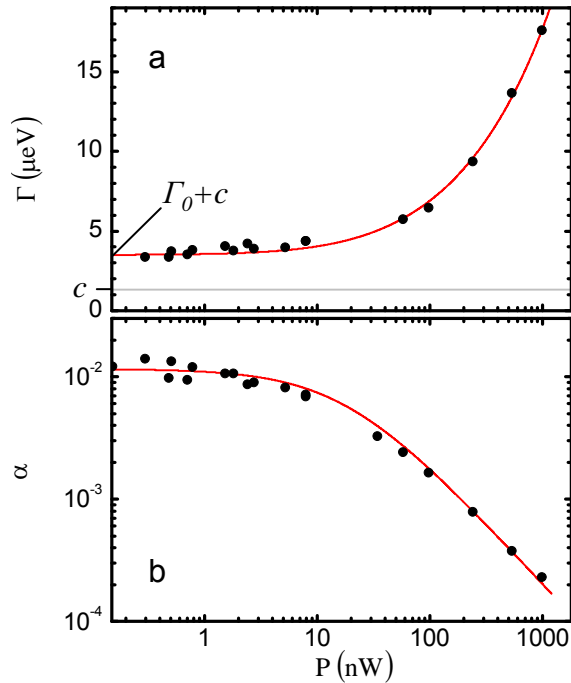


Figure 4.3: Plots of the measured linewidth (a) and contrast (b) of the excitonic transition. The lines are equations (4.2) and (4.3) fit to the data. The power axis has been calibrated by the obtained geometry factor p .

Now we turn to the explicit power dependency the resonance contrast and the linewidth. Using Γ_0 obtained above, we fit equation (4.2) to the measured contrast and using equation (4.3) we fit $\Gamma + c$ to the measured linewidth. The only fit parameters are now α_0 and γ_{sp} which we find to be $\alpha_0 = 0.02$ and $\gamma_{\text{sp}} = 1.0 \mu\text{eV}$. We deduce therefore a $\gamma_{\text{coll}} = 0.18 \mu\text{eV}$. We notice a discrepancy between $\alpha_0 = 0.02$ obtained here and $\alpha_0 = 0.012$ inferred earlier from fig 4.2. Here as well the effect of the slow components of the level fluctuations are likely to explain this discrepancy and $\alpha_0 = 0.02$ would be the contrast without time-averaged inhomogeneous broadening.

From the measured spectra we can furthermore analyze the signal to noise ratio. The noise in our experiment is dominated by the laser shot noise as well as a weak detection dark noise which we systematically subtract. The shot noise is proportional to the square root of the number of photons per unit time ($\dot{N} = P_{\text{det}}/\hbar\omega_L$), while the signal is given by: Signal = $P_{\text{det}}\alpha$. Hence the signal to noise ratio is according to equation (4.2):

$$\frac{\text{Signal}}{\text{Noise}} = \frac{\sqrt{\frac{P_{\text{det}}}{\hbar\omega}}}{\frac{1}{\alpha_0} + \frac{pP_{\text{det}}}{\hbar\omega\gamma_{\text{sp}}}}. \quad (4.4)$$

The measured signal to noise ratio is plotted in Fig. 4.4 as a function of the laser

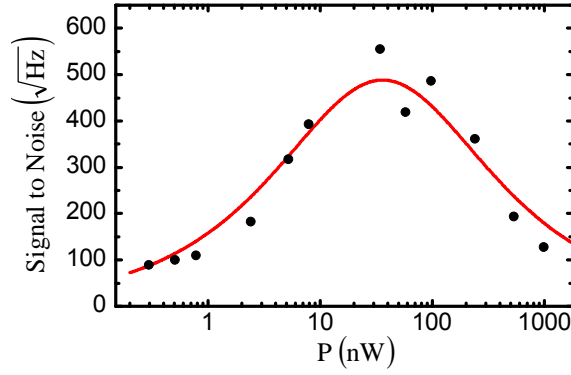


Figure 4.4: Signal to noise ratio is plotted with a fit of eq. (4.4) to the data points, represented by a line.

power P at the detector. In equation (4.4) we used $\alpha_0 = 0.012$ and $p = 17$ and $\gamma_{\text{sp}} = 1.0 \mu\text{eV}$.

4.4 Conclusions

The presented data strengthens the picture of the QD as an artificial atom that can be modelled by a simple two level model. We found that very conveniently the radiation limited lifetime of the quantum dot ground state exciton is obtained through the analysis of the exciton resonance saturation and power broadening even when collisional and inhomogeneous broadening are taken into account. Furthermore high resolution resonant laser spectroscopy highlights the limitations of the two-level model to describe the quantum dot exciton ground state. Here we revealed that collisional broadening is only a tenth of the spontaneous emission broadening which, given the solid state nature of the device, is surprisingly small. The slow spectral fluctuation accounts for half the linewidth broadening and its origin still needs to be elucidated. Should one reach the limit of single exciton absorption, spectral fluctuations are not expected to play a role in the linewidth and contrast of a scattering signal. Recently more efficient optical measurement schemes have been presented [12, 13]. There, the contrast of differential transmission spectroscopy experiments has been dramatically increased opening a path towards single exciton absorption.

References

- [1] A. Zrenner, et al., *Nature* 418, 612 (2002).
- [2] N. Akopian, et al., *Phys. Rev. Lett.* 96, 130501 (2006).
- [3] H. Ishikawa, et al., *J. Vac. Sci. Technol. A* 16, 794 (1998).
- [4] H. Drexler, et al., *Phys. Rev. Lett.* 73(16), 2252, (1994).
- [5] R. J. Warburton, et al., *Nature* 405, 926 (2000).
- [6] A. Högele, et al., *PhysicaE* 21, 175 (2004).
- [7] A. Högele, et al., *Phys. Rev. Lett.* 93, 217401 (2004).
- [8] R. Loudon, *The Quantum Theory of Light*, Oxford University Press, Cambridge, 1995.
- [9] K. Karrai, et al., *Superlattices and Microstructures*, 33, 311 (2003).
- [10] Smith, et al., *Phys. Rev. Lett.* 94, 197402 (2005).
- [11] M. Born and E. Wolf, *Principles of Optics*, Cambridge University Press, Cambridge, 2005.
- [12] S. Seidl, et al., *Phys. Rev. B* 72, 195339 (2005).
- [13] A. N. Vamivakas, et al., *Nano Lett.* 7 (9), 2892 (2007).

Chapter 5

Rabi splitting and ac-Stark shift of a charged exciton

The Rabi splitting of the negatively charged exciton in a single InGaAs quantum dot is observed in resonance transmission spectroscopy. We use a pump laser excitation to drive strongly the unpolarized trion transition in a quantum dot and detect its modified absorption spectrum with a second weak probe laser. By tuning the pump laser near resonance, we observe an ac-Stark effect dispersion, with a power dependent Rabi splitting on resonance, both signatures of a strongly coupled two level system. Although the pump and probe laser fields are resonant with the same transition we do not observe all features in the Mollow spectrum. We combine the results of pump-probe with saturation spectroscopy data to deduce the individual contributions to the low power linewidth.

5.1 Introduction

One of the most attractive features of self-assembled quantum dots (QD), embedded in a field effect device, is that they can be charged with single electrons or holes [1]. Spectroscopy on a single QD allows a detailed study of the optical properties of the emission (PL) [2, 3] and absorption [4, 5, 6, 7, 8] of neutral and charged QDs. The singly charged QD is particularly important since its resident electron can serve as a spin qubit [9, 7]. A major prerequisite for coherent spin control in a QD is the few level nature of the electronic states. The observation of Rabi oscillations of the neutral exciton transition has strengthened the “artificial atom” picture of a single InGaAs QD [10]. Very recently optical pump and probe experiments on a neutral QD led to the observation of the Rabi splitting in the frequency domain [11, 14, 15] and to a Mollow absorption spectrum [11] as observed on atoms [12, 13]. However, spin control is best achieved on a charged exciton [7]. Here we present a resonant pump and probe experiment on the negatively charged exciton revealing optical Stark shift dispersion as well as Rabi splitting at optical resonance.

5.2 Two-laser pump and probe spectroscopy

The sample contains self-assembled InGaAs QDs whose emission wavelength has been shifted to around 950 nm by in-situ annealing during growth. The dot layer is embedded in a field effect structure [1] consisting of an n-doped back contact, 25 nm below the QDs, and a metallic semitransparent NiCr top gate, 276 nm above the back contact. To prevent leakage currents in this structure a blocking barrier was grown between the dot layer and the sample surface. It consists of an AlAs/GaAs superlattice beginning 10 nm above the QD wetting layer. By applying a voltage between gate and back contact we can charge the dots with single electrons by tunnelling from the back contact. Further, the resonance energies of the excitonic transitions are modified by the quantum confined Stark effect [2, 5]. We perform resonant laser spectroscopy in transmission, where gate voltage modulation is used to apply lock-in detection [6]. The sample is mounted in a fiber-based, diffraction-limited confocal microscope that is immersed in He exchange gas in a liquid helium bath cryostat at 4.2 K. We use a continuous wave (cw) pump laser and a separate cw probe laser. The lasers are linearly polarized perpendicularly to each other. The trion (X^{1-}) transition is unpolarized at zero magnetic field [4], such that the choice of polarization does not affect the outcome of the experiment. Behind the sample a lens collimates the transmitted light. In order to separate the pump and probe transmission signals, a polarizing beam splitter divides the light into the two orthogonal polarizations and each polarization is detected by a photodetector. The setup is shown in Fig 5.1(a). Due to losses in the collection path after collimation, we collect less power on the detectors P_{Det} than experienced by the QD: $P_{\text{Dot}} = pP_{\text{Det}}$. This factor we measure to be $p = 11$, the values for the power given below are

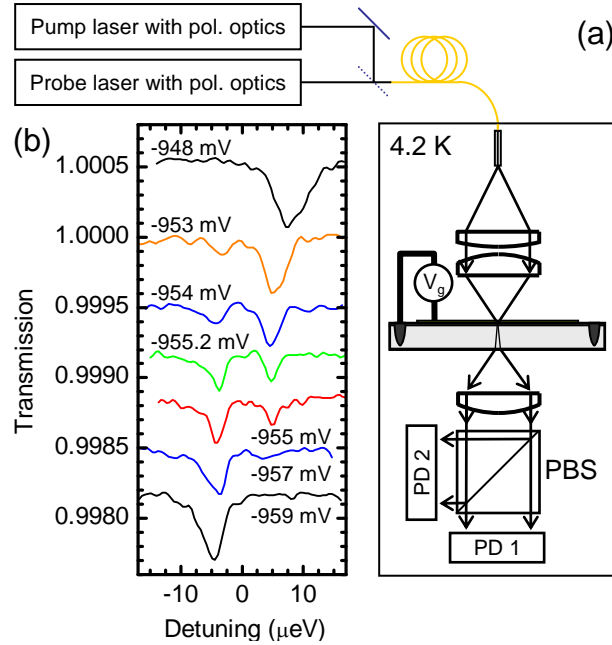


Figure 5.1: (a) Schematics of the polarization sensitive detection scheme. Two tunable narrow band lasers provide the pump and the probe beam whose polarizations can be controlled independently. The two beams are coupled into a single mode fiber that guides them into the cryogenic confocal microscope operating at 4.2 K. After the sample the two transmitted beams are separated by a polarizing beam splitter (PBS) and detected on the two photodetectors PD1 and PD2. The graphs in (b) show the ac-Stark modified spectra measured with the probe beam for different detunings of the pump laser. This was achieved by keeping the pump laser photon energy constant and scanning the probe laser photon energy at different gate voltages. The pump and probe laser powers were: $P_{\text{pump}} = 202$ nW and $P_{\text{probe}} = 9$ nW. The spectra have been shifted by an offset relative to 1 for clarity.

the powers at the location of the quantum dot. The polarization sensitive detection setup allows us to increase the pump intensity up to 40 times the probe laser intensity without significantly affecting the probe detector. For all experiments, the probe laser power is kept at an intensity that lies below optical saturation of the transition [4, 16]: $P_{\text{probe}} = 9$ nW. We keep the pump laser photon energy constant in the middle of the X^{1-} charging plateau [5] with a power 20 times the power of the probe laser. The probe laser photon energy is scanned through the QD trion resonance for different gate voltages.

5.3 The ac-Stark shift of a charged exciton

In Fig. 5.1(b) transmission spectra are shown for different gate voltages and hence for different exciton detunings from the pump laser photon energy ($\Delta = (E_X - E_{\text{pump}}) \propto V_G$, with E_X the energy of the unperturbed X^{1-} transition). The transmission, measured in the probe channel, is plotted as a function of the detuning of

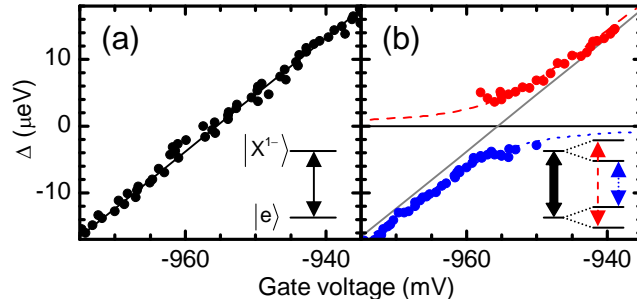


Figure 5.2: (a) Energy shift of the transmission resonance of the X^{1-} transition of a single QD as a function of the applied gate voltage for zero pump power. The insert shows the excited transition in the QD. (b) The measured resonance energies obtained by sweeping the probe photon energy while the strong pump laser photon energy is kept constant (horizontal line) are plotted as a function of the gate voltage. The grey line corresponds to the transition shown in (a). The dotted and dashed lines are a simple anti-crossing behavior as expected from eq. 5.1. The insert indicates the pump (black arrow) and probe (dotted and dashed arrow) transitions.

the probe laser with respect to the pump laser at different gate voltages. The plots clearly show that the single Lorentzian resonance detected by the probe laser at large negative Δ develops a splitting as $|\Delta|$ decreases and shows a doublet structure for $\Delta = 0$. For positive Δ , the oscillator strength is completely transferred to the second resonance and the first one vanishes. In Fig. 5.2(b) the resonance energies of the observed transitions are plotted versus the applied gate voltage, while in (a) the X^{1-} resonance for zero pump power is shown. The behavior of the observed resonances follows a clear anti-crossing with a strong pump laser.

In principle, the X^{1-} exciton represents a 4-level system, with two electron spin ground states and two exciton spin states. However, without a magnetic field, the hyperfine interaction with the nuclei leads to rapid spin relaxation between the two electron spin states, comparable to the exciton spontaneous recombination rate [17]. In fields above about 0.3 T, relaxation via the hyperfine interaction is suppressed but in our device, spin relaxation is enabled by a spin-swap process with the back contact, a cotunnelling phenomenon [7]. This means that there is no pronounced optical pumping of the spin and no chance of any long-lived ground state coherences in this particular case. We therefore attempt to describe these experiments with a 2-level model, including a dephasing term γ_{nr} to represent the spin relaxation. As we show, this approach yields convincing agreement with the experimental data. The anticrossing in Fig. 5.2(b) can be described for a strongly coupled 2-level system by [18]:

$$E_{\pm} = \frac{1}{2} \left(\Delta \pm \sqrt{\Delta^2 + 4|W|^2} \right). \quad (5.1)$$

Here E_{\pm} gives the resonance energies of the two resonances of the strongly driven two level system, depicted by the dotted and dashed lines in Fig. 5.2(b). W quantifies the coupling strength, the Rabi energy $W = \hbar\Omega$ which is power dependent: $\Omega^2 = 2\alpha_0\gamma_0 P_{\text{pump}}/\hbar\omega_{\text{pump}}$ [19]. The parameters α_0 and γ_0 describe the coupling of the

two-level transition to the light field. α_0 is the low power limit of the transmission contrast, and $\gamma_0 = \gamma_{nr} + \gamma_{sp}$ is the dephasing rate for low power, given by the sum of non-radiative rate γ_{nr} and the spontaneous recombination rate $\gamma_{sp} = 1/\tau_{sp}$ where τ_{sp} is the spontaneous lifetime [19, 16]. In the present experiment, the probe and the pump field are resonant with the same transition. This is very similar to a recently reported experiment carried out on the neutral exciton [11]. However while for the neutral exciton a Mollow absorption spectrum with gain was observed, as expected for a strongly driven two level system [13, 12], in the present experiment there was no sign of gain in the spectrum. In order to lift the spin degeneracies, we repeated the experiment in a magnetic field of 1 T and found the same results as in zero magnetic field, namely absence of gain and the central peak. This point is not fully understood but we note that gain and the central peak are sensitive to pure dephasing processes which are larger for the charged exciton than for the neutral exciton because of the hyperfine interaction, the interaction of the electron spin with the nuclear spins.

5.4 Rabi splitting of a charged exciton

In Fig. 5.3(a) probe laser spectra are shown for different pump laser intensities. The resonance resembles a Lorentzian for zero pump power, but develops a splitting that increases with the square root of the pump laser intensity. In Fig. 5.3 (b) the measured splitting is plotted as a function of the square root of the pump power (black dots) and fitted by a linear dependency (black line). This experiment

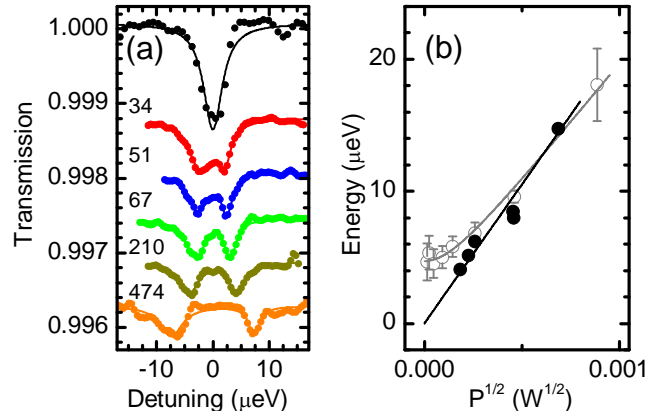


Figure 5.3: (a) The probe laser transmission spectra with pump laser on resonance, with increasing power (values in the figure in nW), as a function of the detuning between the probe and the pump laser photon energy. The spectra have been shifted vertically for clarity and are fitted by two Lorentzian resonances. (b) Splitting of the resonance measured with the probe laser as a function of the square root of the pump laser power (black) and the measured linewidth of the pump laser absorption spectrum (grey open circles). The splitting follows a linear behavior (black line), while the power broadening can be described by formula 5.2 (grey line)).

measures the Rabi energy which depends on γ_0 . To determine γ_{sp} and γ_{nr} separately, we glean additional information from saturation spectroscopy with a single laser where it is known that the measured linewidth increases with increasing laser power [20, 16, 19]. The linewidth follows the power-broadening relation:

$$\Gamma = 2\hbar\gamma_0\left(1 + \frac{P}{\hbar\omega\gamma_{\text{sp}}}\alpha_0\right)^{1/2}, \quad (5.2)$$

with the spontaneous recombination rate γ_{sp} . In this formula two limits can be distinguished. First, for vanishing laser power P the linewidth is power independent: $\Gamma = 2\hbar\gamma_0 + c$. The constant c represents the broadening of the spectra due to spectral fluctuations in the vicinity of the QD. [4, 7, 11]. Second, for large power the linewidth increases with the laser power according to: $\Gamma \simeq 2\hbar\gamma_0\sqrt{P\alpha_0/\hbar\omega\gamma_{\text{sp}}}$. Using the definitions given before for the Rabi frequency this simplifies to: $\Gamma \simeq \sqrt{2\gamma_0/\gamma_{\text{sp}}}\hbar\Omega$. In Fig. 5.3(b) the linewidth measured on the same trion transition in a one-laser experiment is plotted as a function of the square root of the laser power (grey open circles) and fitted by formula 5.2 (grey line). As expected the linewidth converges for low powers towards a constant value $\Gamma = 2\hbar\gamma_0 + c$. Here $\hbar\gamma_0 = 1.7 \mu\text{eV}$ and $c = 1.3 \mu\text{eV}$. For large powers the linewidths exhibit a slope that differs from that of the observed splitting in the pump-probe experiment which follows $2\hbar\Omega$ and we fit: $\hbar\gamma_{\text{sp}} = 1.25 \mu\text{eV}$. This corresponds to a lifetime $\tau_{\text{sp}} = 0.52 \text{ ns}$. This value agrees very well with that obtained by time resolved photoluminescence [21] on similar structures. We get furthermore the contribution of non radiative decay to the linewidth: $\hbar\gamma_{\text{nr}} = 0.45 \mu\text{eV}$. The mechanism responsible for this dephasing process is likely the hyperfine interaction. We note that in the present evaluation, the power loss in the detection arms does not introduce a systematic error since in both experiments, the single laser and pump-probe experiments were performed in the same setup.

5.5 Conclusion

In summary, we present a direct way to measure the Rabi splitting of a trion transition in a single QD and its dispersion when subject to a strong driving field. The data agree very well with a simple anti-crossing model based on a 2-level atom. By combining results from single laser and pump-probe experiments, we are able to infer the contributions of recombination, pure dephasing and spectral fluctuations to the low power linewidth.

References

- [1] H. Drexler, D. Leonard, W. Hansen, J. P. Kotthaus and P. M. Petroff. *Phys. Rev. Lett.*, **73**, 2252 (1994).
- [2] R. J. Warburton, C. Schäflein, K. Karrai, J. M. Garcia, W. Schoenfeld and P. M. Petroff. *Nature*, **405**, 926 (2000).
- [3] J. J. Finley, P. W. Fry, A. D. Ashmore, A. Lemaitre, A. I. Tartakovskii, R. Oulton, D. J. Mowbray, M. S. Skolnick, M. Hopkinson, P. D. Buckle, P. A. Maksym. *Phys. Rev. B*, **63**, 161305R (2001).
- [4] A. Högele, S. Seidl, M. Kroner, K. Karrai, R. J. Warburton, B. D. Gerardot and P. M. Petroff. *Phys. Rev. Lett.*, **93**, 217401 (2004).
- [5] S. Seidl, M. Kroner, P. A. Dalgarno, A. Högele, J. M. Smith, M. Ediger, B. D. Gerardot, J. M. Garcia, P. M. Petroff, K. Karrai, and R. J. Warburton. *Phys. Rev. B*, **72**, 195339 (2005).
- [6] B. Alén, F. Bickel, K. Karrai, R. J. Warburton, and P. M. Petroff. *Appl. Phys. Lett*, **83**, 2235 (2003).
- [7] M. Atatüre, A. Badolato, A. Högele, J. Dreiser, K. Karrai and A. Imamoglu. *Science*, **312**, 551 (2006).
- [8] X. Xu, Y. Wu, B. Sun, Q. Huang, J. Cheng, D. G. Steel, A. S. Bracker, D. Gammon, C. Emary, and L. J. Sham. *Phys. Rev. Lett.*, **99**, 097401 (2007).
- [9] E. Biolatti, R. C. Iotti, P. Zanardi, and F. Rossi. *Phys. Rev. Lett.*, **26**, 5647 (2000).
- [10] A. Zrenner, E. Beham, S. Stuffer, F. Findeis, M. Bichler and G. Abstreiter. *Nature*, **418**, 612 (2002).
- [11] X. Xu, B. Sun, P. R. Berman, D. G. Steel, A. S. Bracker, D. Gammon, L. J. Sham. *Science*, **371**, 929 (2007).
- [12] B. R. Mollow. *Phys. Rev. A*, **5**, 2217 (1972).
- [13] F. Y. Wu, S. Ezekiel, M. Ducloy and B. R. Mollow. *Phys. Rev. Lett*, **38**, 1077 (1977).

- [14] G. Jundt, L. Robledo, A. Högele, S. Fält, and A. Imamoglu, arXiv:0711.4205 (2007).
- [15] B. D. Gerardot, D. Brunner, P. A. Dalgarno, P. Öhberg, S. Seidl, M. Kroner, K. Karrai, N. Stoltz, P. M. Petroff, and R. J. Warburton, *Nature*, **451**, 441 (2008).
- [16] M. Kroner, S. Rémi, A. Högele, S. Seidl, A. W. Holleitner, R. J. Warburton, B. D. Gerardot, P. M. Petroff and K. Karrai, *Physica E* (2007), doi:10.1016/j.physe.2007.09.1
- [17] I. A. Merkulov, Al. L. Efros and M. Rosen, *Phys Rev B*, **65**, 205309 (2002).
- [18] C. Cohen-Tanoudij, B. Diu, F. Laloë. *Quantum Mechanics Wiley-Interscience*, Paris (1977).
- [19] K. Karrai, R. J. Warburton. *Superl. and Microstr.*, **33**, 311 (2003).
- [20] S. Stuffer, P. Ester, A. Zrenner and M. Bichler. *Appl. Phys. Lett.*, **85**, 4202 (2004).
- [21] J. M. Smith, P. A. Dalgarno, R. J. Warburton, A. O. Govorov, K. Karrai, B. D. Gerardot, and P. M. Petroff. *Phys. Rev. Lett.*, **94**, 197402 (2005).

Chapter 6

Voltage-Controlled Linewidth of Excitonic Transitions in a Single Self-Assembled Quantum Dot

We report electron and hole tunnelling phenomena in a single self-assembled quantum dot as a function of the applied electric field. We use absorption spectroscopy which allows us to measure excitonic transitions under conditions where optical recombination can not be observed due to the high, ionizing, electric field.

6.1 Introduction

Based on their promising applicability in quantum computation [1]-[3] and quantum communication [4]-[6]), self-assembled semiconductor quantum dots (QDs) have been the focus of research for several years. Their atomic-like discrete energy states combined with their incorporation in a semiconductor heterostructure allows the study of the optical properties of single quantum dots, tuned by magnetic and electric fields, in a very controlled way [7]-[10]. Recently, tunnelling dynamics of electrons controlled by an electric field have been demonstrated [11]. In this paper we report not only electron tunnelling to the continuum of the back contact but also resonant hole tunnelling phenomena to a two-dimensional hole system. We show that the tunnelling mechanisms are strongly dependent on the applied electric field. Hence the lifetime limited linewidth can be controlled directly by a gate voltage.

In the experiment we present here, we investigated the excitonic transitions in self-assembled InAs/InGaAs quantum dots that are embedded in a field effect structure [12]. In Fig. 6.1 the band structure of the sample is shown schematically. The quantum dots were grown with molecular beam epitaxy. They are separated by a 25 nm thick GaAs tunnel barrier from the back contact (highly n-doped GaAs). The QDs are overgrown with 30 nm of GaAs. In order to prevent charge transfer from the semitransparent metallic top gate (5 nm of NiCr), a 120 nm thick blocking barrier consisting of a periodic AlAs/GaAs superlattice was deposited above the QDs. With this geometry, the electric field the QDs experience can be tuned in a controlled way, simply by applying a dc voltage between the back contact and the top gate. Furthermore the QDs can be charged with single electrons by shifting their electronic levels beneath the Fermi energy [7], [9].

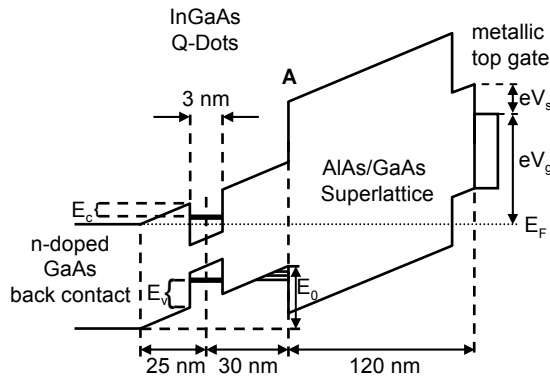


Figure 6.1: Scheme of the energy band structure of the sample along the growth direction. The voltage V_g allows to control the electric field at the position of the QD. E_F is the Fermi energy, E_c and E_v are the conduction and valence ionization energies respectively. A labels the interface between the capping layer of GaAs above the dots and the AlAs/GaAs superlattice. E_0 is the energetic point of origin of the triangular potential well created at this interface.

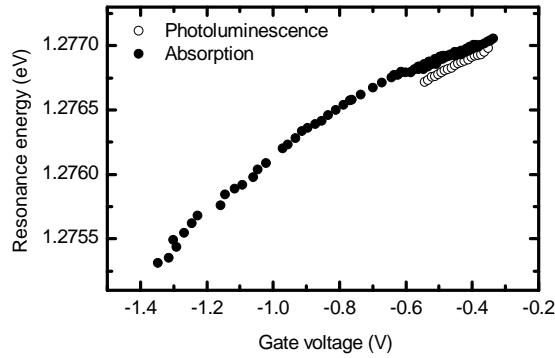


Figure 6.2: Resonance energies of the neutral exciton (X^0) as a function of the applied gate voltage. The absorption data are represented by the black dots, the PL by the open circles. The small discrepancy in energy between the absorption and emission data is due to instrumental reasons.

In this letter we concentrate on the neutral exciton only. The measurements were carried out with Stark-shift modulation absorption spectroscopy [13], [14]. This allows us not only to measure homogeneous linewidths of the excitonic transitions but also to measure at gate voltages where the QD is in the ionization regime. This is the regime where the tunnelling barrier to the back contact (which is voltage dependant) has become so small that the tunnelling rate of the electron in the QD is higher than the recombination rate. If the electron tunnels out of the QD before it can recombine with the hole under emission of photoluminescence (PL), the PL is quenched [17], [18], [19]. However in absorption spectroscopy an exciton is created under absorption of a photon. This can still happen, even if the electron (and the hole) tunnel out of the QD before they can recombine optically. The shorter lifetime of the exciton in the QD will in this case lead to a broader linewidth than in the gate voltage region where PL is observable and the linewidth should represent the lifetime limited by spontaneous emission. The experiment was performed with a confocal microscope at cryogenic temperatures.

The energy dispersion of a neutral exciton (X^0) is shown in Fig. 6.2. Here the black dots represent the resonance energies of the neutral QD, measured in absorption. The fine structure of the neutral exciton is of the order of $20 \mu\text{eV}$ and cannot be resolved in this graph [14]. The open dots represent the PL data of the very same dot. The voltage extent of the X^0 PL shifts to more negative voltages with increasing excitation power [15]. In Fig. 6.2, we plot the PL positions extrapolated to very low powers. The origin of this behavior is hole storage at the interface to the blockingbarrier (A in Fig. 6.1). The holes, a space charge, screen the applied electric field [15] [16].

It can be clearly seen that, as expected, the excitonic transition can be observed to far more negative gate voltages in absorption, than in PL. Two absorption spectra are shown in Fig. 6.3. At gate voltages where PL can be observed we measure very narrow linewidths as small as $1.2 \mu\text{eV}$ (Fig. 6.3 a)). The reason why the measured

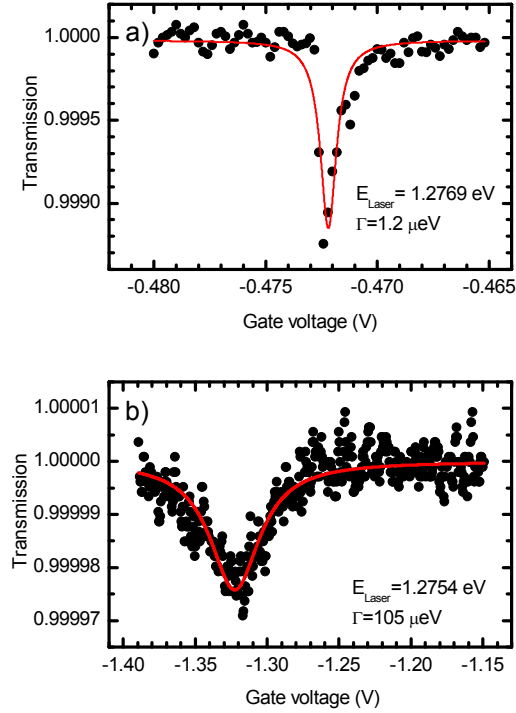


Figure 6.3: Two absorption spectra measured at two different gate voltages. The linewidth can be calculated via the Stark shown in Fig. 6.2.

linewidths are always larger than the expected values is due to fluctuations of the resonance energy of the excitonic transitions of the order of the linewidth [14]. At large negative gate voltages, at which no PL can be observed, the linewidths are up to two orders of magnitude larger (Fig. 6.3 b)).

6.2 Electron tunnelling

In Fig. 6.4 a) the measured linewidth is shown as a function of gate voltage. We observe an exponential increase of the linewidth with decreasing gate voltage. Further oscillations of the linewidth are noticeable this will be discussed later. In the regime (ionization regime) where no PL is observed ($V_g < -0.54$ V) we conclude that the lifetime of the excitonic state is limited by the tunnelling time of the electron. For gate voltages $V_g > -0.54$ V, the lifetime is rather limited by the spontaneous emission of a photon (We neglect phonon assisted dephasing, as the experiment was performed under cryogenic temperatures $T = 4.2$ K, as well as power broadening due to the low excitation powers of ≈ 1 W/cm² [14]) [11]. Considering a triangular tunnelling barrier between the quantum dot and the back contact as shown in Fig. 6.1 we can model the tunnelling time and hence the linewidth with a WKB-

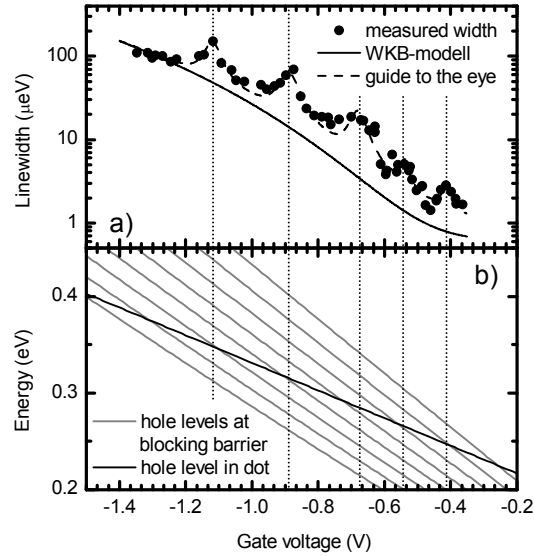


Figure 6.4: Figure a) shows the linewidth as a function of gate voltage. The solid line corresponds to the electron tunnelling that has been modelled with a WKB approximation. Figure b) represents the hole energy levels E_h in the QD (black) and E_n in the triangular potential well formed at the interface A (Fig. 6.1) (gray). The energies are defined relatively to the valence band edge at the back contact.

approximation:

$$\Gamma_{\text{WKB}} = \frac{\hbar^2 \pi}{2m^* L^2} \exp\left(\frac{4}{3\hbar} d(V_g) \sqrt{2m^* E_c}\right). \quad (6.1)$$

Here L is the height of the dot in z -direction (3 nm), E_c is the conduction band offset (Fig. 6.1) and $m^* = 0.07 m_e$ is the effective mass of an electron in GaAs [10]. Also we use the gate voltage dependant tunnelling distance:

$$d(V_g) = \frac{E_c}{e(V_g - V_s)} d \quad (6.2)$$

with the built in voltage $V_s = 0.62\text{V}$ [21]. Fitting formula 6.1 with an offset $\Gamma_0 = 0.62 \mu\text{eV}$ that corresponds to the lifetime limited linewidth we get a value for the conduction band offset of $E_c = 134 \text{ meV}$. This corresponds very well with the value received from analyzing the charging behavior of the dot [20].

6.3 Hole tunnelling

The oscillations of the linewidth as a function of the gate voltage represent a resonant hole tunnelling effect. The AlAs/GaAs superlattice forms a triangular potential well at the interface to the GaAs capping layer (A in Fig. 6.1). This leads to quantized two-dimensional states in the valence band as schematically indicated in Fig. 6.1.

The steepness of the triangular potential well and therefore the energies of the quantized states are dependent on the gate voltage. In Fig. 6.4 b) the energies of the quantized states in the triangular well and the hole state in the QD are plotted as a function of gate voltage. Comparing the gate voltages of the maxima of the linewidth and the crossing points of the two energy levels (the dashed lines are a guide to the eye) reveals a striking agreement. To calculate the energies in the triangular quantum well we used the result [22]:

$$E_n = E_0(V_g) - c_n \left(\frac{(eF(V_g)\hbar)^2}{2m^*} \right)^{\frac{1}{3}}, \quad (6.3)$$

with $m^* = 0.5 m_e$ the effective mass of the heavy hole in GaAs, $c_n \approx \left(\frac{3}{2}\pi\left(n - \frac{1}{4}\right)\right)^{\frac{2}{3}}$ and the electric field $F(V_g) = \frac{V_g + V_s}{175 \text{ nm}}$. The parameter $E_0(V_g) = e \frac{V_g + V_s}{\eta'}$ (with the lever arm $\eta' = \frac{175}{55}$) describes the point of origin of the potential well as shown in Fig. 6.1. The hole level in the dot is described by:

$$E_h = e \frac{V_g + V_s}{\eta} + E_v - E_b \quad (6.4)$$

here the lever arm is $\eta = \frac{175}{25}$ and the valence band offset $E_v = E_c \left(\frac{1}{Q} - 1\right) = 97 \text{ meV}$ with $E_c = 134 \text{ meV}$ from before and $Q = 0.58$ from [23]. The shift of the hole level in the QD by the binding energy of the exciton ($E_b = 6.2 \text{ meV}$) can be calculated in an analog way and is determined to be $E_b = 2.7 \text{ meV}$ [20]. The hole tunnelling is fast whenever a 2D valence continuum state with in-plane wave vector less than $k_{\parallel}^{\text{max}} \simeq 1/r_{\parallel}$ is available where r_{\parallel} is the in-plane extent of the quantum dot wave function. However, when the only available continuum state has $k > k_{\parallel}^{\text{max}}$, tunnelling is suppressed. In these experiments, $r_{\parallel} \approx 5 \text{ nm}$, implying $k_{\parallel}^{\text{max}} \approx 2 \times 10^8 \text{ m}^{-1}$, yet the energetic separation between the $k_{\parallel} = 0$ 2D hole states is about 20 meV, such that a hole wave vector of up to $5 \times 10^8 \text{ m}^{-1}$ is required away from resonance with a $k_{\parallel} = 0$ state. This consideration explains the strongly oscillatory nature of the hole tunnelling in Fig. 6.4. We note that electron tunnelling is not suppressed by the same argument as there is no strong quantization in the z-direction in the back contact.

Another argument why hole tunnelling is expected in our sample structure, is that in the ionization regime we still observe absorption. If only the electron tunneled and the hole remained in the dot, further absorption would be blocked. Our measurements show that this is not the case. The exponential increase in the linewidth is a compelling argument for both electron tunnelling and hole tunnelling.

6.4 Conclusion

In summary, we have shown an electric field dependency of the linewidth of transitions to the excitonic ground state of single self-assembled quantum dots. The

linewidth can be tuned over two orders of magnitude, from linewidths limited by spontaneous emission to linewidths limited by the tunnelling times of the electron or the hole stored in the quantum dot. We modelled the electron tunnelling with a straightforward WKB approximation. Oscillations of the linewidth are deduced to be caused by resonant hole tunnelling to discrete states in a triangular potential well that is formed in our sample by an AlAs/GaAs superlattice.

References

- [1] P. Chen, C Piermarocchi und L. J. Sham, Phys. Rev. Lett. **87**, 067401 (2001).
- [2] A. Imamoglu *et al.*, Phys. Rev. Lett. **83**, 4240 (1999).
- [3] E. Biolatti, R. C. Iotti, P. Zanardi und F. Rossi, Phys. Rev. Lett. **85**, 5647 (2000).
- [4] P. Michler *et al.*, Science **290**, 2282 (2000).
- [5] A. Barenco, D. Deutsch, A. Ekert, R. Jozsa, Phys. Rev. Lett. **74**, 4083 (1995).
- [6] F. Troiani, U. Hohenester, and E. Molinari, Phys. Rev. B **62**, R2263 (2000).
- [7] J. J. Finley *et al.*, Phys. Rev. B **63**, 073307 (2001).
- [8] F. Findeis *et al.*, Phys. Rev B **63**, 121309 (2001).
- [9] R. J. Warburton *et al.*, Nature **405**, 926 (2000).
- [10] K. Karrai *et al.*, Nature **427**, 135 (2004).
- [11] J. M. Smith *et al.*, Phys. Rev. Lett. **94**, 197402 (2005).
- [12] J. M. García *et al.*, Appl. Phys. Lett. **71**, 2014 (1997).
- [13] B. Alen, F. Bickel, K. Karrai, R. J. Warburton, P. M. Petroff, Appl. Phys. Lett. **83**, 2235 (2003).
- [14] A. Högele *et al.*, Phys Rev. Lett. **93**, 217401 (2004).
- [15] Urbaszek *et al.*, Physica E **17**, 35 (2003).
- [16] J. M. Smith *et al.*, Appl. Phys. Lett. **82**, 3761 (2003).
- [17] D. Haft *et al.*, Appl. Phys. Lett. **78**, 2946 (2001).
- [18] F. Findeis, M. Baier, E. Beham, A. Zrenner und G. Abstreiter, Appl. Phys. Lett. **78**, 2958 (2001).
- [19] R. Oulton *et al.*, Phys. Rev. B **66**, 045313 (2002).
- [20] S. Seidl *et al.*, Phys. Rev. B **72**, 195339 (2005).

- [21] R. J. Warburton *et al.*, Phys. Rev. B **58**, 16221 (1998).
- [22] John H. Davis, The Physics of Low-Dimensional Semiconductors, Cambridge University Press (1998).
- [23] J. Brübach, A. Yu. Silov, J. E. M. Haverkort, W. v. d. Vleuten, and J. H. Wolter, Phys. Rev. B **59**, 10315 (1999).

Chapter 7

The nonlinear Fano effect

A QD dot is tunnel coupled to a two-dimensional continuum of states. The coupling between the excitonic transition and the continuum transition leads to a quantum mechanical interference between the two optical transitions. This leads to the observation of Fano-resonances in the absorption spectrum of the exciton. The remarkable feature of these Fano-resonances, the power dependence of their asymmetry is described by a full theoretical treatment of the coupled system of a QD and a continuum of states.

7.1 Introduction

The Fano effect [1] is ubiquitous in spectroscopy, arising for instance in atoms [1, 2], bulk solids [3, 4] and semiconductor heterostructures [5, 6]. It arises when a quantum interference takes place between two competing optical pathways, one connecting the ground state and an excited discrete state, the other connecting the ground state with a continuum. The nature of the interference changes rapidly as a function of energy giving rise to characteristically asymmetric lineshapes. The Fano effect has been widely studied since its original formulation over 40 years ago. It is particularly important in the physics of semiconductors where the Fano resonance concept is widespread in the interpretation of transport [5] and optical spectra [6, 7]. However, Fano’s original theory [1] applies in the linear regime at low power. At high power in the nonlinear regime, a laser field strongly admixes the states and the physics becomes rich including a remarkable interplay of coherent nonlinear transitions, so-called “confluence of coherences” [8]. Nevertheless, despite the general importance of Fano physics, the nonlinear regime has received very little attention experimentally, presumably because the classic autoionization processes [2], the original test-bed of Fano’s ideas [1], occur in an inconvenient spectral region, the deep ultraviolet. We have accessed the nonlinear Fano regime by using semiconductor quantum dots which allow both the continuum states to be engineered and the energies to be rescaled to the near infrared. We measure the absorption cross-section of a single quantum dot and discover clear Fano resonances which we can tune with the device design or even in situ with a bias. In the nonlinear regime, the visibility of the Fano quantum interferences increases dramatically, affording an exquisitely sensitive probe of continuum coupling. A two-level system, or a qubit, is the central element of quantum information schemes and, ideally, should be decoupled from all other states. Our discovery represents a unique method to detect weak couplings of a two-level system to extended states using nonlinear quantum optics.

7.2 Coupling of a QD to a 2-dim continuum of states

We performed our experiments on self-assembled quantum dots. They are known to possess localized discrete energy levels, much like atoms, identified by extremely sharp lines in their optical spectra [9]. Furthermore, when the fundamental cross-gap transition is driven by a strong laser field, the electronic and photon states hybridize. Unmistakable signatures for such dressed states are Rabi oscillations [10, 11], an ac Stark effect [9, 12], and a splitting in a resonant high-Q cavity [13, 14, 15, 16]. We operate with InGaAs quantum dots embedded in a GaAs vertical field-effect device [17]. The structure allows us to control the charge stored on an individual quantum dot [17] and to modulate the transition energies by applying a bias voltage, enabling high noise rejection in single dot laser spectroscopy based on modulation

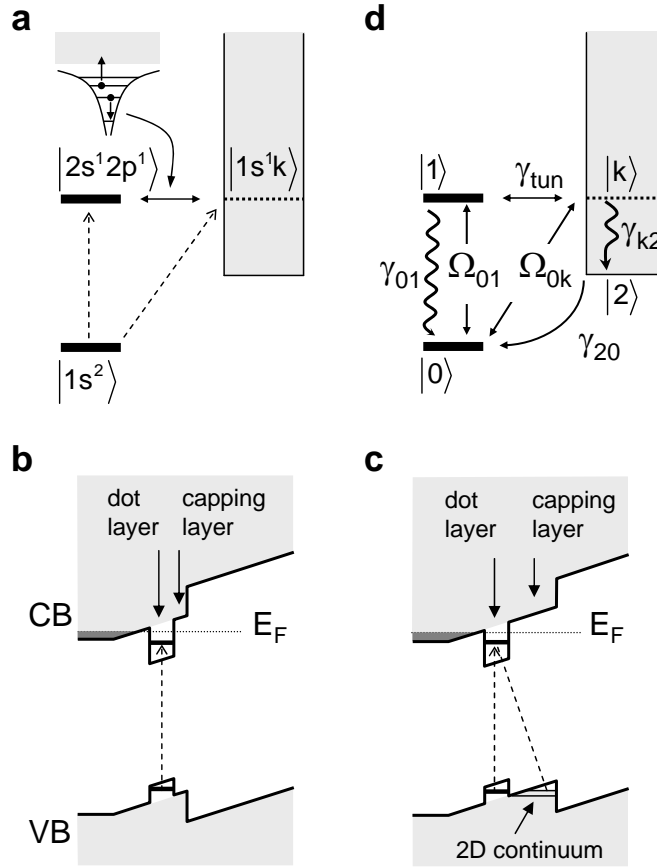


Figure 7.1: Schematic level diagrams. (a) Classical model of autoionization of a He atom leading to a Fano resonance in absorption. (b) Level diagram of sample #1 showing the cross-gap exciton transition. (c) Level diagram of sample #2. In this case, the increased capping layer thickness leads to the appearance of 2D continuum states at the interface between the capping layer and the blocking barrier. These valence continuum states couple via tunnelling with the valence dot level. (d) Levels, transitions and relaxation processes in the model calculations.

techniques [9]. We present here results on the X^{1-} exciton transition, the transition from a ground state containing a single electron to an excited state containing two electrons and a hole. Sample #1 contains a layer of InGaAs dots separated by a 25 nm tunnel barrier from a GaAs electron reservoir and by a 10 nm capping layer from an AlAs/GaAs superlattice blocking barrier, Fig. 7.1(b). Laser spectroscopy on dots from this sample show Lorentzian lineshapes, Fig. 7.2 (a) and (b). At low powers, the spectra are independent of power corresponding to behaviour in the linear regime. At powers above about ~ 1 nW, the spectra depend on power, the nonlinear regime. As the power increases, the resonance broadens and the contrast decreases, i.e. the resonance saturates, exhibiting power broadening and power-induced transparency [18, 19]. The behaviour follows exactly that expected for dressed states in a 2-level atom. In sample #2, the thickness of the capping layer is increased from 10 nm

to 30 nm but otherwise the sample was identical to the control sample #1, Fig. 7.1 (c). In this case, we find that the behaviour at medium and high powers is markedly different: the differential absorption has undershoots and zero crossings, Fig. 7.2(c-h), signatures of Fano-like quantum interferences.

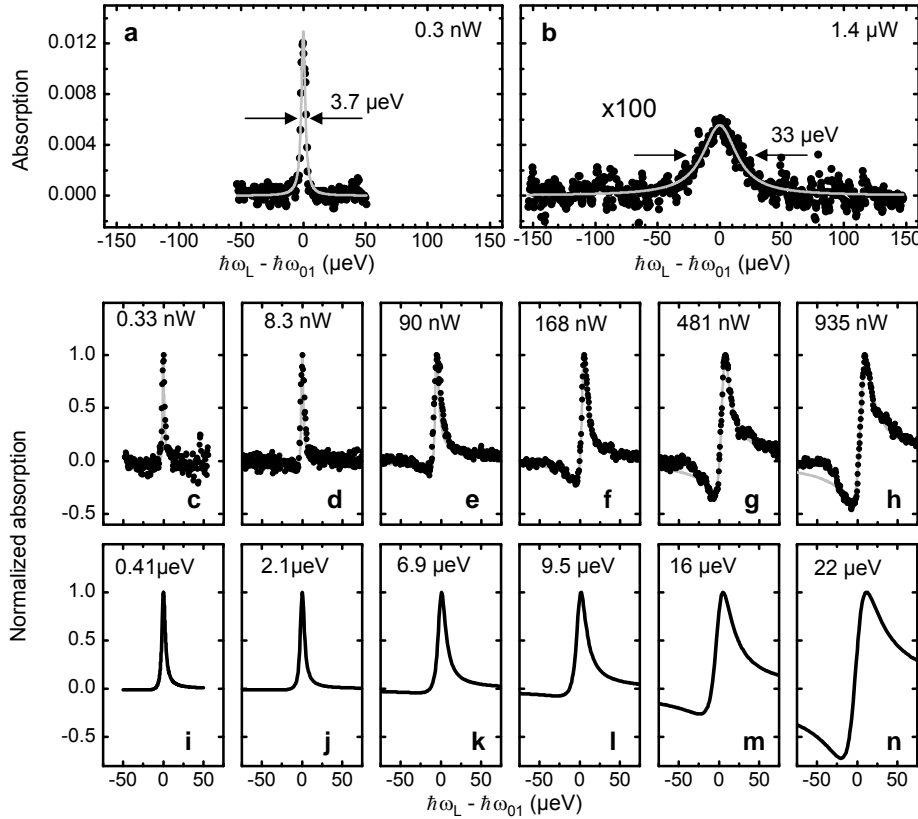


Figure 7.2: Laser spectroscopy on a single quantum dot. (a, b) Absorption of a single quantum dot from sample #1, exhibiting 2-level behaviour, plotted against detuning for two laser intensities, 0.3 nW in the linear regime (a), and 1.4 μW in the nonlinear regime (b). The solid lines are Lorentzian fits to the data. The observed nonlinear behaviour indicates that the dot has no significant coupling to extended electronic states of the crystal. (c-h) X^{1-} absorption spectra from a single dot from sample #2 for several different laser powers as indicated in the figure; the absorption spectrum is given by the change in transmission $\Delta T(\delta)/T$, where $\delta = \omega_L - \omega_{01}$ is the detuning and T is the transmission. Symbols represent the experiment, solid lines are a guide to the eye based on Fano's theory. (i-n) absorption spectra as calculated with the theory described in the text with parameters: $\hbar\gamma_{10} = 2.16 \mu\text{eV}$, $q = 12$, $\Delta = 0.4 \mu\text{eV}$ and $\hbar\gamma_{\text{rep}} = 30 \mu\text{eV}$. The Rabi energies ($\hbar\Omega_{01}$) indicated in the figures correspond to the laser powers of the experiment. The data were measured at 4.2 K with a wavelength ~ 950 nm on the X^{1-} resonance.

7.3 Power dependent Fano effect

Our key result is that the Fano effects become more and more pronounced as the laser power increases, starting out very small at low power in the linear regime but becoming unmistakable at high power in the nonlinear regime, Fig. 7.2. The increased visibility of the Fano interference at high laser power results from a different response of the two optical pathways. The optical transition between the discrete levels saturates at high power, in contrast the weaker continuum transition does not saturate in the range of power we are working in. Increasing the laser power eventually enhances the continuum transition rate to match the saturated discrete level transition. Consequently, the laser power is a convenient experimental control parameter to tune the relative strength of the two competing pathways at the heart of the Fano effect. This observation, which we back up with the theoretical consideration to follow, represents a highly sensitive technique to detect a very weak coupling between a two-level system and a continuum of extended states when the radiative life time of the exciton τ_{rad} is much less than the time required to interact with the continuum (e.g. tunnelling or decay time). In the linear regime, the optical detection of very weak dot-continuum interactions is impossible because the energy uncertainty for the exciton, $\hbar\Gamma$, obeys the Heisenberg principle $\Gamma\tau_{\text{rad}} \sim 1$. In other words, a strong broadening ($\Gamma \sim 1/\tau_{\text{rad}}$) makes the dot-continuum interaction invisible in the absorption spectrum. However, as shown in Fig. 7.3, in the nonlinear regime, the radiative broadening does not play the leading role and even a very weak dot-continuum interaction becomes apparent.

7.4 Voltage dependent tunnel coupling

To verify the asymmetries in Fig. 7.2(c-h) as Fano interferences, we present in Fig. 7.3(b) the voltage dependence, monitoring the strength of the interference with the asymmetry parameter $1/q$, where q is the Fano factor determined at constant power. In its standard definition, the Fano factor q is infinite when the continuum transition is very weak, in which case the line shape is symmetric and entirely determined by the discrete transition. In contrast, when q is near unity, both the continuum and discrete optical transitions are of similar strengths and the line shape becomes very asymmetric. The $1/q$ parameter has a strong bias dependence, disappearing towards the right hand edge of the X^{1-} plateau. The bias dependence cannot be explained with a purely optical interference [20, 21] as in this case the bias would have no effect. Instead, a Fano interference provides a natural explanation. Optical excitation drives the system from its discrete initial state, a quantum dot containing a single electron, $|0\rangle$, to the X^{1-} state containing two electrons and one hole, $|1\rangle$, Fig. 7.1(d). State $|1\rangle$ is in tunnel contact with the continuum: the combination of applied electric field and large capping thickness enables the hole to tunnel out of the dot into an empty continuum state [22], $|k\rangle$, Fig. 7.1(c). The final state of the

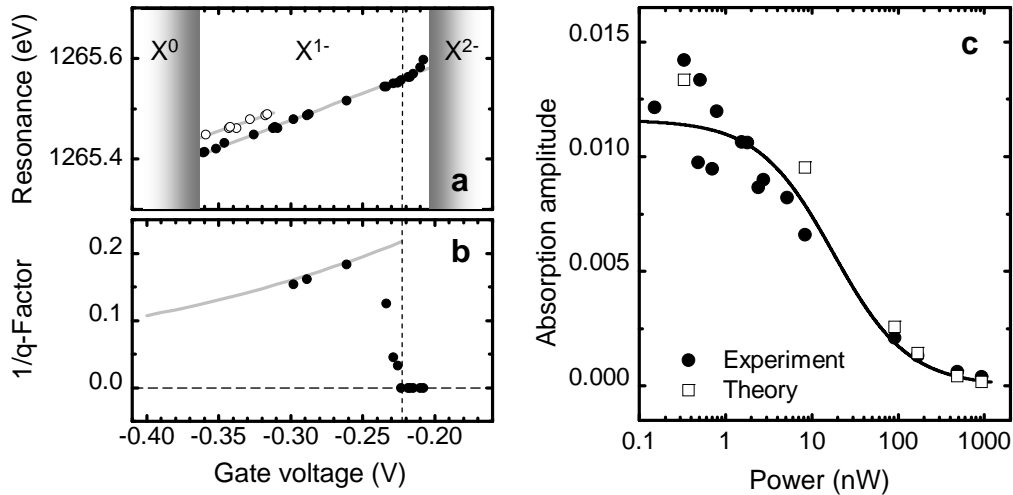


Figure 7.3: Voltage dependence of the Fano resonance. (a) Energy of the X^{1-} resonance ($\hbar\omega_{01}$) as a function of gate voltage. The X^{1-} is observed in the window of gate voltages between -0.36 V and -0.205 V as a result of Coulomb blockade. At the low energy side of the plateau a second resonance line appears, as depicted by the open circles. (b) $1/q$ versus gate voltage at a constant power of 200 nW. At gate voltages below -0.3 V the second peak hinders the fitting of the spectra. The vertical dashed line shows the onset of the asymmetry; the solid line reflects the theoretical voltage dependency of $1/q$ (see appendix A). (c) The measured absorption amplitude of the resonance as a function of laser power is plotted as well as the amplitudes predicted by the theory with the parameters in Fig. 7.2. The line represents a two-level model as guide to the eye.

transition is therefore hybridized with the continuum. Furthermore, a weak optical transition must also exist between $|0\rangle$ and $|k\rangle$. The two conditions for the Fano effect – two competing optical pathways and a hybridized excited state – are satisfied. The tunnelling involves a bound hole and the valence states at the capping layer-blocking barrier interface which have a two-dimensional (2D) character. The tunnelling rate is nonzero when the localized hole level is within the 2D continuum of holes states in the quantum well [22]. This is the explanation for the bias dependence in Fig. 4: at $V_g > -0.22$ V, the quantum dot state moves out of the 2D continuum, the hybridization with the continuum vanishes and $1/q \rightarrow 0$. The modeling of $1/q(V_g)$ confirms our picture of tunnelling (See Fig. 7.3 (b) and appendix A). We stress that virtually any dot in sample #2 shows a nearly symmetric line at low power with quite large $q \simeq 12$, and strongly asymmetric Fano lines at elevated powers.

7.5 Theory of a QD tunnel coupled to a continuum of states

We present a quantum mechanical model of these processes. Fano’s original theory [1] applies for a weak driving field where hybridization arises between basis states $|1\rangle$

and $|k\rangle$. The classic case is the doubly-excited state of the He atom. This state can auto-ionize, Fig. 7.1 (a). In the presence of a strong driving field, the mathematics is doubly difficult but nevertheless analytical results for atomic systems exist [23, 8]. However, the solid-state systems are very different and require a new theory. First, in our case, the quantum dot ground state $|0\rangle$ is repopulated through tunnelling from the reservoir. In the atomic case, the Fano resonance leads to photoionization – excited electrons are ejected at high speed and never return. The large time limits are therefore different: in the quantum dot case, the steady state corresponds to nonzero absorption; in the atomic case it does not, since the system becomes ionized and absorption vanishes. Secondly, energy relaxation processes are crucial in the quantum dot system but not in the atomic system. For instance, the autoionization rate of the $2s^1 2p^1$ He atom state $|1\rangle \rightarrow |k\rangle$ is much faster than spontaneous emission and $q \simeq 1$ whereas in our sample #2, the tunnelling rate, Δ/\hbar , is less than the spontaneous emission rate, $\Delta/\hbar \leq \gamma_{10}$, and $q \gg 1$. In this sense, quantum dot quantum optics can be very different to atom optics as the parameters and conditions can be widely different and controllably designed. We present a generalized theory for a closed system. The levels in our model are sketched in Fig. 7.1 (d): a ground state, $|0\rangle$, a single exciton state $|1\rangle$, and a set of continuum states, $|k\rangle$. Optical absorption processes are described by the matrix elements (Rabi frequencies) Ω_{01} and Ω_{0k} . States $|1\rangle$ and $|k\rangle$ are connected by a tunnel matrix element, γ_{tun} . Fast relaxation in the continuum states is described with a relaxation rate γ_{k2} from state $|k\rangle$ to a shelving state $|2\rangle$; repopulation from $|2\rangle$ to $|0\rangle$ by rate γ_{rep} . In practice, hole tunnelling leaves behind 2 electrons in the dot. The hole relaxes rapidly on a \sim ps timescale to the bottom of the 2D hole continuum; of the two electrons in the dot, one tunnels out to the back contact on a timescale of \sim 10 ps [24] and it is this tunnelling process that is described with rate γ_{rep} . The X^{1-} spectra are recorded in the voltage interval where the electron state is stable owing to the strong Coulomb blockade allowing us to neglect Kondo-like processes [25]. In order to include the various relaxation processes, we perform the calculation with a master equation for the density matrix. We obtain an analytic result for the optical absorbed power, $Q(\delta)$, under the realistic assumption of a small population of the continuum states; indeed, filling of the states in the continuum would require very large powers. The resulting equation is rather complex (eq. A.3, appendix A) but yields the correct limit in the linear regime, $\Omega_{01} \ll \gamma_{10}$:

$$Q(\delta) = \hbar^2 \Omega_{01}^2 \frac{\omega_L}{2q^2 \Delta} \left(1 + \frac{\gamma(q^2 - 1)(\Delta/\hbar)}{\gamma^2 + \delta^2} + \frac{2q\delta(\Delta/\hbar)}{\gamma^2 + \delta^2} \right). \quad (7.1)$$

where $\delta = \omega_L - \omega_{01}$, the detuning of the laser ($\hbar\omega_L$) from the resonance ($\hbar\omega_{01}$); $\Delta = \pi \hbar^2 \gamma_{\text{tun}}^2 \rho$, the tunnel broadening where ρ is the density of continuum states; $q = \hbar \gamma_{\text{tun}} \Omega_{01} / \Delta \Omega_{0k}$, the Fano factor; and $\gamma = \gamma_{10} + \Delta/\hbar$. We assume here that the effective width of the 2D continuum is much larger than Ω_{01} and Δ . This is similar to saying that γ_{tun} is a slow varying function of k and gate voltage (see appendix A). The final term in eq. 7.1 is negligible when $q \gg 1$ and $\Delta/\hbar < \gamma_{10}$ leading to

an almost symmetric lineshape. In other words, the tunnel coupling is masked by strong radiative damping. In the limit $\Omega_{01} \gg \Delta/\hbar, \gamma_{10}$, the line becomes symmetric but instead of a maximum it has a minimum at $\delta = 0$:

$$Q(\delta) = \hbar^2 \Omega_{01}^2 \frac{\omega_L}{2q^2 \Delta} \left(1 - \frac{(q^2 + 1)\Omega_{01}^2}{4q^2 \delta^2 + 2(q^2 + 1)\Omega_{01}^2} \right). \quad (7.2)$$

This behaviour corresponds to a “negative resonance” or strongly destructive interference in the limit of very large power. At realistic, finite Ω_{01} , the destructive interference shows up as a large undershoot to the resonance with a zero crossing, Fig. 7.2(h).

The experimental data in Fig. 7.3 are given for the absorption coefficient $\alpha = \Delta T/T = Q/P$, where T and P are the transmission and light power, respectively. In the linear regime, the maximum absorption coefficient depends on the laser spot area A as $\alpha_0 = 3(\lambda/n)^2/(2\pi A)$ that follows from $\Omega_{01}^2 = 2\alpha_0 \gamma_{01} P/(\hbar\omega_L)$ [19]. We compare the theory to the experimental data by taking the known values of γ_{10} , by determining q through a fit to the data at low power, and then adjusting Δ and γ_{rep} to account for the data at high power. We find very good agreement with the theory, Fig. 7.2(i-n). Here Δ is small resulting in a large q . This is consistent with the electron tunnelling rates we established in another context [24].

7.6 Conclusions

The significance of the negative signals in Fig. 7.2 is that even very weak coupling to the continuum becomes easy to detect by enhancing the interference at large laser power. At small power, the fundamental spontaneous emission process destroys the interference effect. In principle, the spontaneous emission could be suppressed exploiting the Purcell effect in a microcavity [15, 26]. However, this method is very challenging technologically and would require elaborate sample preparations. Our method is certainly more flexible. In the control sample #1, it now becomes striking that there are no hints of the Fano effect even at the highest power, demonstrating that in this case, the quantum dot behaves extremely closely to a few-level system. We should note that, with the nonlinear Fano effect, we are able to suppress the role of spontaneous emission dephasing in our quantum dots; however, other types of dephasing need to be analyzed specially and, in principle, they may wash out the Fano asymmetry. Fortunately, the exciton resonance in our dots is predominantly dephased by spontaneous emission [9].

Two overriding points emerge. The first is the tunability of the quantum dot system: Fano effects can be turned on and off. The second is that the nonlinear Fano effect can be employed for the detection of very weak interactions with continuum states in quantum systems. The nature of the interaction is not restricted: tunnelling, Auger processes and Foerster transfer are all included [27]. We would like to note that a very strong nonlinear Fano effect was also observed on p-doped samples, where

the continuum of states is most probably generated by impurity states due to the doping atoms. Interactions of very different nature may result in the nonlinear Fano resonance described here since the three-state scheme demonstrating the quantum interference effect (Fig. 7.1 (d)) is generic, appearing in a variety of physical systems including solids, atoms, molecules, and photonics.

References

- [1] Fano, U. Effects of configuration interactions on intensities and phase shifts. *Phys. Rev.*, **124**, 1866 – 1878 (1961).
- [2] Madden, R. P. & Codling, K. New autoionizing atomic energy levels in He, Ne, and Ar. *Phys. Rev. Lett.* **10**, 516 – 518 (1963).
- [3] Cerdeira, F., Fjeldly, T. A., & Cardona, M. Effect of free carriers on zone-center vibrational modes in heavily doped p-type Si. II. Optical modes. *Phys. Rev. B* **8**, 4734 – 4745 (1973).
- [4] Hase, M., Demsar, J., & Kitajima, M. Photoinduced Fano resonance of coherent phonons in zinc. *Phys. Rev. B*, **74**, 212301 (2006).
- [5] Faist, J., Capasso, F., Sirtori, C., West, K. W., & Pfeiffer, L. N. Controlling the sign of quantum interference by tunnelling from quantum wells. *Nature*, **390**, 589 – 592 (1997).
- [6] Bar-Ad, S., Kner, S., Marquezini, M. V., Mukamel, S. & Chemla, D. S. Quantum Confined Fano Interference. *Phys. Rev. Lett.* **78**, 1363 – 1366 (1997).
- [7] Wagner, J., & Cardona, M. Electronic Raman scattering in heavily doped p-type germanium, *Phys. Rev. B* **32**, 8071 – 8077 (1985).
- [8] Rzazewski, K. & Eberly, J. H. Confluence of bound-free coherences in laser-induced autoionization. *Phys. Rev. Lett.*, **47**, 408 – 412 (1981).
- [9] Högele, A. *et al.* Voltage-controlled optics of a quantum dot. *Phys. Rev. Lett.* **93**, 217401 (2004).
- [10] Zrenner, A. *et al.* Coherent properties of a two-level system based on a quantum dot photodiode *Nature*, **418**, 612 – 614 (2002).
- [11] Gammon, D. & Steel, D. G. Optical studies of single quantum dots. *Phys. Today* **55**, 36 (2002).
- [12] Stuffer, S., Ester, P., Zrenner, A., & Bichler, M. Quantum optical properties of a single $\text{In}_x\text{Ga}_{1-x}\text{As}$ -GaAs quantum dot two-level system. *Phys. Rev. B* **72**, 121301(R) (2005).

- [13] Reithmaier, J. P. *et al.* Strong coupling in a single quantum dot-semiconductor microcavity system. *Nature* **432**, 197 – 200 (2004).
- [14] Yoshie, T. *et al.* Vacuum Rabi splitting with a single quantum dot in a photonic crystal nanocavity. *Nature* **432**, 200 – 203 (2004).
- [15] Peter, E. *et al.* Exciton-photon strong-coupling regime for a single quantum dot embedded in a microcavity. *Phys. Rev. Lett.* **95**, 067401 (2005).
- [16] Hennessy, K. *et al.* Quantum nature of a strongly coupled single quantum dot-cavity system. *Nature* **445**, 896 – 899 (2007).
- [17] Warburton, R. J. *et al.* Optical emission from a charge-tunable quantum ring. *Nature* **405**, 926 – 929 (2000).
- [18] Loudon, R. *The quantum theory of light*. 3rd ed (Oxford University Press, 2000).
- [19] Kroner, M. *et al.* Resonant saturation laser spectroscopy of a single self-assembled quantum dot. *Physica E* (2007), doi:10.1016/j.physe.2007.09.1
- [20] Alen, B. *et al.*, Absorptive and dispersive optical responses of excitons in a single quantum dot. *Appl. Phys. Lett.* **89**, 123124 (2006).
- [21] Atature, M., *et al.* Observation of Faraday rotation from a single confined spin. *Nature Physics* **3**, 101 – 105 (2007).
- [22] Seidl, S. *et al.* Absorption and photoluminescence spectroscopy on a single self-assembled charge-tunable quantum dot. *Phys. Rev. B* **72**, 195339 (2005).
- [23] Rzazewski, K. & Eberly, J. H. Photoexcitation of an autoionizing resonance in the presence of off-diagonal relaxation. *Phys. Rev. A* **27**, 2026 – 2042 (1983).
- [24] Smith, J. M. *et al.* Voltage control of the spin dynamics of an exciton in a semiconductor quantum dot. *Phys. Rev. Lett.* **94**, 197402 (2005).
- [25] Govorov, A.O. Warburton, R. J. & Karrai, K. Kondo excitons in self-assembled quantum dots. *Phys. Rev. B* **67**, 241307(R) (2003).
- [26] Bayer, M. *et al.* Inhibition and enhancement of the spontaneous emission of quantum dots in structured microresonators. *Phys. Rev. Lett.* **86**, 3168 (2001).
- [27] Zhang, W., Govorov, A. O., & Bryant, G. W. Semiconductor-metal nanoparticle molecules: hybrid excitons and non-linear Fano effect. *Phys. Rev. Lett.* **97**, 146804 (2006).

Chapter 8

High-resolution, Resonant Two-color Spectroscopy on a Negatively Charged Exciton in a Magnetic Field

We have performed high resolution resonant two-color laser spectroscopy on single, self-assembled InGaAs quantum dots. The negatively charged exciton in a quantum dot can decay radiatively into both spin ground states - an electron in the quantum dot with its spin parallel or antiparallel to an applied magnetic field. The two decay paths can be used for optical spin alignment via optical pumping. We apply two laser fields, at two different colors resonant to the two Zeeman split optical transitions, to study the properties of the spin of the resident electron in the quantum dot, in Faraday and Voigt geometry. The resonant two-color signal is monitored as a function of the laser-power as well as the applied magnetic and electric field allowing us to determine spin decay and dephasing rates. We find the rate at which the optical spin alignment can be performed depends on the direction and the magnitude of the applied magnetic field. Finally we demonstrate the feasibility of performing coherent, all-optical spin manipulation of an electron spin in a quantum dot.

8.1 Introduction

The spin of an electron or a hole that is confined to a low-dimensional solid-state quantum system is a promising candidate for realizing a qubit - the fundamental building block of novel, quantum based, information processing devices [1, 2]. This is mainly due to long spin coherence and lifetimes that have been observed in self-assembled quantum dots (QD) [3, 4]. Single spin initialization by optical pumping is a powerful tool to study the spin relaxation and decoherence mechanisms in solid state quantum systems such as self-assembled InGaAs quantum dots [5, 6, 7, 8]. Optical spin pumping (OSP) makes electron spin measurements on single electrons at low magnetic field possible. In QDs the electron spin dynamics are dominated by hyperfine interaction [8]. For large magnetic fields the lifetime of an electron spin in a QD is limited by spin-orbit coupling [4]. Little is known so far about the nuclear spin dynamics in QDs [9, 10]. The inhomogeneous strain in the material strongly influences the Overhauser-field fluctuations and hence the electron spin dynamics [11]. In optically detected single electron spin resonance experiments that utilized OSP for spin initialization, this becomes apparent [12]. Here, we demonstrate a purely optical way to study the relaxation mechanisms of a single electron spin in a quantum dot. Furthermore, we point out a method to manipulate optically the electron spin in a coherent way. We present a scheme that eventually allows the application of coherent spin manipulation, known from atom optics, based on optically induced coherence between two ground states coupled to a common excited state.

8.2 Methods

8.2.1 The Sample

We study single InGaAs QDs that are embedded in a field effect device [13]. This allows us to charge the quantum dot in a controlled way with single electrons [14, 15, 16], simply by applying a gate voltage to the sample. As a back gate we have a two-dimensional electron gas (2DEG) (charge carrier density $n_e = 1.2 \times 10^{12} \text{ cm}^{-2}$ and mobility $\mu_e = 8.1 \times 10^3 \text{ cm}^2/\text{Vs}$), separated from the QD-layer by a 25 nm thick tunnel barrier of intrinsic GaAs. The QD-layer is buried 251 nm below the surface of the sample, on which a semitransparent metallic (5 nm NiCr) top gate is deposited, yielding a leverarm $\eta = 12$ [14, 16]. The electrostatic energy of the electronic QD state is then $E_{\text{el}} = e(V_g + V_g^0)/\eta$, with the applied gate voltage V_g and the build-in Schottky voltage $V_g^0 = 0.62 \text{ V}$. An AlAs-GaAs superlattice between the QD-layer and the sample surface prohibits leakage currents to the top gate. Choosing the applied bias V_g such that the electronic conduction state of the QD is shifted just below the Fermi energy, of the 2DEG, an electron is trapped in the QD via tunnelling from the back contact. For a second electron to tunnel into the QD, the Coulomb repulsion energy has to be overcome and hence there is a voltage

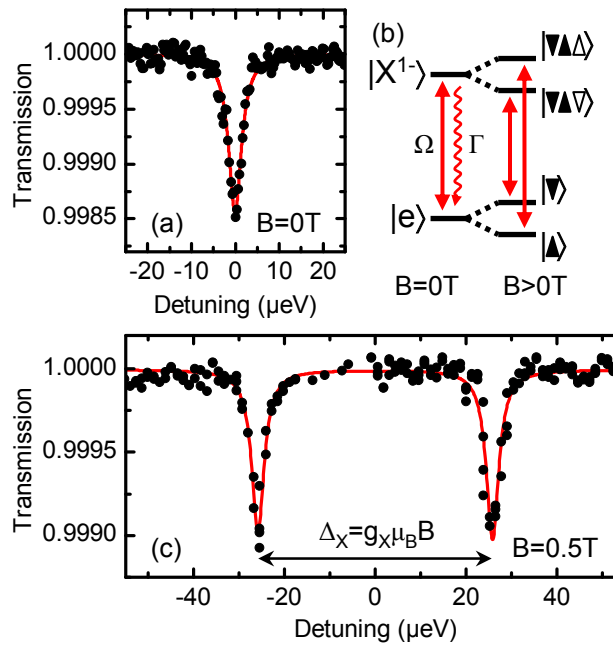


Figure 8.1: High resolution, resonant laser spectroscopy on a single QD in Faraday geometry. In (a) the unpolarized resonance line of a QD charged with one electron is shown against energy detuning. The change in transmission of a narrow band laser is measured, through the sample, while the exciton resonance is detuned from the laser photon energy by the DC-Stark shift. The transition is depicted in (b) on the right side, when no magnetic field is applied. The resonant laser drives the transition with a Rabi frequency Ω , while the exciton decays spontaneously with a rate Γ . On the right side of (b) the transitions of a negatively charged exciton are shown, with a magnetic field applied along the growth direction. The ground and excited states are split by the Zeeman energy. A transmission spectrum for a magnetic field of 0.5 T is shown in (c). The laser was linearly polarized to resolve both Zeeman-split resonances. The energy difference between the two resonances corresponds to the sum of the Zeeman splittings of the excited and ground states. As depicted in (b) the Zeeman splitting of the exciton is given by the hole, the Zeeman splitting of the ground state is given by the electron. The lines are Lorentzian fits to the data, yielding a linewidth at half maximum of $\approx 3.5 \mu\text{eV}$.

range extending over $\approx 0.25 \text{ V}$ in which the QD ground state is charged with a single electron [13, 14, 15, 16].

8.2.2 Resonant Laser Spectroscopy

The sample is mounted in a fiber-based confocal microscope which itself is located in a hermetically-sealed thin wall stainless steel tube filled with a small amount of He exchange gas ($\sim 30 \text{ mbar}$ at room temperature). To operate at 4.2 K, the whole setup is immersed in a liquid He bath cryostat, which is equipped with a superconducting coil to generate magnetic fields up to 9 T [17, 18, 19, 20]. The sample is positioned in the focus of the microscope objective ($NA = 0.55$) using low temperature positioners for all three axes. In this way, a single QD can be chosen

from the ensemble in situ, and kept reliably in the focus of the microscope for the duration of the experiment. Due to the diffraction-limited focal spot ($\sim 1.2 \mu\text{m}$), and the low QD density on the sample, it is possible to have only one single QD in the illuminated area. For illumination, a tunable narrow band laser is used (linewidth $< 3 \text{ MHz}$, $\lambda = 930 - 990 \text{ nm}$) and the transmitted light is detected by a Si photodetector, mounted directly behind the sample at 4.2 K. When the laser light is resonant with the excitonic transition, the QD acts as a scatterer, and we detect the resonant Rayleigh scattering in the forward direction as a change in the transmitted light [21, 22, 23]. For noise reduction, a modulation technique with lock-in detection is used. We exploit the quantum confined Stark effect to control the QD resonance energy via an applied bias [22]. The gate voltage is modulated with a square wave ($V_{\text{pp}} = 100 \text{ mV}$, $f = 77 \text{ Hz}$), while a dc voltage offset is swept to measure the differential transmission as a function of the detuning of the exciton resonance relative to the laser photon energy, which is kept constant. Alternatively, the gate voltage is kept constant, apart from the modulation, and the laser photon energy is swept. In Fig.8.1(a) a transmission spectrum is shown for a single, negatively charged QD. The corresponding optical transition is illustrated in Fig.8.1(b) with and without magnetic field. The laser drives the transition and at high enough laser fluence it leads to a power broadening of the resonance line. The spontaneous relaxation rate Γ corresponds to the lifetime limited linewidth [23, 24, 25].

On applying a magnetic field, the unpolarized resonance line of the negatively charged exciton splits into two resonances [26, 27]. The two resonances can be excited by left- and right-handed circularly polarized light [20], as shown on the right of Fig.8.1(b). The splitting is given by $\Delta_X = g_X \mu_B B$, with the excitonic g-factor $g_X = g_e + g_h$, the sum of the g-factor of an electron and a hole in the QD. In Fig.8.1(c) a spectrum of a negatively charged exciton in a magnetic field is shown for linearly polarized excitation. The Zeeman-split resonances are separated by $\Delta_X = 51.7 \mu\text{eV}$ corresponding to an excitonic g-factor $g_X = -1.8 \pm 0.01$.

8.3 Spin Dependent Laser Spectroscopy

8.3.1 Optical Spin Pumping

Optical spin pumping of a resident electron in a QD was pioneered by M. Atatüre *et al.* [5] and studied in detail by J. Dreiser *et al.* [8]. OSP was successfully used for single electron spin resonance experiments [12]. However, a description is given here to introduce the optical transitions and their rates. Here the tunnelling interaction between the QD and the back contact was reduced by reducing the density of states in the 2D back contact, in contrast to the earlier work [5, 8] where the tunnelling barrier from the QD to a n-doped 3D back contact was increased.

In an external magnetic field, the Zeeman split ground and excited states of the

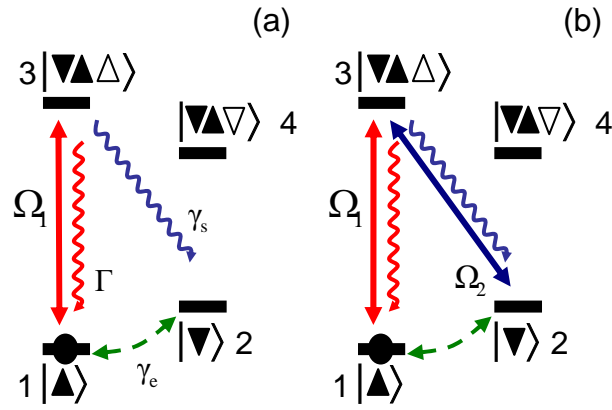


Figure 8.2: Level schemes of a negatively charged QD in a magnetic field. In (a) the transitions are shown that are responsible for the OSP. A laser pumping resonantly the transition $|1\rangle \leftrightarrow |3\rangle$ with a Rabi frequency Ω_1 creates an exciton. The exciton decays spontaneously into the ground state $|1\rangle$, $|2\rangle$ with a rate Γ , γ_s respectively, where transition rate $\gamma_s \ll \Gamma$ yielding the labelling of the transition $|2\rangle \leftrightarrow |3\rangle$ as “forbidden” transition. The spin flip rate γ_e leads to a relaxation of the spin polarization, towards equal population of the two states $|1\rangle$ and $|2\rangle$. In (b) the two-laser repump scheme is shown. An additional laser resonantly pumps the “forbidden” transition $|2\rangle \leftrightarrow |3\rangle$, with a Rabi frequency Ω_2 . This leads to a transfer of ground state population from $|2\rangle$ to $|1\rangle$ and hence frustrates the OSP.

X^{1-} exciton, as depicted in Fig.8.1(b), represent a 4-level system. In the Faraday geometry the magnetic field is applied along the sample growth axis. Optical selection rules allow the two circularly polarized transitions $|\blacktriangle\rangle \leftrightarrow |\blacktriangle\blacktriangledown, \Delta\rangle$ for σ^+ -polarization and $|\blacktriangledown\rangle \leftrightarrow |\blacktriangle\blacktriangledown, \nabla\rangle$ for σ^- -polarization. A relaxation of the selection rules also allows weakly the decay into the ground states, with opposite electron spin ($|\blacktriangle\blacktriangledown, \Delta\rangle \rightsquigarrow |\blacktriangledown\rangle$ and $|\blacktriangle\blacktriangledown, \nabla\rangle \rightsquigarrow |\blacktriangle\rangle$). By pumping resonantly one of the optically-allowed transitions (e.g $|\blacktriangle\rangle \leftrightarrow |\blacktriangle\blacktriangledown, \Delta\rangle$), with a Rabi frequency Ω_1 as depicted in Fig.8.2(a), the electron spin eventually becomes trapped in the $|\blacktriangledown\rangle$ state, by undergoing a “forbidden” transition at a rate γ_s [5]. The optical spin pumping fidelity is $\vartheta = (n_2 - n_1)/(n_2 + n_1)$, where $n_{1,2}$ is the population of the state $|\blacktriangle\rangle$, $|\blacktriangledown\rangle$ respectively. It is limited by the ratio of the “forbidden” transition rate γ_s at which the state $|\blacktriangledown\rangle$ is populated and the spin-flip rate γ_e that brings the system back into equilibrium $n_1 = n_2 = 0.5$, which is true for $g_e\mu_B B \ll k_B T$ [20]. We measure the change in transmission, due to absorption of the laser that is resonantly driving the transition $|\blacktriangle\rangle \leftrightarrow |\blacktriangle\blacktriangledown, \Delta\rangle$. In case of spin pumping, the Boltzmann-distributed population of the ground states is modified and the probability for the electron to be in the $|\blacktriangle\rangle$ -state is reduced: $n_1 < 0.5$. Since the transmission signal is a measure of the population of the ground state [20], the signal is also reduced [5, 6]. We get a simple expression for the spin pumping fidelity from rate equations:

$$\vartheta \approx \frac{1}{1 + 4\frac{\gamma_e}{\gamma_s}} \quad (8.1)$$

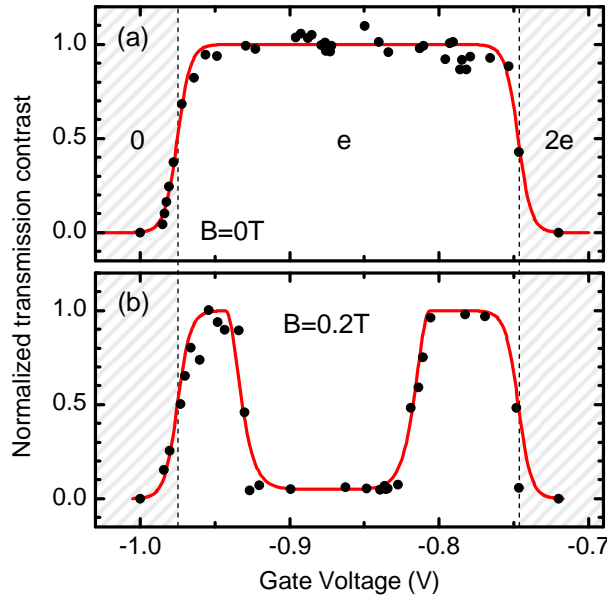


Figure 8.3: Measured transmission contrast versus gate voltage, over the charging plateau, where the QD contains one resident electron (e). The transmission is normalized to the maximum contrast on the plateau. (a) the X^{1-} -plateau with no magnetic field applied. At the edges towards the empty (0) and doubly negatively charged QD ($2e$), the transmission contrast decays following eq.8.4 (line), corresponding to a temperature $T = 4.2$ K. In (b) the transmission contrast is plotted in the same gate voltage range, with a magnetic field of 0.2 T applied. In the middle of the plateau the OSP leads to a drastic reduction of the transmission contrast. The line is a fit to the data of a product of eq.8.2 using eq.8.1 to describe ϑ and eq.8.5 to calculate the gate voltage dependent spin-flip rate γ_e ($\hbar\Gamma_{\text{tun}} = 0.05$ μeV).

which we use to estimate the transmission signal α as

$$\alpha \approx \alpha_0(1 - \vartheta), \quad (8.2)$$

where α_0 is the transmission signal for equal population of the two ground states, e.g. in case of $B = 0$.

In Fig.8.3(a) the normalized transmission contrast is plotted for the X^{1-} over the whole gate voltage range, where the single electron state is stable [16]. While over the plateau, between the two charging events, the transmission contrast is constant, at voltages below -0.975 V, where the ground state is the empty QD, and at voltages above -0.75 V, where a second electron tunnels into the dot, the transmission contrast drops to zero. The amplitude of the transmission signal over the plateau edge maps the probability of finding one electron (the ground state of the probed optical transition) in the QD. Following the analysis in [28], the probability to find a single electron in the QD is:

$$f(E) = \frac{1}{2 + e^{\frac{E}{k_B T}}} \quad (8.3)$$

with a temperature of $T = 4.2$ K, the Fermi energy is defined as $E_F \equiv 0$. The transmission contrast is then:

$$\alpha = \alpha_0 f(E_{\text{el}}(V_1)) [1 - f(E_{\text{el}}(V_2))]. \quad (8.4)$$

Here $E_{\text{el}}(V) = e(V_g - V)/\eta$ is the electrostatic energy of the electron in the QD, with the lever arm $\eta = 12$ [14, 16]. The result is plotted in Fig.8.3(a), the only fit parameters are the charging voltages for the first electron V_1 and the second electron V_2 . Repeating this experiment with an external magnetic field of $B = 0.2$ T yields the result shown in Fig.8.3(b). While at the edges of the plateau, the amplitude of the transmission contrast is similar to the zero-field situation, in the middle of the plateau, the signal is strongly suppressed. In the middle of the plateau, the spin of the resident electron is optically pumped into the $|\blacktriangledown\rangle$ -state [5, 6]. At the edges of the plateau, the electronic state of the first electron in the QD for the left edge, the state for the second electron in the QD for the right edge, are close to the Fermi energy and hence resonant to empty or occupied electronic states in the back contact. This allows cotunnelling events that consist of spin swapping between the QD and the back contact so that the spin information of the electron in the QD is lost [29, 5, 8]. To describe the gate voltage dependency of this effect, we use the expression for the cotunnelling rate γ_{cot} from the work of Smith *et al.* [29]:

$$\gamma_{\text{cot}} = \frac{\hbar\Gamma_{\text{tun}}^2}{2\pi} \int_{\epsilon} \left| \frac{1}{E_{\text{el}}(V_1) + \epsilon + \frac{i}{2}\hbar\Gamma_{\text{tun}}} + \frac{1}{-E_{\text{el}}(V_2) - \epsilon + \frac{i}{2}\hbar\Gamma_{\text{tun}}} \right|^2 f(\epsilon) [1 - f(\epsilon)] d\epsilon. \quad (8.5)$$

The solid line in the plot in Fig.8.3(b) is a guide to the eye, based on an evaluation of eqn.8.5 with the tunnelling energy $\hbar\Gamma_{\text{tun}} = 0.05 \mu\text{eV}$ which is very similar to the values obtained for similar structures [29, 8]. We assume it to be constant over the gate voltage range of constant charge. In general, for small magnetic fields, where the spin-phonon interaction is weak [8, 4], the spin relaxation rate is composed of the sum of the cotunnelling rate γ_e and the gate voltage independent hyperfine spin flip rate γ_{hf} :

$$\gamma_e = \gamma_{\text{cot}} + \gamma_{\text{hf}}. \quad (8.6)$$

Using this equation with a constant $\gamma_{\text{hf}} = 0.1$ MHz, and the gate voltage dependency of γ_{cot} as discussed above together with 8.2 and 8.3, we obtain the behavior of the transmission signal, in the middle of the plateau, as a function of the gate voltage, as shown by the line in Fig.8.3(b). Here $\gamma_s = 50$ MHz was obtained from fitting the curve to the data points. This transition rate for the weak transition is to be compared to $\Gamma = 1.2$ GHz which we obtain by power broadening analysis [25]. It has to be said that in principle only the ratio between the spin-flip rate and the “forbidden” transition rate can be gained by fitting eqn 8.2 to the data. To gain a more precise knowledge of the magnitude of the spontaneous decay rate of

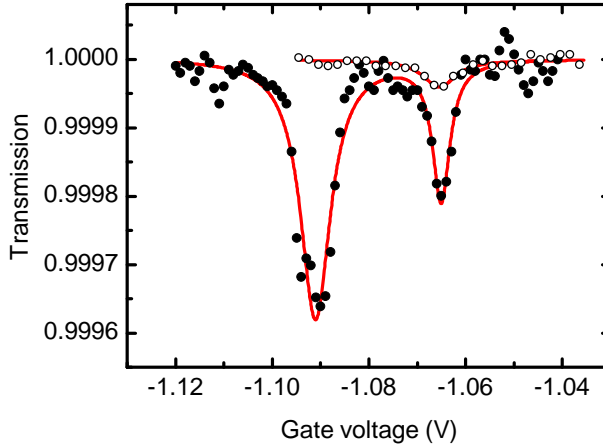


Figure 8.4: Transmission spectra in the OSP regime of the X^{1-} gate voltage range, close to the cotunnelling regime. The open circles are obtained from a one-laser transmission experiment at a magnetic field of 0.5 T with the laser being circularly polarized. The weak remaining signal at $V_G = -1.065$ V arises because cotunnelling suppresses OSP sufficiently. On the center of the charging plateau the signal is too weak to be resolved in the noise. According to the pump scheme in Fig. 8.2, a second, linearly polarized laser is focused on the sample. The photon energy of this second laser is chosen such that at a gate voltage of $V_G = -1.065$ V the laser photons are resonant with the “forbidden” transition. The experiment is repeated: the transmission is monitored as the gate voltage is scanned while the photon energy of the two lasers remains constant. At the gate voltage where in the one-laser experiment a faint resonance is observed, now an enhanced signal appears. At an ≈ 25 mV more negative gate voltage, a second resonance becomes visible, it originates from the second laser, whose energy matches the excitonic transition $|\blacktriangle\rangle \leftrightarrow |\blacktriangle\nabla, \Delta\rangle$ at this gate voltage. The resonance condition of the second laser with the excitonic transition falls into the cotunnelling regime, yielding a strong resonance. Because the experiment was performed on a different QD, the gate voltage differs from that in Fig. 8.3

the “forbidden” transition γ_s , as well as all the other transition rates involved in the system, we use a two-laser spectroscopy scheme, as discussed in the following section.

8.3.2 Optical Pumping of the “Forbidden” Transition

The weakly allowed “forbidden” transition depicted in Fig.8.2(a), obviously leads to a decay of the excited state $|\blacktriangle\nabla, \Delta\rangle$ to state $|\blacktriangledown\rangle$, on emission of a photon. The decay rate is too weak and its emission was not directly detectable in a photoluminescence experiment. However, using the transmission signal of the pump laser, a sensitive tool exists to measure the population of the state $|\blacktriangledown\rangle$. To measure the coupling strength of the “forbidden” decay path to the light field, we use a second laser, resonant with the “forbidden” transition, to “repump” the electron from the shelving state $|\blacktriangledown\rangle$ to the excited state $|\blacktriangle\nabla, \Delta\rangle$ of the pumping laser cycle. The pumping scheme is shown in Fig.8.2(b). Monitoring the transmission signal of the pump laser, we expect an increase of the signal when the repump laser is resonant with the “forbidden” transition [12]. In Fig.8.4 two gate voltage scans are shown. The

open circles represent the transmission signal measured for the pump laser only that drives for a gate voltage $V_g = -1.065$ V the transition $|\blacktriangle\rangle \leftrightarrow |\blacktriangle\nabla, \Delta\rangle$ with a Rabi frequency Ω_1 , is depicted in Fig.8.2(a). The experiment was performed at an external field of $B = 0.5$ T, a magnetic field at which, for a photon energy in the middle of the plateau, the transmission signal is strongly reduced due to OSP and it can not be resolved in the noise. For the spectrum in Fig. 8.4 the laser photon energy was chosen such that the resonance occurs close to the cotunnelling regime, and hence it can still be resolved above the noise level. The black dots in Fig.8.4 represent the signal measured with a second laser. The second laser is resonant with the “forbidden” transition $|\blacktriangledown\rangle \leftrightarrow |\blacktriangle\nabla, \Delta\rangle$ with a Rabi frequency Ω_2 . The resonance condition is fulfilled at a gate voltage $V_g = -1.065$ V. An increase of a factor 5 in the transmission signal of the pump laser resonantly driving the $|\blacktriangle\rangle \leftrightarrow |\blacktriangle\nabla, \Delta\rangle$ -transition is observed. The enhanced signal arises due to the “repump” of the electron into the pumping cycle of the first laser as shown in Fig.8.2(b). Experiments with only the second laser reveal that the direct absorption of photons by resonantly pumping the “forbidden” transition can not be resolved (Data not shown here)[12]. At more negative gate voltages ($V_g = -1.09$ V) a second resonance peak is observed in the spectrum measured with two lasers. This resonance is also observed for a gate voltage scan with only the second laser and it originates from a resonance condition of the laser with the $|\blacktriangle\rangle \leftrightarrow |\blacktriangle\nabla, \Delta\rangle$ -transition which is fulfilled for the given laser photon energy at this particular gate voltage. Since the resonance condition lies at a lower gate voltage, it takes place in the cotunnelling regime and hence spin pumping does not reduce the transmission amplitude. From the gate voltage difference and the linear Stark effect, as well as the photon energy differences of the two laser fields, the Zeeman splitting of the electronic ground state can be calculated to be $E_{Z,e} = g_e\mu_B B = 23.1$ μeV , which corresponds to an electronic g-factor $g_e = -0.70 \pm 0.01$ [12]. The sign of the g-factor has been obtained from earlier polarization sensitive absorption measurements on an X^{1-} in a magnetic field [20].

8.3.3 Polarization Dependence

First we investigate the polarization properties of the two-laser signal: The transmission contrast of the pump laser, which is circularly polarized σ^+ to match the optical selection rule for the transition $|1\rangle \leftrightarrow |3\rangle$, is measured for different polarizations of the repump laser, resonant to the $|2\rangle \leftrightarrow |3\rangle$ “forbidden” transition. The “forbidden” transition is expected to be mediated also by a σ^+ polarized laser field. Both cases that can lead to a finite oscillator strength of this transition, correspond to a change of +1 of the total angular momentum: electron spin state mixing by hyperfine interaction or heavy-hole light-hole mixing. However, we see that the repump signal is equally strong for linear (π) and both circular (σ^+ , and σ^-) polarizations in Fig. 8.5). The finding leads to the assumption that the “forbidden” transition is unpolarized. This is true at least at the magnetic field of 0.5 T, at which the

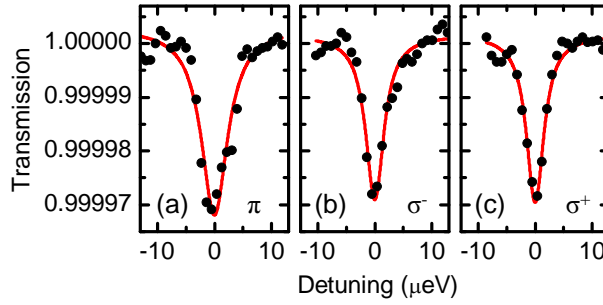


Figure 8.5: Two color, repump spectra of the $|1\rangle \leftrightarrow |3\rangle$ transition by pumping the $|2\rangle \leftrightarrow |3\rangle$ “forbidden” transition with differently polarized laser fields. In (a) the second laser was linearly polarized, according to the linear polarization basis defined by the neutral exciton fine structure splitting. In (b) and (c) the second laser field is left- and right-handed circularly polarized. The circular polarization basis was defined by one color spectroscopy on the X^{1-} in a magnetic field [21]. No effect relating to the polarization of the repump laser is seen. The laser pumping the $|1\rangle \leftrightarrow |3\rangle$ -transition was σ^+ polarized. The lines are Lorentzian fits to the data.

experiment was performed. A more detailed study of the polarization properties of the repump signal at different magnetic fields is necessary to gain deeper insight into the mechanisms leading to the breaking of the selection rules and hence to the finite oscillator strength of the “forbidden” transition.

In the following experiments the laser pumping the $|1\rangle \leftrightarrow |3\rangle$ -transition is σ^+ polarized, while the other laser is linearly polarized, to gain a consistent set of data.

8.4 Quantum Optics of the X^{1-} -state at a finite Magnetic field

The ability to perform resonant two-laser absorption experiments on the λ -system, formed by the X^{1-} in a magnetic field, allows us to obtain a comprehensive understanding of the involved rates and their physical origin. To do this, we first develop a quantum optical description of the 3-level system in Fig.8.2(b). Then we show results of the spin repump experiment as a function of gate-voltage, magnetic field and laser power, to gain access to the rates connecting the electronic and excitonic states of the X^{1-} .

8.4.1 Quantum Optical Model

To describe the experiments that are shown in section 8.5 and 8.6 a master equation is derived. This is done by using the density matrix formalism describing the three-level system of an X^{1-} in a magnetic field. In section 8.4.2 the derived theoretical model is linked to the resonant laser spectroscopy experiment.

The λ -system of the X^{1-} in a magnetic field is formed out of two ground states $|1\rangle \equiv |\blacktriangle\rangle$ and $|2\rangle \equiv |\blacktriangledown\rangle$ with the energies $E_1 = 0$ and $E_2 = \hbar\omega_{12}$ and the excited

state $|3\rangle \equiv |\blacktriangle\blacktriangledown, \Delta\rangle$ with energy $E_3 = \hbar\omega_{13}$. The energy $E_2 = |g_e|\mu_B B \approx 20 \mu\text{eV}$ is the Zeeman splitting of the electronic state in the QD directly obtained from the optically determined g_e , while the energy of the excited state E_3 is around $\approx 1.2 \text{ eV}$. The states $|1\rangle$ and $|3\rangle$ and $|2\rangle$ and $|3\rangle$ are coupled by two coherent laser fields with energies $\hbar\omega_1$ and $\hbar\omega_2$ respectively, as depicted in Fig. 8.2(b) by the straight arrows. The Hamilton operator of the system is

$$\hat{H} = \hat{H}_0 + \hat{H}_{\text{opt}} \quad (8.7)$$

with the Hamilton operator of the unperturbed system,

$$\hat{H}_0 = \hbar\omega_{12}|2\rangle\langle 2| + \hbar\omega_{13}|3\rangle\langle 3|. \quad (8.8)$$

We use a semi-classical ansatz in which the light fields are treated classically and the QD quantum mechanically. The light fields induce a dipole moment in the QD. We take the electromagnetic fields of the light waves as stationary, oscillating parallel to the excitonic dipole moment in the QD so that $\mathbf{F}(\mathbf{r}, t) = F_i \cos(\omega_i t) \mathbf{F}(\mathbf{r}) \rightarrow F = F_i \cos(\omega_i t)$, $i = 1, 2$ [30]. By defining the Rabi frequency as $\Omega_i = \frac{D_{i3}F_i}{\hbar}$, $i = 1, 2$ we write the Hamilton operator for the light fields as

$$\begin{aligned} \hat{H}_{\text{opt}} &= \frac{\hbar\Omega_1}{2} (e^{i\omega_1 t}|1\rangle\langle 3| + e^{-i\omega_1 t}|3\rangle\langle 1|) + \\ &\quad \frac{\hbar\Omega_2}{2} (e^{i\omega_2 t}|2\rangle\langle 3| + e^{-i\omega_2 t}|3\rangle\langle 2|). \end{aligned} \quad (8.9)$$

Fast oscillating terms are neglected, based on the rotating wave approximation, since the laser frequency is close to the resonance frequency of the dipole transition [32]. The Schrödinger equation $\hat{H}\psi = i\hbar\partial_t\psi$ for the wave function $|\psi\rangle = \sum_i c_i|i\rangle$ can be written in the basis of the QD states $|i\rangle$ $i = 1, \dots, 3$ as:

$$\hat{H} = \frac{1}{2}\hbar \begin{pmatrix} 0 & 0 & \Omega_1 e^{i\omega_1 t} \\ 0 & 2\omega_{12} & \Omega_2 e^{i\omega_2 t} \\ \Omega_1 e^{-i\omega_1 t} & \Omega_2 e^{-i\omega_2 t} & 2\omega_{13} \end{pmatrix}. \quad (8.10)$$

Both optical couplings ($|1\rangle \leftrightarrow |3\rangle$ and $|2\rangle \leftrightarrow |3\rangle$) are hereby treated non-perturbatively. To eliminate the time dependence, we choose a rotating frame:

$$\begin{aligned} c_1 &= \tilde{c}_1 \\ c_2 &= \tilde{c}_2 e^{-i(\omega_1 - \omega_2)t} \\ c_3 &= \tilde{c}_3 e^{-i\omega_1 t}. \end{aligned} \quad (8.11)$$

Introducing the detunings,

$$\begin{aligned} \delta_1 &= \omega_{13} - \omega_1 \\ \delta_2 &= \omega_{23} - \omega_2, \end{aligned} \quad (8.12)$$

we obtain the time independent Hamilton operator in the rotating frame [36]:

$$\hat{H} = \frac{1}{2}\hbar \begin{pmatrix} 0 & 0 & \Omega_1 \\ 0 & 2(\delta_1 - \delta_2) & \Omega_2 \\ \Omega_1 & \Omega_2 & 2\delta_1 \end{pmatrix}. \quad (8.13)$$

The Hamiltonian \hat{H} describes the coherent interaction of the QD with the two laser fields. However, the excited state $|3\rangle$ decays radiatively into the ground state $|1\rangle$ at rate Γ and into state $|2\rangle$ at rate γ_s . The rate γ_e describes spin flip processes between the states $|1\rangle$ and $|2\rangle$, which is symmetric for small magnetic fields since $g_e\mu_B B \gg k_B T$, meaning that $|1\rangle \rightarrow |2\rangle$ and $|2\rangle \rightarrow |1\rangle$ happen with the same rate. Furthermore, we introduce the dephasing rate γ_2 , describing the pure dephasing of $|2\rangle$ with respect to $|1\rangle$. In state $|3\rangle$ dephasing is omitted since the spontaneous emission rate is dominating the recombination process. We include the decoherence terms in the Lindblad form [30]:

$$\begin{aligned} L\rho &= \sum_{i,j} \frac{1}{2} \gamma_{ij} (2|j\rangle\langle i|\rho|i\rangle\langle j| - (|i\rangle\langle i|\rho + \rho|j\rangle\langle j|)) \\ &= \frac{1}{2}\Gamma(2|1\rangle\langle 3|\rho|3\rangle\langle 1| - |3\rangle\langle 3|\rho + \rho|3\rangle\langle 3|) \\ &+ \frac{1}{2}\gamma_s(2|2\rangle\langle 3|\rho|3\rangle\langle 2| - |3\rangle\langle 3|\rho + \rho|3\rangle\langle 3|) \\ &+ \frac{1}{2}\gamma_e(2|1\rangle\langle 2|\rho|2\rangle\langle 1| - |2\rangle\langle 2|\rho + \rho|2\rangle\langle 2|) \\ &+ \frac{1}{2}\gamma_e(2|2\rangle\langle 1|\rho|1\rangle\langle 2| - |1\rangle\langle 1|\rho + \rho|1\rangle\langle 1|) \\ &+ \frac{1}{2}\gamma_2(2|2\rangle\langle 2|\rho|2\rangle\langle 2| - |2\rangle\langle 2|\rho + \rho|2\rangle\langle 2|). \end{aligned} \quad (8.14)$$

With this the master equation for the density matrix $\rho_{ij} = \tilde{c}_i\tilde{c}_j$ is given by:

$$i\frac{d\rho_{ij}}{dt} = \frac{1}{\hbar} \sum_{k=1}^3 \left(\tilde{H}_{ik}\rho_{kj} - \rho_{ik}\tilde{H}_{ik} \right) + i(L\rho)_{ij}. \quad (8.15)$$

8.4.2 Connection to the Experiment

In the experiment we measure the differential transmission of the laser field resonant with the transition $|1\rangle \leftrightarrow |3\rangle$. The laser interacts with the QD by resonant Rayleigh scattering. On the detector the transmitted laser light interferes with the coherently scattered light of the QD [31]. The differential transmission signal is given by [23]:

$$\frac{\Delta T}{T} = 1 - \left\langle \frac{|F_1 + F_s|^2}{|F_1|^2} \right\rangle. \quad (8.16)$$

Here F_1 is the electric field of the impinging laser and F_s is the field scattered by the QD. Since the experiment measures the steady state of the interference the square modulus of the electric field components is time averaged, indicated by the brackets. F_s is proportional to the derivative of the oscillating dipole moment D_{13} which is itself connected to the density matrix element ρ_{13} [32]

$$F_s = \frac{eD_{13}}{2A\epsilon_0cn} i\omega_1 (\rho_{31}e^{-i\omega_1 t} + \rho_{13}e^{i\omega_1 t}). \quad (8.17)$$

Here A is the laser focus area, ϵ_0 is the permeability, c the velocity of light and $n = 3.6$ the refractive index of GaAs, the material surrounding the QD. In the derivation of eqn. 8.17 the Gouy phase is considered, which leads to a phase shift of $-\pi/2$ in the focus of a Gaussian beam [33]. Since $E_s \ll E_1$ and using the definition for the Rabi frequency Ω_1 above and the maximum transmission contrast in case of resonance ($\omega_1 = \omega_{13}$): $\alpha_0 = 2e^2 D_{13}^2 \omega_{13} / A\epsilon_0 cn \hbar \Gamma$ we can write

$$\frac{\Delta T}{T} \approx \alpha_0 \frac{\Gamma}{\Omega_1} \text{Im}[\rho_{13}]. \quad (8.18)$$

In this analysis we assume that also in the two-laser experiment, only one laser resonant to the $|1\rangle \leftrightarrow |3\rangle$ transition contributes to the differential transmission signal. The other laser only generates a constant contribution on the detector. To calculate ρ_{13} from eqn. 8.15 we consider the limit $t \rightarrow \infty$ since the usual integration times, of one second or more, are significantly larger than all expected timescales in the system. In this way the dynamics can be neglected. We calculate numerically the solution for the eight optical Bloch equations 8.15 with $d\rho_{ij}/dt = 0$ and the condition for the occupation of the three states $\rho_{33} = 1 - \rho_{11} - \rho_{22}$. The calculation leads to differential transmission spectra as a function of the rates γ_s , γ_e and γ_2 . At the same, time we determine from laser saturation spectroscopy and power broadening the spontaneous recombination rate Γ [25]. The Rabi frequency Ω_1 and Ω_2 we can estimate from the laser powers [25].

8.5 Faraday Geometry

To gain experimental access to the transition rates connecting the three level of the X^{1-} in a magnetic field applied parallel to the light propagating path, we study the response of the two-laser repump experiment as a function of various parameters that we can control in situ. In particular, our experimental setup allows controlling independently one or two of the interaction rates, while the other parameters are kept constant. The cotunnelling rate γ_{cot} is controlled by the gate voltage as already discussed above. The magnetic field changes the hyperfine interaction-mediated electron spin flip rate γ_{hf} and also, by modifying the intermixing of the electronic states, the “forbidden” transition rate γ_s . By studying the dependence of the repump signal on the power of the second laser and hence the Rabi frequency Ω_2 , we can

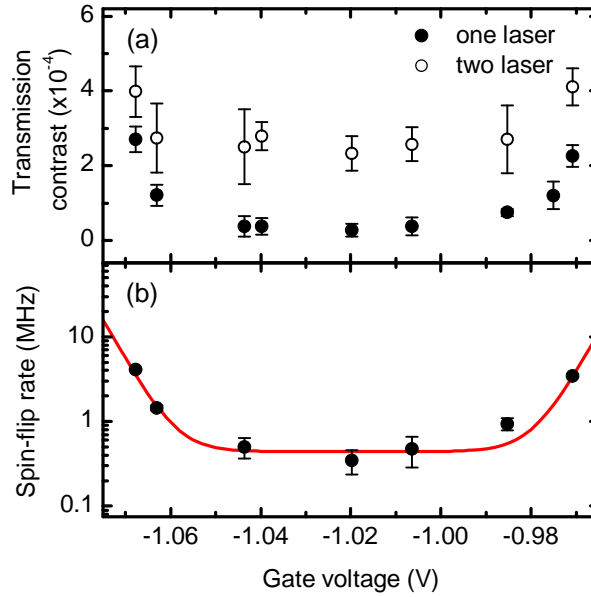


Figure 8.6: (a) Transmission contrast of a laser pumping the $|1\rangle \leftrightarrow |3\rangle$ -transition, with (open circles) and without (black dots) a second laser pumping the $|2\rangle \leftrightarrow |3\rangle$ “forbidden” transition. A magnetic field of $B = 0.5$ T is applied to obtain OSP. In (b) the spin flip rate γ_e that was obtained from fitting the quantum optical theory to the measured spectra, is plotted as a function of gate voltage. The line is a fit of eq.8.5 to the data points, with a $\hbar\Gamma_{\text{tun}} = 0.05 \mu\text{eV}$. To account for the gate voltage independent hyper-fine mediated spin-flip events, a constant offset $\gamma_{\text{hf}} = 0.42$ MHz was added (see eg.8.6).

finally access the dephasing rate γ_2 . The data is then fitted by the model in an iterative way to selectively determine the individual rates. This means that the spectra of the different data sets are fit by the theoretical model 8.18 repeatedly until a set of fit parameter is found that consistently describes all data sets (see table 8.1). In the following the different experiments will be discussed. In the section 8.5.4 the obtained values for the different rates will be presented in an overview. The interplay between the obtained rates will be discussed as well. All presented experiments have been performed on the same QD.

8.5.1 Gate Voltage Dependence

In section 8.3.1 the gate voltage dependence of the spin flip rate γ_e via cotunnelling was shown. There we measure a change in the transmission contrast as a function of the gate voltage over the plateau. Only one laser is resonantly driving the excitonic transition (Fig.8.3(b)). In the following, we repeat the experiment in a two-laser experiment. The transmission contrast is measured with and without a second laser, repumping the optical spin polarization, for each position on the plateau. Since the repump scheme only works in case of OSP, the experiment is limited to a gate voltage range in the middle of the charging plateau. In Fig.8.6(a) the measured transmission

contrast is plotted against the resonance gate voltage. The black dots represent the one-laser experiment, while the open circles were obtained by performing a two-laser experiment, with a second laser resonant to the “forbidden” transition. The data shows clearly that the transmission contrast is always larger in a two-laser experiment. We can fit both spectra, for each resonance gate voltage with the model derived in section 8.4.1. To simulate the second laser being switched on and off, the Rabi frequency is set to a finite value (which we determine to $\Omega_2 = 58$ MHz) or to zero ($\Omega_2 = 0$) respectively. All other parameters remain fixed. We perform this fitting routine for each pair of data points by adjusting the spin flip rate γ_e . The obtained values for γ_e are plotted in Fig.8.6(b) as black dots. As expected, the spin flip rate increases, as the gate voltage is tuned closer to the cotunnelling regime. As before, we can describe this behavior with eqn 8.5. The calculated spin flip time is plotted directly into the graph, given by the line in Fig.8.6(b). The fitting parameters are again the charging voltages $V_1 = -1.085$ V and $V_2 = -0.949$ V. These voltages are slightly different than those obtained for the QD described in section 8.3.1. The calculated cotunnelling rate γ_{cot} is modified by a constant offset to account for the remaining hyperfine mediated spin flip rate $\gamma_{hf} = 0.42$ MHz (see eqn 8.6). The tunnelling energy is as before $\hbar\Gamma_{tun} = 0.05$ μ eV. For the other rates the following values are used: $\Gamma = 1.2$ GHz obtained from power broadening and saturation spectroscopy, $\gamma_s = 35$ MHz, $\gamma_2 = 22$ MHz and the Rabi frequencies are $\Omega_1 = 2$ GHz and $\Omega_2 = 58$ MHz. Most of these values are evaluated by analyzing their dependencies on the different control parameters (i. e. magnetic field, gate voltage, laser power) iteratively.

The good agreement between the spin flip rates, obtained from the evaluation of the quantum optical treatment of the data, and the cotunnelling integral, confirms the assumption that both the tunnelling energy $\hbar\Gamma_{tun}$ as well as the “forbidden” rate γ_s are gate voltage independent.

8.5.2 Magnetic Field Dependence

Similarly to the approach in the previous section, we investigate the effect of the applied magnetic field on the repump signal. The transmission contrast in a one-laser and in a two-laser experiment is measured at various magnetic fields. By fitting the quantum optical model to pairs of spectra, the values for the spin flip rate γ_e and the “forbidden” transition rate γ_s were found to have a magnetic field dependence. The results are shown in Fig.8.7(a) for γ_e and (b) for γ_s by the black dots. The spin flip rate γ_e has to be varied as well as the “forbidden” transition rate γ_s , to obtain reasonably good agreement between the measured spectra and the calculated curves based on the model from section 8.4.1. We interpret the magnetic field dependence of the “forbidden” transition rate by the hyperfine contribution to the rate γ_s at low magnetic fields [8]. This contribution however is strongly reduced at large magnetic fields. Finally remains only the magnetic field independent contribution due to valence band mixing. In the work of J. Dreiser *et al.* [8] this contribution

is estimated to be rather small ($\approx 1\%$ of the spontaneous recombination rate). To model the hyperfine effect on the spin flip rate γ_e and the “forbidden” transition rate γ_s , we use a very simple model developed by O. Krebs [34]. We assume that the finite lifetime of the electron spin in the states $|1\rangle$ and $|2\rangle$ lead to an effective broadening of these states. Their distribution functions are given by two Lorentzians with a finite width $\hbar\delta\omega$, centered at an energy $\pm\epsilon$, where $2\epsilon = E_{Z,e}$:

$$f(E) \propto \frac{2}{\pi} \frac{\hbar\delta\omega}{4(E \pm \epsilon)^2 + (\hbar\delta\omega)^2}. \quad (8.19)$$

Because the magnetic moments of the nuclear spins are orders of magnitude smaller than the Zeeman splitting of the electrons, an electron spin flip-flop event can only happen with the probability of finding two electrons of opposite spin at the same energy. The angular momentum can then be absorbed by a flipping a nuclear magnetic moment in the QD. This probability is given by the ratio of the area of the gray overlap region of the two distribution functions to their total area. This is illustrated in the inset in Fig.8.7(a). For the hyperfine contribution for the spin flip

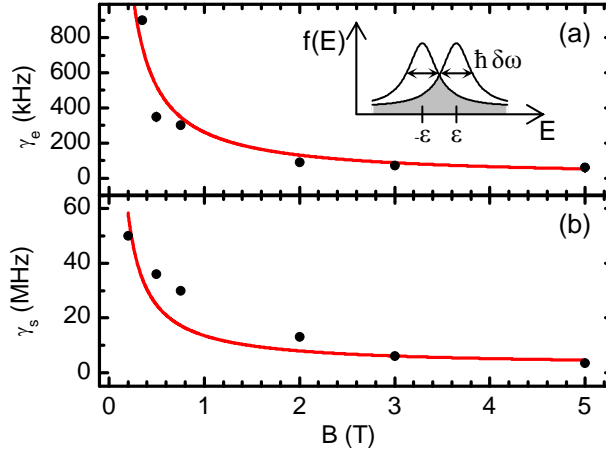


Figure 8.7: Spin flip rate γ_e (a) and “forbidden” transition rate γ_s (b) as a function of the applied magnetic field. The data was obtained from fitting the quantum optical theory to the spectra measured in one and two-laser spectroscopy. The evolution of the rates with the magnetic field are explained by a simple model describing electron-nuclear spin flip-flop processes. The inset in (a) illustrates the model [34], which is based on a finite broadening $\hbar\delta\omega$ of the electronic states $|1\rangle$ and $|2\rangle$, separated by the Zeeman energy ($2\epsilon = g_e\mu_B B$). The ratio of the overlap region (gray) of the two Lorentzians, depicting the density of states distribution, to the whole area of the Lorentzians gives the probability of equal energy of the two spin states. With this probability, the electron spin flip can occur, where the spin is transferred to a nucleus. The lines in (a) and (b) are fits of equation (8.20) to the datapoints with the fitting parameter $\hbar\delta\omega = 6.4$ neV which is of the same order of magnitude as the dephasing rate γ_2 of an electron spin in this QD. In (b) an additional offset of 2.5 MHz is added, to account for the admixture of light holes to the excitonic state.

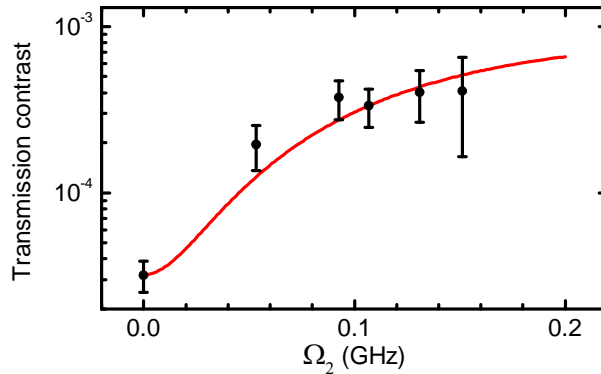


Figure 8.8: The transmission contrast of the first laser, resonant to the $|1\rangle \leftrightarrow |3\rangle$ -transition, is plotted against the Rabi frequency Ω_2 of the second laser. The line is a fit of the contrast predicted by the quantum optical theory to the data points. The parameters were $\Gamma = 1.2$ GHz, $\Omega_1 = 2$ GHz, $\gamma_s = 35$ MHz, $\gamma_e = 1.2$ MHz and the maximum transmission contrast $\alpha_0 = 1.93 \times 10^{-3}$. From the fit, an upper bound for the dephasing rate $\gamma_2 = 22$ MHz is obtained. The experiment was performed with an external magnetic field $B = 0.5$ T applied.

rate we get:

$$\gamma_{\text{hf}}(B) = \gamma_{\text{hf}}^0 \left(1 - \frac{2}{\pi} \arctan \left(\frac{g_e \mu_B B}{\hbar \delta \omega} \right) \right). \quad (8.20)$$

Here γ_{hf}^0 is the hyperfine mediated spin flip rate at zero magnetic field. We fit this relation to the magnetic field dependence of the spin flip rate and the “forbidden” transition rate. The results are shown in Fig.8.7(a) and (b) by the line. In both cases, we use a constant broadening of the electron state $\hbar \delta \omega = 6.4$ neV, which is of the order of the dephasing rate of the electron $\hbar \gamma_2 = 14.5$ neV which we get from the power dependence of the repump signal (section 8.5.3). However the value for the dephasing rate is only an upper bound and the real spin dephasing rate might be smaller. The electron g-factor is measured before, as described in section 8.3.2 to be $|g_e| = 0.70 \pm 0.01$. Considering that a constant $\delta \omega$ is a rather crude estimation, we find a good agreement between the measured values for the rates γ_e and γ_s and the simple hyperfine interaction model. To describe the “forbidden” transition rate γ_s , a constant offset is added to the fit equation 8.20: $\gamma_s = \gamma_{\text{s hf}} + \gamma_{\text{s}}^{\text{HH-LH}}$. This offset we interpret as accounting for the magnetic field independent contribution of the heavy-hole light-hole mixing to the “forbidden” transition, which is here $\gamma_{\text{s}}^{\text{HH-LH}} = 2.5$ MHz. This corresponds to an admixture of light-holes into the excitonic state of $< 1\%$. The rates for Γ , γ_2 and $\Omega_{1,2}$ are the same as in the previous section.

8.5.3 Power Dependence

To investigate the dependence of the repump signal on the power of the laser that pumps resonantly the “forbidden” transition (P_2), the magnetic field is fixed at $B = 0.5$ T and the gate voltage at $V_G = -1.07$ V corresponding to a spin flip rate $\gamma_e = 1.2$ MHz. Furthermore the power of the laser pumping the excitonic transition

$|1\rangle \leftrightarrow |3\rangle$ is fixed corresponding to a Rabi frequency $\Omega_1 = 2$ GHz. In Fig.8.8 the transmission contrast in case of resonance $\delta_1 = \delta_2 = 0$ (see eq.8.12) is plotted against the Rabi frequency Ω_2 .

The curve in Fig.8.8 is a fit of the quantum optical model to the data. The parameters for the fit are the same as in the sections above: $\Gamma = 1.2$ GHz and the dephasing rate $\gamma_2 = 22$ MHz.

For large laser power P_2 , when $\Omega_2 \approx \Omega_1$, the transmission spectra of the two-laser experiment are predicted to develop a splitting, accompanied by a reduced transmission contrast in case of resonance $\delta_1 = \delta_2 = 0$. This phenomena is called electromagnetically induced transparency (EIT) [35, 36]. It is due to a destructive interference of the two transitions, first observed on Sr-atoms by K. J. Boller, A. Imamoglu and S. E. Harris in 1991 [35]. The two ground states form a coherent superposition, a dark state that can not be excited by the two laser fields anymore. This coherent optical effect is of great interest, since it constitutes a prerequisite for purely optical coherent spin manipulation via stimulated Raman adiabatic passage (STIRAP) pump schemes [37, 38]. However, at laser powers strong enough to expect EIT, the measurement is challenging because the transmission detector is over illuminated. To reach equal Rabi frequencies $\Omega_1 = \Omega_2$, here $P_2 \approx 35P_1$ is required. In the experiment only $P_2 = 8P_1$ is achieved with a sufficient signal to noise ratio that would allow the recognition of a splitting in the spectrum.

To overcome this restriction which is due to the strongly different decay rates $\Gamma \gg \gamma_s$, a magnetic field perpendicular to the growth direction can be applied. It is expected that then the rates Γ and γ_s become equal (see section 8.6) [39, 40].

8.5.4 Discussion

A summary of the rates, obtained from an analysis of the different experiments with the theoretical model, is given in table 8.1. The spontaneous decay rate of the exciton Γ is obtained by one color saturation spectroscopy and power broadening [25]. The Rabi Frequency Ω_1 is directly linked to the laser power and the spontaneous decay rate of the exciton [25]. The Rabi frequency Ω_2 can be calculated from the known laser power P_2 and the “forbidden” transition rate γ_s . Therefore, there are three remaining unknown rates: the spin-flip rate γ_e , the “forbidden” transition rate γ_s and the dephasing rate γ_2 . Since the three parameters we can control in situ (V_g , B and P_2) correspond to these rates, we have a system of equations containing three equations and three rates. To obtain the values for these three rates all three data sets are fit in an iterative way until a consistency between the rates and an agreement between the data and the calculated spectra is obtained.

	Ω_1	Ω_2	Γ	γ_e	γ_s	γ_2	Fitparameter
V_g	2 GHz	58 MHz	1.2 GHz	varied	35 MHz	22 MHz	γ_e
B	2 GHz	58 MHz	1.2 GHz	varied	varied	22 MHz	γ_e, γ_s
P_2	2 GHz	varied	1.2 GHz	1.2 MHz	35 MHz	22 MHz	γ_2

Table 8.1: All parameters used to describe the data obtained from the two-laser repump experiments. The first column gives the Parameter, that was modified in the experiment. In the last column, the parameter that was used to fit the theory to the data, is listed.

8.6 Voigt Geometry

If a magnetic field is applied in the plane of the QD, while the light propagation direction is still normal to this plane (Voigt Geometry) the "forbidden" transition becomes allowed. The electron and hole spins are quantized parallel to the applied magnetic field, perpendicular to the light propagation vector. In the basis of the light propagating direction we have new eigenstates of the electronic and excitonic states introduced in section 8.3.1 and Fig. 8.2. These states are $|\tilde{1}\rangle = 1/\sqrt{2}(|1\rangle + |2\rangle)$, $|\tilde{2}\rangle = 1/\sqrt{2}(|1\rangle - |2\rangle)$ and $|\tilde{3}\rangle = 1/\sqrt{2}(|3\rangle + |4\rangle)$ as well as $|\tilde{4}\rangle = 1/\sqrt{2}(|3\rangle - |4\rangle)$. The transition between the states $|1\rangle \leftrightarrow |3\rangle$ is mediated by right-handed circularly polarized light and between the states $|2\rangle \leftrightarrow |4\rangle$ by left-handed circularly polarized light. Hence, the transitions $|\tilde{1}\rangle \leftrightarrow |\tilde{3}\rangle$ and $|\tilde{2}\rangle \leftrightarrow |\tilde{4}\rangle$ are mediated by linearly polarized light $\pi_x = 1/\sqrt{2}(\sigma^+ - \sigma^-)$, while the transitions $|\tilde{1}\rangle \leftrightarrow |\tilde{4}\rangle$ and $|\tilde{2}\rangle \leftrightarrow |\tilde{3}\rangle$

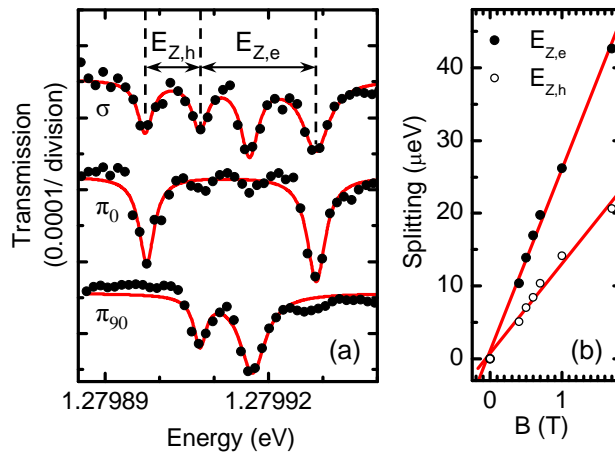


Figure 8.9: (a) One laser transmission spectra of a singly charged QD with an in-plane magnetic field applied ($B = 0.7$ T). The three spectra were obtained for different polarizations of the laser field. For the upper curve, the laser was circularly polarized. The lower were obtained for linear polarization, orthogonal to each other (see main text). The lines are Lorentzian fits to the data, an offset was added to the spectra for clarity. From the energy differences between the resonances, the Zeeman splitting of the electron and hole states can be calculated. In (b) these splittings are plotted as a function of the magnetic field. From a linear fit of the data points, the absolute values of the electron and hole g-factors are determined to be $|g_e| = 0.47$, $|g_h| = 0.24$.

are mediated by $\pi_y = 1/\sqrt{2}(\sigma^+ + \sigma^-)$ and are therefore allowed. To study these transitions the microscope was modified to perform spectroscopy in Voigt geometry. All following experiments have been performed on the same single QD. However, it was a different QD than that of the previous chapters.

8.6.1 High Resolution laser spectroscopy

With an in-plane magnetic field applied the unpolarized resonance line splits in four lines, as expected. In Fig.8.9(a) three transmission spectra are shown, measured with three different polarizations of the laser field. The magnetic field is $B = 0.7$ T and the experiment was performed at a gate voltage in the cotunnelling regime to prevent OSP. For the upmost spectrum the laser is circularly polarized, and all four resonance lines are visible. With a linearly polarized laser, the inner and outer resonances can be probed selectively, as shown in Fig.8.9(a) in the middle and lower spectrum. The laser light is coupled into the microscope with a normal single mode fiber, so we can determine the relative angle between the two linear polarizations to be 90° , but their angle relative to the magnetic field direction remains unknown. From the polarization properties of the lines, it is reasonable to assume that $\pi_0 \equiv \pi_x$ and $\pi_{90} \equiv \pi_y$ and the signs of the in-plane g-factors of the electron and hole are negative and thereby the same as in growth direction [40]. Hence we can allocate all four transitions to the four excitonic transitions in the QD.

From this the Zeemann splitting of the electron and hole can be measured. In Fig.8.9(a) and (b) the splittings are plotted against magnetic field. From a linear fit to the measured splittings the absolute values of the g-factors are acquired as

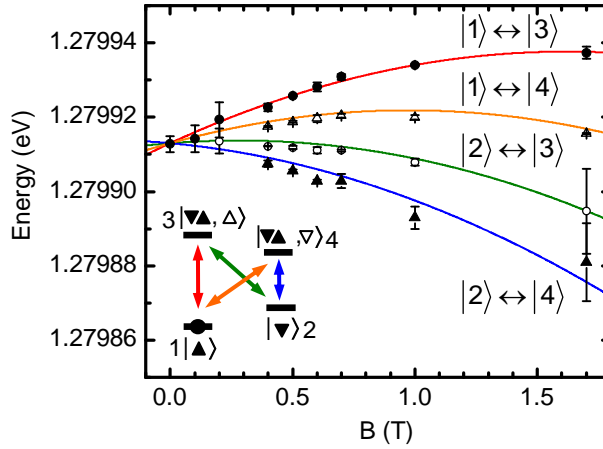


Figure 8.10: Resonance energy of the excitonic resonances of an X^{1-} in Voigt geometry as a function of the magnetic field. The data points were obtained by fitting the spectra with Lorentz functions (see Fig.8.9 (a)). The spectra were measured in the cotunnelling regime to avoid OSP. The data points are fit by parabolas, using the g-factors from Fig.8.9(b) and a diamagnetic shift of $-9.4 \mu\text{eV}/\text{T}$. In the inset, the electronic and excitonic level are sketched, together with the optical transitions between them.

$|g_e| = 0.47$ and $|g_h| = 0.24$. In contrast to the measurements in Faraday geometry, here the electron g-factor is larger than the hole g-factor. While the electron spin in a QD follows the direction of the applied magnetic field direction, the hole spin is expected to remain aligned along the growth direction of the QD. This would lead to an in-plane g-factor for holes of zero [41]. The fact that we observe a finite value for the hole g-factor suggests to perform further theoretical and experimental studies on holes in QD in order to gain a comprehensive understanding. The inset in Fig.8.10 depicts all electronic and excitonic states and the optical transitions connecting them.

The data in Fig.8.10 shows the magnetic field dependence of the resonance energies of all four resonances that were assigned to the four transitions. The magnetic field dependence of all four transition energies can be fitted with parabolas, yielding the diamagnetic shift to be $-9.4 \mu\text{eV}/\text{T}^2$. Although the magnitude of the diamagnetic shift is very similar to the diamagnetic shift that was measured in Faraday geometry [17], we are surprised to find the sign of the diamagnetic shift is negative, which would imply that the final state is more extended than the initial state, a fact which is not obvious in case of a negatively charged QD with an in-plane magnetic field applied. It has to be stated that we have not performed a statistical study of this effect and Xu *et al.* [39] report in a similar experiment a positive diamagnetic shift. The neutral exciton transition of the very same QD exhibits a positive diamagnetic shift (data not shown here), which points toward a strong influence of the Coulomb interactions, between the electrons and holes, on the diamagnetic behavior in Voigt geometry.

8.6.2 Optical Spin Pumping in Voigt Geometry

As in Faraday geometry, with an in plane magnetic field applied, the spin of the resident electron can be optically pumped with a resonant laser field [39]. In Fig.8.11(a) the transmission contrast is plotted in a grey scale plot, against the gate voltage and resonance energy. The experiment is performed at $B = 0.7$ T with a circular polarization of the laser field (see also Fig.8.9). At voltages below -0.975 V the QD is uncharged, and only the neutral exciton (X^0) can be observed. The resonance is shifted in energy by the electron hole Coulomb energy. For voltages above -0.75 V the QD is charged with a second electron and resonant pumping of the s-shell transition is blocked due to the Pauli exclusion principle [21, 16]. Between those voltages the X^{1-} is accessible to resonant laser spectroscopy. At the edges of the plateau (-0.975 V to -0.935 V and -0.79 V to -0.75 V) the fast spin relaxation via cotunnelling suppresses any significant OSP and all four transitions are visible (shown in Fig. 8.9). In the middle of the plateau the OSP strongly reduces the transmission contrast and no resonances are observed.

In Fig.8.11(b) the result of a two-laser repump experiment is shown. For this a second laser at a constant energy 1.27997 eV and a linear π_y -polarization is used. The first laser is scanned in energy as in Fig.8.11(a), its linear polarization is π_x . As

a result, in the cotunnelling regime, only two, the high and the low energy resonances are visible. In the middle of the plateau, the repump signal appears as a double resonance in energy at two different gate voltages. The positions are marked by arrows and labelled with (c), (d) and (e) according to the repump process as they are depicted in Fig.8.11. In case (c), the scanned laser is resonant to the transition $|1\rangle \leftrightarrow |3\rangle$, which corresponds to the energetically highest resonance in Fig.8.9 (the labelling of the states follows the definition given in the inset in Fig.8.10). The electron spin is shelved into the state $|2\rangle$, but at the given gate voltage ($V_G = -0.875$ V) the constant laser is resonant to the $|2\rangle \leftrightarrow |3\rangle$ -transition (corresponding

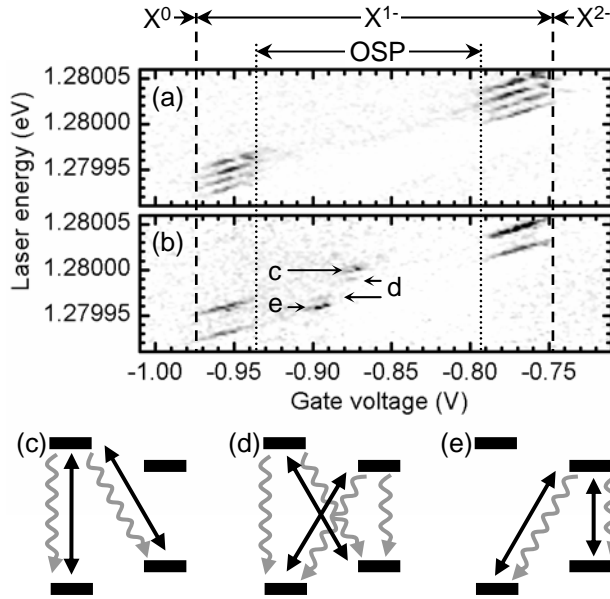


Figure 8.11: OSP of the resident electron spin in a QD in Voigt geometry. (a) the transmission contrast (dark colors correspond to high transmission contrast) as a function of the gate voltage and the laser energy. Between the dashed lines, lies the voltage range, where the QD is charged with one single electron (compare Fig.8.3(a)). The dotted lines mark the region where the electron spin is optically pumped, leading to a reduced transmission contrast. At the edges the transmission contrast is high because of fast spin relaxation due to cotunnelling (see also Fig.8.3(b)). The experiment was performed in a magnetic field of $B = 0.7$ T, with a circularly polarized laser field, yielding four distinct resonances (compare Fig.8.9(a)). In (b), a second laser at a fixed energy 1.27997 eV, was additionally used. This second laser was linearly π_y polarized, the scanned laser was orthogonally polarized, along π_x . At the edges of the plateau again the signal due to cotunnelling appears. In the middle of the plateau, the transmission signal of the scanned laser reappears due to optical repumping, according to the three repumping schemes (c), (d) and (e). In (c) the second, fixed laser is resonant to the $|2\rangle \leftrightarrow |3\rangle$ transition, while the scanned laser hits the $|1\rangle \leftrightarrow |3\rangle$ transition. In (d) the fixed and scanned laser are resonant to the $|1\rangle \leftrightarrow |4\rangle$, $|2\rangle \leftrightarrow |3\rangle$ respectively. Depending, which laser hits which resonance at the given gate voltage, these repump signal appear as marked in (b). The recovery for the repump scheme (d) is weaker, than for (c) and (e), because the polarization of the scanned laser does not match the polarization of the resonance it is pumping. In (e), similar to (c), the fixed laser is resonantly pumping the transition $|1\rangle \leftrightarrow |4\rangle$, while the scanned laser photon energy matches the $|2\rangle \leftrightarrow |4\rangle$ transition energy.

to the second lowest resonance energy in Fig.8.9), repumping the electron into the state $|1\rangle$. For (e) the situation is the same only for the two other transitions. The scanned laser is shelving the spin via the $|2\rangle \leftrightarrow |4\rangle$ -transition into the state $|1\rangle$, while the laser with constant energy is resonant to the $|1\rangle \leftrightarrow |4\rangle$ -transition. The resonance condition for this case is fulfilled at a lower gate voltage $V_G = -0.895$ V, because the energy of the $|1\rangle \leftrightarrow |4\rangle$ -transition is higher than for the $|2\rangle \leftrightarrow |3\rangle$ -transition. At both resonance voltages, weak repump signals appear at lower (in case of (c)) or higher (e) energies. They arise from the case, where the scanned laser is resonant to the $|1\rangle \leftrightarrow |4\rangle$, $|2\rangle \leftrightarrow |3\rangle$ -transition respectively. The scheme for this case is shown in (d). In this case the contrast is weaker, than for (c) and (e) because the polarization of the scanned laser is mostly along the π_x direction. Only a small contribution, due to imperfect polarization selection, is along π_y and can hence pump the transitions $|1\rangle \leftrightarrow |4\rangle$ or $|2\rangle \leftrightarrow |3\rangle$.

8.6.3 Power Dependence of the Repump Signal

In Fig.8.11(b) the recovery of the transmission contrast of the laser pumping the excitonic transition $|1\rangle \leftrightarrow |3\rangle$ is achieved by a second laser, resonant to the $|2\rangle \leftrightarrow |3\rangle$ -transition. This corresponds to a λ -system, as it is necessary for EIT (Fig.8.11(c)), similar to the experiment that was performed in Faraday geometry described in section 8.5. The difference is that in Voigt geometry the two spontaneous decay rates Γ from $|3\rangle \rightarrow |1\rangle$ and γ_s from $|3\rangle \rightarrow |2\rangle$ are equal, which is clear from the spectra shown in Fig.8.9. This implies that OSP is much more efficient in Voigt geometry

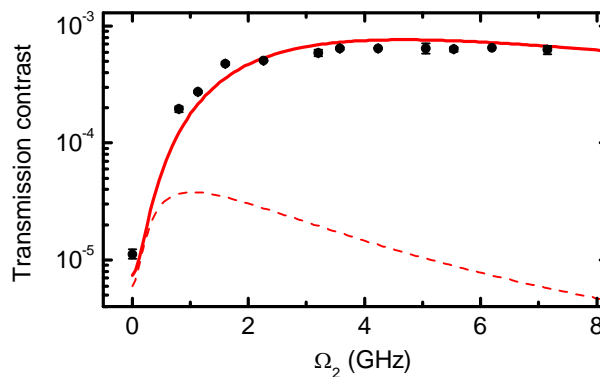


Figure 8.12: Power dependence of the repump signal in a two-laser experiment. One laser resonantly pumps the $|1\rangle \leftrightarrow |3\rangle$ -transition, with a Rabi frequency $\Omega_1 = 2.5$ GHz. The Rabi frequency of the second laser, resonant with the transition $|2\rangle \leftrightarrow |3\rangle$, is varied. The line represents a fit of the quantum optical theory to the data, with a dephasing rate $\gamma_2 = 6$ GHz. The other parameters are $\Gamma = \gamma_s = 4.2$ GHz, $\gamma_e = 1.2$ MHz and $\alpha_0 = 1.8 \times 10^{-3}$. The magnetic field was $B = 0.7$ T. The Rabi frequency of $\Omega_1 = 2.5$ GHz, which leads to a power broadening and a reduced transmission contrast compared to Fig.8.8, was chosen for optimum signal to noise ratio. The dashed line is a plot of the calculated transmission contrast that is expected for a dephasing rate $\gamma_2 = 22$ MHz that was measured as an upper bound for the QD in section 8.5.

and the laser fields couple equally well to the two optical transitions $|1\rangle \leftrightarrow |3\rangle$ and $|2\rangle \leftrightarrow |3\rangle$. Hence, for equal laser powers P_1 and P_2 the Rabi frequencies Ω_1 and Ω_2 are also equal. With this assumption, the quantum optical theory described above predicts a significant EIT dip for the case of double resonance $\delta_1 = \delta_2 = 0$. In Fig.8.12 the dashed line gives the expected transmission contrast as a function of Ω_2 , for a constant $\Omega_1 = 2.5$ GHz and for $\Gamma = \gamma_s = 4.2$ GHz. These rates are obtained from saturation spectroscopy for this QD [25]. We use the dephasing rate $\gamma_2 = 22$ MHz as it is obtained in section 8.5.3.

The experiment, however, yields a different result. It is shown by the black dots in Fig.8.12. Even for large Ω_2 that were accessible with a reasonable signal to noise, the spectra show no sign of a double resonance. The line in the Figure is a fit of the theoretically calculated normalized transmission contrast for $\delta_1 = \delta_2 = 0$ to the data points. The only fit parameter is the dephasing rate $\gamma_2 = 6$ GHz, a value agreeing reasonably with the observed linewidth of the resonance in one-laser transmission spectroscopy. The spin flip rate $\gamma_e = 1.2$ MHz. The result of finding two QD with different spin dephasing times for confined electrons is not surprising since the spin dephasing time is strongly dependent on the dynamics of the Overhauser-field that is generated by the randomly oriented, and fluctuating nuclear magnetic moments. In single electron spin resonance experiments on similar QDs [12], completely different spin dynamics have been observed on two different QDs. Similar as in the presented experiment, one QD exhibits a slowly fluctuating Overhauser-field on a timescale $\gg 10$ s, yielding a long coherence time of the electron spin. The behavior of another QD can be explained by an Overhauser-field fluctuation on the timescale of the electron spin lifetime, which leads to fast spin dephasing. For reaching the goal of EIT, an elaborate statistics of the electron spin dephasing rate on different QDs has to be performed.

8.7 Summary and Conclusion

We have performed high resolution two-laser resonant spectroscopy on a single, negatively charged QD. We showed the optical pumping of the spin of the resident electron, in a magnetic field, with one-laser and the repump of the electron spin in a two-laser experiment. The experiments have been performed in Faraday and in Voigt geometry which allowed a control of the efficiency of the OSP and the optical repump. From studying the response of the repump signal to varying different parameters like the electric and magnetic field as well as the laser power, we could obtain all relevant rates occurring in the four-level system that a charged QD represents, in a magnetic field. To do this we developed a quantum optical theory, based on a master equation for the density matrix of the four level system of a negatively charged QD in a magnetic field. The analysis of the data allowed us to draw conclusions to the physical mechanisms responsible for the spin flip properties in a QD. Furthermore, the power dependency of the repump signal, allows the

estimation of an upper bound of the dephasing rate. Based on these results, we investigated the feasibility to generate optically spin-coherent, long lived, electronic states in the QD and to apply quantum optical, coherent spin manipulation schemes, known from atom optics. In the presented experiment the dephasing rate was too fast to observe such an optically generated coherent state. We explain this by fast fluctuating nuclear magnetic moments. The demonstrated experiments confirm the applicability of high resolution laser spectroscopy to study single spin phenomena in charged QDs. For a reliable way of generating and controlling spin states, schemes that are based on singlet-triplet transitions seem to be more promising, since then the influence of the Overhauser field is reduced [42].

References

- [1] A. Imamoglu, D. D. Awschalom, G. Burkard, D. P. DiVincenzo, D. Loss, M. Sherwin, and A. Small, *Phys. Rev. Lett.* **83**, 4204 (1999).
- [2] D. Loss, D. P. DiVincenzo, *Phys. Rev. A.* **57**, 120 (1998).
- [3] A. Greilich, D. R. Yakovlev, A. Shabaev, Al. L. Efros, I. A. Yugova, R. Oulton, V. Stavarache, D. Reuter, A. Wieck and M. Bayer, *Science* **313**, 341 (2006).
- [4] M. Kroutvar, Y. Ducommun, D. Heiss, M. Bichler, D. Schuh, G. Abstreiter and J. J. Finley, *Nature* **432**, 81 (2004).
- [5] M. Atatüre, J. Dreiser, A. Badolato, A. Högele, K. Karrai and A. Imamoglu, *Science* **312**, 551 (2006).
- [6] M. Kroner, S. Seidl, B. D. Gerardot, B. Biedermann, A. Badolato, P. M. Petroff, K. Karrai and R. J. Warburton, *Int. J. Mod. Phys. B* **21**, 1307 (2007).
- [7] B. Gerardot, D. Brunner, P. A. Dalgarno, P. Öhberg, S. Seidl, M. Kroner, K. Karrai, N. G. Stoltz, P. M. Petroff and R. J. Warburton, *Nature* **451**, 441 (2008).
- [8] J. Dreiser, M. Atatüre, C. Galland, T. Müller, A. Badolato, and A. Imamoglu, *Phys. Rev. B* **77**, 075317 (2008).
- [9] P. Maletinsky, A. Badolato and A. Imamoglu, *Phys. Rev. Lett.* **99**, 056804 (2007).
- [10] A. I. Tartakovskii, T. Wright, A. Russell, V. I Fal'ko, A. B. Van'kov, J. Skiba-Szymanska, I. Drouzas, R. S. Kolodka, M. S. Skolnick, P. W. Fry, A. Tahraoui, H. Y. Liu and H Hopkinson, *Phys. Rev. Lett.* **98**, 026806 (2007).
- [11] R. I. Dzhioev and V. L. Korenev, *Phys. Rev. Lett.* **99**, 037401 (2007).
- [12] M. Kroner, K. M. Weiss, B. Biedermann, S. Seidl, S. Manus, A. W. Holleitner, A. Badolato, P. M. Petroff, B. D. Gerardot, R. J. Warburton and K. Karrai, arXiv:0710.4901.

- [13] H. Drexler, D. Leonard, W. Hansen, J. P. Kotthaus and P. M. Petroff, *Phys. Rev. Lett.* **73**, 2252, (1994).
- [14] R. J. Warburton, C. Schäfflein, D. Haft, F. Bickel, A. Lorke, K. Karrai, J. M. Garcia, W. Schoenfeld and P. M. Petroff, *Nature* **405**, 926 (2000).
- [15] J. J. Finley, A. D. Ashmore, A. Lemaitre, D. J. Mowbray, M. S. Skolnick, I. E. Itskevich, P.A. Maksym, M. Hopkinson, and T. F. Krauss, *Phys. Rev. B* **63**, 073307 (2001).
- [16] S. Seidl, M. Kroner, P. A. Dalgarno, A. Högele, J. M. Smith, M. Edinger, B. D. Gerardot, J. M. Garcia, P. M. Petrogg, K. Karrai and R. J. Warburton, *Phys. Rev. B* **72**, 195339 (2005).
- [17] C. Schulhauser, D. Haft, R. J. Warburton, K. Karrai, A. O Govorov, A. V. Kalameitsev, A. Chaplik, W. Schoenfeld, J. M. Garcia and P. M Petroff, *Phys. Rev. B* **66**, 193303 (2002).
- [18] K. Karrai, R. J. Warburton, C. Schulhauser, A. Högele, B. Urbaszek, E. J. McGhee, A. O. Govorov, J. M. Garcia, B. D. Gerardot and P. M. Petroff, *Nature* **427**, 6970 (2004).
- [19] A. Högele, S. Seidl, M. Kroner, K. Karrai, C. Schulhauser, O. Sqalli, J. Scrimgeour, and R. J. Warburton, *Rev. Sci. Instrum.* **79**, 023709 (2008).
- [20] A. Högele, M. Kroner, S. Seidl, M. Atatüre, J. Dreiser, A. Imamoglu, R. J. Warburton, A. Badolato, B. D. Gerardot, P. M. Petroff and K. Karrai, *Appl. Phys. Lett.* **86**, 221905 (2005).
- [21] A. Högele, S. Seidl, M. Kroner, R. J. Warburton, B. D. Gerardot, P. M. Petroff and K. Karrai, *Phys. Rev. Lett.* **93**, 217401 (2004).
- [22] B. Alèn, F. Bickel, R. J. Warburton, P. M. Petroff and K. Karrai, *Appl. Phys. Lett.* **83**, 112235, (2003).
- [23] K. Karrai, R. Warburton, *Superlattice Microst.* **311**, 33, (2003).
- [24] M. Kroner, C. Lux, S. Seidl, A. W. Holleitner, A. Badolato, P. M. Petroff, R. J. Warburton, and K. Karrai, *Appl. Phys. Lett.* **92**, 031108 (2008).
- [25] M. Kroner, S. Rémi, A. Högele, S. Seidl, A. W. Holleitner, R. J. Warburton, B. D. Gerardot, P. M. Petroff and K. Karrai, *Physica E* (2007), doi:10.1016/j.physe.2007.09.1
- [26] M. Bayer, A. Kuther, A. Forchel, A. Gorbunov, V. B. Timofeev, F. Schäfer, J. P. Reithmaier, T. L. Reinecke and S. N. Walck, *Phys. Rev. Lett.* **82**, 1748, (1999).
- [27] M. Bayer, G. Ortner, O. Stern, A. Kuther, A.A. Gorbunov, A. Forchel, P. Hawrylak, S. Fafard, K. Hinzer, T.L. Reinecke, S.N. Walck, J.P. Reithmaier, F. Klopff, and F. Schäfer, *Phys. Rev. B* **65**, 195315 (2002).

-
- [28] N. W. Ashcroft, N. D. Mermin, *Solid State Physics*, Holt, Rinehart and Winston, New York (1976).
- [29] J. M. Smith, P. A. Dalgarno, R. J. Warburton, A. O. Govorov, K. Karrai, B. D. Gerardot and P. M. Petroff, *Phys. Rev. Lett.* **94**, 197402 (2005).
- [30] L. Mandel, E. Wolf, *Optical coherence and quantum optics*, Cambridge University Press, Cambridge (1995).
- [31] B. R. Mollow. *Phys. Rev. A*, **5**, 2217 (1972).
- [32] R. Loudon *The Quantum Theory of Light*, Oxford University Press, Oxford (2000).
- [33] L. G. Gouy, *Compt. Rend. Acad. Sci. Paris* **110**, 1251 (1890).
- [34] O. Krebs, *private communication*.
- [35] K. J. Boller, A. Imamoglu and S. E. Harris, *Phys. Rev. Lett.* **66**, 2593 (1991).
- [36] M. Fleischhauer, A. Imamoglu, J. P. Marangos, *Rev. Mod. Phys.* **77**, 633 (2005).
- [37] J. R. Kuklinski, U. Gaubatz, F. T. Hioe, and K. Bergmann, *Phys. Rev. A*. **40**, 6741 (1989).
- [38] U. Gaubatz, P. Rudecki, S. Schiemann and K. Bergmann, *J. Chem. Phys.* **92**, 5363 (1990).
- [39] X. Xu, Y. Wu, B. Sun, Q. Huang, J. Cheng, D. G. Steel, A. S. Bracker, D. Gammon, C. Emary and L. J. Sham, *Phys. Rev. Lett.* **99**, 097401 (2007).
- [40] M. Bayer, O. Stern, A. Kuther and A. Forchel, *Phys. Rev. B* **61**, 7273 (2000).
- [41] W. Sheng, and P. Hawrylak, *Phys. Rev. B* **73**, 125331 (2006).
- [42] J. R. Petta, A. C. Johnson, J. M. Taylor, E. A. Laird, A. Yacoby, M. D. Lukin, C. M Marcus, M. P. Hanson and A. C. Gossard, *Science* **309**, 2180 (2005).

Chapter 9

Optical detection of single electron spin resonance

We demonstrate optically detected spin resonance of a single electron confined to a self-assembled quantum dot. The dot is rendered dark by resonant optical pumping of the spin with a laser. Contrast is restored by applying a radio frequency (rf) magnetic field at the spin resonance. The scheme is sensitive even to rf fields of just a few μT . In one case, the spin resonance behaves exactly as a driven 3-level quantum system (a λ -system) with weak damping, in another one, the dot exhibits remarkably strong (67% signal recovery) and narrow (0.34 MHz) spin resonances with fluctuating resonant positions, evidence of unusual dynamic processes of non-Markovian character.

9.1 Introduction

The control of few-level systems is a major challenge for the development of novel computation schemes based on quantum states. Solid state-based nanostructures can be tailored and tuned in situ, offering significant advantages over conventional quantum systems such as atoms and ions. Furthermore, in a strongly quantized solid state system, electron spin is remarkably robust as the quantization suppresses phonon-related spin relaxation [1, 2, 3], adding weight to proposals using spin as a qubit [4]. Recently, spin relaxation times as long as $T_1 \sim 1$ s [2, 5] and a lower bound on the coherence time T_2 of 1 μ s [6, 7, 8] have been established on quantum dots. It is clearly of fundamental importance to develop spin resonance schemes with single spin resolution. In the longer term, spin resonance provides the capability of performing arbitrary spin rotations in the Bloch sphere; in the shorter term, it provides unique insights into the complex spin interactions in the solid state environment. Single spin resonance has been achieved on an electrostatically-defined quantum dot with electrical detection leading to the observation of Rabi flopping [9]. An alternative is to detect the spin resonance optically. This is potentially very sensitive because of the in-built amplification of $\sim 10^5 - 10^7$ since absorption of a microwave photon leads to absorption of an optical photon. While optically detected single spin resonance on the NV^- center, a deep impurity level in diamond, is established [10], optically detected single spin resonance, on a quantum dot has not been demonstrated before. The crucial difference is the length scale: we report here a spin resonance of a single electron with a wave function extending over $\sim 10^4$ atoms.

9.2 ESR pumping scheme

Our electron spin resonance (ESR) scheme is shown in Fig. 9.1(a). A single electron is confined to the dot and a magnetic field is applied, splitting the electron spin states, $|\downarrow\rangle$ and $|\uparrow\rangle$, by the Zeeman energy. The first step is to project the electron into, say, the $|\downarrow\rangle$ state. We do this with optical pumping: a laser drives the $|\uparrow\rangle \leftrightarrow |\uparrow\downarrow, \uparrow\rangle$ transition where $|\uparrow\downarrow, \uparrow\rangle$ represents the X^{1-} exciton consisting of two spin-paired electrons and a spin-up hole. Spontaneous emission damps the laser-driven oscillations and in the presence of some symmetry breaking projects the electron into the $|\downarrow\rangle$ state where the population is shelved. This method of spin initialization is highly efficient provided the spin relaxation rate from $|\downarrow\rangle$ to $|\uparrow\rangle$ is slow. The signature for spin-initialization is the disappearance of a signal related to resonant Rayleigh scattering of the optical laser [11, 12, 13]. The second step is to apply a radio frequency (rf) magnetic field at the Zeeman frequency. The rf field drives the spin resonance transition, $|\downarrow\rangle \leftrightarrow |\uparrow\rangle$. This causes the $|\uparrow\rangle$ state to be repopulated, reestablishing the Rayleigh scattering. The scheme is a contemporary application of magnetic resonance developed originally with Hg atoms [14], replacing a huge ensemble of atoms with a single quantum dot, an incoherent source with a

laser and fluorescence detection with Rayleigh scattering.

We perform spin resonance on single InAs/GaAs self-assembled quantum dots. The dots are embedded in a field effect structure which allows for controlled charging with single electrons via a tunnelling interaction with an electron reservoir [15, 16]. In the present device, the tunnelling barrier is 25 nm thick and the back contact is a two-dimensional electron gas with carrier concentration 10^{12} cm^{-2} . The sample is mounted in a 4 K optical microscope, a magnetic field of $B_{\text{ext}} = 0.5 \text{ T}$ is applied in the growth direction (Faraday geometry), and a voltage V_G is applied to a surface Schottky barrier in order to trap a single electron in a particular dot, Fig. 9.1(b). The interaction with a narrowband laser tuned to the fundamental cross-gap transition is detected in transmission: a dip in transmission with linewidth $\sim 2 \mu\text{eV}$ is observed on resonance [17]. The quantum dot is tuned relative to the laser by sweeping V_G which shifts the exciton through the quantum confined Stark effect. The microwave field is generated by a single loop antenna (Fig. 9.1(b)) with a geometry designed to emit over a broad frequency spectrum. The investigated quantum dot lies close to the antenna on its symmetry axis ensuring that the dot experiences only the near-field of the antenna, which contains a magnetic but nearly no electric field component. From the geometry and the electrical characteristics of the setup, we

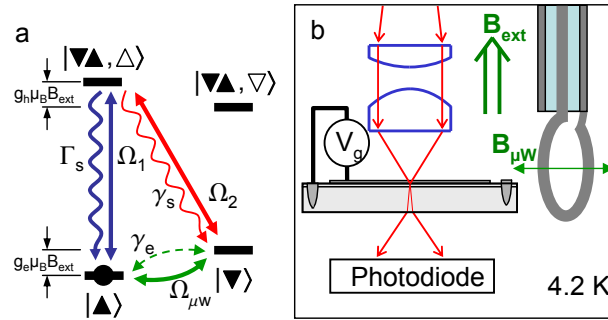


Figure 9.1: (a) Level scheme for optically detected spin resonance. The electron spin states, $|\uparrow\rangle$ and $|\downarrow\rangle$ are split by the electron Zeeman energy $g_e\mu_B B_{\text{ext}}$ ($g_e < 0$). $|\uparrow\downarrow, \uparrow\rangle$ denotes the spin-up exciton state, X^{1-} . The σ^+ -polarized transition $|\uparrow\rangle \leftrightarrow |\uparrow\downarrow, \uparrow\rangle$ is driven on resonance with a coherent laser. The spin resonance transition, $|\downarrow\rangle \leftrightarrow |\uparrow\rangle$, is driven with an oscillating magnetic field $B_{\mu W}$ at right angles to the dc external magnetic field, B_{ext} . Incoherent processes are spontaneous radiative decay, $|\uparrow\downarrow, \uparrow\rangle \rightarrow |\uparrow\rangle$ (fast), $|\uparrow\downarrow, \uparrow\rangle \rightarrow |\downarrow\rangle$ (slow); and spin relaxation, $|\downarrow\rangle \leftrightarrow |\uparrow\rangle$ (very slow). (b) Schematic of experimental setup. The laser excitation at wavelengths around 950 nm is focused onto the sample with an objective with numerical aperture 0.5 and gives a spot size of $\sim 1 \mu\text{m}$ at the sample. A gate voltage V_G is applied between surface Schottky gate and the back contact and controls the quantum dot charge via Coulomb blockade and within one charge plateau, the energy of the exciton transition via the Stark effect. The transmitted light is detected with an in situ photodiode. A dc magnetic field, B_{ext} , is applied perpendicular to the sample. An ac magnetic field, $B_{\mu W}$, is generated with a closed loop antenna of diameter 2 mm positioned 2 mm along its axis from the quantum dot. The loop is connected to a microwave oscillator via a semirigid high frequency cable. The objective, sample and antenna are all at 4.2 K.

estimate the ac magnetic field $B_{\mu W}$ to be a few μT .

9.3 Spin initialization

The primary signature of optical spin pumping is a loss of transmission signal as a magnetic field is applied [11, 12, 13], Fig. 9.2 (a). The hyperfine interaction plays a dual role here [13]. In the absence of any induced nuclear polarization, the electron experiences an Overhauser field B_N on account of the incomplete cancellation of the magnetic fields generated by each nucleus in the quantum dot. B_N evolves randomly. First, for small B_{ext} , fluctuations in B_N induce rapid electron spin relaxation [13, 18]. As B_{ext} increases, this relaxation mechanism is suppressed on account of the energetic mismatch in nuclear and electronic Zeeman energies. Secondly, the in-plane component of B_N is responsible for the symmetry breaking required for the “forbidden” $|\uparrow\downarrow, \uparrow\rangle \rightarrow |\downarrow\rangle$ transition, Fig. 9.1(a). The in-plane field admixes the $|\downarrow\rangle$ and the $|\uparrow\rangle$ states; equivalently it tilts the electron (but not the exciton) quantization axis away from the z -axis. The in-plane Overhauser field is ~ 30 mT for these dots, as deduced either from the dot size and hyperfine coupling constants or from an interpretation of optical spin pumping [13]. The spin admixture is small at $B_{\text{ext}} = 0.5$ T but nevertheless sufficient for spin pumping. Heavy hole-light hole mixing can also allow the “forbidden” optical transition but this contribution is only important at very high magnetic fields [13]. The spin relaxation rate can also be controlled via V_G : at the edges of the Coulomb blockade plateau, spin relaxation is rapid via a spin-swap with the back contact, a cotunnelling process [11, 12, 13, 19], but highly suppressed in the plateau center. Similarly, the spin orbit-related electron

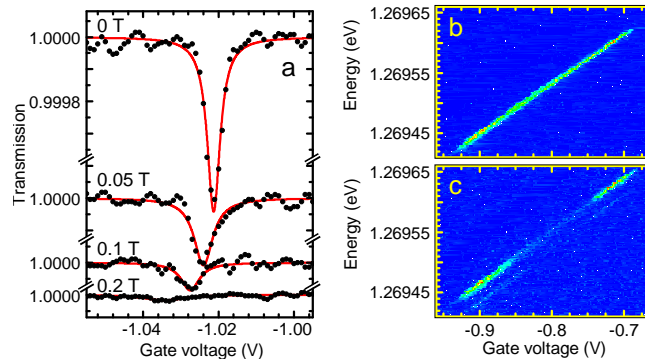


Figure 9.2: Spin shelving via optical pumping. (a) shows differential transmission data on a single quantum dot at 4.2 K as a function of the applied magnetic field, B_{ext} , recorded with a V_G at the center of the charging plateau. The contrast disappears as B_{ext} increases. (b), (c) color scale plots of the V_G -dependence. (b) At $B_{\text{ext}} = 0$, the optical signal is maintained across the plateau; (c) at $B_{\text{ext}} = 0.5$ T, the optical signal is suppressed in the plateau center signifying spin shelving, but recovers at the plateau edges signifying rapid spin relaxation via cotunnelling. In (c), the two resonances correspond to the two Zeeman-split exciton transitions. The polarization is right-handed circularly polarized with a weak left-handed component.

spin-flip mechanism is weaker at low magnetic fields than cotunnelling in our device as can be anticipated from both experimental [2] and theoretical work [1].

9.4 Determination of the electron g-factor

One of the challenges in the ESR experiment is that the electron g-factor, g_e , for a given quantum dot is unknown. g_e is strongly dependent on the detailed morphology of the quantum dot [20], varying in our case from -0.5 to -0.8 from dot to dot. Furthermore, in the Faraday configuration, conventional laser spectroscopy measures only the sum of the electron and hole Zeeman energies, and the hole Zeeman energy is typically two or three times larger than the electron Zeeman energy. Compounding this, the ESR is potentially very narrow in frequency space. This represents a spectral “needle in a haystack” problem. To solve it, we have developed a laser spectroscopy technique to determine g_e . The concept is to exploit the sensitivity of the spin pumping to any transition, even a very weak one, involving the shelved electron spin state. As shown in Fig. 9.3(d), we apply two laser fields, the first on resonance with the strong $|\uparrow\rangle \leftrightarrow |\uparrow\downarrow, \uparrow\rangle$ transition which projects the spin into the $|\downarrow\rangle$ state, and the second tuned in energy to the weak $|\downarrow\rangle \leftrightarrow |\uparrow\downarrow, \uparrow\rangle$ transition. On resonance, the second laser frustrates the spin shelving induced by the first laser, leading to a recovery of the optical transmission signal.

To implement this scheme for determining g_e , we choose the frequency of the first laser ν_1 such that it comes into resonance with the higher energy Zeeman transition,

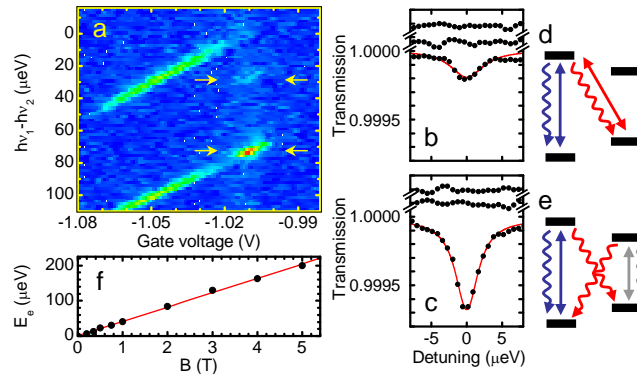


Figure 9.3: Optical characterization with 2 coherent lasers. The energy of laser 1 is chosen to come into resonance with the higher energy Zeeman transition, $|\uparrow\rangle \leftrightarrow |\uparrow\downarrow, \uparrow\rangle$, at $V_G = -1.01$ V where the transmission contrast is immeasurably small owing to spin shelving in the $|\downarrow\rangle$ state. The power of laser 1 is 1 nW. The energy of a second laser, $h\nu_2$, with power 1 nW is red-shifted relative to laser 1 and the differential transmission is recorded as a function of V_G . Both lasers are linearly polarized. The process is repeated for different $h\nu_2$. (a) shows the data as a color plot. (b) and (c) show the transmission spectra for laser 1 alone, laser 2 alone and for laser 1 and laser 2 (offset for clarity) for the two double resonances marked in (a). (d) and (e) are the respective interpretation of the double resonances in terms of the level diagram, Fig. 9.1 (a). (f) Difference in absorbed photon energy of the two lasers, as in (d), against magnetic field with a linear fit.

$|\uparrow\rangle \leftrightarrow |\uparrow\downarrow, \uparrow\rangle$, at a V_G far from the plateau edge (-1.01 V in Fig. 9.3 (a)) and the transmission signal is therefore quenched by efficient spin pumping. The frequency of the second laser, ν_2 , is then gradually red-shifted relative to the first. Both lasers are linearly-polarized so that all circularly-polarized transitions can be pumped and both lasers are incident on the same transmission detector. For each ν_2 we scan the gate voltage, Fig. 9.3(a). The two regions of high transmission contrast between -1.06 and -1.03 V represent the interaction of the second laser with the two Zeeman-split transitions, $|\uparrow\rangle \leftrightarrow |\uparrow\downarrow, \uparrow\rangle$ and $|\downarrow\rangle \leftrightarrow |\uparrow\downarrow, \downarrow\rangle$, at the plateau edge where the contrast is large. For $V_G \geq -1.03$ V, spin shelving starts and the contrast from the strong Zeeman transitions quenches. However, there are two values of $h\nu_2$ where contrast is reestablished at $V_G = -1.01$ V signifying double resonances, arrows in Fig. 9.3(a). Fig. 9.3(b),(c) show line cuts through the two double resonances. The spectra were measured with each laser separately (no visible transmission dip) and then with both together (transmission dip) and are interpreted with the level diagrams of Fig. 9.3(d),(e). In (c) and (e), laser 1 pumps the higher energy Zeeman transition, and laser 2 pumps the lower energy Zeeman transition. Laser 2 frustrates the spin-shelving from laser 1 and vice versa, leading to a recovery in contrast, a repumping phenomenon [11]. In (b) and (d) however, laser 2 pumps the weaker cross-transition, and $h\nu_1 - h\nu_2$ corresponds to the electron Zeeman energy allowing its experimental determination. We have repeated this procedure as a function of B_{ext} and find that the splitting $h\nu_1 - h\nu_2$ depends linearly on B_{ext} , passing through the origin, exactly the behavior for a Zeeman splitting, Fig. 9.3(f), yielding $g_e = -0.56 \pm 0.05$ for this particular dot.

The power of our scheme for determining g_e is that, by monitoring the strong $|\uparrow\rangle \leftrightarrow |\uparrow\downarrow, \uparrow\rangle$ transition in the spin pumping regime, we can detect the presence of the weak $|\downarrow\rangle \leftrightarrow |\uparrow\downarrow, \uparrow\rangle$ transition which is completely hidden either in conventional laser spectroscopy or photoluminescence characterization. The detection of ESR proceeds in a similar way, in this case the spin resonance frustrates the spin shelving.

9.5 Optically detected electron spin resonance

We concentrate on two dots, dot A with $g_e = -0.56 \pm 0.05$ and dot B with $g_e = -0.63 \pm 0.05$. At $B_{\text{ext}} = 0.5$ T, the predicted ESR frequency is 3.9 ± 0.3 (4.4 ± 0.3) GHz for dot A (B). To search for ESR, we scanned the rf over a 1 GHz bandwidth with a resolution of 0.1 MHz integrating over 1 second, a time-consuming task. To ensure that the optical laser remains in resonance with the $|\uparrow\rangle \leftrightarrow |\uparrow\downarrow, \uparrow\rangle$ transition throughout, we operated in a regime of V_G close to the plateau edges where cotunnelling is sufficiently strong to give us a small optical signal. For each rf, we performed a V_G sweep. Fig. 9.4 is a contour plot of V_G (optical detuning) versus rf for dot A; Fig. 9.5 optical signal versus rf at zero optical detuning for dot B. For all rf, the optical resonance can be just made out in Fig. 9.4, demonstrating that the optical resonance is maintained throughout. However, at very specific

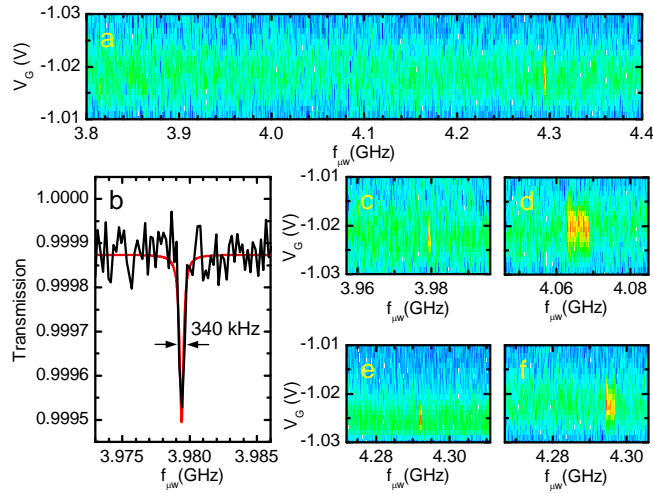


Figure 9.4: Optically detected spin resonance for dot A at $B_{\text{ext}} = 0.5$ T. Color scale plot of the optical transmission signal with microwave frequency, $f_{\mu\text{W}}$, along the x-axis, gate voltage (equivalently optical detuning, δ) along the y-axis. The Stark shift $d\delta/dV_G$ is $0.9 \mu\text{eV/mV}$. For each microwave frequency, the gate voltage is swept from -1.01 to -1.03 V. A weak optical resonance can be made out at all microwave frequencies proving that the dot remains in resonance with the optical laser. The strong signal close to 4.3 GHz is the electron spin resonance (ESR). (c)-(f) other experimental runs on the same dot under identical conditions; (b) optical transmission versus microwave frequency at zero optical detuning from (c) showing ESR close to 3.98 GHz.

microwave frequencies, there is an increase in optical signal. For dot A, the signal recovers to 67% of its value at $B_{\text{ext}} = 0$ and the ESR linewidth is extremely small, 0.34 MHz. For dot B, the signal recovery is smaller, 12%, and the ESR linewidth is larger, 24 MHz. These resonances correspond to ESR because, first, for both dots the resonances occur at the known Zeeman frequencies, and second, no resonances were ever observed, with the rf source turned off.

For dot B, each ESR experiment yields the same resonance position, contrast and linewidth. This shows that for dot B the integration time permits ensemble averaging: slow fluctuations in B_N lead (as we show for dot A) to fluctuating resonance positions. We therefore analyze dot B using the steady state solution to the density matrix with Markovian decay dynamics, treating both optical and rf couplings non-perturbatively. The assumption is that over the course of the integration, the z -component of B_N averages to zero, and that the in-plane component can be taken as the root-mean-square (rms) value, $B_{N,xy}$. We consider 3 levels, $|\uparrow\rangle$, $|\downarrow\rangle$ and $|\uparrow\downarrow, \uparrow\rangle$ with a coherent optical coupling between $|\uparrow\rangle$ and $|\uparrow\downarrow, \uparrow\rangle$ with Rabi energy $\hbar\Omega_1$ and a coherent rf coupling between $|\uparrow\rangle$ and $|\downarrow\rangle$ (ESR) with Rabi energy $\hbar\Omega_{\mu\text{W}} = g_e\mu_B B_{\mu\text{W}}$ where μ_B is the Bohr magneton. The master equation includes decay terms: spontaneous radiative recombination from $|\uparrow\downarrow, \uparrow\rangle$ to $|\uparrow\rangle$ at rate Γ_s ; spontaneous radiative recombination from $|\uparrow\downarrow, \uparrow\rangle$ to $|\downarrow\rangle$ at rate γ_s ($\gamma_s \ll \Gamma_s$); and spin relaxation $|\uparrow\rangle \leftrightarrow |\downarrow\rangle$ at rate γ_e . The transmission signal depends on the optical susceptibility. Γ_s is known from the measured radiative decay rates on

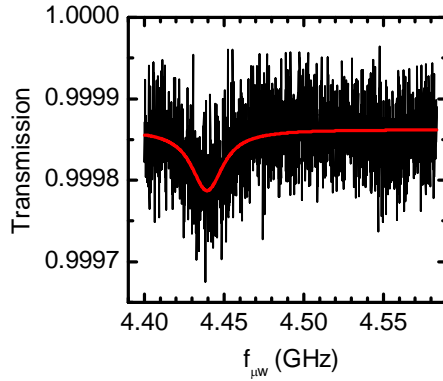


Figure 9.5: Optically detected spin resonance for dot B at 0.5 T. Optical transmission signal at zero optical detuning is plotted against microwave frequency, $f_{\mu W}$. The black line corresponds to the experimental data; the red line the theory. The theory uses parameters $\hbar\Gamma_s = 1.0 \mu\text{eV}$ (0.66 ns radiative decay time), $\gamma_s = 0.0008\Gamma_s$, $\hbar\gamma_e = 2.4 \text{ peV}$ ($T_1 = 0.27 \text{ ms}$), $\Omega_1 = 0.30 \mu\text{eV}$, $\Omega_{\mu W} = 0.36 \text{ neV}$ ($B_{\mu W} = 11 \mu\text{T}$, $g_e = -0.63$).

these dots and $\hbar\Omega_1$ is known from saturation curves of the optical resonance without spin pumping. The branching ratio γ_s/Γ_s depends on $B_{N,xy}$. For $B_{N,xy} \ll B_{\text{ext}}$, $\gamma_s/\Gamma_s = (B_{N,xy}/2B_{\text{ext}})^2 = 0.08\%$ with $B_{N,xy} = 28 \text{ mT}$ [13]. To fit the ESR, Fig. 9.5, we require $\hbar\gamma_e = 2.4 \text{ peV}$ ($T_1 = 0.27 \text{ ms}$, limited by cotunnelling) and $\hbar\Omega_{\mu W} = 0.36 \text{ neV}$ corresponding to $B_{\mu W} = 11 \mu\text{T}$ for $g_e = -0.63$. This $B_{\mu W}$ agrees reasonably with the rough estimate based on Fig. 9.1. Fig. 9.5 shows that we achieve an excellent fit to the ESR data. The theory shows that in general the ESR linewidth depends on both the optical and microwave couplings. In Fig. 9.5, the optical coupling makes the larger contribution, dephasing arising via spontaneous emission from the exciton. However, if $B_{\mu W}$ is increased by an order of magnitude, the theory predicts that the ESR signal on resonance will increase from 12% to close to 100% with an increase in the linewidth through power broadening of the ESR. Accessing this regime is clearly possible with a microscopic rather than a macroscopic antenna [9].

Dot A behaves differently to dot B: from run to run, the ESR frequency fluctuates by $\pm 150 \text{ MHz}$, Fig. 9.4, translating into a variation in magnetic field of $\pm 19 \text{ mT}$. The obvious culprit is the effective magnetic field from the nuclei: the fluctuations in resonance position correspond to the rms average of $B_{N,z}$ [13]. In dot A therefore, fluctuations in $B_{N,z}$ are slow relative to the measurement, unlike dot B. In fact for dot A where a V_G sweep was performed for each microwave frequency, Fig. 9.4 shows that $B_{N,z}$ must remain constant for tens of seconds. Remarkably, despite the difference in the nuclear field correlation time t_N ($t_N \gg 1 \text{ s}$ for dot A; $t_N \ll 1 \text{ s}$ for dot B), the optical properties of dots A and B are the same. The origin of the different t_N lies either in the differing strain fields in the two dots – strain influences the quadrupole interaction of each nucleus leading to position-dependent and nonequidistant nuclear Zeeman splittings [21] – or in differences in the electron tunnelling dynamics. t_N for dot A is reminiscent of bulk GaAs for which t_N is tens of seconds [22]; t_N for dot B

is consistent with the decay time of dynamic nuclear spin polarization in an InGaAs dot where, in the presence of an electron, decay times of \sim ms were determined [23].

9.6 Conclusion

The large ESR signals and narrow ESR linewidths are very striking for dot A, Fig. 9.4. It is impossible to reproduce the signal and linewidth with the 3-level model without reducing the optical power by an unrealistic factor of \sim 100. An assumption in the model must be broken for dot A. The experiment itself provides a clear pointer: in some cases, Fig. 9.4(d),(e),(f), the ESR has a strange lineshape, with hints that the ESR locks on to the rf driving field over a band of frequencies. There is therefore a back action of the nuclear spins on the electron spin; equivalently, the ESR cannot be described with a constant $B_{N,xy}$. We speculate that the cycle in the ESR detection, $|\downarrow\rangle \rightarrow |\uparrow\rangle \rightarrow |\uparrow\downarrow, \uparrow\rangle \rightarrow |\downarrow\rangle$, leads to some alignment of the nuclear field when t_N is large. A significant nuclear polarization is very difficult to achieve with resonant excitation [24, 25] and in fact can be ruled out as a large nuclear polarization would detune the dot from the laser. Instead, it is possible that our experiment aligns the residual field, B_N : when B_{ext} , $B_{N,z}$ and microwave frequency satisfy the ESR condition, B_N and the electron spin become aligned, at which point, $B_{N,xy} \rightarrow 0$, electron spin shelving becomes very slow and the full optical signal is recovered. In this picture, the ESR resonance fluctuates in frequency as the exact position depends on $B_{N,z}$ which is both random and long-lived for dot A. A theory treating the full electron *and* nuclear spin dynamics on an equal footing is required [26].

References

- [1] V. N. Golovach, A. Khaetskii, and D. Loss, *Phys. Rev. Lett.* **93**, 016601 (2004).
- [2] M. Kroutvar, Y. Ducommun, D. Heiss, M. Bichler, D. Schuh, G. Abstreiter, and J. J. Finley, *Nature* **432**, 81 (2004).
- [3] J. M. Elzerman, R. Hanson, L. H. Willems van Beveren, B. Witkamp, L. M. K. Vandersypen, and L. P. Kouwenhoven, *Nature* **430**, 431 (2004).
- [4] D. Loss and D. P. DiVincenzo, *Phys. Rev. A* **57**, 120 (1998).
- [5] S. Amasha, K. MacLean, I. P. Radu, D. M. Zumbuhl, M. A. Kastner, M. P. Hanson, A. C. Gossard, [arXiv:cond-mat/0607110](https://arxiv.org/abs/cond-mat/0607110) and *Phys. Rev. Lett.* **100**, 046803 (2008).
- [6] J. R. Petta, A. C. Johnson, J. M. Taylor, E. A. Laird, A. Yacoby, M. D. Lukin, C. M. Marcus, M. P. Hanson, and A. C. Gossard, *Science* **309**, 2180 (2005).
- [7] A. Greilich, D. R. Yakovlev, A. Shabaev, Al. L. Efros, I. A. Yugova, R. Oulton, V. Stavarache, D. Reuter, A. Wieck, and M. Bayer, *Science* **313**, 341 (2006).
- [8] M. H. Mikkelsen, J. Berezovsky, N. G. Stoltz, L. A. Coldren, and D. D. Awschalom, *Nature Physics* **3**, 770 (2007).
- [9] F. H. L. Koppens, C. Buizert, K. J. Tielrooij, I. T. Vink, K. C. Nowack, T. Meunier, L. P. Kouwenhoven, and L. M. K. Vandersypen, *Nature* **442**, 766 (2006).
- [10] F. Jelezko, T. Gaebel, I. Popa, A. Gruber, and J. Wrachtrup, *Phys. Rev. Lett.* **92**, 076401 (2004).
- [11] M. Atatüre, J. Dreiser, A. Badolato, A. Högele, K. Karrai, and A. Imamoglu, *Science* **312**, 551 (2006).
- [12] M. Kroner, S. Seidl, B. D. Gerardot, B. Biedermann, A. Badolato, P. M. Petroff, K. Karrai, and R. J. Warburton, *Int. J. Mod. Phys. B* **21**, 1307 (2007).

- [13] J. Dreiser, M. Atatüre, C. Galland, T. Müller, A. Badolato, and A. Imamoglu, *Phys. Rev. B* **77**, 075317 (2008).
- [14] J. Brossel and A. Kastler, *Compt. Rend.* **229**, 1213 (1949).
- [15] R. J. Warburton, C. Schäfflein, D. Haft, F. Bickel, A. Lorke, K. Karrai, J. M. Garcia, W. Schoenfeld, and P. M. Petroff, *Nature* **405**, 926 (2000).
- [16] S. Seidl, M. Kroner, P. A. Dalgarno, J. M. Smith, A. Högele, M. Ediger, B. D. Gerardot, J. M. Garcia, P. M. Petroff, K. Karrai, and R. J. Warburton, *Phys. Rev. B* **72**, 195339 (2005).
- [17] A. Högele, S. Seidl, M. Kroner, K. Karrai, R. J. Warburton, B. D. Gerardot and P. M. Petroff, *Phys. Rev. Lett.* **93**, 217401 (2004).
- [18] I. A. Merkulov, A. L. Efros, and M. Rosen, *Phys. Rev. B* **65**, 205309 (2002).
- [19] J. M. Smith, P. A. Dalgarno, R. J. Warburton, A. O. Govorov, K. Karrai, B. D. Gerardot, and P. M. Petroff, *Phys. Rev. Lett.* **94**, 197402 (2005).
- [20] T. P. Alegre, F. G. Hernández, A. L. Pereira, and G. Medeiros-Ribeiro, *Phys. Rev. Lett.* **97**, 236402 (2006).
- [21] R. I. Dzhioev and V. L. Korenev, *Phys. Rev. Lett.* **99**, 037401 (2007).
- [22] D. Paget, *Phys. Rev. B* **25**, 4444 (1982).
- [23] P. Maletinsky, A. Badolato, and A. Imamoglu, *Phys. Rev. Lett.* **99**, 056804 (2007).
- [24] A. Imamoglu, E. Knill, L. Tian, and P. Zoller, *Phys. Rev. Lett.* **91**, 017402 (2003).
- [25] H. Christ, J. I. Cirac, and G. Giedke, *Phys. Rev. B* **75**, 155324 (2007).
- [26] J. Danon and Y. V. Nazarov, *Phys. Rev. Lett.* **100**, 056603 (2008).

Chapter 10

Optical pumping and probing of holes

We present high resolution laser spectroscopy on a single self-assembled InGaAs quantum dot (QD) charged with a single hole. The QD is embedded in a n-type field effect device which allows controlled charging of the dot with electrons via tunnelling from an electron reservoir. To charge the dot with a single hole a pump laser is used so that photo generated holes are captured in the dot. This allows us to perform resonant high resolution laser spectroscopy on the same quantum dot charged with one single electron, hole or completely free of charges. The hole life time was measured in a time resolved pump and probe experiment.

10.1 Introduction

The sharp, atom like, optical resonances that were observed on semiconductor self-assembled quantum dots (QD), lead to their designation as “artificial atoms” [1, 2]. The key features of these QDs that stand in contrast to atoms are given by their solid state nature. So especially no electrostatic or optical traps are necessary to study single QDs and they can easily be incorporated into conventional electronic or optoelectronic devices. The most common semiconductor device, which is used to control the optical properties of self-assembled quantum dots so far, is a field effect device [3]. It can be used to charge the QD in a controlled way with single electrons [3, 4, 5, 6, 7], or holes [8] and to change the resonance energy of the excitonic transitions via the quantum confined Stark effect [4, 7, 8]. In these systems the QDs are charged by a charge carrier (electrons [4] or holes [8]) injection from either a negative (n-type) or positive (p-type) doped back contact that is usually separated from the QD layer by a few tens of nanometers of intrinsic GaAs. The ground state of a singly charged QD is of particular interest for the implementation of quantum information processing schemes in solid state systems, since it is spin qubit [9]. Initialization of a single electron spin in a QD via optical pumping has been demonstrated [10, 11] and recently also hole spin initialization was shown on a QD charged with holes via tunnelling from a reservoir [12]. Because of their valence band nature and hence suppressed interaction with nuclear spins, hole spins are expected to have even longer spin live times than electrons. The spin lifetime of the ground state is in principle limited by cotunnelling between carriers in the QD and the reservoir because in a field effect device the charge is provided by a reservoir in tunnel interaction with the QD. Increasing the tunnel barrier reduces the cotunnelling spin flip rate, but at the same time also slows down the charging dynamics of the QD. In this letter, we explore the possibility of creating a charged ground state in a QD that is not tunnel coupled to a reservoir with the prospect of increasing the spin lifetime.

10.2 Optical pumping of holes

The sample structure consists of a single layer of self-assembled InGaAs QDs, emitting around 950 nm wavelength. 25 nm below the QD-layer an n-doped back contact acts as an electron reservoir from which the QD can be charged with single electrons [3]. On the surface of the sample, 251 nm above the QD-layer, a semitransparent metallic (NiCr) top gate was deposited, to apply an electric field to the QD device. Between QD-layer and the surface an AlAs/GaAs superlattice acts as a blocking barrier preventing a current flow in the sample. The blocking barrier is separated by 10 nm i-GaAs from the QD-layer as shown in Fig. 10.1(b) and (c). Due to this short distance, the 2-dim valence band hole sub-bands that are being formed by the triangular potential well of the hetero-structure, are shifted out of resonance with

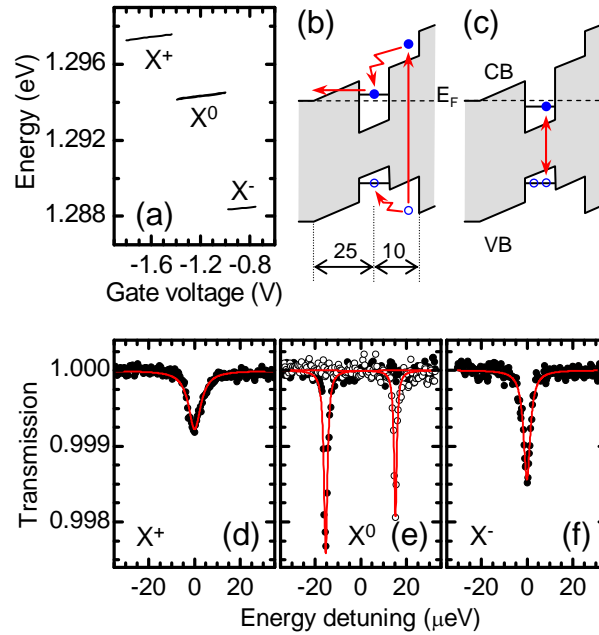


Figure 10.1: (a) Charging diagram of a single QD. The resonance energies of the X^{1+} , X^0 and X^{1-} are plotted as a function of the gate voltage. In (b) and (c) the potential landscape of the conduction band (CB) and valence band (VB) of the sample in growth direction is sketched to illustrate the optical charging of the QD. In (a) the non-resonant created exciton is captured, followed by the ionization of the dot by the electric field. In the experiment the excitation takes place into the wetting-layer. The distances of the QD-layer from the back contact and the blocking barrier are given in nm. The resonant pumping of the X^{1+} -transition is depicted in (c). The electronic level of the QD is shifted below the Fermi energy (E_F) by the electron - hole Coulomb interaction, resulting in a stable X^{1+} -state. (d) - (f) transmission spectra of the X^{1+} , X^0 and X^{1-} as a function of the energy detuning. The lines are Lorentzian fits to the data. In (e) the black dots and open circles depict measurements with two orthogonal linear polarizations of the laser field, allowing to distinguish the fine structure resonances.

the QD hole state [7, 13, 14]. This prohibits hole tunnelling out of the QD and allows optical generation of holes in the QD [15]. To perform resonant laser spectroscopy on the positively charged QD, a second laser-field is required to create the positive charge. We achieve this in two different ways. One is to have a laser resonant with the neutral exciton transition creating an exciton in the dot. The other possibility is to pump non-resonantly into the wetting layer, as it is done for PL measurements. This also creates an exciton in the QD. In both cases an electric field is applied to the sample such that the exciton is ionized. The electron tunnels from the dot into the back contact, while the hole remains trapped in the dot. A second laser field can then resonantly pump the the X^{1+} transition. The positive exciton state is stable in the QD for a certain gate voltage range as shown in Fig. 10.1(a), where the Coulomb attraction of the additional hole is sufficient to pull the electronic conduction band state of the QD below the fermi level (Fig.10.1(c)). This pump scheme is sketched in Fig. 10.1(b) and (c) for the case of non-resonant pumping. In Fig. 10.1(d)-(f),

resonances for the three charging states measured in transmission are plotted as a function of the energy detuning. In Fig. 10.1(e) the fine structure of the neutral exciton is clearly resolved allowing a doubtless assignment of the charge states [6]. The experiment was performed on a sample with a low QD density $\sim 1 \mu\text{m}^{-2}$. It was mounted in a fiber-based confocal microscope, with a diffraction-limited spatial resolution of $\sim 1 \mu\text{m}$. Hence, only one QD was in the focus of the objective, a necessary prerequisite to assign all observed lines to excitonic transitions of the same QD. The microscope was placed in a stainless steel tube, filled with a few mbar He exchange gas, immersed in a liquid He bath cryostat, to keep the sample at a constant temperature ~ 4.2 K. Below the sample, a Si-pin diode detects the transmitted light. Lock-In technique is used for noise reduction. The gate voltage is modulated with a square wave [6, 16]. To record a spectrum either the laser wavelength is scanned at a constant gate voltage, or the gate voltage is scanned shifting the excitonic resonance energy via the quantum confined Stark effect, while the laser wavelength is constant. For resonant laser spectroscopy of the X^{1+} exciton the resonance condition is twofold. For the gate voltage where the narrow band laser pumping the X^{1+} -transition, also the second laser has to be resonant with the X^0 -transition. Already small fluctuations of one of the two laser wavelengths lead to large fluctuations of the signal amplitude. For more reliable measurements, it turned out to be more practical to charge the QD with a hole by non-resonant pumping into the wetting-layer.

10.3 Power dependent hole lifetime

In Fig. 10.2 the amplitude of the transmission signal, as well as the PL signal of the X^{1+} are plotted as a function of the non-resonant pump power. The PL intensity of the signal increases with increasing pump power reaching a maximum at around $1 \mu\text{W}$. For larger powers, multi-excitons are created which lead to a decay of the signal. The resonant laser spectroscopy signal has a maximum at $\sim 0.1 \mu\text{W}$. The lower the pump power, the lower the probability of the QD being occupied with a hole. For larger pump powers, the QD will be more often occupied with a non-resonantly created X^{1+} , as suggested by the PL signal in this power range. We use a simple rate-equation description to describe the observed power dependency. The underlying three-level system is depicted by the inset in Fig. 10.2. The ground state is the empty QD $|0\rangle$. We assume that the creation of a hole in the QD $|h\rangle$ is a two step process. First a non-resonantly created exciton is captured by the dot with rate α (this is the rate of the exciton creation and the capture rate by the QD). Then the electron will tunnel out of the QD with a tunnelling rate $\gamma_{\text{tun}} = 1 - 5$ GHz. This rate can be deduced from linewidth measurements on samples with a large QD-layer to superlattice distance [7, 13]. The capture rate for an exciton in the wetting-layer is $\sim 20 - 200$ GHz [17]. In this simple model we assume the resonant laser to be a weak perturbation to the system. Hence, a significant population of

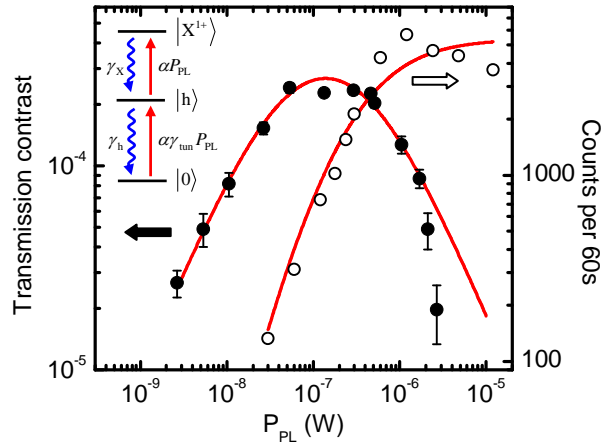


Figure 10.2: Transmission contrast (black dots) and PL intensity (open circles) of the X^{1+} -transition, as a function of the non-resonant pump power P_{PL} . The lines are fits to the data of rate equations describing the population of the $|h\rangle$ -state in case of the transmission contrast and the $|X^{1+}\rangle$ -state for the PL signal. The rates connecting the states of the underlying three-level system are depicted in the inset. γ_X and γ_h are the decay rates of the exciton and the hole respectively, while α stands for the filling rate of the QD with non-resonantly created excitons and γ_{tun} is the tunnel rate of the electron out of the QD.

the excited state, a QD occupied by a positively charged exciton $|X^{1+}\rangle$ can only be reached by capturing another non-resonantly created exciton, again with the rate α . The amplitude of the PL signal represents the occupation probability of the $|X^{1+}\rangle$ -state, while the resonant transmission contrast is given by the occupation probability of the $|h\rangle$ -state. The continuous line in Fig. 10.2 is a fit with $\gamma_X = 1$ GHz the spontaneous recombination rate of the excitonic state [18] and $\gamma_h = 10$ MHz the escape rate of the hole from the QD as fit parameter.

10.4 Conclusion

The ability to resonantly pump a X^{1+} exciton in a QD allows to perform optical spin shelving of the hole spin as shown recently by B. Gerardot *et al.* in [12]. Here we demonstrated the resonant pumping of an X^{1+} in a QD where the ground state, the QD charged with a single hole, was created optically. The QD device in use allows to charge the same QD with an electron or a hole. This opens the possibility to optically align the spin of an electron or a hole in the same QD and to study the spin dynamics of electrons and holes in the same QD meaning the same composition of In Ga and As as well as in the same strain field. Furthermore the hole spin lifetime in the used device is not limited by cotunnelling processes anymore, allowing in principle to enhance the already long hole spin lifetimes that were observed in QDs [12, 19].

References

- [1] P. Hawrylak. *Phys. Rev. B*, **60**, 5597, (1999).
- [2] J.-Y. Marzin, J.-M. Gérard, A. Izraël, and D. Barrier. *Phys. Rev. Lett.*, **73**, 716 (1994).
- [3] H. Drexler, D. Leonard, W. Hansen, J. P. Kotthaus and P. M. Petroff. *Phys. Rev. Lett.*, **73**, 2252 (1994).
- [4] R. J. Warburton, C. Schäfflein, K. Karrai, J. M. Garcia, W. Schoenfeld and P. M. Petroff. *Nature*, **405**, 926 (2000).
- [5] J. J. Finley, P. W. Fry, A. D. Ashmore, A. Lemaitre, A. I. Tartakovskii, R. Oulton, D. J. Mowbray, M. S. Skolnick, M. Hopkinson, P. D. Buckle, P. A. Maksym. *Phys. Rev. B*, **63**, 161305R (2001).
- [6] A. Högele, S. Seidl, M. Kroner, K. Karrai, R. J. Warburton, B. D. Gerardot and P. M. Petroff. *Phys. Rev. Lett.*, **93**, 217401 (2004).
- [7] S. Seidl, M. Kroner, P. A. Dalgarno, A. Högele, J. M. Smith, M. Ediger, B. D. Gerardot, J. M. Garcia, P. M. Petroff, K. Karrai, and R. J. Warburton. *Phys. Rev. B*, **72**, 195339 (2005).
- [8] J. J. Finley, M. Sabathil, P. Vogl, G. Abstreiter, R. Oulton, A. I. Tartakovskii, D. J. Mowbray, M. S. Skolnick, S. L. Liew, A. G. Cullis, and M. Hopkinson. *Phys. Rev. B*, **70**, 201308(R) (2004).
- [9] A. Imamoglu, D. D. Awschalom, G. Burkard, D. P. DiVincenzo, D. Loss, M. Sherwin, and A. Small *Phys. Rev. Lett.*, **83**, 4204 (1999).
- [10] M. Atatüre, J. Dreiser, A. Badolato, A. Högele, K. Karrai and A. Imamoglu, *Science* **312**, 551 (2006).
- [11] M. Kroner, S. Seidl, B. D. Gerardot, B. Biedermann, A. Badolato, P. M. Petroff, K. Karrai and R. J. Warburton, *Int. J. Mod. Phys. B* **21**, 1307 (2007).
- [12] B. D. Gerardot, D. Brunner, P. A. Dalgarno, P. Öhberg, S. Seidl, M. Kroner, K. Karrai, N. Stoltz, P. M. Petroff, and R. J. Warburton, *Nature* **451**, 441 (2008).

- [13] M. Kroner, A.Högele, S. Seidl, R. J. Warburton, B. D. Gerardot, A. Badolato, P. M. Petroff, and K. Karrai. *Physica E*, **32**, 61 (2006).
- [14] M. Kroner, A. O. Govorov, S. Remi, B. Biedermann, S. Seidl, A. Badolato, P. M. Petroff, W. Zhang, R. Barbour, B. D. Gerardot, R. J. Warburton, and K. Karrai, *Nature* **451**, 311 (2008).
- [15] M. Edinger, G. Bester, A. Badolato, P. M. Petroff, K. Karrai, A.Zunger, and R. J. Warburton. *Nature Physics*, **3**, 774 (2007).
- [16] B. Alén, F. Bickel, K. Karrai, R. J. Warburton, and P. M. Petroff. *Appl. Phys. Lett*, **83**, 2235 (2003).
- [17] S. Trumm, M. Wesseli, H. J. Krenner, D. Schuh, M. Bichler, J. J. Finley, and M. Betz. *Appl. Phys. Lett*, **87**, 153113 (2005).
- [18] *Private communication*
- [19] D. Heiss, S. Schaeck, H. Huebl, M. Bichler, G. Abstreiter, J.J. Finley, D.V. Bulaev, and Daniel Loss, *Phys. Rev. B*, **76**, 241306 (2007).

Chapter 11

Optically controlled hole spin lifetime in a optically charged quantum dot

We report optical hole spin initialization in a single quantum dot that was charged optically with a single hole. We perform resonant laser spectroscopy on the excitonic transition of a quantum dot as a function of its charge. By comparing the polarization dependent differential transmission signals of the negatively (X^{1-}) and positively (X^{1+}) charged exciton on the same quantum dot, we find hole spin initialization already at zero magnetic field to the extent of the purity of the circular polarization. With finite magnetic field we observe a spin polarization with a fidelity of up to 90%. By varying the intensity of the pump laser field that is used to charge the quantum dot non-resonantly with a single hole, we can control the hole spin lifetime in a range of 13 to 84 ns.

11.1 Introduction

Since the proposal of realizing quantum bits [1] utilizing the spin degree of freedom [2] of individual charge carriers, confined to solid state nano systems [3], a lot of progress has been made in understanding the basic properties of controlling spins in a solid state environment. It has been demonstrated that the spin of an electron can be prepared [4], read out [5, 6] and controlled [7, 8, 9]. However, in the low magnetic field limit the electron spin lifetime is finally limited by the hyperfine interaction with the nuclei of the host material of the quantum dot [10, 11, 12, 13]. This is due to the Bloch function of the electron in the conduction band, which is s-type and has therefore a maximum at the position of the nucleus. The hole has a p-type Bloch wave function with a node at the nucleus and hence strongly suppressed hyperfine interaction. This allows the optical alignment of the spin of a resident hole in a quantum dot even at zero magnetic field, as has been demonstrated recently [14]. In ref. [14], a self-assembled InGaAs quantum dot (QD) that was embedded in a field effect hetero-structure with a positively doped back contact, was charged with a hole via tunnelling.

Here we present a complementary approach to perform spin alignment in a self-assembled QD. In our case the QD layer is embedded in a standard n-doped field effect structure. In general, such a structure is designed to allow controlled charging of the dot with electrons only. The electrons tunnel into the dot from the reservoir of the back contact [15, 16, 17, 18, 19]. However, the specific structure under investigation was prepared such that the QD could be charged with a hole by optical

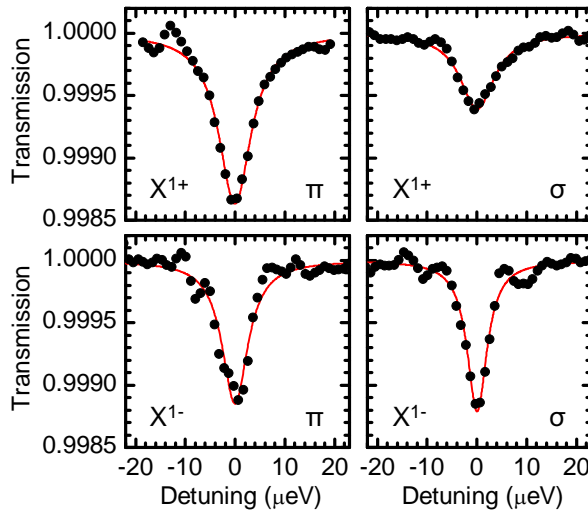


Figure 11.1: High resolution laser transmission spectra of the negatively (X^{1-}) and positively (X^{1+}) charged exciton in the same single QD at zero magnetic field. For the X^{1-} , the transmission contrast is independent of the polarization of the laser field, while for the X^{1+} the contrast is significantly lower for a circular polarization (σ) than for a linear polarization (π). This can be explained by spin shelving at zero magnetic field.

means. Therefor, an AlAs/GaAs superlattice was grown at a distance of only 10 nm above the QD layer. The AlAs/GaAs superlattice is necessary, to prevent current flow in the sample, from the top gate to the back contact. At the Interface of the GaAs capping layer that separates the QD layer from the superlatttice, a triangular potential well is formed in the valence band, yielding a two-dimensional hole sub-band [19]. Due to the short distance from the QD layer to the superlattice, the hole states in the QD are out of resonance with the lowest sub-band. This prohibits the hole in the QD to tunnel out of the dot even under strong bias [19]. Hereby the positive states of the QD can be optically excited, as has recently been demonstrated in photoluminescence [20] and in resonant, high resolution, laser spectroscopy [21]. The presented method allows in principle to optically align the spin of a hole or an electron in the same QD. Hence, the influence of the hyperfine interaction on the spin dynamics of the electron and the hole in the same environment can be studied.

11.2 Spin shelving of an optically created hole in a QD

The experiment is performed on a QD sample containing a single layer of InGaAs/GaAs QDs embedded in a n-doped field effect structure. The i-GaAs tunnelling barrier separating the QD layer from the back contact is 25 nm thick. An AlAs/GaAs superlattice was grown 10 nm above the QD layer to prevent hole tunnelling. 176 nm above the QD layer, on the sample surface, a 5 nm thick semi-transparent NiCr top gate electrode was evaporated. By applying a voltage to the top gate with respect to the back contact, the electronic conduction band levels in the QDs can be shifted with respect to the Fermi energy of the back contact. This allows a controlled charging of the dot with single electrons [16]. Furthermore, the electric field experienced by the QD induces an dc-Stark-effect that can be used to fine tune the excitonic resonance energy of the QD in situ. To charge the QD with a hole a bias is applied to the structure, at which the neutral excitonic state is not bound anymore, but the electron will tunnel out of the QD into the back contact, leaving behind a hole. We generate the hole by non-resonantly, optically pumping the wetting layer as for a PL experiment [21]. A tunable narrow band laser is tuned into resonance with the transition of the positively charged exciton (X^{1+}). The transmitted laser power is detected by a Si-photodiode and monitored as a function of the energy detuning between the laser and the excitonic transition. The sample and the photodiode are mounted in a fiber-based confocal microscope that is immersed in a liquid helium bath cryostat, operating at 4.2 K. For noise deduction lock-in technique is used [18, 22].

In Fig. 11.1 the transmission spectra of the negative and positive exciton is plotted as a function of the energy detuning. For both charging states the transmission signal was measured for circular and linearly polarized resonant laser excitation. The polarization of the non-resonant laser has no effect, since the spin information

of the excited electrons and holes is lost in the relaxation process. It is clear from the spectra that for the negative exciton the polarization makes no difference for the transmission contrast. This finding, we interpret in a way that the two spin states of the resident electron are equally populated and hence the transition is unpolarized. For the positive excitation the situation is different. Here, for perfect circular polarization one would expect to see no contrast in the transmission signal even at zero magnetic field [14]. This is because perfectly circularly polarized light only pumps one of the two possible transitions of the X^{1+} . In Fig. 11.2(a) the inset shows the schematic transitions of the X^{1+} . In the case of σ^- polarized light, the hole spin up ground-state \uparrow is coupled to the electron spin up state \uparrow . In the excited state the electron spin is exposed to the Overhauser field; the magnetic field generated by the magnetic moments of the nuclei. The magnitude of this field is of the order of a few mT [11, 12]. The electron spin will precess around the Overhauser field which will have a non-zero component (B_N^{xy}) perpendicular to the QD growth direction. This leads to an oscillation of the occupancy of the two excited states, $|\uparrow\downarrow\uparrow\rangle$ and $|\uparrow\downarrow\downarrow\rangle$. The limited lifetime of the excited state of the order of ≈ 1 ns will lead to a decay into the hole spin up ground state. The vanishing hyperfine interaction of the hole spin with the nuclei leads to a long lifetime of the hole in this spin state. Similar to the electron spin pumping scheme, as presented in [4],

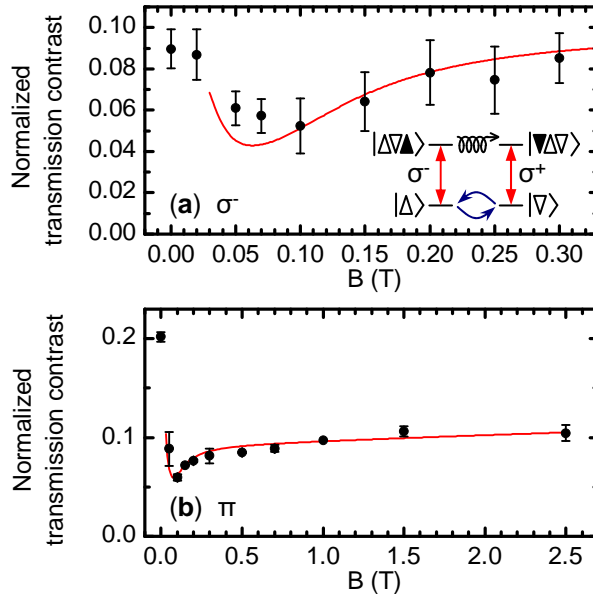


Figure 11.2: Normalized transmission contrast $\Delta T(B)/2\Delta T(B = 0)$ versus the applied magnetic field B for two different polarizations (σ^- (a) and π (b)). The line is a fit of the theory to the data as explained in the text. The inset shows the level scheme of the X^{1+} at zero magnetic field. The ground and excited states are coupled via a σ^+ or σ^- polarized light field. The spin of the photogenerated electron will precess around the Overhauser field, which will lead to spin shelving into the hole spin down state for pure σ^- optical pumping and into the spin up state for σ^+ pumping. The hole spin lifetime is limited by the non-resonant exciton generation rate.

the described process leads to an optical pumping of the hole spin, and hence to a vanishing transmission contrast of the pumped optical σ^- transition. If, however, the polarization of the resonant laser field is not perfectly circular, the same laser field will “repump” the hole spin with the ratio of the power of the two circular polarization components of the laser field [14, 4]. In our case the fiber-based setup scrambles the polarization of the laser field, and it is very challenging to feed a laser field with an arbitrary polarization into the fiber that will leave the fiber with a perfect circular polarization. We can only use the QD response itself to measure the degree of polarization and the signal to noise ratio limits the resolution to a ratio of σ^+/σ^- in this case to $1/5$. In Fig. 11.1 the remaining signal for circular polarization of the X^{1+} is due to this imperfection of the circular polarization.

By applying a magnetic field in growth direction to the QD the ground and excited states are split by the Zeeman energy $E_{Z,e,h} = g_{e,h}\mu_B B$. This energy lifts the degeneracy of the two optical transitions. Hence, the optical repump of the signal is decreased, due to the imperfect laser field polarization [14]. In Fig. 11.2 (a) the amplitude of transmission contrast for the circular excitation is plotted as a function of the magnetic field. The contrast is normalized to the maximum contrast at low power [23] that would correspond to a 100 % occupancy of the hole spin up ground state $|\uparrow\rangle$. For equal occupancy the normalized transmission contrast would be 0.5. The normalized transmission contrast shows a minimum for a magnetic field of ≈ 100 mT due to the reduced repump. For a larger magnetic field the signal recovers because the Zeeman splitting of the electronic levels reduces the hyperfine interaction. The line is a fit to the data with the theory based on the optical Bloch equations for two coupled two level systems, as described in detail in ref. [14]. To fit the data the parameters were chosen as follows. The perpendicular component of the Overhauser field $B_N^{xy} = 46$ mT. The Rabi energy for the optical transitions where: $\hbar\Omega_{\sigma^-} = 3.8 \mu\text{eV}$, $\hbar\Omega_{\sigma^+} = 1.6 \mu\text{eV}$. The g-factors for the electron and hole where $g_e = -0.66$ and $g_h = -1.32$ corresponding to optical measurements as reported in ref. [9]. The electron precession frequency in the excited state is assumed to be $\hbar\Omega_N = 0.2 \mu\text{eV}$, leading to a hole spin lifetime $T_1^h = 16$ ns. For linearly polarized resonant excitation, the normalized transmission contrast is plotted in Fig. 11.2 (b). Again the line is a fit to the data using the same parameters as before only that now $\hbar\Omega_{\sigma^-} = \hbar\Omega_{\sigma^+} = 2.7 \mu\text{T}$, as expected for linearly polarized light. It has to be stated that the spectra that were calculated with the above mentioned theory, did not reproduce the measured spectra at low magnetic fields ($B < 30$ mT). Therefore, we apply the theory only to the data at a magnetic field $B < 30$ mT. For the linear polarization we see again a reduction of the transmission contrast for a small magnetic field ≈ 100 mT, which arises from the energy detuning of the two optical transitions and hence to a more efficient optical spin pumping, with respect to the zero field situation.

11.3 Laser power dependent hole spin lifetime

The highest spin initialization fidelity that we measure for circularly polarized excitation light is 90% at $B = 100$ mT. All the presented measurements are performed with a resonant excitation power of $P_{\text{res}} = 10$ nW, and a non-resonant laser power $P_{\text{PL}} = 30$ nW to achieve a maximum signal to noise ratio. In Fig. 11.3(a) the differential transmission contrast ($\Delta T/T$) is plotted for a linear resonant excitation as a function of the non-resonant laser power P_{PL} . For zero external magnetic field the signal can be described by a simple rate equation formalism [21]. At $B = 150$ mT we measure a reduced signal whose power dependence can not be explained by the rate equation model anymore. The ratio of the transmission contrast with finite and zero magnetic field is plotted in Fig. 11.3(b). For a decreasing laser power we see that the ratio of the signal increases. We explain this behavior by the increasing hole spin lifetime with decreasing non-resonant laser power. The non-resonant excitation creates electrons and holes with undefined spin that will relax into the QD, leading to an equal population of the two excited states ($|\uparrow\downarrow\uparrow\rangle$ and $|\uparrow\downarrow\downarrow\rangle$) and hence, after recombination to an equal population of the two ground states ($|\uparrow\rangle$ and $|\downarrow\rangle$). For a theoretical analysis we assume that the rate at which excitons are created non-resonantly in the QD depends linearly on the non-resonant laser power (obtained from the rate equations to be 5.5 MHz/nW). Hence, the hole spin

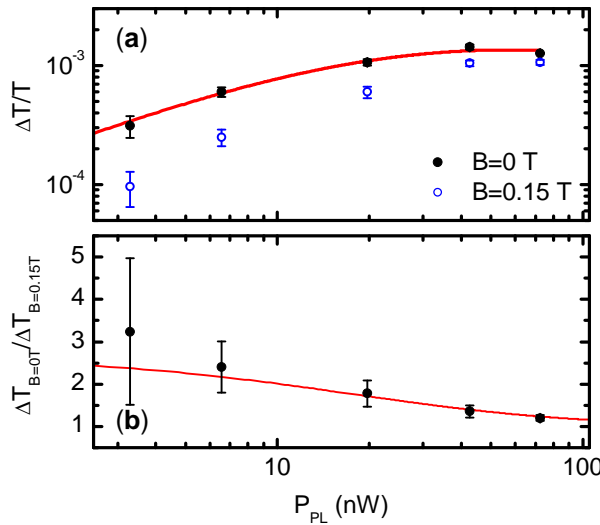


Figure 11.3: (a) Transmission contrast is plotted as function of the non-resonant laser power (P_{PL}), at finite magnetic field (open circles) and zero magnetic field (dots). For zero field the power dependence can be explained by simple rate equations [21]. In (b) the ratio of the transmission contrast with and without magnetic field is plotted as a function of the non-resonant laser power P_{PL} . The decrease in the ratio corresponds to a reduced hole spin lifetime with increasing pump power. The solid line shows the predictions for the ratio of the transmission contrast predicted by the optical Bloch equations model, with the assumption of a linear dependence of the hole spin lifetime on P_{PL} .

lifetime depends linearly on P_{PL} . The line in Fig. 11.3 (b) is the calculated ratio using the theoretical model from [14] with the same parameters as before. Except that the hole spin lifetime is now varied as a linear function of P_{PL} from $T_1^{\text{h}} = 13$ ns to $T_1^{\text{h}} = 84$ ns.

11.4 Conclusion

Compared to the results presented in [14] the measured hole spin lifetimes are three to four orders of magnitude smaller. A finding which we attribute to the non-resonant creation of excitons. Using resonant pumping of the neutral exciton to create a positively charged QD, in principle the hole spin could be prepared as well. This might lead to strongly enhanced hole spin lifetimes [21]. The corresponding theme remains under investigation. In general the presented way to create a hole in a QD and align its spin allows to study electron and hole spin relaxation processes in the very same QD. Especially the influence of the hyperfine interaction on the spin decay of an electron or a hole in a QD can be studied in more detail, when the influence of different QD hetero-structures on the spin dynamics like the strain-field, can be excluded.

References

- [1] D. P. DiVincenzo, *Fortschr. Phys.*, **48**, 771-783 (2000).
- [2] A. Imamoglu, D. D. Awschalom, G. Burkard, D. P. DiVincenzo, D. Loss, M. Sherwin, and A. Small, *Phys. Rev. Lett.*, **83**, 4204 (1999).
- [3] D. Loss, D. P. DiVincenzo, *Phys. Rev. A*, **57**, 120 (1998).
- [4] M. Atatüre, A. Badolato, A. Högele, J. Dreiser, K. Karrai, and A. Imamoglu, *Science*, **312**, 551 (2006).
- [5] J. M. Elzerman, R. Hanson, L. H. Willems van Beveren, B. Witkamp, L. M. K. Vandersypen, and L. P. Kouwenhoven, *Nature*, **430**, 431 (2004).
- [6] M. H. Mikkelsen, J. Berezovsky, N. G. Stoltz, L. A. Coldren, and D. D. Awschalom, *Nature physics*, **3**, 770 (2007).
- [7] F. H. L. Koppens, C. Buizert, K. J. Tielrooij, I. T. Vink, K. C. Nowack, T. Meunier, L. P. Kouwenhoven, and L. M. K. Vandersypen, *Nature*, **442**, 766 (2006).
- [8] J. R. Petta, A. C. Johnson, J. M. Taylor, E. A. Laird, A. Yacoby, M. D. Lukin, C. M. Marcus, M. P. Hanson, and A. C. Gossard, *Science*, **309**, 2180 (2005).
- [9] M. Kroner, K. M. Weiss, B. Biedermann, S. Seidl, S. Manus, A. W. Holleitner, A. Badolato, P. M. Petroff, B. D. Gerardot, R. J. Warburton, and K. Karrai, *arXiv:0710.4901* (2007).
- [10] J. Dreiser, M. Atatüre, C. Galland, T. Müller, A. Badolato, and A. Imamoglu, *Phys. Rev. B* **77**, 075317 (2008).
- [11] A. V. Khaetskii, D. Loss, and L. Glazman, *Phys. Rev. Lett.*, **88**, 186802 (2002).
- [12] P. F. Braun, X. Marie, L. Lombez, B. Urbaszek, T. Amand, P. Renucci, V. K. Kalevich, K. V. Kavokin, O. Krebs, P. Voisin, and Y. Masumoto, *Phys. Rev. Lett.*, **94**, 116601 (2005).
- [13] P. Maletinsky, A. Badolato, and A. Imamoglu, *Phys. Rev. Lett.*, **99**, 056804 (2007).

- [14] B. Gerardot, D. Brunner, P. A. Dalgarno, P. Öhberg, S. Seidl, M. Kroner, K. Karrai, N. G. Stoltz, P. M. Petroff and R. J. Warburton, *Nature* **451**, 441 (2008).
- [15] H. Drexler, D. Leonard, W. Hansen, J. P. Kotthaus, and P. M. Petroff. *Phys. Rev. Lett.*, **73**, 2252 (1994).
- [16] R. J. Warburton, C. Schäflein, K. Karrai, J. M. Garcia, W. Schoenfeld, and P. M. Petroff. *Nature*, **405**, 926 (2000).
- [17] J. J. Finley, P. W. Fry, A. D. Ashmore, A. Lemaitre, A. I. Tartakovskii, R. Oulton, D. J. Mowbray, M. S. Skolnick, M. Hopkinson, P. D. Buckle, P. A. Maksym. *Phys. Rev. B*, **63**, 161305R (2001).
- [18] A. Högele, S. Seidl, M. Kroner, K. Karrai, R. J. Warburton, B. D. Gerardot, and P. M. Petroff. *Phys. Rev. Lett.*, **93**, 217401 (2004).
- [19] S. Seidl, M. Kroner, P. A. Dalgarno, A. Högele, J. M. Smith, M. Ediger, B. D. Gerardot, J. M. Garcia, P. M. Petroff, K. Karrai, and R. J. Warburton. *Phys. Rev. B*, **72**, 195339 (2005).
- [20] M. Edinger, G. Bester, A. Badolato, P. M. Petroff, K. Karrai, A. Zunger, and R. J. Warburton, *Nature physics*, **3**, 774 (2007).
- [21] M. Kroner, B. Biedermann, K. M. Weiss, C. Lux, S. Seidl, A. W. Holleitner, G. Fernandez, M. Atatüre, A. Imamoglu, A. Badolato, P. M. Petroff, R. J. Warburton, and K. Karrai, *to be published*.
- [22] B. Alén, F. Bickel, K. Karrai, R. J. Warburton, and P. M. Petroff. *Appl. Phys. Lett*, **83**, 2235 (2003).
- [23] M. Kroner, S. Rémi, A. Högele, S. Seidl, A. W. Holleitner, R. J. Warburton, B. D. Gerardot, P. M. Petroff, and K. Karrai. *Physica E* (2007), doi:10.1016/j.physe.2007.09.1

Summary and perspectives

In the frame work of this theses, optical transitions of single self-assembled quantum dots have been studied by high resolution resonant laser spectroscopy [1]. The quantum dots are embedded in a solid state heterostructure that strongly influences their physical properties. Common to all devices is the possibility to charge the quantum dot with single electrons in a controlled way [2, 3]. Therefor the quantum dot layer is incorporated into a field effect structure formed by a highly n-doped back contact and a metallic top gate on the sample surface [4]. The quantum dot was studied by resonant laser absorption spectroscopy in transmission [1, 5, 6, 7]. The sample is mounted in a diffraction-limited microscope that was described in detail in chapter 2. The microscope was designed such that it operates at the cryogenic temperature of liquid helium and a magnetic field of up to 9 T [P17]. Different microscope geometries have been used to apply the magnetic field parallel or perpendicular to the light propagation direction, in so called Faraday or in Voigt geometry.

In power dependent resonant laser spectroscopy experiments the two-level nature of a single quantum dot was investigated [8, P10]. Saturation of the transmission contrast and power broadening of the resonance line was analyzed yielding the contribution of radiative decay, dephasing and spectral fluctuations to the homogenous linewidth of an excitonic transition in a quantum dot. Introducing a second laser, a probe laser, to the experimental setup, led to the observation of Rabi splitting and the ac-Stark effect. A polarization sensitive detection optics allowed to pump and probe the very same excitonic transition in a quantum dot with two cross polarized laser beams, and to distinguish the signal of the two lasers [7, P15].

In one sample structure a two-dimensional continuum of states was introduced in the vicinity of the quantum dot layer [9, 10]. This led to the observation of a gate voltage controllable tunnel coupling of the holes in the quantum dot to the two-dimensional continuum states [P7]. The tunnel energy can be rather small - much smaller than the energy uncertainty associated to the radiative decay of the excitonic state. Still a signature of the tunnel coupling of the excited state of the discrete exciton state to the continuum of states was discovered, the nonlinear Fano effect [11, P13]. The two optical pathways that can lead from the ground state of the exciton to the two tunnel coupled excited states are distinguishable. One connecting two discrete states, the other one a discrete and a continuum state. For low excitation powers the continuum

transition, yielding a weak oscillator strength, is vanishing while the spectrum is dominated by the two level nature of the discrete transition. However, for increasing laser power the two-level transition saturates and the continuum transition becomes more and more pronounced leading to a stronger asymmetry of the resonance line, the characteristic Fano resonance [11]. The observation of the non-linear Fano effect in a quantum dot underlines their strong point over atoms, which is that the coupling strengths and transition rates in an artificial quantum system can be tailored for certain quantum optical experiments. Furthermore it emphasizes that even small couplings can lead to unmistakable effects in the optical spectra of quantum systems. To study the physical properties of a single spin in a quantum dot, a device was designed to reduce the tunnel coupling of the resident electron in the quantum dot to the back contact [12, 6]. Therefore the three dimensional back contact was replaced by a two-dimensional electron gas. This effectively reduced the tunnel coupling by a reduced density of states in the back contact. In a small magnetic field the spin of the resident electron was initialized by resonant optical pumping [6, P11, 13]. There, a dipole forbidden but in the reality of a solid state system weakly allowed optical transition was exploited. With a second laser the optical absorption of the weakly allowed transition was measured yielding the electron g-factor [P18]. Knowing the ground state Zeeman splitting, an optical detected single electron spin experiment was performed [P16]. The microscope was equipped with a microwave antenna to resonantly induce a spin flip of the initialized electron spin. We found that the electron spin dynamics are dominated by the interaction with the ensemble of nuclear magnetic moments of the atoms that form the quantum dot [14, 15, 16, 17]. Hence in this experiment the solid state nature of the quantum dot played a major role.

The spin of a hole in a quantum dot does not interact with the nuclear magnetic moment due to its p-like Bloch wave-function. This leads to significantly enhanced spin life and coherence times [18, P14]. For the realization of qubits for quantum information processing schemes this is of major importance.

A quantum dot was charged with a single hole by non-resonant optical pumping. Such an optical pumping of holes allows in general to investigate the spin dynamics of electrons and holes in the very same quantum dot. Again, spin initialization was performed by resonant optical pumping, yielding a significant fidelity even at zero magnetic field [P14]. However, in the presented experiments, the hole spin lifetime is limited by the non-resonant optical pumping. A pulsed experiment is probably feasible [19], which might lead to even longer spin lifetimes than observed in devices where the holes are charged into the quantum dot from a reservoir [P14]. In such tunnel coupled systems the spin lifetime is always limited by cotunnelling events [12, 13].

Pulsed experiments are in general highly desirable for future resonant pumping schemes. In the two color experiments that were performed on the lambda-system formed by a negatively charged exciton in a quantum dot with a magnetic field applied in Voigt geometry (chapter 8) [P18] the possibility to create coherent super-

position of the two ground states was investigated. In the presented experiments the coherence time of the electron was not sufficient to observe the coherent population trapping (CPT) in the dark superposition of the ground states [20, 21]. However, this might very well be observable on a different quantum dot [P18]. If CPT can be reached, more sophisticated pump schemes from quantum optics can be envisioned for quantum dots. In a pulse train laser experiment coherent optical spin manipulation via stimulated Raman by adiabatic passage (STIRAP) is a promising step towards optical qubits in a solid state system [22, 23]. For such an experiment a pulse width as short as ≈ 20 ns are expected to be sufficient. This kind of pulses do not require a pulsed laser system but they can be generated by an acusto-optical modulator [24], this would be a simple way to introduce time resolution into the resonant Rayleigh scattering experiment.

Another experiment that requires time resolution is a pulsed electron spin resonance experiment [25]. In chapter 9 a continuous-wave optical detected electron spin resonance experiment was described [P16]. With a pulsed readout, manipulation and initialization the electron spin could be positioned arbitrarily on the Bloch-sphere as recently demonstrated by Koppens *et al.* in transport experiments [25]. This would allow a direct access to the dephasing time of the spin of a single electron in a quantum dot. Before such an experiment can be performed the electron spin interaction with the nuclear magnetic moments has to be understood [15, 26]. In chapter 9 we showed that the electron spin dynamics in a quantum dot are strongly dominated by the dynamics of the magnetic moment of the nuclei that form the quantum dot. The anisotropic strain distribution in the quantum dot is responsible for a complex behavior of the nuclear spins [27]. The quantum dot acts here as a local probe to gain insight into the rich physics of semiconductor nanostructures [28].

The non-linear Fano effect that was pioneered in this work and described in chapter 7 represents a step towards a coherent coupling of a discrete state and a continuum of states in a solid. In case of the Fano effect the coupling took place between a quantum dot state and an empty continuum of states. If the spin degree of freedom of an electron or an exciton in a quantum dot was coupled to a filled continuum of states the Kondo effect could be observable [29, 30, 31]. Here finally nano technology would demonstrate again its universality by making the Kondo effect, originating from the physics of condensed matter, accessible by the quantum optical means of coherent laser spectroscopy and thereby guaranteeing a rich and unexplored field of physics.

References

- [1] A. Högele, S. Seidl, M. Kroner, K. Karrai, R.J. Warburton, B.D. Gerardot, P.M. Petroff, *Phys. Rev. Lett.* **93**, 217401 (2004).
- [2] R.J. Warburton, C. Schäflein, D. Haft, F. Bickel, A. Lorke, K. Karrai, J.M. García, W. Schoenfeld, and P. M. Petroff, *Nature* **405**, 926 (2000).
- [3] J.J. Finley, A.D. Ashmore, A. Lemaître, D.J. Mowbray, M.S. Skolnick, I.E. Itskevich, P.A. Maksym, M. Hopkinson, and T.F. Krauss, *Phys. Rev. B* **63**, 073307 (2001).
- [4] H. Drexler, D. Leonard, W. Hansen, J.P. Kotthaus, and P.M. Petroff, *Phys. Rev. Lett.* **73**, 2252 (1994).
- [5] B. Alèn, F. Bickel, R.J. Warburton, P.M. Petroff and K. Karrai, *Appl. Phys. Lett.* **83**, 112235, (2003).
- [6] M. Atatüre, J. Dreiser, A. Badolato, A. Högele, K. Karrai, and A. Imamoglu, *Science* **312** 551 (2006).
- [7] X. Xu, B. Sun, P.R. Berman, D.G. Steel, A.S. Bracker, D. Gammon, L.J. Sham. *Science*, **371**, 929 (2007).
- [8] A. Zrenner, E. Beham, S. Stuffer, F. Findeis, M. Bichler, and G. Abstreiter, *Nature* **418**, 612 (2002).
- [9] J.M. Smith, P.A. Dalgarno, B. Urbaszek, E.J. McGhee, G.S. Buller, G.J. Nott, R.J. Warburton, J.M. Garcia, W. Schoenfeld, and P.M. Petroff, *Appl. Phys. Lett.* **82**, 3761, (2003).
- [10] S. Lüttjohann, C. Meier, A. Lorke, D. Reuter and A.D. Wieck, *Appl. Phys. Lett.* **87**, 163117 (2005).
- [11] U. Fano, *Phys. Rev.*, **124**, 1866 (1961).
- [12] J.M. Smith, P.A. Dalgarno, R.J. Warburton, A.O. Govorov, K. Karrai, B.D. Gerardot and P.M. Petroff, *Phys. Rev. Lett.* **94**, 197402 (2005).
- [13] J. Dreiser, M. Atatüre, C. Galland, T. Müller, A. Badolato and A. Imamoglu, *Phys. Rev. B* **77**, 075317 (2008).

- [14] D. Paget, Phys. Rev. B **25**, 4444 (1982).
- [15] P. Maletinsky, A. Badolato, and A. Imamoglu, Phys. Rev. Lett. **99**, 056804 (2007).
- [16] H. Christ, J. I. Cirac, and G. Giedke, Phys. Rev. B **75**, 155324 (2007).
- [17] J. Danon and Y. V. Nazarov, Phys. Rev. Lett. **100**, 056603 (2008).
- [18] D. Heiss, S. Schaeck, H. Huebl, M. Bichler, G. Abstreiter, J.J. Finley, D.V. Bulaev, and Daniel Loss, Phys. Rev. B **76**, 241306 (2007).
- [19] G. Fernandez, A. Imamoglu, *private communication*.
- [20] K. J. Boller, A. Imamoglu and S. E. Harris, Phys. Rev. Lett. **66**, 2593 (1991).
- [21] M. Fleischhauer, A. Imamoglu, J. P. Marangos, Rev. Mod. Phys. **77**, 633 (2005).
- [22] J.R. Kuklinski, U. Gaubatz, F.T. Hioe, and K. Bergmann, Phys. Rev. A **40**, 6741 (1989).
- [23] J. Volz, M. Weber, D. Schlenk, W. Rosenfeld, J. Vrana, K. Saucke, C. Kurt-siefer, and H. Weinfurter, Phys. Rev. Lett. **96**, 030404 (2006).
- [24] J. Volz, H. Weinfurter, *private communication*.
- [25] F.H.L. Koppens, C. Buizert, K.J. Tielrooij, I.T. Vink, K.C. Nowack, T. Meunier, L.P. Kouwenhoven, and L.M.K. Vandersypen, Nature **442**, 766 (2006).
- [26] A.I. Tartakovskii, T. Wright, A. Russell, V.I. Fal'ko, A.B. Van'kov, J. Skiba-Szymanska, I. Drouzas, R.S. Kolodka, M.S. Skolnick, P.W. Fry, A. Tahraoui, H.-Y. Liu, and M. Hopkinson, Phys. Rev. Lett. **98**, 026806 (2007).
- [27] R.I. Dzhioev and V.L. Korenev, Phys. Rev. Lett. **99**, 037401 (2007).
- [28] K. Karrai, R.J. Warburton, C. Schulhauser, A. Högele, B. Urbaszek, E.J. McGhee, A.O. Govorov, J.M. Garcia, B.D. Gerardot, and P.M. Petroff, Nature **427**, 135 (2004).
- [29] L. Kouwenhoven and L. Glazman, *Revival of the Kondo effect*, Physics World, January 2001, 33-38 (2001).
- [30] A.O. Govorov, K. Karrai, and R.J. Warburton, Phys. Rev. B **67**, 241307 (2003).
- [31] R.W. Helmes, M. Sindel, L. Borda, and J. von Delft, Phys. Rev. B **72**, 125301 (2005).

List of publications

- [P1] A. Högele, S. Seidl, M. Kroner, K. Karrai, R. J. Warburton, B. D. Gerardot, and P. M. Petroff, *Voltage-Controlled Optics of a Quantum Dot*, Phys. Rev. Lett. **93**, 217401 (2004).
- [P2] A. Högele, M. Kroner, S. Seidl, K. Karrai, M. Atatüre, J. Dreiser, A. Imamoglu, R. J. Warburton, B. D. Gerardot, and P. M. Petroff, *Spin-selective optical absorption of singly charged excitons in a quantum dot*, Appl. Phys. Lett. **86**, 221905 (2005).
- [P3] A. Högele, S. Seidl, M. Kroner, K. Karrai, R. J. Warburton, M. Atatüre, J. Dreiser, A. Imamoglu, B. D. Gerardot, and P. M. Petroff, *Voltage-controlled electron-hole interaction in a single quantum dot*, Journ. of supercond. **18**, 245-249 (2005).
- [P4] S. Seidl, M. Kroner, P. A. Dalgarno, A. Högele, J. M. Smith, M. Ediger, B. D. Gerardot, J. M. Garcia, P. M. Petroff, K. Karrai, and R. J. Warburton, *Absorption and photoluminescence spectroscopy on a single self-assembled charge-tunable quantum dot*, Physical review B **72**, 195339 (2005).
- [P5] S. Seidl, A. Högele, M. Kroner, K. Karrai, A. Badolato, P.M. Petroff, R.J. Warburton, *Tuning the cross-gap transition energy of a quantum dot by uniaxial stress*, Physica E **32**, 14-16 (2006).
- [P6] S. Seidl, M. Kroner, A. Högele, K. Karrai, R. J. Warburton, A. Badolato, P. M. Petroff, *Effect of uniaxial stress on excitons in a self-assembled quantum dot*, Appl. Phys. Lett. **88**, 203113 (2006).
- [P7] M. Kroner, A. Högele, S. Seidl, R. J. Warburton, B. D. Gerardot, A. Badolato, P. M. Petroff, and K. Karrai, *Voltage-Controlled Linewidth of Excitonic Transitions in a Single Self-Assembled Quantum Dot*, Physica E **32**, 61-64 (2006).
- [P8] B. Alén, A. Högele, M. Kroner, S. Seidl, K. Karrai, R. J. Warburton, A. Badolato, G. Medeiros-Ribeiro, and P. M. Petroff, *Absorptive and dispersive optical responses of excitons in a single quantum dot*, Appl. Phys. Lett. **89**, 123124 (2006).

- [P9] S. Seidl, A. Högele, M. Kroner, K. Karrai, R. J. Warburton, J. M. Garcia, and P. M. Petroff, *Modulation spectroscopy on a single self assembled quantum dot*, Phys. Stat. Sol. (a) **204**, No. 2, 381 (2007).
- [P10] M. Kroner, S. Remi, A. Högele, S. Seidl, A. W. Holleitner, R. J. Warburton, B. D. Gerardot, P. M. Petroff, and K. Karrai, *Resonant saturation laser spectroscopy of a single self-assembled quantum dot* Physica E (2007), doi:10.1016/j.physe.2007.09.1
- [P11] M. Kroner, S. Seidl, B. D. Gerardot, B. Biedermann, A. Badolato, P. M. Petroff, K. Karrai, and R. J. Warburton, *Resonant interaction between a quantum dot and a narrow band laser: spectroscopy and optical pumping of a single spin*, Int. J. Mod. Phys. B **21**, 1307 (2007).
- [P12] B. D. Gerardot, S. Seidl, P. A. Dalgarno, M. Kroner, K. Karrai, A. Badolato, P. M. Petroff, R. J. Warburton, *Contrast in transmission spectroscopy of a single quantum dot*, Appl. Phys. Lett. **90**, 221106 (2007).
- [P13] M. Kroner, A. O. Govorov, S. Remi, B. Biedermann, S. Seidl, A. Badolato, P. M. Petroff, W. Zhang, R. Barbour, B. D. Gerardot, R. J. Warburton, and K. Karrai, *The nonlinear Fano effect*, Nature **451**, 311-314 (2008).
- [P14] B. D. Gerardot, D. Brunner, P. A. Dalgarno, P. Öhberg, S. Seidl, M. Kroner, K. Karrai, N. Stoltz, P. M. Petroff, and R. J. Warburton, *Optical pumping of a single hole spin in a quantum dot*, Nature **451**, 441-444 (2008).
- [P15] M. Kroner, C. Lux, S. Seidl, A. W. Holleitner, A. Badolato, P. M. Petroff, R. J. Warburton, and K. Karrai, *Rabi splitting and ac-Stark shift of a charged exciton*, Appl. Phys. Lett. **92**, 031108 (2008).
- [P16] M. Kroner, K. M. Weiss, B. Biedermann, S. Seidl, S. Manus, A. W. Holleitner, A. Badolato, P. M. Petroff, B. D. Gerardot, R. J. Warburton, and K. Karrai, *Optical detection of single electron spin resonance in a quantum dot*, Phys. Rev. Lett. **100**, 156803 (2008).
- [P17] A. Högele, S. Seidl, M. Kroner, K. Karrai, C. Schulhauser, O. Sqalli, J. Scrimgeour, and R. J. Warburton, *Fiber-based confocal microscope for cryogenic spectroscopy*, Rev. Sci. Instrum. **79**, 023709 (2008).
- [P18] M. Kroner, K. M. Weiss, B. Biedermann, S. Seidl, A. W. Holleitner, A. Badolato, P. M. Petroff, P. Öhberg, R. J. Warburton, and K. Karrai, *High-resolution, resonant two-color spectroscopy on a negatively charged exciton in a magnetic field*, in preparation.
- [P19] M. Kroner, B. Biedermann, K. M. Weiss, C. Lux, S. Seidl, A. W. Holleitner, G. Fernandez, M. Atatüre, A. Imamoglu, A. Badolato, P. M. Petroff, R. J. Warburton, and K. Karrai, *Optical pumping and probing of holes in a single quantum dot*, in preparation.

-
- [P20] M. Kroner, K. M. Weiss, S. Seidl, A. W. Holleitner, R. J. Warburton, A. Badolato, P. M. Petroff, and K. Karrai, *Optical controlled hole spin lifetime in a single, optically charged quantum dot*, in preparation.

Appendix A:

Theoretical treatment of a single QD coupled to a two-dimensional continuum of states

A.1 General description

The concept of Fano resonance is widely exploited in physics since it describes a physical situation often appearing in a variety of atoms, molecules, and solid-state systems. It is not surprising that the original paper by Fano [1] has been so heavily used in many research fields. The situation leading to the Fano interference involves three sorts of states: the ground state $|0\rangle$, an excited state with a discrete energy level $|1\rangle$, and an infinite collection of extended states $|k\rangle$ (i.e. a continuum of states). Imagine now that these states are somehow coupled (Fig. A.1(a)). Two of the couplings, $|0\rangle \rightarrow |1\rangle$ and $|0\rangle \rightarrow |k\rangle$, are optically induced and the coupling $|1\rangle \leftrightarrow |k\rangle$ appears due to an intrinsic interaction in the system. Such an intrinsic interaction may be an instability due to Auger auto-ionization [1], tunnelling (Fig. 7.1(d) in chapter 7), energy transfer [2], etc. Then, if we look at the process of absorption of incident photons, we can see that the system can move to a particular state $|k\rangle$ in two ways: (a) $|0\rangle \rightarrow |k\rangle$ and (b) $|0\rangle \rightarrow |1\rangle$ (Fig. A.1). In quantum mechanics, the amplitudes of two paths, (a) and (b), must be added and the resultant sum must be squared to obtain the net probability of absorption: $P \propto |A_a A_b|^2$. Since the quantum amplitudes of paths (A_a and A_b) can be positive or negative, the probability of the process can be enhanced or suppressed, depending on the signs of the amplitudes. For the Fano scheme, it turns out that the amplitude A_b can change sign as a function of the photon energy! This means that the processes (a) and (b) can suppress or enhance each other, depending on the excitation photon energy. In other words, constructive or destructive interference can take place (Fig. A.1(b)). Using first-order perturbation theory, we can write: $P \propto \left| v + \frac{V_0 w}{\hbar\omega_{\text{laser}} - E_{10}} \right|^2$, where v , w and V_0 are the matrix elements of transitions, defined below in Fig. A.2 and $E_{10} = E_1 - E_0$ is the resonance energy of the transition $|0\rangle \rightarrow |1\rangle$. Of

THIS CHAPTER RESULTS FROM THE CLOSE AND FRUITFUL COLLABORATION WITH A. O. GOVOROV AND W. ZHANG (OHIO UNIVERSITY, ATHENS, USA), AND IS PUBLISHED AS SUPPLEMENTARY MATERIAL TO [P18]

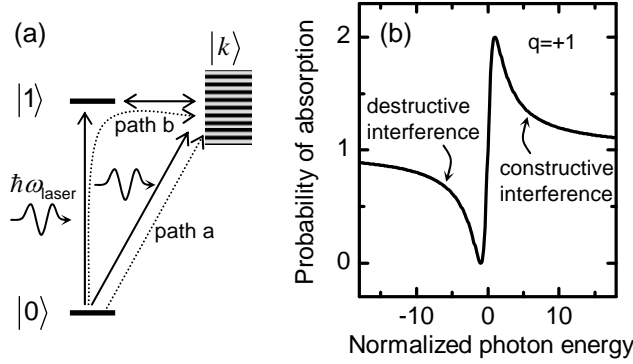


Figure A.1: (a) The scheme of transitions in the Fano effect. (b) The probability of photon absorption as a function of the normalized photon energy $(\hbar\omega_{\text{laser}} - E_{01})/\Delta$, where Δ is the broadening of the level due to the coupling to the continuum.

course, the above equation is not exact and has problems (infinity at $\hbar\omega_{\text{laser}} = E_{01}$). Nevertheless, the above equation is able to reproduce the effect qualitatively. If $V_0 w/v > 0$, the probability is suppressed below the resonance ($\hbar\omega_{\text{laser}} < E_{01}$) and enhanced above the resonance energy ($\hbar\omega_{\text{laser}} > E_{01}$). The exact solution of the linear Fano absorption has the form [1]:

$$P \propto \frac{(\delta E + q\Delta)^2}{\delta E^2 + \Delta^2}, \quad (\text{A.1})$$

where $\delta E = \hbar\omega_{\text{laser}} - E_{01}$ is the detuning from the resonance. In this equation, the q-factor “controls” the strength of the interference effect. Historically, the Fano resonance was derived first for the experiments on scattering of electrons by helium atoms [1]. This classic case is the $1s^2 \rightarrow 2s^1 2p^1$ transition at 60.1 eV of the He atom. This doubly-excited state ($2s^1 2p^1$) undergoes auto-ionization: one electron returns to the 1s state and the other is ejected into the continuum (Fig. 7.1(a) in chapter 7). If we now describe the Fano effect in the helium atom with the scheme of Fig. A.1, we should say the following. The excited level $|1\rangle$ depicts the state $2s^1 2p^1$, the levels $|k\rangle$ represent a continuum of states $1s^1 k^1$, and the coupling $|1\rangle \leftrightarrow |k\rangle$ occurs owing to Auger processes.

A.2 Nonlinear Fano effect

The nonlinear Fano effect, like the linear effect, can appear in many systems. Here, it was demonstrated for self-assembled quantum dots. In the theoretical paper [2], a similar effect was calculated for colloidal nano-particles coupled by the Coulomb interaction. Our theory indicates that the nonlinear Fano effect can also appear in atomic and solid-state systems undergoing Auger ionization. A really striking property of the nonlinear Fano effect is that it allows the observation of very weak

interactions that are usually invisible. Mathematically, the optical absorbed power is derived, starting from the equation of motion of the density matrix:

$$\frac{\partial \hat{\rho}}{\partial t} = \frac{i}{\hbar} \left[\hat{\rho}, \hat{H}_0 + \hat{V}(t) \right] + \hat{\Gamma} \hat{\rho}, \quad (\text{A.2})$$

where the operator $\hat{V}(t) = -erE_0 \cos \omega t$ describes the light-matter interaction. The term $\hat{\Gamma} \hat{\rho}$ introduces relaxation processes in the system. After solving equation A.2 for the optical and relaxation processes shown in Fig. 7.1 in chapter 7, we derive the following equation for the light energy absorption rate:

$$\begin{aligned} Q(\delta) &= \omega \Omega \left(-B + \left(a + bB + cA + \frac{-\Omega B + A\Omega/q}{\hbar\gamma_{11} + 2\Delta} \right) \frac{\Omega}{2\Delta q^2} - \frac{1}{q} A \right), \quad (\text{A.3}) \\ A &= -\frac{\Omega}{2} \frac{\delta E - \frac{\hbar\gamma}{q}}{(\delta E^2 + (\hbar\gamma)^2) \left(1 + \frac{\Omega}{2} \frac{\delta E - \frac{\hbar\gamma}{q}}{\delta E^2 + (\hbar\gamma)^2} c \right)} (a + bB) \\ B &= -\frac{\Omega}{2} \frac{\hbar\gamma + \frac{\delta E}{q}}{\delta E^2 + (\hbar\gamma)^2} a \frac{1 - \frac{c\frac{\Omega}{2}(\delta E - \frac{\hbar\gamma}{q})}{(\delta E^2 + (\hbar\gamma)^2) \left(1 + \frac{\Omega}{2} \frac{\delta E - \frac{\hbar\gamma}{q}}{\delta E^2 + (\hbar\gamma)^2} c \right)}}{1 + \frac{\Omega}{2} \frac{\hbar\gamma + \frac{\delta E}{q}}{\delta E^2 + (\hbar\gamma)^2} b \left(1 - \frac{c\frac{\Omega}{2}(\delta E - \frac{\hbar\gamma}{q})}{(\delta E^2 + (\hbar\gamma)^2) \left(1 + \frac{\Omega}{2} \frac{\delta E - \frac{\hbar\gamma}{q}}{\delta E^2 + (\hbar\gamma)^2} c \right)} \right)} \\ a &= 1 - \frac{\Omega^2/q^2}{2\hbar\gamma_{20}\Delta + \Omega^2/q^2} \\ b &= 2 \left(\frac{\Omega}{\hbar\gamma_{11} + 2\Delta} - \frac{-\frac{\Omega}{2} + \frac{\frac{\Omega}{2}(\frac{\Omega^2}{2q^2\Delta} + \hbar\gamma_{11})}{\hbar\gamma_{11} + 2\Delta}}{\hbar\gamma_{20} + \frac{\Omega^2}{2q^2\Delta}} \right) \\ c &= -2 \left(\frac{\Omega/q}{\hbar\gamma_{11} + 2\Delta} - \frac{-\frac{\Omega}{2q} - \frac{\frac{\Omega}{2q}(\frac{\Omega^2}{2q^2\Delta} + \hbar\gamma_{11})}{\hbar\gamma_{11} + 2\Delta}}{\hbar\gamma_{20} + \frac{\Omega^2}{2q^2\Delta}} \right). \end{aligned}$$

The following notations were used:

$$\begin{aligned}
 \delta E &= \hbar\omega_{\text{laser}} - \hbar\omega_{01}, \\
 \Omega &= \hbar\Omega_{01} = V_0 E_0, \\
 \hbar\Omega_{0k} &= v E_0, \\
 w &= \hbar\gamma_{\text{tun}}, \\
 \Delta &= \pi\rho w^2, \\
 q &= \frac{\hbar\gamma_{\text{tun}}\Omega_{01}}{\Delta\Omega_{0k}} = \frac{wV_0}{\Delta v}, \\
 \hbar\gamma &= \hbar\gamma_{10} + \Delta, \\
 \gamma_{10} &= \gamma_{11}/2.
 \end{aligned}$$

Here we assume the matrix elements $w = \hbar\gamma_{\text{tun}}$ and $v = \hbar\Omega_{0k}/E_0$ to be independent of the continuum state index k . We note that the complicated equation A.3 has all the correct asymptotical behaviors. In the linear regime ($\Omega_{01(10)} \rightarrow 0$), it reproduces the Fano resonance lineshape, whereas in the non-Fano nonlinear regime ($q \rightarrow \infty$ and Ω_{01} arbitrary) it gives the usual symmetric line broadened by the Rabi energy Ω_{01} .

A.3 Fano factor for a tunnel coupling

Finally, we describe how the voltage dependence of the Fano factor q can be obtained. Figure A.2 shows the potential landscape for the valence and conduction band edges of the system in the z -direction (growth direction). For convenience, the origin on the energy axis corresponds to the state of a hole in the quantum dot, i.e. $E_{\text{h,dot}} = 0$. The tunnel coupling between the dot and the 2D well exists, if the bottom of the first 2D sub-band is above $E_{\text{h,dot}}$, i.e. $\epsilon_1 > 0$. When an electron tunnels into the dot, its 2D momentum satisfies the equality $-\frac{\hbar^2 k_{\parallel}^2}{2m_{\text{h}}} + \epsilon_1 = E_{\text{h,dot}}$, i.e. $\frac{\hbar^2 k_{\parallel}^2}{2m_{\text{h}}} = \epsilon_1$.

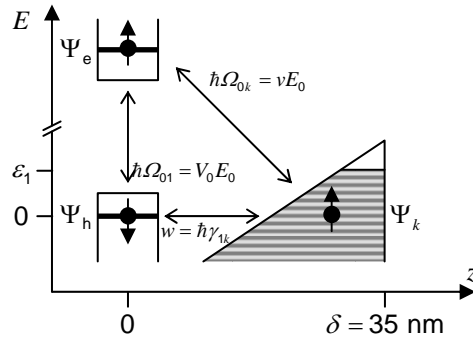


Figure A.2: The scheme for the Fano effect in our structures with a tunnel coupling.

The experimental structure is voltage-tunable and $\epsilon_1 = -|e|\Delta V_g \frac{\delta}{D}$, where $\Delta V_g = V_g - V_{g,\text{crit}}$, $V_{g,\text{crit}} \approx -0.22$ V is the critical voltage below which the tunnel coupling takes place, δ is the distance between the 2D well and dot, D is the total spatial separation between the back contact and top gate ($\delta = 30$ and $D = 175$ nm). There we obtain for the in-plane momentum of electron participating in the tunnel process: $k_{\parallel} = \sqrt{-|e|\Delta V_g \frac{2m_h\delta}{\hbar^2 D}}$, where $\Delta V_g < 0$. The Fano factor includes the amplitudes of three processes $q = \frac{wV_0}{\Delta v} \approx \frac{V_0}{\rho(E_{h,\text{dot}})wv}$, where $\rho(E_{h,\text{dot}}) = \rho(0) = \frac{m_h}{\pi\hbar}\theta(\epsilon_1)$. The direct absorption matrix element is proportional to the electron-hole overlap integral: $V_0 = d_0\langle\Psi_e|\Psi_h\rangle$, where $\Psi_{e(h)}$ are the electron (hole) envelope functions and d_0 is the dipole matrix element of interband optical transition. For the optical transition between the 2D continuum and the dot ($|\Psi_k\rangle \rightarrow |\Psi_e\rangle$ in Fig. A.2), $v = d_0\langle\Psi_e|\Psi_k\rangle$. The tunnelling process $|\Psi_k\rangle \rightarrow |\Psi_h\rangle$ is described by the matrix element $w = \hbar\gamma_{1k} = \langle\Psi_h|U_{\text{dot},v}(r_{\parallel}, z)|\Psi_k\rangle$ [3, 4], where $U_{\text{dot},v}(r_{\parallel}, z)$ is the dot potential in the valence band and $U_{\text{dot},v} \rightarrow 0$ as $r_{\parallel}, z \rightarrow \infty$; here z is the ‘‘vertical’’ variable, and $\mathbf{r}_{\parallel} = (x, y)$ is the in-plane position vector. The above approach to estimate the tunnel coupling in self-assembled dots was used before in [3, 4]. In the wave functions, we can separate the vertical and in-plane variables: $\Psi_{\alpha} = \varphi_{\alpha}(z)\psi_{\alpha}(r_{\parallel})$, where $\alpha = e, h$. For the delocalized state, $\Psi_k = A_0\chi(z)\exp(i\mathbf{k}\mathbf{r}_{\parallel})$, where $\chi(z)$ describes the quantized electron states in the 2D well; this function penetrates the barrier and overlaps with the state Ψ_h . Assuming that $\chi(z)$ is a slow function inside the barrier, we obtain:

$$\begin{aligned} v &= d_0\langle\Psi_e|\Psi_e\rangle \approx d_0A_0\chi(z) \int dz\varphi_e(z) \int dx dy \psi_e(r_{\parallel}) \exp(i\mathbf{k}\mathbf{r}_{\parallel}) \\ w &= \langle\Psi_h|U_{\text{dot},v}(r_{\parallel}, z)|\Psi_k\rangle \approx A_0\chi(0)U_{\text{dot},v} \int dz\varphi_h(z) \int dx dy \psi_h(r_{\parallel}) \exp(i\mathbf{k}\mathbf{r}_{\parallel}), \end{aligned} \quad (\text{A.4})$$

where $U_{\text{dot},v}$ is the dot depth in the valence band; the coordinate $z = 0$ corresponds to the position of the dot. In Eq. A.4, we made a valid estimation: $U_{\text{dot},v}(r_{\parallel}, z) \approx U_{\text{dot},v}$ within the spatial range of the wave function Ψ_h . Using A.4 we obtain the voltage-dependence of the q-factor:

$$1/q \propto \rho(E_{h,\text{dot}})wv \propto \rho(V_g) \int dx dy \psi_h(r_{\parallel}) \exp(i\mathbf{k}\mathbf{r}_{\parallel}) \int dx dy \psi_e(r_{\parallel}) \exp(i\mathbf{k}\mathbf{r}_{\parallel}). \quad (\text{A.5})$$

Taking harmonic-oscillator functions for the states of electron and hole, $\Psi_{e(h)}(r_{\parallel}) \propto \exp\left(-r_{\parallel}^2/2l_{e(h)}^2\right)$, and performing integration we obtain

$$1/q(\Delta V_g) \approx \theta(-\Delta V_g) \exp\left(\frac{|e|\Delta V_g\delta}{D\hbar\omega_{\text{eff}}}\right), \quad (\text{A.6})$$

where $1/\omega_{\text{eff}} = 1/\omega_e + 1/\omega_h$ and $\omega_{e(h)}$ is the in-plane quantization energy of an electron (hole) in a dot. Taking typical parameters $\hbar\omega_e = 30$ meV and $\hbar\omega_h = 20$ meV, we calculate the voltage dependence A.6 and obtain good agreement (Fig.

7.3(b) in chapter 7). Our formula A.6 describes the Fano factor for the case of a continuum of 2D delocalized states. Therefore, the quantity $1/q(\Delta V_g)$ is nonzero for $\Delta V_g < 0$ and has a step at $\Delta V_g = 0$, i.e. at $V_g = -0.22$ V. In the real experiment (Fig. 7.3(b) in chapter 7), we would not expect to see an abrupt step. Instead, we would expect to see a smooth rise at the threshold voltage (-0.22 V). The reason is that the 2D quantum well states with small kinetic energy ($k_{\parallel} \approx 0$) are typically localized and, therefore, the formula A.6 is not applicable for $\Delta V_g \approx 0$. If the well states are localized and located at various distances from the dot, the function $\rho(E_{h,dot})wv$ should smoothly increase for $\Delta V_g \approx 0$. Simultaneously, for sufficiently large k_{\parallel} , the states are delocalized and Eq. A.6 can be applied. This is what we see in Fig. 7.3(b) in chapter 7.

We note that Eq. A.6 provides us with the important voltage dependence. But, the magnitudes of the key parameters (Δ and q) were yet extracted from fitting between theory and experiment. Ideally, of course, we would determine these parameters from the known heterostructure geometry; in practice, the tunnelling rates and bound continuum transition rates depend exponentially on barrier heights we know with only very limited precision, rendering a first principles approach challenging.

References

- [1] Fano, U. Effects of configuration interactions on intensities and phase shifts. *Phys. Rev.*, **124**, 1866 – 1878 (1961).
- [2] Zhang W. *et al.* Semiconductor-metal nanoparticle molecules: hybrid excitons and non-linear Fano effect. *Phys. Rev. Lett.* **97**, 146804 (2006).
- [3] Luyken, R.J. *et al.* The dynamics of tunneling into self-assembled InAs dots. *Appl. Phys. Lett.* **74**, 2486 (1999).
- [4] Dalgarno, P.A. *et al.* Decay dynamics of the positively charged exciton in a single charge tunable self-assembled quantum dot. *Appl. Phys. Lett.* **89**, 043107 (2006).

Appendix B:

List of setup components

- [B 1] Low-temperature microscope attoCFMII, attocube systems.
- [B 2] Aspheric Collimator Lens, Geltech 350260-B.
- [B 3] Aspheric Collimator Lens, Geltech 350390-B.
- [B 4] Silicon *p-i-n* photodiode, BPW34, Siemens.
- [B 5] Low-temperature positioning unit, ANP-xyz-100, attocube systems.
- [B 6] Bath cryostat, 22 l, CryoVac.
- [B 7] 9 T - 11 T Superconducting solenoid magnet, 2" bore, Oxford Instruments
- [B 8] Low-temperature microscope attoCFMIII, attocube systems.
- [B 9] Single-mode 2 x 2 fiber beam-splitter, design wavelength 950 nm, ratio 1/99, G2569, FONT Canada.
- [B 10] Polarizing beam-splitter, PBS-930-020, CVI.
- [B 11] Quarter-waveplate, QWPO-950-04-4, CVI.
- [B 12] Right angle prism mirror, MRA05-G01, Thorlabs.
- [B 13] External-cavity tunable diode laser 940 nm to 980 nm, TEC500, Sacher Lasertechnik.
- [B 14] Faraday isolator, DLI1, Linos GmbH.
- [B 15] Glan Thompson polarizer 100,000:1, GTH 10, Thorlabs.
- [B 16] Multi-order $\lambda/4$ waveplate, WPMQ05M-980, Thorlabs.
- [B 17] Multi-order $\lambda/2$ waveplate, WPMH05M-980, Thorlabs.
- [B 18] PAX Polarimeter, PAX5710IR1, Thorlabs.
- [B 19] Broadband Non-Polarizing Beam Splitter Cube, 700-1100 nm, BS017, Thorlabs.
- [B 20] Single-mode 2 x 2 fiber beam-splitter, design wavelength 850 nm, ratio 50/50 (40/60 ratio for 950 nm wavelength), 2340541, Gould Fiber Optics.
- [B 21] Wavemeter, WA-1150, Burleigh.

- [B 22] Scanning Fabry-Perot 900 - 1100 nm, 1.5 GHz Free spectral range, SA200-9A, Thorlabs.
- [B 23] Preamplifier, Ithaco 1211, DL Instruments, noise = $5 \text{ fA}/\sqrt{\text{Hz}}$.
- [B 24] Lock-in amplifier, 7260, EG&G.
- [B 25] DC-Calibrator, S525, Knick GmbH.
- [B 26] PCI-6014 data acquisition board, with BNC-2110 connector box, National Instruments.
- [B 27] Synthesized function generator, DS335, Stanford Research Systems Inc.

Acknowledgements

The work presented in this thesis was funded by the Deutsche Forschungsgemeinschaft in the framework of the Collaborative Research Center (Sonderforschungsbereich) SFB 631 ‘Solid-State Based Quantum Information Processing’ and the German Excellence Initiative via “Nanosystems Initiative Munich” (NIM).

The high-quality samples central to the presented work were grown by W. V. Schoenfeld, J. M. Garcia, B. D. Gerardot and A. Badolato in the group of P. M. Petroff (University of California, Santa Barbara, USA). The experimental work was carried out in the group of K. Karrai in collaboration with A. W. Holleitner at the Ludwig–Maximilians–Universität München, Germany, together with A. Högele, S. Seidl, B. Alén, S. Rémi, B. Biedermann, K. Weiss and C. Lux and in close cooperation with the group of J. P. Kotthaus (Ludwig–Maximilians–Universität München). I would like to acknowledge the substantial scientific and personal contribution of my co-workers in Munich as well as that of A. O. Govorov and W. Zhang (Ohio University, Athens, USA), A. Imamoğlu (Eidgenössische Technische Hochschule, Zürich, Switzerland) and members of his group M. Atatüre and J. Dreiser, further that of R. J. Warburton (Heriot–Watt University, Edinburgh, United Kingdom) and members of his group P. A. Dalgarno, M. Ediger and B. D. Gerardot. I also wish to acknowledge helpful and valuable discussions with H. Weinfurter, Ludwig–Maximilians–Universität München and E. Lifshitz, Technion, Haifa, Israel. Further the collaboration with O. Sqalli, C. Schulhauser and the team of attocube systems AG, München, is gratefully acknowledged.

Danksagung

Zusammen mit der Zeit der Diplomarbeit habe ich nun fast viereinhalb Jahre an dem Lehrstuhl für Festkörperphysik verbracht. Ich habe hier viel über Physik gelernt, aber auch viele Menschen kennengelernt die in dieser langen Zeit zu so etwas wie einer Ersatzfamilie für mich geworden sind. Diesen Menschen möchte ich nun für ihre Unterstützung und Freundschaft danken.

Zunächst ist da Khaled, mein Doktorvater, von dem ich gelernt habe worauf es in der Physik wirklich ankommt. Er hat mir nicht nur jede Unterstützung zukommen lassen, sondern er gab mir auch Freiheiten und Verantwortung, die nicht selbstverständlich sind. Richard möchte ich dafür danken, dass er sich trotz der Ferne immer begeistert in die Experimente und deren Interpretation eingebracht hat. Außerdem möchte ich ihm dafür danken, dass er durch seine sprachliche Gewandtheit so manches Paper lesbar gemacht hat. Für seinen unermüdlichen Einsatz vor allem bei dem nicht-linearen Fano Experiment möchte ich Sasha danken, der von Anfang an an dieses Projekt geglaubt hat.

In einem Labor ist man nie allein, zumindest nicht in unserer Gruppe. Die Experimente die in dieser Arbeit präsentiert wurden waren nur möglich, durch die exzellente Vorarbeit von Alex, Benito und Stefan, die mich in die Geheimnisse der Quantenpunktspektroskopie eingeführt haben. Darunter geht ein besonderer Dank an Alex, von dem ich gelernt habe wie man ein wohldefiniertes Experiment macht, wie man einen XY-Schreiber benutzt und der immer noch großen Einfluss auf meine Arbeit hat.

Aber auch die, die letztendlich die Experimente mit mir durchgeführt haben, hatten einen großen Anteil an den tollen Ergebnissen in dieser Arbeit: Vielen Dank an meine Diplomanden Sebastian, Benjamin, Kathrina und Christine. Ich bin stolz auch euch! Ohne euch wäre das alles nicht möglich gewesen.

Aber auch jenseits der Gruppe gab es viele Leute die das produktive und kreative Arbeiten in diesem Lehrstuhl erst möglich machten. Zunächst ist da Jörg, der diesen Lehrstuhl zu einer Insel im Haifischbecken der Physik gemacht hat. Außerdem möchte ich ihm danken, dass er wenn es drauf an kam, hinter unserer Arbeit und der Gruppe stand. Dafür möchte ich auch Alexander W. Holleitner danken,

der in einer schwierigen Phase die Verantwortung übernommen hat und sich auch in unsere Experimente einbrachte. Für das menschliche Antlitz der Verwaltung und die Seele des Lehrstuhls geht mein Dank an Bert, der unermüdlich den Lehrstuhl am Laufen hält.

Stephan Manus, der bei elektronischen Problemen immer ein offenes Ohr hatte und bei vielen Experimenten unersetzlich war, sowie Pit, der auch wenn die Heliumversorgung schwierig wurde eine Kanne für uns hatte, möchte ich danken.

Und meinen Computer-Administrator Kollegen gilt mein Dank, darunter vor allem Andy, Daniel, Quirin und Simone.

Aber am Lehrstuhl wurde nicht nur gearbeitet sondern auch gelebt. Das beginnt mit der Mensa und der treuen Mensafraktion, Clemens, Chris, Alex, Stefan, Udo, Benjamin, Kathi, Daniel, Sebastian, Georg, Matthias, Michael, Christian, Klaus und Andy, möchte ich für diese Konstante im Lehrstuhl-Leben danken. Für die Sonderseminare und Schafkopfrunden geht mein Dank an Kathi, Stefan, Quirin, Clemens, Daniel, Christine, Georg und Matthias. Auch die unterhaltsamen Diskussionen über physikalische und unphysikalische Themen mit Quirin, Klaus, Daniel, Matthias, Stefan vor allem mit Clemens möchte ich nicht missen.

Ganz besonders möchte ich noch Stefan hervorheben. Bei ihm möchte ich mich nicht nur für die tolle Zusammenarbeit im Labor bedanken. Auch für die guten Zeiten, die wir zusammen im Atzinger, Tumult oder Crash oder auch in Gemeinsamen Urlauben hatten. Auch hier sollen Alex, Kathi, Chris und Khaled nicht vergessen, sein, mit denen ich jeder Zeit wieder durch die Wüste gehen würde, oder Benjamin mit dem man Seen durchschwimmen kann.

Schließlich sind da noch die Attocubs, Dirk, Angelika, Chris, Tiff und Omar, die bei technischen fragen immer hilfsbereit waren. Die uns oft im "AttoTruck" mit zu Konferenzen genommen haben und mit denen man dann auch auf der Konferenz eine gute Zeit haben konnte.

Zu guter Letzt möchte ich mich noch bei meiner Mutter und meiner Schwester bedanken, die mich während der ganzen Zeit des Studiums und der Doktorarbeit immer unterstützt haben. Auch für das Korrekturlesen der Arbeit möchte ich mich bei ihnen sowie bei Wolfgang, Elli, Stefan, Kathi, Quirin, Clemens und Alex ganz herzlich bedanken.

Lebenslauf

Martin Kroner, geboren am 8. 11. 1976 in Neuendettelsau, ledig

1983 - 1987 Volksschule Neuendettelsau

1987 - 1991 Laurentius-Gymnasium, Neuendettelsau

1991 - 1995 Platen-Gymnasium, Ansbach

1995 - 1997 Laurentius-Gymnasium, Neuendettelsau

1997 Abitur

1997 - 1998 Zivildienst im Alten- und Pflegeheim der
Arbeiterwohlfahrt in Göggingen (Augsburg)

1998 - 2004 Studium der Physik an der Ludwig-Maximilians-Universität München

2000 Vordiplom

2001 - 2002 Auslandsstudium an der Universität Nottingham (UK)

2003 - 2004 Diplomarbeit zum Thema:
*Spektroskopie an einzelnen ladungsdurchstimmbaren
selbstorganisierten Halbleiterquantenpunkten*

2004 Diplom

2004 - 2008 Promotionsstudium und wissenschaftlicher Mitarbeiter am
Center for NanoScience und Fakultät für Physik,
Ludwig-Maximilians-Universität München